The Isospin Symmetry of the A=48, T=2 Mirror Nuclei Studied Through the Mirrored Knockout Technique

Rehab Ali Yajzey

Doctor of Philosophy

University of York

Physics

December 2021

Abstract

The study of excited states of mirror nuclei helps in the extraction of information pertaining to charge-dependent interactions between nucleons. An in-beam γ-ray spectroscopy experiment has been performed to establish a sequence of excited states for the first time in the proton-rich nucleus (T_z=−2) ^{48}Fe (Z = 26, N = 22) and to compare it with its well-known mirror nucleus (T_z = +2) ^{48}Ti (Z = 22, N = 26) in the $f_{7/2}$ shell.

The method of mirrored (i.e., analogue) one-nucleon knockout reactions was applied, in which the $T_z = \pm 2$ mirror pair, ^{48}Fe/^{48}Ti were populated via one-neutron/ one-proton knockout from the secondary beams ^{49}Fe/^{49}V, respectively. The new level scheme of ^{48}Fe was established using the analogue properties of the reactions. The inclusive and exclusive cross sections for knockout have been analyzed for the populated states and also compared with reaction model calculations. In the analysis, large differences between the cross sections of the two mirrored reactions were observed and interpreted in terms of different degrees of binding of the mirror nuclei.

The mirror energy differences (MED) between the isobaric analogue $T = 2$ states of the ^{48}Fe/^{48}Ti have been determined and compared with large-scale shell-model calculations and interpreted in terms of isospin non-conserving (INC) effects. The present study demonstrates the importance of including all isospin-breaking terms to explain the experimental observations. The MED for this mirror pair $A = 48$, as a result of their location in the precise centre of an isolated $f_{7/2}$ shell, are especially sensitive to excitations outside the $f_{7/2}$ shell, and hence, they present a stringent test of the shell–model calculations.

Contents

Abstract **2**

List of Figures **7**

List of Tables **21**

Acknowledgement **26**

Declaration **27**

1 Introduction **28**

1.1 Thesis Structure 34

2 Theory and Background **36**

2.1 Isospin 36

2.1.1 Mirror Energy Differences MED 40

2.2 Nuclear Shell Model 41

2.2.1 Nuclear potentials 42

2.2.2 Residual Interactions 46

2.2.3 MED within the Shell model Calculations 49

2.2.3.1 Multipole Coulomb Term 49

2.2.3.2 The Monopole Radial Term 50

2.2.3.3 The Monopole Single Particle Term 51

2.2.3.4 Additional Effective Isovector Term 53

2.3 Reaction Mechanism 55

2.3.1 Projectile Fragmentation Reaction 55
2.3.2 Nucleon Knockout 56
2.3.2.1 Single Nucleon Knockout Reactions (Eikonal Approximation) 59

3 Experimental Details 62
3.1 Experimental Overview 62
3.2 Experimental Setup 63
3.2.1 Experimental Settings and Plans 63
3.2.2 Primary Beam Production 67
3.2.3 Secondary Beam: A1900 Separator 67
3.2.4 The S800 Spectrometer 70
3.2.4.1 S800 Analysis Line 71
3.2.4.2 S800 Spectrograph and Focal Plane Detectors . . . 72
3.2.4.3 Cathode Readout Drift Chambers (CRDCs) 73
3.2.4.4 Ionisation Chamber (IC) 75
3.2.4.5 Scintillation Detectors 76
3.2.4.6 Recoil Trajectory Reconstruction 77
3.2.5 Gamma Ray Spectroscopy: GRETINA Array 78
3.3 Data Acquisition Triggers 85

4 Calibrations and Corrections Data and Analysis Technique 87
4.1 XFP-OBJ Time Shift Correction 87
4.2 S800 Calibrations and Corrections 88
4.2.1 Ionisation Chamber Gain Matching 88
4.2.2 CRDC Calibration 90
4.2.2.1 CRDC Pad Corrections 90
4.2.2.2 Mask Run Calibrations 91
4.2.2.3 CRDC Drift Corrections 94
4.2.3 Timing Corrections 96
4.2.4 Ionisation Chamber Corrections 97

4.2.5 Particle Identification 99
4.2.6 Particle Detection Efficiency 102
4.3 GRETINA Corrections and Calibrations 104
4.3.1 Efficiency of GRETINA 104
4.3.2 Boosted Efficiency and Doppler Reconstruction of Gamma Rays 107
4.3.2.1 Boosted Efficiency 107
4.3.3 Doppler Reconstruction of Gamma Rays 108
4.4 Analysis Techniques 111
4.4.1 Doppler Correction Analysis 111
4.4.1.1 Optimising the β Value 112
4.4.1.2 Determining Effective Target z-Position 113
4.4.1.3 Determining Effective Target x- and y-Positions . . 115
4.4.1.4 Examining the ϕ-Dependence of the Doppler-Corrected γ-Ray Energies 118
4.5 Production of clean γ-ray spectra 119
4.6 $\gamma - \gamma$ Coincidence Analysis 120

5 Results of Mirrored One-Nucleon Removal Reactions 122
5.1 Population of States in the $T_z = \pm 2$ Mirror Pair 123
5.1.1 Spectroscopy of ^{48}Ti 124
5.1.2 Spectroscopy of ^{48}Fe 129
5.2 Knockout Cross Sections T_z=$\pm$2 Mirror Pair 139
5.2.1 Inclusive Cross-Section Measurements 139
5.2.1.1 N_f 141
5.2.1.2 N_i 142
5.2.1.3 Systematic Errors 143
5.2.1.4 Inclusive Reaction Analysis 144
5.2.2 Exclusive Cross-Sections Analysis 146
5.3 Mirror Energy Differences of ^{48}Fe/^{48}Ti 150
5.4 The $A = 45, T_z = \pm\frac{1}{2}$ mirror pair 151

5.4.1 Spectroscopy of ^{45}V/^{45}Ti Mirror Nuclei 151
5.4.2 Inclusive Cross-Sections of ^{46}V$(-1p,-1n)^{45}$Ti,^{45}V Reactions 157

6 Knockout Cross Sections **158**
6.1 Shell-Model and Cross-Section Calculations $T_z = \pm 2$ Mirror Pair . . 159
6.1.1 Spectroscopic Factors C^2S 159
6.1.2 Theoretical Reaction Cross Sections 161
6.2 Comparison of Experimental and Theoretical Data 172
6.3 Discussion 175
6.3.1 Interpretation of $A = 48$ Data 175
6.3.1.1 Inclusive Cross Section 175
6.3.1.2 Exclusive Cross Section 183
6.3.2 Mirrored Knockout Reaction Result of $A = 45$ 186

7 Mirror Energy Differences **189**
7.1 An Overview of Shell-Model Calculations 189
7.2 Calculations of Isospin-Breaking Terms 190
7.3 Results of MED Shell-Model Calculations 194
7.4 Discussion 197
7.4.1 Interpretation of MED $A = 48$ Data 197

8 Conclusion and Future Work **204**

Abbreviations **207**

References **210**

List of Figures

1.1 The ratio of experimental to theoretical inclusive cross sections for one-nucleon knockout as a function of ΔS. A linear representation of the totality of collected data points from the different regions of the nuclear chart is given by 0.61 – 0.016 ΔS (10). Taken from [26]. 33

2.1 The isospin diagram shows the allowed and forbidden isospin states of nuclei for a particular value of T with different total isospin projection T_z along the z-axis in isospin space. Even-even nuclei exhibit ground states with isospin $T = |T_z|$, as shown by the red line. Taken from [20]. 37

2.2 Shapes of different potentials. Taken from [40]. 43

2.3 Nuclear mean-field depicted with Woods-Saxon potential using Eq. 2.13 of $V_0 = 50$ MeV, $r_0 = 1.25$ fm, $a = 0.7$ fm for an $A = 48$ nucleus. . 44

2.4 The single-particle energy levels of the nuclear shell model from a simple harmonic oscillator potential showing the effect of the surface and spin-orbit correction. The experimentally observed magic numbers are only reproduced after both the l^2 and spin-orbit ($\vec{\boldsymbol{l}}.\vec{\boldsymbol{s}}$) terms have been included. Taken from [41]. 45

2.5 A schematic representation of the components of a shell-model calculation, showing the inert core (^{40}Ca such as used in present work) within the harmonic oscillator potential. The two types of fermions, protons and neutrons, are arranged in some valence single particle levels, $f_{\frac{7}{2}}$, $p_{\frac{3}{2}}$, $f_{\frac{5}{2}}$, and $p_{\frac{1}{2}}$. The truncation region shows that some single particle levels are not included in the shell-model calculation. Adapted from [44]. 48

2.6 A calculated spatial overlap of two protons coupled to different angular momentum in the $f_{\frac{7}{2}}$ shell. Taken from [47]. 50

2.7 A comparison of experimental and theoretical MED for four mirror pairs in the $f_{\frac{7}{2}}$ region. The solid line represents the predicted MED, including the fitted V_B term, whereas the dashed line represents the predicted MED without the V_B term. Taken from [9]. 54

2.8 Abrasion-ablation fragmentation model. Adapted from [52]. 56

2.9 The single-nucleon knockout reaction types: stripping reaction process (on the top right) and diffraction reaction process (on the bottom right). 57

2.10 The coordinate system adopted for the core, valence nucleon, and target three–body systems. Adapted from [66]. 61

3.1 The ^{58}Ni primary beam is fragmented into the cocktail secondary beams of interest (squared in blue), such as ^{49}Fe/^{49}V and ^{46}V (see text for more details) at the entrance of the A1900 separator. The mirror pairs of interest (squared in red), ^{48}Fe/^{48}Ti and ^{45}V/^{45}Ti, are populated via one nucleon-knockout reaction from these secondary beams. 63

3.2 A schematic of the ion source (SuSI) coupled with K500/K1200 cyclotrons and the A1900 separator. Taken from [67]. 68

3.3 The incoming secondary beams are shown with the A1900 tuned to produce ^{49}Fe and the other beams produced with same setting, which can be observed from the XFP and OBJ scintillators times of flight relative to the E1 scintillator in the S800 spectrograph focal plane. 69

3.4 The S800 spectrometer consists of the analysis line and spectrograph. The beam of interest enters the S800 spectrometer at the object and then passes through the analysis line. The resulting particles are separated using the spectrograph after the reaction at the secondary target [74]. 70

3.5 Schematic of the detectors located in the focal plane of the S800 spectrometer [75]. 73

3.6 A diagram illustrating the CRDC detector, where the particles are ionised as they pass through each CRDC, creating free electrons that drift towards the anode wire. As a result, a positive ion is produced on one of the cathode pads. A Gaussian function is fitted to determine the x-position of the particle, and the y-position is calculated based on the electron drift time to the anode wire in relation to the trigger at the E1 scintillator. Taken from [74]. . . . 74

3.7 The standard configuration of GRETINA at the NSCL located in front of the S800 spectrograph's entrance and surrounding the secondary target. This figure shows seven GRETINA modules (taken from different work [68]), four of which are mounted in the 58° ring and the remaining three modules are mounted at 90°. The data presented in this work were obtained with nine GRETINA modules. Four modules are mounted in the 58° ring and five are located at 90° ring. Taken from [68]. 79

3.8 An illustration of four crystals packed in one module, each crystal is segmented into six separate electrical contacts along the length of the crystal α to ϕ, and a further six segments in the radial direction (numbered one to six), resulting in a total of 36 segments. On the right, the preamplifier compartment for each module is shown to amplify and extract signals from the detector and a liquid nitrogen dewar of the GRETINA detector module. Taken from [69]. 80

3.9 A demonstration of the angular coverage of GRETINA extracted from the current data, which consists of 36-fold segmented HPGe detectors (four detectors at 58° and five detectors at 90°) directed at the secondary target position. 82

3.10 Comparison of the add-back methods of GRETINA, the calorimeter (green), cluster (red) and neighbour (black) and without add-back (blue) implemented for the same ^{133}Ba calibration source γ-ray run taken at the beginning of the experiment. The inset spectrum displays the same plot at the 383 keV peak of ^{133}Ba, where it clearly shows the difference of the improved peak-to-background ratio for add-back. 84

3.11 The histograms of recorded events of the triggers-register pattern is plotted against their channel number (a) with and without applying Downscaler (which rejects a fraction of the incoming events) (a) and (b), respectively. Channel 1 represents S800 events only; channel 2 represents COINC events only; channel 3 represents both S800 and COINC events. 86

4.1 The outgoing PID plot of the energy loss in the IC against the ToF measured in between the OBJ scintillator and the E1 scintillator, gated by the ^{47}Cr secondary beam, where (a) before and (b) after the IC calibrations were applied. There is an apparent decrease in background counts post calibration and an increase in statistics for some of the outgoing recoils. 89

4.2 Plot of the 16 channels in the IC before (a) and after (b) correcting the IC. All the channels were matched to channel 0 such that the gains and offsets produced are not overestimated. 90
4.3 The CRDC pads vs energy loss before (a) and after (b) pad calibrations have been applied to an outgoing beam. 92
4.4 The CRDC mask pattern used for the mask calibrations. The blue circles correspond to holes in the mask, while the red lines correspond to slits through which particles can pass. The four points forming the L shape in blue are used as reference points at 0, 10, 20, and 30 mm. Left-hand values correspond to the y-position of the points on the mask in mm, while right-hand values are used to denote the rows of blue points. 92
4.5 (a) The CRDC1 mask run before calibration, with dots from the distinctive L shape, was used to measure the y-positions of the dots, which were plotted versus the actual positions of the masks, to obtain the gain. (b) Demonstrates the same mask run after a gain and offset calibration was applied to match the positions of each dot on the pattern to the values shown in Fig. 4.4. 94
4.6 The change in the CRDC y-position in each of the runs while gated on ^{46}Cr populated through the ^{47}Cr secondary beam. (a) before the CRDC drift correction and (b) after the offsets and gains $\times$ gain factors have been applied. It can be seen that after applying the drift correction, the y-position of the runs was shifted to 0 mm. . . 96
4.7 CRDC spectra of dispersive x position (x_{fp}) and dispersive angle (a_{fp}) at the S800 focal plane relative to the time-difference between E1 and OBJ scintillators (i.e. ToF). These spectra are shown before (a,c) and after (b,d) applying the ToF corrections (see text for more information). The effects of applying ToF corrections display that the blobs in (b) and the streaks in (d) have become vertical and separated. 97

4.8 Spectra of ion chamber energy loss (dE) against x-position measured of the first CRDC, before (a) and after (b) the positional corrections when gating on ^{46}Cr outgoing recoil (populated through the ^{47}Cr secondary beam). 98

4.9 The outgoing PID in coincidence with incoming ^{47}Cr secondary beam shows the effect of S800 focal plane detector corrections. The outgoing recoils in the PID plot appear to be sharper and well separated. 99

4.10 The PID spectrum produced from the reaction at secondary target gated on incoming ^{49}Fe secondary beam. The vertical lines represent the total isospin, T_z. The labels refer to the ^{49}Fe beam and the main nucleus of interest, ^{48}Fe. 100

4.11 The PID spectrum produced from the reaction at the secondary target gated on incoming ^{49}V secondary beam. The labels indicate the ^{49}V beam and the main nucleus of interest, ^{48}Ti. 101

4.12 The PID spectrum produced from the reaction at the secondary target gated on incoming ^{46}V secondary beam. The labels indicate the ^{46}V beam and the main nucleus of interest, ^{45}V. 101

4.13 The PID spectrum produced from the reaction at secondary target gated on incoming ^{46}V secondary beam. The labels indicate to the ^{46}V beam and the main nucleus of interest, ^{45}Ti. 102

4.14 The singles efficiency of GRETINA in the nine-module configuration without add-back (single-crystal) (red) and with add-back (blue) using ^{56}Co, ^{133}Ba, and ^{152}Eu sources placed at the centre of GRETINA. 106

4.15 The boosted efficiency curve based on the configuration of the nine detectors used in the current experiment. 108

4.16 A comparison of the Doppler-corrected γ-ray spectra for ^{46}Cr (1n knockout from ^{47}Cr secondary beam) with (red) and without (blue) including the drift correction through using the inverse map (a_{ta}, b_{ta}, and y_{ta}) in the Doppler correction process. 111

4.17 Optimising β value for decays with a short lifetime, 1094.9 keV corresponding to $4^+ \rightarrow 2^+$ transition in ^{46}Cr to examine any possible dependence of the Doppler reconstruction. (a) and (c) demonstrate the dependence of the Doppler-corrected energy on the GRETINA θ angle, as well as the corresponding γ-ray spectrum, respectively, corrected to $\beta = 0.305$. The same plots are shown in (b) and (d) with Doppler correction having an optimum value of $\beta = 0.383$, eliminating any dependency on the GRETINA θ angle. 114

4.18 A comparison of the Doppler-corrected γ-ray energy of 1094.9kev with no target z-position offset (black) and with using an optimum target z-position (red) (the combined effect of z_{mid} value of -1.2 mm for the first half and -0.2 mm for the second half of the data) where the measured energy aligned with that in the literature. The two spectra are Doppler corrected with a β value of 0.383. 115

4.19 A comparison of the Doppler-corrected γ-ray energy indicates the literature energy of 892.16 keV, $2^+ \rightarrow 0^+$ decay of ^{46}Cr while adjusting the effective target x- and y-positions used in the Doppler correction process. (a) and (b) show the same plots of the 58° detector ring of GRETINA before and after adjusting the effective target positions, respectively. 117

4.20 A comparison of the Doppler-corrected γ-ray energy indicates the literature energy of 892.16 keV, $2^+ \rightarrow 0^+$ decay of ^{46}Cr while adjusting the effective target x- and y-positions used in the Doppler correction process. (a) and (b) show the same plots of the 90° detector ring of GRETINA before and after adjusting the effective target positions, respectively. 117

4.21 Examining the dependence of Doppler-corrected energy of 1094.9 keV, $4^+ \rightarrow 2^+$ decay of ^{46}Cr with respect to the difference in the angle of the beam and the front and back angles of the position of detection in GRETINA, dϕ. The spectrum appears flat at 1094.9 keV, which means that there is no dependence on the angle of the beam θ with respect to dϕ. 118

4.22 Doppler-corrected γ-ray energy spectra of ^{46}Cr obtained by summing all interactions within one crystal (black histogram) and using the add-back method (red histogram). 119

4.23 A 2D histogram of $\gamma - \gamma$ matrix, gated on incoming ^{47}Cr beam and outgoing ^{46}Cr nucleus. The x and y axes both show γ-ray energies for coincident events. 121

5.1 The Doppler-corrected energy spectrum for γ rays, using an add-back procedure, in coincidence with ^{48}Ti fragments, populated via one-proton knockout reactions from ^{49}V. The $\beta = v/c = 0.402$ value used for the Doppler reconstruction is optimised for fast transitions. 124

5.2 γ-γ coincidence spectra of ^{48}Ti when gating on (a) 983, (b) 175, (c) 1037, (d) 1312 (e) 1212, and (f) 1557 keV transitions. These spectra were produced by projecting 2D $\gamma - \gamma$ matrix spectrum around these peaks and performing a local background subtraction from the right and left the peak. (a–f) spectra have been produced using an average $\beta = v/c$ value of 0.402. 126

5.3 Level scheme of ^{48}Ti showing the γ rays observed in this work. Energies, ordering, and spins and parities are taken from [29], and the ordering was also confirmed in the present work through γ-γ coincidence analysis. The dashed lines indicate tentative transitions, and the tentative γ rays are presented in parentheses. Transition widths are proportional to γ-ray intensities measured in this work and are determined relative to the intensity of the $2_1^+ \rightarrow 0^+$ transition. . . . 127

5.4 The Doppler-corrected γ-ray spectra using the add-back procedure (see text) for (a) ^{48}Ti and (b) ^{48}Fe populated through one-nucleon knockout from ^{49}V and ^{49}Fe. The $\beta = v/c$ value is optimised for fast transitions in (a) and (b), while a lower β value is utilised for the spectrum insert of (b) for the 971-keV transition (see text). The spectrum used in the insert in (b) was created without add-back, as the fits in the analysis were applied to spectra without add-back. . . 131

5.5 Gamma-gamma coincidence matrices using (a) add-back and (b) no add-back for ^{48}Fe were produced in one-neutron knockout from ^{49}Fe. The insets show the projections of the $\gamma - \gamma$ coincidence matrices. This illustrates the effect of add-back, especially in $\gamma-\gamma$ coincidence analysis, which moves the counts from the background into peaks. 132

5.6 A spectra from γ-γ coincidence analysis, using add-back, was measured to be in coincidence with the (a) 256 keV(1), (b) 971 keV(1), and (c) 1284(1) keV transitions in ^{48}Fe. These spectra were produced by projecting Fig. 5.5 around the 971, 256, and 1284 keV peaks and performing a local background subtraction from the right and left of the peak. The dashed lines indicate the strongest peaks that have been observed from the gamma-ray coincidence analysis. (b) and (c) spectra have been produced using an average $\beta = v/c$ value of 0.395, while (a) spectrum has been produced with the lower β value of 0.390 (see text). 134

5.7 A spectra from γ-γ coincidence analysis, using add-back, was measured to be in coincidence with the (a) 1407 keV(3) and (b) 2505(5) keV transitions in ^{48}Fe. These spectra were produced by projecting Fig. 5.5 around the 1407 and 2505 keV peaks and performing a local background subtraction from the right and left of the peak. (a) and (b) spectra have been produced using an average $\beta = v/c$ value of 0.395. 135

5.8 The new energy level scheme for ^{48}Fe (a) observed in this work compared with the level scheme of ^{48}Ti (b) as observed in this experiment. The intensities of the γ rays are indicated by the width of the arrows and are determined relative to the intensity of the $2_1^+ \rightarrow 0^+$ transition. Tentative transitions are represented by the dashed lines. 136

5.9 Experimental level scheme for ^{48}Fe alongside shell-model predictions. The shell-model calculations have been performed in ANTOINE with the KB3G interaction [45]. 138

5.10 Spectra of the parallel momentum distribution, d_{ta} against the number of counts, gated on the (a) incoming ^{49}Fe beam and outgoing ^{48}Fe recoil and (b) incoming ^{49}V beam and outgoing ^{48}Ti recoil. These spectra show quite a substantial loss of counts due to the limited acceptance angle of the S800 spectrograph. Since the spectra are asymmetric, a Gaussian fit was applied separately to the right-hand side (blue line) and the left-hand side (green line) of the histogram, while the red fit considered the total number of events, including the missing part, to correct the acceptance of the residue, A. 142

5.11 The particle identification spectra of the ^{49}Fe and ^{49}V secondary beams from the unreacted beam runs. The particle identification gates used in the ^{49}Fe and ^{49}V unreacted beam runs are shown. . . 142

5.12 Change in the purity from one run to the next as a function of the run number. 144

5.13 The measured relative cross sections to states in (a) ^{48}Fe and (b) ^{48}Ti via one-neutron and one-proton knockout, respectively. The sum of the statistical and systematic uncertainties are given. 148

5.14 Experimental MED for the $A = 48$, $T_z = \pm 2$ mirror pair that were measured using Eq. 2.7. The MED for the $J \neq 0$ yrare states in (b) are plotted relative to the $J = 0$ ground state. 150

5.15 The Doppler-corrected spectra for (a) ^{45}Ti and (b) ^{45}V identified following one-nucleon knockout from ^{46}V. The $\beta = v/c$ values utilised in (a) 0.386 and (b) 0.380 were chosen to optimise the γ-ray spectra to acquire the best resolution for the observed transitions. A number of the new γ rays were observed at high energy and require further analysis to assign these transitions. 152

5.16 A large γ-ray peak at (a) 292 keV and (b) 329 keV in ^{45}Ti and ^{45}V Doppler-corrected spectra, respectively, associated with the decay of states with a long lifetime. 153

5.17 Energy level schemes for ^{45}Ti (top) and ^{45}V (bottom). Energy of states, γ-ray energies, spins and parities were assigned based on the previous study [89] and confirmed in the present work. The widths of the arrows are proportional to the relative intensity of the γ-ray transitions populated through knockout reactions and are determined relative to the intensity of the $11/2^- \rightarrow 7/2^-$ transition. For the decays of the $3/2^+$ states, the intensity is not known hence they are indicated by dashed lines. 156

6.1 A flowchart of the procedure for calculating the nucleon removal cross sections from the projectile. 162

6.2 (a) Calculated and (b) experimental relative cross sections for excited states in ^{48}Fe populated via one-neutron knockout from ^{49}Fe ground state ($J^\pi = 7/2^-$). The sum of the statistical and systematic uncertainties are presented. The model-space used for (a) is limited to positive-parity states; therefore, for (b), the total experimental cross section is determined based on the positive-parity states only. 173

6.3 (a) Calculated and (b) measured final state exclusive cross sections for the population of individual states in ^{48}Ti populated through one-proton knockout from ^{49}V ground state $7/2^-$. 174

6.4 The ratios, R_s, of the experimental and theoretical inclusive one-nucleon removal cross sections for each of the projectile nuclei indicated to ^{48}Fe (red) as an upper limit (due to missing *sd* strength) and ^{48}Ti (blue). R_s is shown as a function of the parameter ΔS. The trend line (solid line) given in Eq. (2), as reported in [26], and a band of half-width 0.1 (dashed lines) have been applied, which represent the totality of the collected data points. The R_s value of ^{48}Ti was plotted as the lower limit (estimate) since a theoretical (maximum) inclusive cross section to ^{48}Ti was estimated by evaluating the sum-rule strength for removal of $f_{7/2}$- and *sd*-shell protons, see text for details. 178

6.5 A diagram demonstrating the estimated excitation-energy centroids of the single-particle strength distribution (the sum-rule strength) for the removal of the $f_{7/2}$-shell and full *sd*-shells protons. All these final states are expected to be bound for ^{48}Ti, whilst, for the analogue states in ^{48}Fe, only the states resulting from $f_{7/2}$ removal are expected to be bound. 182

6.6 The ratio of the experimental to the theoretical cross sections for yrare states 2_2^+, 4_2^+ and 6_2^+ plotted against the separation energies ΔS for both mirrored one-nucleon-knockout reactions. The red data represent one neutron knockout from ^{49}Fe to ^{48}Fe and the blue data represent one-proton knockout from ^{49}V to ^{48}Ti. 186

6.7 A diagram demonstrating the estimated excitation-energy centroids of the single-particle strength distribution (the sum-rule strength) for the removal of the $f_{7/2}$-shell and full *sd*-shells protons. All these final states are expected to be bound for ^{45}Ti (except the $d_{5/2}$ removal), whilst, for the analogue states in ^{45}V, only the states resulting from $f_{7/2}$ removal are expected to be bound. 187

7.1 A schematic diagram of the MED calculations of the $A = 48$, $T_z = \pm 2$ mirror pair using the full fp space shell-model calculations, implemented using the ANTOINE code. 191

7.2 Proton and neutron fp-shell occupancies for states ((a) yrast states and (b) yrare states) in ^{48}Fe. Calculations performed with ANTOINE and the KB3G [45] interaction in the full fp-shell space. The $p_{\frac{1}{2}}$ occupation is negligible and the $f_{\frac{7}{2}}$ occupation increases with a corresponding decrease in $p_{\frac{3}{2}}$. 193

7.3 Contributions to the $A = 48$, $T_z = \pm 2$ MED (for both (a) yrast states and (b) yrare states) from individual isospin-breaking terms, along with the resultant predicted MED (the sum of the four components) in solid lines in (a) and (b). The solid line uses a single -100 keV INC matrix element for J=0 for all fp orbitals. In (b), the MED for the $J \neq 0$ yrare states are plotted relative to the $J = 0$ ground state. 195

7.4 The experimental and theoretical MED for the A=48, $T_z = \pm 2$ mirror yrast (a) and yrare states (b). The solid line and the dashed line in (a) and (b) both are the shell-model calculations, which include all the four components and correspond to two different ways of defining the INC term V_B. The solid line uses single -100 keV INC matrix element for J=0 for all fp-orbitals and the dashed line uses four parameters extracted from the fit across the $f_{\frac{7}{2}}$ shell [9]. The sum of the four components of the shell-model calculations (defined in the text) is presented in solid lines in (a) and (b) and also were graphed in Fig. 7.3. In (b), the MED for the $J \neq 0$ yrare states are plotted relative to the $J = 0$ ground state. 198

7.5 A theoretical MED results for the A=48, $T_z = \pm 2$ mirror yrast (a) and yrare states (b) with the particle restricted in $f_{7/2}$ shell ($t = 0$) where MED = 0. The MED changes dramatically once the particles are excited out of the $f_{7/2}$ shell (t = 1, 2, 3, 4, 5, 6, 7, and 8). In (b), the MED for the $J \neq 0$ yrare states are plotted relative to the $J = 0$ ground state. 201

7.6 Theoretical energy-level schemes predicted by large-scale shell-model calculations using KB3G interaction in comparison with experimental energy-levels schemes of populated states in one-neutron knock-out from ^{49}Fe to ^{48}Fe. The figure shows the evolution of theoretical levels with the number of excitations allowed to the upper fp shell, t. The negative parity states ($J^\pi = 3^-$ and 5^-) cannot be made from KB3G shell-model calculations and, hence, are not present in the t schemes. Theoretical energies converge towards experimental values, reaching good agreement from $t = 4$ up to 8. 203

List of Tables

3.1 Summary of the different settings and data for the sub-experiments performed at the NSCL. The beam purity, Downscaler (Ds) and duration of the runs are also shown. The nuclei used in this analysis are highlighted in blue. 66

4.1 An overview of the CRDC mask run used for CRDC position calibrations for each experimental run. The experimental runs began with run 19, and all runs before it were test runs and calibration of the γ-ray efficiency using sources. 94

5.1 The energy for excited states, γ-ray energies (in keV) and relative intensities (with and without the add-back procedure) for γ decays for the ^{48}Fe and ^{48}Ti mirror pair. 128

5.2 The data for the ^{48}Fe and ^{48}Ti residues in reacted beam runs. The correction factor C_{live}, the total particle detection efficiency ϵ, downscaler factor Ds, the number of observed residue N^R_{obs}, and the acceptance for the reacted runs A calculations are described in Section 5.2.1.1. 144

5.3 The data for the ^{49}V and ^{49}Fe secondary unreacted beam runs. The live-time correction factor C_{live}, the total particle detection efficiency ϵ, downscaler factor and the unreacted beam normalisation rate K_{norm}, downscaler factor Ds, the number of observed bean particle N^u_{obs} and the acceptance for the unreacted runs A calculations are described in Section 5.2.1.2. 145

5.4 The experimental inclusive cross section for the two reactions ^{49}Fe $\rightarrow$ ^{48}Fe and ^{49}V $\rightarrow$ ^{48}Ti determined from the number of measured particles in the A1900 separator and S800 spectrometer. 145
5.5 The experimental exclusive cross sections for states directly populated in this work through one-nucleon knockout, see text for details. 149
5.6 The excitation energy for excited states, γ-ray energies (in keV) and relative intensities measured in this work for γ decays for the ^{45}V and ^{45}Ti mirror pair. 155
5.7 The experimental inclusive cross section for the two reactions populated from the same secondary beam, ^{46}V $\rightarrow$ ^{45}V and ^{46}V $\rightarrow$ ^{45}Ti. 157

6.1 The ground state of ^{49}Fe/^{49}V calculated using the ANTOINE code [43] in the full fp valence space using the KB3G interaction [45]. This table displays all the ground state admixtures greater than 1%. 160
6.2 C^2S of $A = 48$ mirror nuclei in the full fp valence space was calculated using the ANTOINE code [43] using the KB3G interaction [45]. 161
6.3 Hartree-Fock neutron single-particle radii (rms) and energies for each orbital of ^{49}Fe projectile, where the fp orbitals (highlighted in blue) were used in the single-nucleon cross-section calculations. . . 165
6.4 Hartree-Fock proton single-particle radii (rms) and energies for each orbital of ^{49}V projectile, where the fp orbitals (highlighted in blue) were used in the single-nucleon cross-section calculations. 166
6.5 The potential radius r_0 parameters of the nucleon removal from fp and sd (in case of ^{49}V (-1p) only) orbitals with diffuseness $a = 0.7$ fm and spin-orbit strength $V_{so} = 6$ MeV. 167

6.6 A summary of the relevant results from the present study, where the predicted cross sections for states observed in ^{48}Fe (^{49}Fe - 1n) reaction, 0^+, 2^+, 4^+, and 6^+ states resulted from a direct neutron removal from the fp orbital in the projectile. The S_n of ^{49}Fe is 14.813(9) MeV [96], and the mass dependent, $(A/A-1)^3$, is 1.0638. The individual stripping and diffraction break-up components, as well as their summed single-particle reaction cross section, were calculated using the reaction model. The C^2S are taken from the ANTOINE [43] shell-model calculations from Table 6.2. j value is the orbital of the neutron removal from the initial state of the projectile. 168

6.7 A summary of the relevant results from the present study, where the predicted cross sections for states are observed in ^{48}Ti(^{49}V - 1p) reaction, 0^+, 2^+, 3^+, 4^+ and 6^+ states as a result of a direct proton removal from the fp orbital in the projectile. The S_p of ^{49}V is 6.758(8) MeV [96] and the mass dependent, $(A/A-1)^3$, is 1.0638. The individual stripping and diffraction break-up components, as well as their summed single-particle reaction cross section, were calculated using the reaction model. The C^2S are taken from the ANTOINE [43] shell-model calculations from Table 6.2. j value is the orbital of the proton removal from the initial state of the projectile. 169

6.8 The experimental and theoretical exclusive cross sections for states directly populated in this work through one-nucleon knockout. The inclusive cross sections are listed in the final row (the theoretical inclusive cross section could not be determined for ^{48}Ti, see text for details). The theoretical cross sections are calculated using the experimental separation- and residue-excitation energies. 171

6.9 This table shows the relevant results from the present study. The experimental and theoretical exclusive cross sections for both ^{48}Fe and ^{48}Ti and the angular momentum and parity J^{π} values. The separation energy differences ΔS, $(S_n + E_x) - S_p$ for neutron knockout (^{48}Fe) and $(S_p + E_x) - S_n$ for proton knockout (^{48}Ti) for the positive-parity yrast and yrare states are shown, as well as the ratio between the experimental to the theoretical inclusive cross sections (R_s) with the separation energy differences ΔS only for ^{48}Fe is listed. The theoretical inclusive cross section could not be determined for ^{48}Ti; hence, the R_s also could not be determined, see text for details. 179

6.10 An estimate of the maximum possible cross sections of ^{48}Ti(^{49}V - 1p) reaction due to removals from the assumed-filled *sd*-shell orbitals. 183

7.1 Experimental and theoretical $A = 48$ MED. The theoretical MED is presented with both $J = 0$ and fitted parameters for V_B term. This data has been graphed in Fig. 7.4. 196

Acknowledgements

I would like to thank the Saudi Arabian Cultural Bureau and Jazan University for the scholarship and their support and the funds they provided to me to pursue my PhD degree at University of York.

Through my PhD journey, there were so many wonderful people who accompanied me. First and foremost, I was lucky enough to enjoy doctoral life under a great supervisor, to whom I will be eternally grateful, Professor Michael Bentley, whose constant support and guidance as well as his regular feedbacks and suggestions gave me important insights and leads throughout this research. I would also like to thank him for having the confidence in me to work in this project and for clarifying various subtleties of nuclear physics that pushed me to explore more in my research area. I learned a huge amount under his supervision, and appreciate all his efforts in seeing my PhD towards completion. Working with Prof Bentley during the last four years has been a thoroughly enjoyable experience, and my time as a PhD student has been enriched by his expertise.

I would also like to thank all my colleagues in the Nuclear Physics Group at York, for their assistance throughout my PhD, particularly Dr Ryan Llewellyn and Sivi Uthayakumaar for their continues discussion with me on data analysing. Thanks also to Dr Suso Pereira-Lopez, Dr Ryo Taniuchi and Dr Aliyu Bala for their help and advice. I would like to give special thanks to my close friend and colleague Dr Faten Alsomali, who always believed in me and encouraged me to do my best.

Thanks also to Professor Jeffrey Tostevin for providing advice on the cross-section discussion and for providing the codes to calculate the reaction cross sections. Furthermore, I'd like to say a big thank you to Dr Ed Simpson for kindly discussing

the method of the knockout calculations. I also gratefully acknowledge Dr Mark Spieker for providing discussions on data analysis.

My biggest and deepest thanks go to my parents, my father Mr. Ali Yajzey and my mother Mrs. Ameria Alsaayigh, for their love and prayers, and for their support. Making them proud was my primary goal to pursue my graduate studies. I am grateful to all my family in Saudi Arabia for their prayers, love, and support, especially my sisters, brothers, aunts, grandmother, and grandfather who passed away while I was in my third year of my PhD. A special thank you to my father-in-law Mohammed Arishi for his help and support.

It is with deep gratitude that I thank my husband, Mr. Hassan Arishi and my young children, Alma Arishi, Alin Arishi, Mohammed Arishi, and Ziad Arishi, who traveled thousands of miles with me for this long adventure abroad. They have shown patience and support beyond comprehension during a difficult extended stay when I was most of the time away from home to conduct my work at the university campus–as well as in the pandemic circumstances.

Special thanks to my devoted lovely husband who has been my solid rock. I fondly remember my husband calling me every day when I worked from the university campus to ask about my progress and staying up all night while doing my work from home. His unquestioned support starting from my high school, Bachelor's degree, Master's project to my PhD project motivated me to work harder and faster to overcome difficulties and achieve my daily goals. To my husband I say Thank you without you all my journeys would have been a lot more difficult, if not impossible.

Declaration

The submission of this thesis for the degree of Doctor of Philosophy is in accordance with the regulations of the University of York. The work presented herein has not been previously submitted for any other degree or qualification at this, or any other, university. I declare that this thesis is a presentation of original work and that I am the sole author. All sources of information that have been used are acknowledged as references.
All work was carried out under the supervision of Prof. M. A. Bentley. The experimental work outlined in this thesis was undertaken in collaboration with staff at the National Superconducting Cyclotron Laboratory of Michigan State University, as well as other collaborators.

Some of the work presented in this thesis has now been published in the paper:

Yajzey, R., et al. "Spectroscopy of the T= 2 mirror nuclei ^{48}Fe/^{48}Ti using mirrored knockout reactions.", Phys. Lett. B 823, 136757 (2021)

Signed

Chapter 1

Introduction

Mirror nuclei are a particularly significant research area since they provide a way to test the basic symmetry of the strong nuclear force as well as the principle of isospin symmetry [1]. Isospin symmetry is connected to the approximate charge independence and charge symmetry of the strong nuclear force, which is a cornerstone of our understanding of nuclear structure. The isospin dependence of nucleon–nucleon forces and its implication for nuclear masses and structural effects, including level structures and neutron-proton pairing, is now one of the key research areas in nuclear structure physics. The assumption of isospin symmetry would result in isobaric multiplets being degenerate in energy, except for the effects of the Coulomb force [2].

This work is aimed at investigating and understanding isospin symmetry by studying two main aspects in the $f_{\frac{7}{2}}$ shell, in the $A = 48$ nuclei with $T = 2$: (a) mirror energy differences, MED, study and (b) the examination of analogue spectroscopic factors, i.e., the evaluation of the structure of analogue states, through direct reactions, to understand what happens to the symmetry of the underlying wavefunctions in nuclei that are unbound or weakly bound. To address these questions, the experiment was performed at NSCL through the mirrored-knockout method. This method was first applied by Milne *et al.* [3], in which the proton (neutron)-rich

member of the mirror pair is populated by one-neutron (one-proton) knockout. Pairs of reactions where the parents and the daughter nuclei are themselves mirrors are defined as mirrored reactions. This technique involves a complete analogue pair of reactions reflected along the $N = Z$ line; thus, a comprehensive comparison of both of the analogue reactions is conducted. The experiment seeks to measure a range of observables, including the MED, inclusive cross sections from single nucleon removal (σ_{inc}) and exclusive cross sections (σ_{exc}) for populating the excited states in the residue.

The first observation of the excited states of $T_z = -2$, ^{48}Fe and the comparison to the analogous states in its mirror nuclei, $T_z = +2$ ^{48}Ti, allows for the extension of MED studies of mirror nuclei in the $f_{\frac{7}{2}}$ shell in order to evaluate these energy differences. For the proton-rich nucleus, ^{48}Fe, no excited states have been previously observed apart from a tentative 2^+ state at 969.5(5) keV that has been reported in one previous study populated via beta-delayed proton decay of ^{49}Ni [4]. In the existing literature, there are only two studies of $T = 2$ mirror pairs system [5] and [6]. The first study measured the strength of the 0^+_{gs} to 2^+_1 in the mirror nuclei ^{32}Ar and ^{32}Si by employing the techniques of intermediate-energy Coulomb excitation and inelastic proton scattering in inverse kinematics, respectively [5]. The second study in the $T = 2$ system used a direct 2N-knockout reaction to populate mirror nuclei ^{52}Ni/^{52}Cr [6].

Analogue states belonging to the same isobaric multiplet are almost identical, with the few differences arising from isospin non-conserving (INC) interactions such as the Coulomb interaction. The differences in their excitation energies, known as mirror energy differences (MED) for mirror pairs, have been widely used to investigate the microscopic structure of atomic nuclei, using Coulomb effects.

INC interactions leads states of different isospin to mix with each other [7]. A detailed explanation of these INC phenomena is provided in Ref [8, 9]. A significant understanding of these effects is needed in shell model calculations in order to reproduce experimental data successfully [10]. In an early MED study by O'Leary *et al.* [11], the MED for the $T_z = \pm\frac{1}{2}$ mirror pair ^{49}Mn and ^{49}Cr demonstrated

how the spin affects the MED, i.e., for larger spins, larger MED were observed. This was interpreted as particle alignment, which suggested that proton–proton spatial separation would increase with an increase in the alignment of the nucleon angular momentum vectors.

As well as these INC interactions, which are expected to contribute to the MED, there is an additional effective isovector (V_B) interaction that has to be included in the model to reproduce the data. Recently, there have been extensive studies on the MED in the upper *sd* and lower *pf* shell regions, coupled with detailed shell-model calculations– e.g. [6, 8, 10, 12–20]. The effective isovector INC effect can be studied by examining energy differences (such as MED) and observing by their J-dependence (i.e., it is a multipole effect). The inclusion of a spin-dependent, nuclear isospin-breaking term had earlier been noted in the case of the $A = 42$ and 54 mirror pairs [7, 21]. It has been shown that this term is as significant as the contributions from the Coulomb force. It has also been demonstrated that most other $f_{7/2}$ nuclei require additional effective isospin breaking effects [22]. A comprehensive study in the $f_{7/2}$ shell using the combined approach of spectroscopy of the most accessible proton-rich nuclides and detailed shell-model analysis has allowed for reliable interpretation of MED with respect to a wide range of INC effects [7].

In the shell-model calculations, the MED is largely insensitive to the absolute values of effective isovector INC matrix elements but greatly reliant on the J dependence of these matrix elements [9]. Bentley *et al.* [9] determined a complete set of spin-dependent effective isovector ($V_{pp} - V_{nn}$) matrix elements by fitting the shell model to all experimental MED data obtained to date in the $f_{\frac{7}{2}}$ shell. Matrix elements of $V_B = -72(7)$, $+32(6)$, $+8(6)$, $-12(4)$ keV for the $J = 0$, 2, 4, 6 couplings, were obtained and included in shell-model calculations. These values improved the model's theoretical fit to experimental data [9].

Therefore, the structure of mirror nuclei has now been described by a shell-model prescription in detail. To test this prescription, more data from the $f_{7/2}$ shell

is needed and more research is required to be conducted with larger differences in isospin for mirror nuclei, as a number of INC terms are strongly dependent on T_z. There has also been some discussion on the effects of weak binding in the proton-rich member of the pair and how that affects the interpretability of MED [23]. Although it is clearly important to perform a systematic study of states in mirror nuclei that are unbound or weakly bound in the proton-rich system, very few such data exist in the $f_{7/2}$ shell, and a partial aim of the current work is to conduct such an analysis. There is still mystery surrounding the effective isospin-breaking component, making mirror energy difference studies useful tools for understanding nuclear structure into an interesting independent research field.

For the MED, the mirror pair chosen for this study, $A = 48$, has a unique feature in being at the precise centre of an isolated single-j shell, i.e., $A = 48$ mirrors are at the centre of an isolated $f_{\frac{7}{2}}$ shell. These nuclei are also cross-conjugate nuclei, which means that all the MED would be precisely zero assuming an isolated $f_{\frac{7}{2}}$ shell. Therefore, these features make MED in $A = 48$ nuclei extremely sensitive to cross-shell excitations, and hence, they provide an especially stringent test for checking the propriety of the valence space in the shell-model calculations.

In this work, as well as studying isospin symmetry through MED, isospin symmetry will be studied through the examination of mirrored direct reactions. The aim of the experiment goes further by measuring direct one-nucleon knockout cross sections to the analogue states in mirror nuclei in question, giving information on spectroscopic factors for both sets of analogue states. Evaluating this is a key aim of this work, as spectroscopic factors may be more sensitive to analogue wavefunctions than MED.

Isospin symmetry suggests that the wavefunctions of the two sets of analogue states of the mirror nuclei must be identical; hence, it is assumed that both mirror nuclei will have similar spectroscopic strengths and hence cross sections. The well-documented observation of the suppression of spectroscopic strength [24–26] was also the motivation for mirror-knockout technique. These studies show that

single-nucleon removal reactions on light solid targets have experimentally suppressed inclusive cross sections as compared to theoretical direct-reaction models. This suppression appears to be strongly dependent on the asymmetry between the separation energies of the two types of nucleon, ΔS, see Fig. 1.1. Fig. 1.1 presented by Gade *et al.* [24–26] was plotted as the ratio of the inclusive cross sections (experimental to theoretical), R_S, for 1n- and 1p-knockout as a function of ΔS. The downward trend in Fig. 1.1 indicates that the suppression of the spectroscopic strength is a function of ΔS.

Mirror pairs that are well separated in Z, such as the ones studied here, have very different ΔS values and so Fig. 1.1 implies different cross sections. An understanding of the behaviour of analogue reactions in this context is of great interest, and it requires an analysis of exclusive cross sections in order to ensure the analogue nature of the reactions.
Such approaches, lead to the emergence of the question of how analogue-exclusive cross sections (for pairs of analogue final states) behave. This question has not been considered fully before, and no detailed studies to date have dealt with this type of comparison. This work is the first attempt at doing a detailed state-by-state examination of analogue cross sections. Although there have been two studies previously that quoted analogue exclusive cross sections [27] and [28], this aspect was not fully discussed. This work aims to test if analogue-exclusive experimental cross sections for pairs of analogue final states of mirror nuclei well separated in ΔS follow a similar trend as shown by the published data in Fig. 1.1.

The thesis is focused almost entirely on the $A = 48$, $T_z = \pm 2$ mirror pair, ^{48}Fe/^{48}Ti, populated via one-neutron/one-proton knockout from the secondary beams ^{49}Fe/^{49}V, respectively. A small portion of the thesis is dedicated to inclusive cross-section measurements of $A = 45$, $T_z = \pm\frac{3}{2}$ mirror pair ^{45}V/^{45}Ti which were populated via one-neutron/one-proton knockout from the same secondary beam, $N = Z$ ^{46}V. The purpose of selecting these mirror nuclei ($A = 45$) is to check the

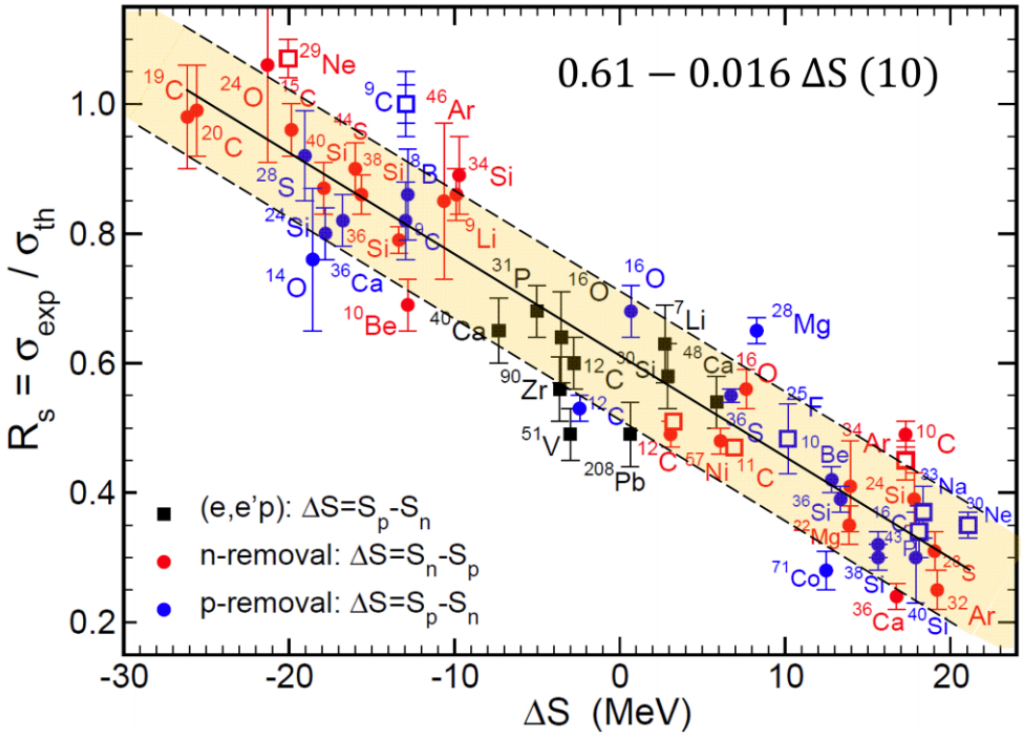

Figure 1.1: The ratio of experimental to theoretical inclusive cross sections for one-nucleon knockout as a function of ΔS. A linear representation of the totality of collected data points from the different regions of the nuclear chart is given by 0.61 – 0.016 ΔS (10). Taken from [26].

symmetry of the analogue wavefunctions caused by the removal of protons and neutrons from the **same** parent nucleus ^{46}V.

In summary, this work aims to evaluate the mirrored knockout cross sections with a large difference in ΔS, as well as to identify a range of new excited states in the exotic nucleus ^{48}Fe and to use the shell-model methodology to analyze the MED. The objectives of this thesis are, therefore, as

* To establish a sequence of new excited states for the first time in the proton-rich, $T_z = -2$ nucleus ^{48}Fe, and to compare it to its well-studied, stable, mirror nucleus ^{48}Ti [29].

* Using the population of new excited states to study the MED between isobaric analogue states in this $T_z = \pm 2$ pair in the $f_{\frac{7}{2}}$ shell, and to perform

large-scale shell-model calculations to interpret them in terms of INC effects.

* To conduct a detailed comparison of experimental and predicted cross sections, both inclusive and exclusive, for the $A = 48$, $T_z = \pm 2$ mirror pair and only inclusive cross sections for the $A = 45$, $T_z = \pm\frac{3}{2}$ mirror pair, using mirrored knockout to examine the question of the suppression of spectroscopic strength. This requires the calculation, in this work, of the analogue spectroscopic factors in the shell model and the reaction-model knockout cross sections.

1.1 Thesis Structure

The present study is structured in the following manner: Chapter 2 describes the concept of isospin and the theory of the shell model. This is followed by a description of both the shell model calculations and knockout calculation cross sections performed to interpret the MED and the single-nucleon-knockout reaction mechanism, respectively, along with a brief discussion on the reaction techniques applied in this thesis. In Chapter 3, the experimental setup that was utilised at NSCL in MSU has been discussed. In Chapter 4, all of the calibrations and correction methods for the various detectors are discussed, along with the analysis techniques used for the thesis. Chapter 5 presents the experimental analysis and results of mirrored one-nucleon removal reactions obtained from experiment at MSU, including MED and cross sections. In Chapter 6, the theoretical cross-section calculations performed in this project are compared with the experimental results. A discussion of the results obtained from the mirrored one-nucleon knockout analyses are also presented. In Chapter 7, the theoretical shell model MED are compared with the experimental data. This chapter will also provide a discussion of the main results related to MED at the end. Finally, in Chapter 8, conclusions are drawn, and future work in this field is discussed in detail.
All the calculations performed in this thesis work have been undertaken by the

author (R. Yajzey).

Chapter 2

Theory and Background

2.1 Isospin

Studying exotic isotopes close to the proton drip line near the $N = Z$ region is an area of particular interest for investigating the significant role of isospin symmetry. There are strong nuclear forces acting between protons and neutrons. The observation of similar behaviour of protons and neutrons under the strong force suggested and led to the introduction of the concept of isospin [30]. Isospin symmetry is related to the charge symmetry and charge independence of strong interactions. In the absence of electromagnetic interaction, both protons and neutrons can be considered as different states of the same particle known as the nucleon.

All nucleons have an isospin quantum number $t = \frac{1}{2}$ with different projections for a proton ($t_z = -\frac{1}{2}$) and a neutron ($t_z = +\frac{1}{2}$). Moreover, the nucleus has a total isospin projection on the z-axis T_z, and the total isospin of the individual nucleons denoted by quantum number T are given by Eqs. 2.1 and 2.2.

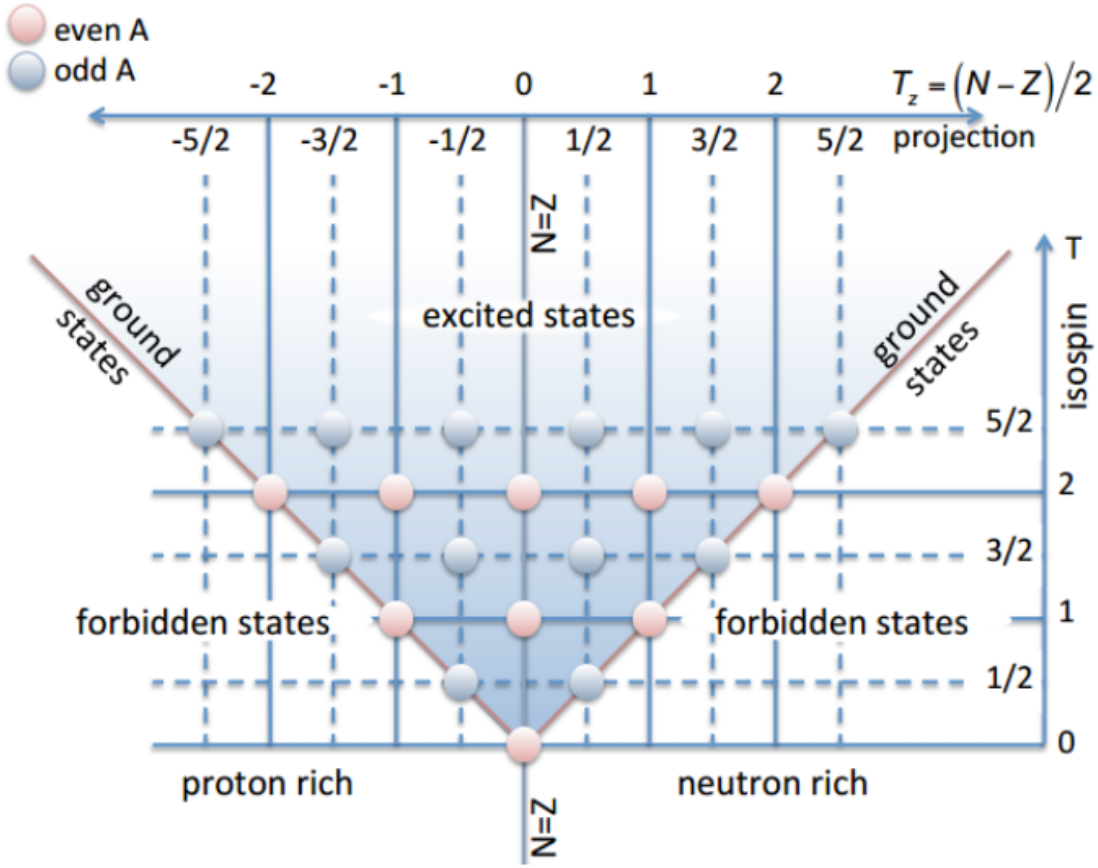

Figure 2.1: The isospin diagram shows the allowed and forbidden isospin states of nuclei for a particular value of T with different total isospin projection T_z along the z-axis in isospin space. Even-even nuclei exhibit ground states with isospin $T = |T_z|$, as shown by the red line. Taken from [20].

$$T_z = \sum t_z = \frac{N - Z}{2} \tag{2.1}$$

$$\frac{|N - Z|}{2} \leq T \leq \frac{|N + Z|}{2} \tag{2.2}$$

where N is the number of neutrons, and Z is the number of protons.

Different nuclei with a corresponding total isospin projection, T_z, have allowed and forbidden isospin T states, satisfying the isospin rules in Eq. 2.2 and can be observed in the diagram created by M. A. Bentley in Fig. 2.1 [20]. The red circles

represent even mass number A, and the blue circles represent odd mass number A. For nuclei with odd mass number A, the spin and isospin states have half-integer values, as seen in the dashed lines, and for nuclei with even mass number A, the spin and isospin states have an integer number, as seen in the solid lines.
For most nuclei (apart from those on the $N = Z$ line), yrast states (the lowest excitation energy states for a particular spin) usually have the minimum value of isospin ($T = T_z$), whereas nuclei with higher T will typically have much higher energy. Most even-even nuclei exhibit a ground state where $T = |T_z|$, as indicated by the red line in Fig. 2.1. It can also be seen that $T = 0$ states are only allowed in $N = Z$ nuclei ($T_z = 0$). However, Fig. 2.1 might not be applicable to odd-odd $N = Z$ nuclei, where some of these nuclei are observed to have $T = 0$ ground states, whereas the others have $T = 1$ ground states. Odd-odd $N = Z$ nuclei where $A < 42$ they have $T = 0$ ground states. It has been observed that for some odd-odd $N = Z$ nuclei, especially those in the mid-fpg shell ($A \sim 46$) the first $T = 1$ states are lower in energy (i.e., are the ground state) than the $T = 0$ states [31, 32].

The charge symmetry of strong nuclear forces requires neutron-neutron (V_{nn}) and proton-proton (V_{pp}) interactions to be virtually identical, Eq. 2.3. In addition, charge independence requires the strength of the nuclear force between a neutron and a proton (V_{np}) to be equal to the average of the nuclear force between the proton-proton (V_{pp}) and neutron-neutron (V_{nn}) pairs, Eq. 2.4,

$$V_{nn} = V_{pp}, \tag{2.3}$$

$$V_{np} = \frac{V_{pp} + V_{nn}}{2}. \tag{2.4}$$

Experimental evidence confirms that the conditions for charge symmetry and

charge independence are broken [33]. Nucleon-nucleon scattering measurements have shown that there is a slight charge asymmetry in the nuclear interaction (explained in detail in [33]).

It has been found in scattering experiments (when the nuclear force is measured in free space) that neutron-neutron interactions are slightly stronger than proton-proton interactions by about $\sim$0.5%, and neutron-proton interactions are stronger than the average of proton-proton interactions and neutron-neutron interactions by approximately $\sim$2.5% [33].

In the absence of isospin-breaking interactions, the analogue states in nuclei of the same isospin T, known as isobaric analogue states (IASs), are degenerate. Differences in excitation energies of IASs will result from the combined Coulomb interactions, charge symmetry breaking (CSB) and any charge-dependent components of the nucleon-nucleon interaction (isospin non-conserving (INC) terms), resulting in isospin symmetry violation. These INC forces lift the degeneracy of analogue states, break isospin symmetry, and may result in isospin mixing of the states in question. Analysing the differences in energy levels is an effective way of examining the Coulomb force. INC effects, in particular their spin (J) dependence, are often studied by evaluating either isovector and isotensor effects, given in Eq. 2.5 and Eq. 2.6, respectively. The most common testing ground for studying isospin breaking interactions are mirror nuclei pairs (nuclei with the same mass A, where the number of protons of one is equal to the number of neutrons of the other) and triplet nuclei (a set of three nuclei, of which one is an odd-odd $N = Z$ nucleus, and the other two are neighbouring even-even nuclei with $Z + 1$, $N - 1$ and $Z - 1$, $N + 1$). These effects are understood through mirror energy differences (MED) and triplet energy differences (TED), respectively,

$$V_{isovector} = V_{pp} - V_{nn}, \tag{2.5}$$

$$V_{isotensor} = V_{pp} + V_{nn} - 2V_{np}. \tag{2.6}$$

2.1.1 Mirror Energy Differences MED

The MED between isobaric analogue states can be used to investigate isovector effects. These excitation energies are normalized to the ground state; therefore, MED can be calculated using the following equation

$$MED_J = E^*_{J,T,-T_z} - E^*_{J,T,+T_z}, \tag{2.7}$$

where E^*_{J,T,T_z} is the excitation energy of a state with spin J, total isospin T, and isospin projection T_z.

As these excitation energies are measured relative to the ground state of each nucleus, the effects of displacement energies between the ground states of mirror nuclei, known as mirror displacement energies (MDE), are eliminated. Therefore, a number of spin-dependent contributions to the excitation energy are considered, which lift the degeneracy of the analogue states.

The Coulomb force and other INC effects need to be modelled in order to understand how isospin symmetry is broken. In order to understand these effects, a theoretical framework needs to be developed to help investigate the implications of these contributions to the MED (discussed in Section 2.2.3). For this purpose the shell model is used.

TED are sensitive to isotensor effects and probe the strength of the *np* interaction compared to the average of the *pp* and *nn* interactions, whose interpretation depends entirely on the charge independence concept. The TED are defined as follows,

$$TED_J = E^*_{J,T,T_z=-1} - E^*_{J,T,T_z=1} - 2E^*_{J,T,T_z=0}, \tag{2.8}$$

where T and T_z represent the isospin quantum number and its corresponding z-projection, respectively.

To understand the dependence of the binding energy of a set of IASs as a function of T_z, the famous Isobaric Multiplet Mass Equation (IMME), proposed by Wigner [34] in 1957, can be used. A detailed description of this can be found in [35, 36]. The IMME formula shows that the energy (and therefore, mass) of isobaric multiplet states is quadratic in T_z [9], and it can be written as

$$\Delta BE(\alpha T T_z) = a + bT_z + cT_z^2 \tag{2.9}$$

where α contains all the additional quantum numbers of the state. The coefficient a is related to the isoscalar component, with a small contribution from the isotensor effect. The coefficients b and c depend on the isovector and isotensor components, respectively. Therefore, one can define MED and TED as isovector (b) and isotensor (c) effects whose interpretation relies entirely on the charge symmetry and charge independence of the attractive nucleon-nucleon interaction, respectively.

2.2 Nuclear Shell Model

The nucleus is a multi-body quantum system and exhibits a variety of phenomena. Several nuclear models are available. A good model must showcase observable properties such as energies of states, spin and parity quantum numbers, electromagnetic moments of nuclei, and regular sequences of excited states. A good model also predicts some new properties that can be confirmed through experiments.

The first nuclear shell model was introduced in 1949 by Maria Goeppert-Mayer [37] and Johannes Hans Daniel Jensen [38]. The nuclear shell model provides the arrangement of nucleons (protons and neutrons) in the nucleus. These two types of fermion arrange themselves in the orbital according to the Pauli exclusion princi-

ple. The shell model explains the existence of the traditional magic numbers 2, 8, 20, 28, 50, 82, and 126 as closed shells [39]. The magic numbers of protons or neutrons appear as one moves from the valley of stability towards the drip lines. The nuclear shell model is analogous to the atomic shell model, wherein the electrons orbit the atomic nucleus in quantum shells bound by the attractive Coulomb potential of the nucleus. The external potential is created as a result of the Coulomb force from a positively charged nucleus. In contrast, the nuclear shell model does not have a clearly defined central potential; the nuclei are bound by a potential created as a result of their motion. The central potential is created by the collective motion of nucleons – their mutual interaction; therefore, the shape of potential follows the distribution of nucleons.

The shell model Hamiltonian can be classified using kinetic energy, T, and potential energy, V, and can be written as

$$H = T + V = \frac{\hat{p}^2}{2m_0} + V(r) \tag{2.10}$$

2.2.1 Nuclear potentials

Different forms of central potential are shown in Fig. 2.2. The simplest ones are the infinite square well (Eq. 2.11) and the harmonic oscillator (Eq. 2.12). These two potentials can reproduce 2, 8, and 20 magic numbers but failed to reproduce higher shell closures, see Fig. 2.4.

$$V(r) = \begin{cases} 0, & : for\ r < R \\ \\ \infty, & : for\ r > R \end{cases} \tag{2.11}$$

$$V(r) = \frac{1}{2}kr^2 \tag{2.12}$$

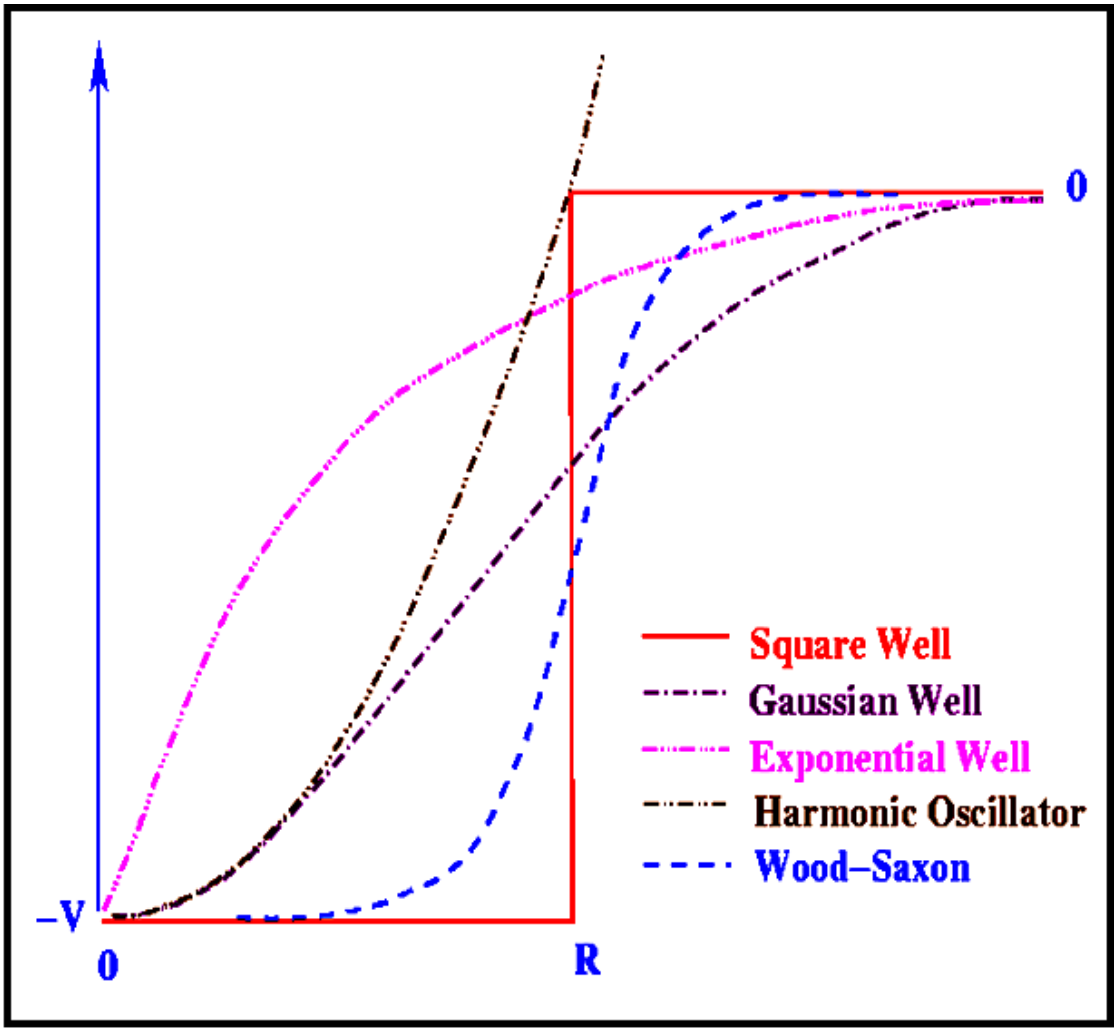

Figure 2.2: Shapes of different potentials. Taken from [40].

The nuclear potential is typically represented by either a Woods-Saxon potential or a harmonic oscillator potential. The Woods-Saxon potential is the most usual parametrization used to describe the nuclear potential, a spherically symmetric potential that smoothly decreases to zero with increasing r (see Fig. 2.3), in accordance with the nuclear matter distribution. It can be written as follows

$$V(r) = \frac{-V_0}{1 + exp(\frac{r-R}{a})}, \tag{2.13}$$

where V_0 is the depth of the potential well ($\sim$ 50 MeV); R is the radius of the

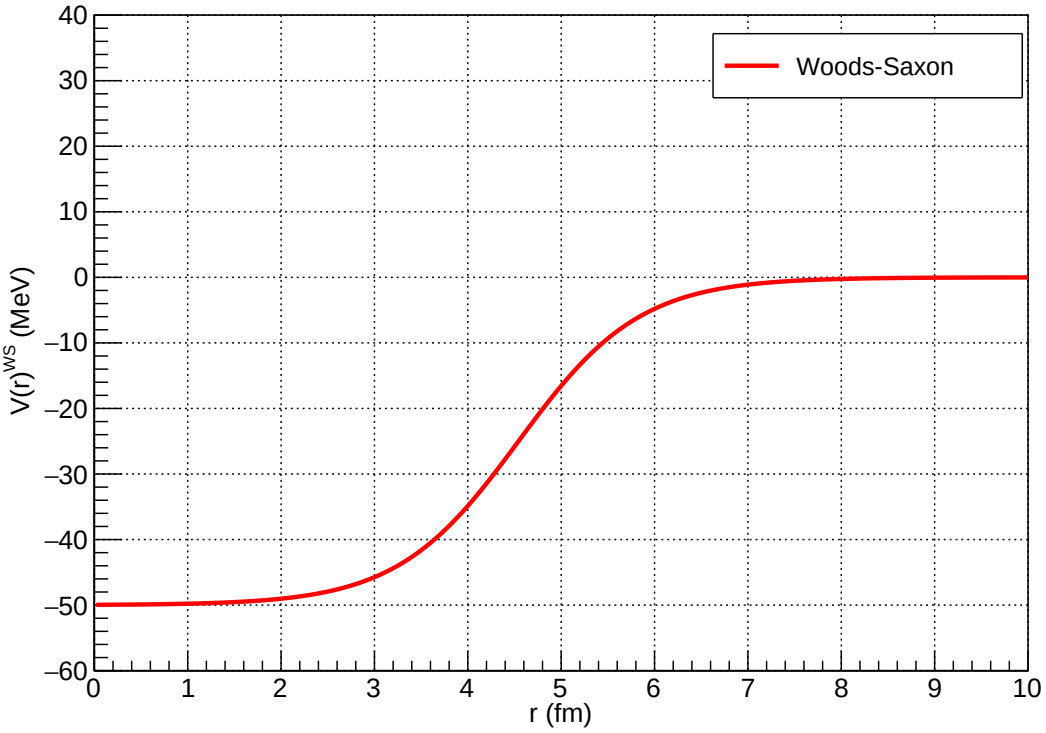

Figure 2.3: Nuclear mean-field depicted with Woods-Saxon potential using Eq. 2.13 of $V_0 = 50$ MeV, $r_0 = 1.25$ fm, $a = 0.7$ fm for an $A = 48$ nucleus.

nucleus (R = 1.2 $A^{\frac{1}{3}}$); a is the surface diffuseness term (0.7 fm). However, Woods-Saxon potential still fails to replicate magic numbers beyond 40, as can be seen in Fig. 2.4.

Two additional terms are required along with the central potential for reproducing known spherical magic numbers. The first term is the spin-orbit interaction (SO) that comes from the nuclear surface and is introduced as a derivative of the central potential. Spin-orbit coupling $\vec{\boldsymbol{l}}.\vec{\boldsymbol{s}}$ splits energy levels with the same n and l into two levels due to interaction between intrinsic spin s and orbital angular momentum l. Different orientations of $\vec{\boldsymbol{l}}$ and $\vec{\boldsymbol{s}}$ change the shape of the potential. Therefore, parallel coupling gives wider potential and, consequently, lower energy for $j_1 = l+s$, whereas antiparallel coupling gives a narrower potential and, hence, higher energy for $j_2 = l - s$. The second contribution is the inclusion of an l^2 term that accounts for the change in the binding energy from the angular momentum of nucleons.

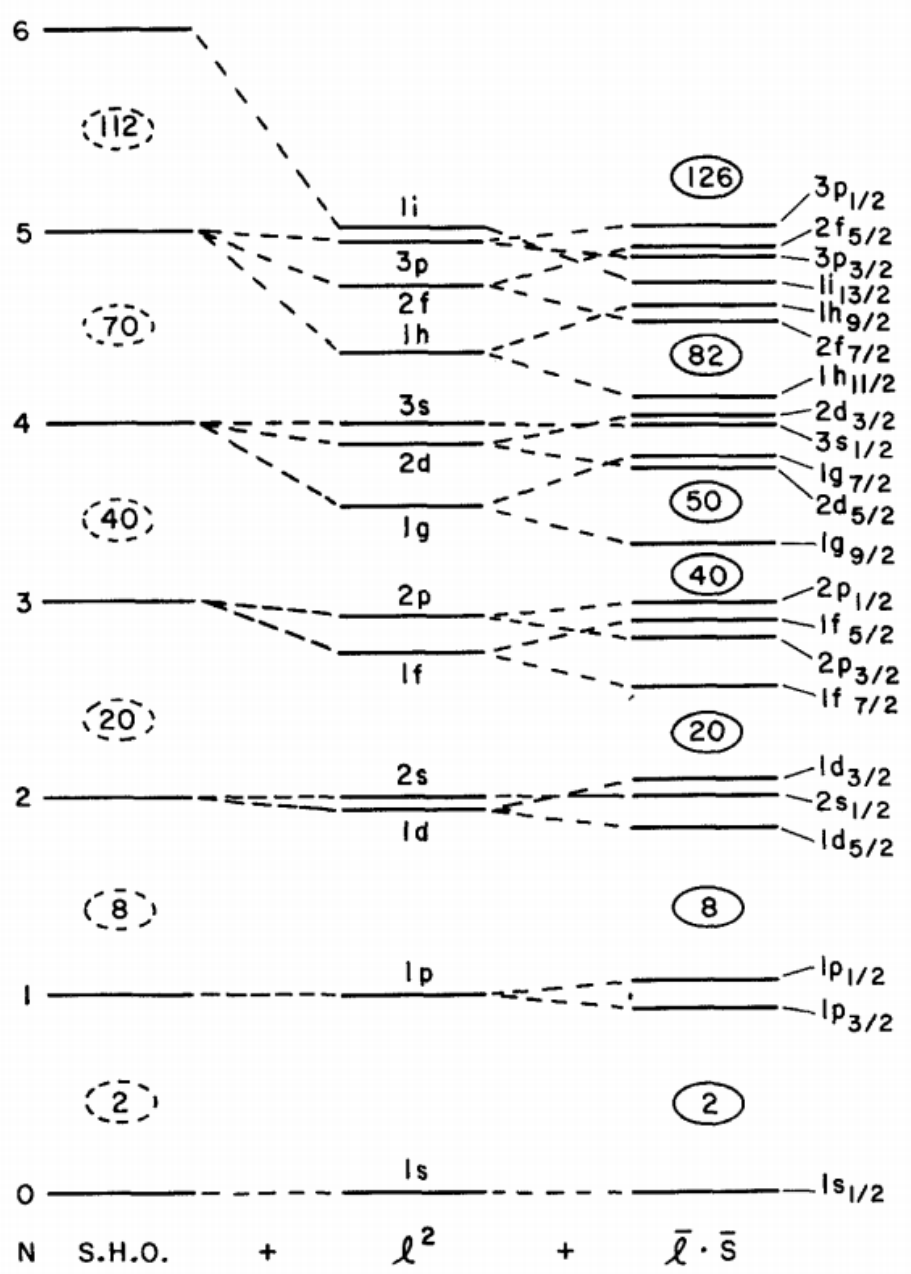

Figure 2.4: The single-particle energy levels of the nuclear shell model from a simple harmonic oscillator potential showing the effect of the surface and spin-orbit correction. The experimentally observed magic numbers are only reproduced after both the l^2 and spin-orbit ($\vec{\boldsymbol{l}}.\vec{\boldsymbol{s}}$) terms have been included. Taken from [41].

Thus, the total potential, with the inclusion of the two additional effects and the Coulomb potential, V_C, can be written as:

$$V(r) = V_C(r) + \frac{1}{2}kr^2(r) + V_{ll}\vec{\boldsymbol{l}}^{\vec{\boldsymbol{2}}}(r) - V_{ls}\vec{\boldsymbol{l}}.\vec{\boldsymbol{s}}(r) \tag{2.14}$$

The Coulomb part of the potential is taken to be the potential arising from a uniform charge distribution over a sphere of radius R.

The single-particle energy levels that nucleons can occupy inside the nucleus shown in Fig. 2.4, are produced by solving the Schrödinger equation, with the potential defined in Eq. 2.14 to predict magic numbers at 2, 8, 20, 28, 50, 82, and 126 in agreement with the experimental observations.

2.2.2 Residual Interactions

The single-particle shell model described previously is based on the assumption that all nucleons except one in a nucleus are paired and therefore, nuclear properties arise from the only unpaired nucleon [39]. Adding a residual interaction to the single-particle Hamiltonian is required to treat all the nucleons in the last shell instead of only the last one and accounts for the influences not included in the effective potential, for example, pairing effects between valence nucleons and p-n interactions.
The Hamiltonian resulting from the interaction between the nucleons can be formed as follows

$$H = H_0 + H_{res}, \tag{2.15}$$

where H_0 is the shell model Hamiltonian that contains only the potential from Eq. 2.14. The two-body matrix elements are the calculated energies of the different interactions between particles, which accounts for the residual interaction, H_{res}. Thus, the H_{res} is considered a small perturbation on H_0, which interprets

the remainder of the effects of nucleon-nucleon interactions in order to find a potential that influences all nucleons.

The matrix elements can be determined from nuclear data with the help of different methods and approaches using shell-model calculations. Thus, to calculate for a specific region, often more than one interaction can be employed.

The shell-model calculations begin with calculated single-particle levels derived by solving Schrödinger equation for the shell-model Hamiltonian H_0 [42]. For heavier systems, calculations must be restricted to all possible configurations of the valence nucleons that notably contribute to the states of interest, and effective residual interactions H_{res} must be used. Therefore, the calculations are based on the three ingredients of a shell model, see Fig. 2.5.

The first consideration is an inert core in which all the nucleons are paired, tightly bound in their single-particle levels, and do not get excited to other single particle levels. These nucleons are not considered by the residual interaction. For the calculations in this thesis, the ^{40}Ca ($N = Z = 20$) is used as an inert core. Second, the valence space is the space in which the valence nucleons can freely move outside of the core and interact with each other. Therefore, the states of interest can be identified by different configurations of the interaction of these valence nucleons. The valence space used in this calculation is $f_{\frac{7}{2}}$, $p_{\frac{3}{2}}$, $f_{\frac{5}{2}}$, and $p_{\frac{1}{2}}$. The last consideration is a truncation of the shell model space, i.e., the restriction of the occupancy of the valence nucleons on the single-particle energy levels that are only considered by the residual interaction between these nucleons. Sometimes, the calculation cannot be undertaken without further truncation as a result of computational restrictions. Therefore, additional truncation is often required within the valence space.

Shell-model calculations may provide reasonable results; however, these calculations can be particularly limited in the case of some nuclear regions. It is because the nuclei studied are usually heavily deformed, and thus, the spherical shell model is a poor approximation. A shell-model calculation was performed in this thesis using the shell-model code ANTOINE [43].

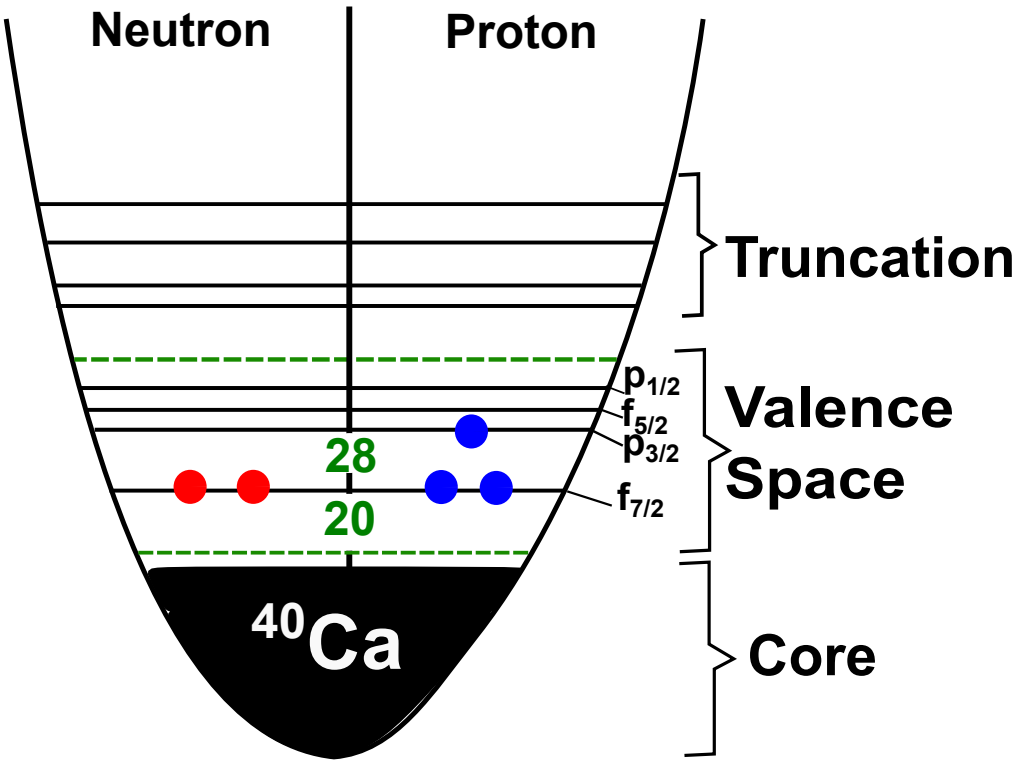

Figure 2.5: A schematic representation of the components of a shell-model calculation, showing the inert core (^{40}Ca such as used in present work) within the harmonic oscillator potential. The two types of fermions, protons and neutrons, are arranged in some valence single particle levels, $f_{\frac{7}{2}}$, $p_{\frac{3}{2}}$, $f_{\frac{5}{2}}$, and $p_{\frac{1}{2}}$. The truncation region shows that some single particle levels are not included in the shell-model calculation. Adapted from [44].

The fp space is the shell model region of interest for the experiment discussed in this thesis. A number of different residual interactions are available to choose from to be used in this region that utilizes a ^{40}Ca core and valence space $f_{\frac{7}{2}}$, $p_{\frac{3}{2}}$, $f_{\frac{5}{2}}$, and $p_{\frac{1}{2}}$. The most popular interactions used are the KB3G [45] and GXPF1 [46] interactions. The KB3G interaction is a set of two-body matrix elements deduced analytically from nucleon-nucleon interactions and gives a good description for light ($42 \leq A \leq 54$) nuclei, in the fp-shell [9]. In contrast, the shell model interaction GXPF1 is a set of matrix elements resulting from nucleon-nucleon interactions determined by fitting to 669 experimental energy levels from nuclei between $A = 47$ and $A = 66$.

All shell-model calculations presented in this thesis were performed using the full fp orbital space implemented using the ANTOINE code [43] with the KB3G interaction [45].

2.2.3 MED within the Shell model Calculations

The nuclear shell model has been used in this work to interpret the MED, which are compared to experimental MED data as well as predicted spectroscopic factors for mirrored (symmetric) knockout reactions from mirror pairs in the $f_{\frac{7}{2}}$ shell. Traditionally, theoretical modelling of MED takes place within the framework of shell models, which interpret INC effects as a result of a lack of missing physics such as CSB and the Coulomb effect. Since mirror nuclei are those in which the numbers of protons and neutrons are interchanged, both nuclei will have the same number of np pairs but swapped numbers of nn and pp pairs and so isovector effects should be included. MED are analysed using four isospin-breaking components in shell-model calculations. These four effects are the multipole Coulomb interactions (V_{CM}), the radial effect (V_{Cr}), the single-particle effect (V_{ll}+V_{ls}), and an additional effective isovector interaction (V_B). The main contributions to MED have been highlighted by numerous researchers of many different mirror pairs. INC effects were formalised within this shell-model prescription by Zuker et al. [7], and later, these effects were further discussed in more detail by Bentley and Lenzi [8,9]. The main contributions will be addressed in the following sections.

2.2.3.1 Multipole Coulomb Term

The multipole Coulomb term V_{CM} accounts for the changes in Coulomb energy resulting from recoupling angular momentum vectors of proton pairs with increasing excitation energy. Two particles (proton or neutron) in the middle of the $f_{\frac{7}{2}}$ shell

can be coupled to higher angular momentum $J = 0$, 2, 4, or 6 according to the Pauli exclusion principle, which results in an increase in the spatial separation of their orbits. This is be shown in Fig. 2.6, which illustrates the calculated spatial overlap of a pair of protons as a function of their coupled angular momentum in the $f_{\frac{7}{2}}$ shell [47].

A pair of protons (pp) coupled to a low J has a large Coulomb repulsion as compared to a high J with less Coulomb repulsion between the nucleons, which results from an increase in spatial separation. However, no change in the Coulomb repulsion occurs in the case of the coupling of two neutrons (nn). To study MED, the Coulomb matrix elements are calculated using harmonic oscillator wave functions, with the resulting Coulomb interaction added to the effective two-body interaction of protons in both mirrors.

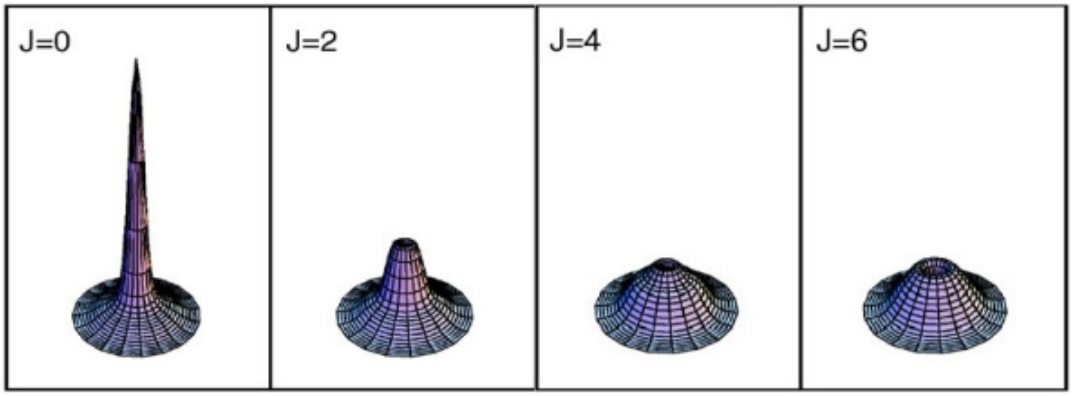

Figure 2.6: A calculated spatial overlap of two protons coupled to different angular momentum in the $f_{\frac{7}{2}}$ shell. Taken from [47].

2.2.3.2 The Monopole Radial Term

The radial effect (V_{Cr}) is the monopole Coulomb energy associated with changes in mean nuclear radii and deformation effects as a function of spin [7]. The mean nuclear radius varies due to differences in the occupation of different orbitals l, where orbitals with different angular momentum have different nuclear mean radii.

Hence, changes in the occupation of orbitals will result in energy differences. There are likely to be a considerable number of admixtures from the upper fp shell in the low-spin states of the $f_{\frac{7}{2}}$ shell, especially in the mid-shell region where deformation results in the partial occupation of the upper fp orbitals. These admixtures tend to reduce as the band termination gets smaller [14]. Based on the mirror symmetry arguments, the total occupation numbers for each member of a mirror pair will be the same (interchanged numbers of protons and neutrons), and then, it is the difference in charge between the two members of the mirror pair that produces the spin-dependent energy difference, due to the variation of Coulomb energy with radius.

The occupation of the p orbitals can also increase with deformation due to configuration mixing. Therefore, it is possible that the V_{Cr} term also accounts for the deformation effects. In the $f_{\frac{7}{2}}$ shell nuclei, the (V_{Cr}) effect is produced using the shell model by tracking the occupancy of the $p_{\frac{3}{2}}$ orbital as a function of spin since this orbital is expected to have a larger mean radius as compared to the $f_{\frac{7}{2}}$ orbital. The contribution of the monopole Coulomb radial term (ΔV_{Cr}) to the MED of mirror nuclei is calculated using the equation offered in [8] that has been presented below

$$\Delta V_{Cr}(J) = 2\ |T_z|\ \alpha_r \left(\frac{m_\pi(g.s.) + m_v(g.s.)}{2} - \frac{m_\pi(J) + m_v(J)}{2} \right), \tag{2.16}$$

where α_r (200 keV) is a constant deduced from $A = 41$ data [44], m_π and m_v are the proton and neutron occupancies of the ground state (g.s.), respectively, and J is the angular momentum quantum number of the state in question.

2.2.3.3 The Monopole Single Particle Term

The monopole single-particle term accounts for the differences in single-particle shell-model levels for a proton or a neutron. This term includes two effects of the

single-particle levels: V_{ll} and V_{ls} for the Coulomb [7] and electromagnetic spin-orbit shifts [48], respectively. Since the MED is related to energy, the change in energy, E_{ll} and E_{ls} due to both single-particle effects (ll and ls), which results from the differential of the potentials of V_{ll} and V_{ls}, should be computed. The V_{ll} effect related to the proton orbitals accounts for Coulomb energy in a proton orbital due to the overlap of that orbital with the core [49] such that

$$E_{ll} = \frac{-4.5 Z_{cs}^{\frac{13}{12}} [2l(l+1) - n(n+3)]}{A^{\frac{1}{3}}(n+\frac{3}{2})} keV, \tag{2.17}$$

where the Coulomb energy effect E_{ll}, is based on the proton number of the core Z_{cs}, principal quantum number n, and orbital angular momentum l.
The second effect is the electromagnetic spin-orbit interaction V_{ls}, which relates to the interaction between the spin moment of the nucleon and the Coulomb field of the nucleus [48] such that

$$E_{ls} \simeq (g_s - g_l)\frac{1}{2m_N^2 c^2}\left(-\frac{Ze^2}{R_C^3}\right) < \overrightarrow{\boldsymbol{l}} . \overrightarrow{\boldsymbol{s}} >, \tag{2.18}$$

where g_s and g_l are spin and orbit gyromagnetic factors, which differ for a proton and a neutron, 5.586 & 1 and -3.828 & 0, respectively. The terms m_N and R_C are the nucleon mass and nuclear radius, respectively [8]. The spin-orbit coupling, $< \overrightarrow{\boldsymbol{l}} . \overrightarrow{\boldsymbol{s}} >$, is given by $\frac{l}{2}$ for $j = l + s$ and $\frac{-(l+1)}{2}$ for $j = l - s$.
This effect is different for protons and neutrons, where the single-particle energies of proton levels sink relative to the neutrons, contributing to the MED. Moreover, if there occurs a single-particle excitation from an orbital with $j = l+s$ to another one with $j = l - s$ or vice-versa and if the excitation happens for a proton in one member of a mirror pair and a neutron in the other, a significant energy difference will be produced, contributing to the MED of the excited state.

2.2.3.4 Additional Effective Isovector Term

The shell-model calculation carried out with the inclusion of the three terms discussed above is not enough to fully reproduce the MED in the $f_{\frac{7}{2}}$ shell. It was reported by Zuker et al. [7] that there is a need to include an additional matrix element to the other terms in the MED calculations.
The isospin-breaking isovector V_B term is an additional, empirical isovector interaction, $V_{pp} - V_{nn}$, and has been shown in [9] to be strongly dependent on the angular-momentum coupling of nucleon pairs.

Zuker et al. [7] first suggested the need for this additional isovector term. To achieve reasonable agreement with experimental MED and TED data, an isovector matrix element of 100 keV was added to two-body matrix elements $J = 2$, $f_{\frac{7}{2}}$ coupling protons [8] and an isotensor matrix element of 100 keV has been added to $J = 0$, $f_{\frac{7}{2}}$, respectively. The additional matrix element values were obtained empirically based on the MED and TED measurements from $A = 42$ and $A = 54$ systems (two nucleons or two-nucleon holes in the $f_{\frac{7}{2}}$ shell). The additional isovector term of 100 keV MED for the $J = 2$, $f_{\frac{7}{2}}$ couplings observed by [7] is often referred to as the $J = 2$ *anomaly*.
A full set of effective spin-dependent isovector ($V_{pp} - V_{nn}$) matrix elements (V_B) was later obtained by fitting the shell model to all experimental MED data that have been obtained so far in the $f_{\frac{7}{2}}$ shell. Thus, matrix elements of $V_B = -72(7)$, $+32(6)$, $+8(6)$, $-12(4)$ keV for J= 0, 2, 4, 6 couplings, respectively, were obtained [9], where an increase of ~ 100 keV between $J = 0$ and $J = 2$ couplings was suggested, which is consistent with previous studies [8]. For example, a comparison between the experimental and theoretical MED data for different mirror pairs in the $f_{\frac{7}{2}}$ shell, including four matrix elements V_B, as shown by a solid line, or excluding the fitted V_B term, as shown by a dashed line, are presented in Fig. 2.7 [9]. In these examples, the theoretical agreement with experimental MED data is significantly improved by including these effective empirical isovector, $V_{pp} - V_{nn}$ matrix elements. The origin of isospin non-conserving effect (V_B) term is still unclear, but

it can be described by a Coulomb modification of the nucleon two-body interaction, which is simply absent from the shell-model prescription.

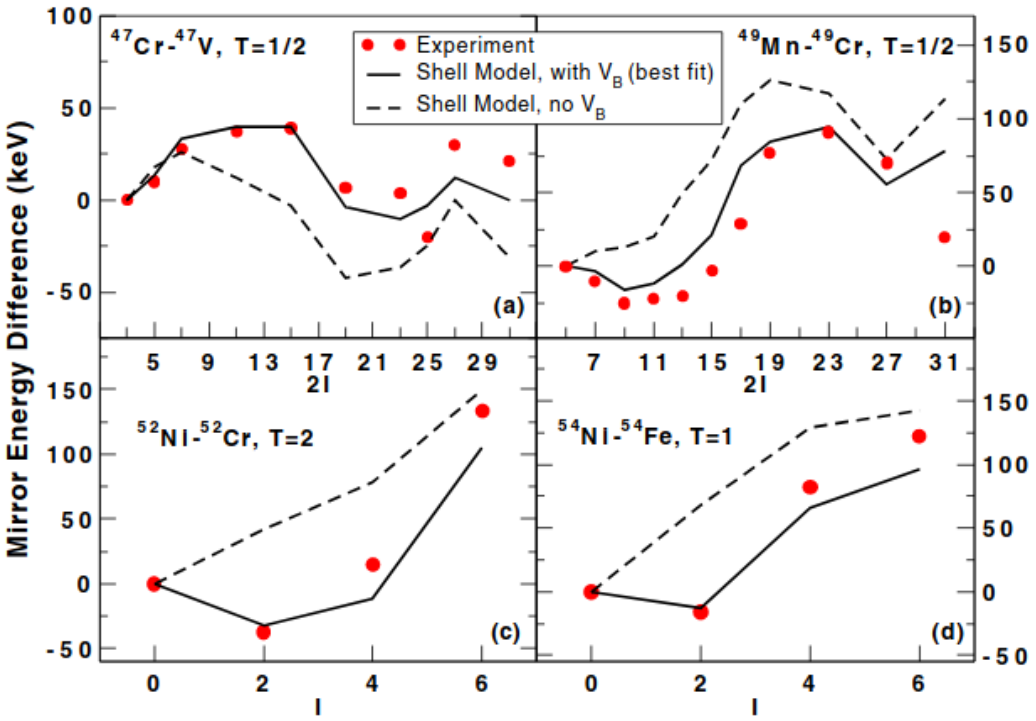

Figure 2.7: A comparison of experimental and theoretical MED for four mirror pairs in the $f_{\frac{7}{2}}$ region. The solid line represents the predicted MED, including the fitted V_B term, whereas the dashed line represents the predicted MED without the V_B term. Taken from [9].

In this work, two different methods are used for defining the INC term V_B in order to match the shell model to the experimental MED. Both methods are the shell-model calculations which include all the four components with, (a) a V_B of a single -100 keV INC matrix element for J=0 for all fp-orbitals, and (b) a V_B of four parameters extracted from the fit across the $f_{\frac{7}{2}}$ shell [9]. From all the above discussions, it is clear that the contributions of the MED shell-model calculations with the inclusion of the four components of INC effect (developed based on the prescription of [7,9]) achieved a reasonable agreement with the experimental MED data. The steps taken to apply the MED shell-model calculations to the mirror nuclei chosen in this work will be described in Chapter 7.

2.3 Reaction Mechanism

In the analysis discussed in this thesis, the excited states of the exotic proton-rich ^{48}Fe, ^{45}V, and their mirror pairs ^{48}Ti and ^{45}Ti were achieved via a one-nucleon knockout reaction mechanism. These reaction products are derived using radioactive beams produced by fragmentation. The fragmentation and knockout reaction processes and the knockout calculations used in this analysis will be discussed in the following sections.

2.3.1 Projectile Fragmentation Reaction

The fragmentation technique involves a high-intensity beam of stable nuclei accelerated to between 0.1 and 1 GeV/nucleon to impinge on thick targets in order to produce radioactive nuclei (fragments), which are then filtered and shaped into a secondary beam using a fragment separator.

The high-energy fragmentation reactions can take place via a variety of processes. When the beam and target particles collide head-on, both are divided into many small fragments. However, the collisions can directly remove particles from either the target or the beam. As a result of low-impact parameter collisions, many nucleons can be removed, leaving a lower-mass nucleus to carry on via the separator (fragmentation). The intermediate processes of the fragmentation of heavy, high-energy ions are described in a simple abrasion-ablation fragmentation model [50] (see Fig. 2.8). This model for reactions between relativistic heavy fragments is extracted from Glauber's multiple scattering theory [51]. Severe collisions break off several particles in the interaction region, and this process is described as an abrasion. The remaining nuclei leave in an excited state, which decays through particle emission; this is known as ablation.

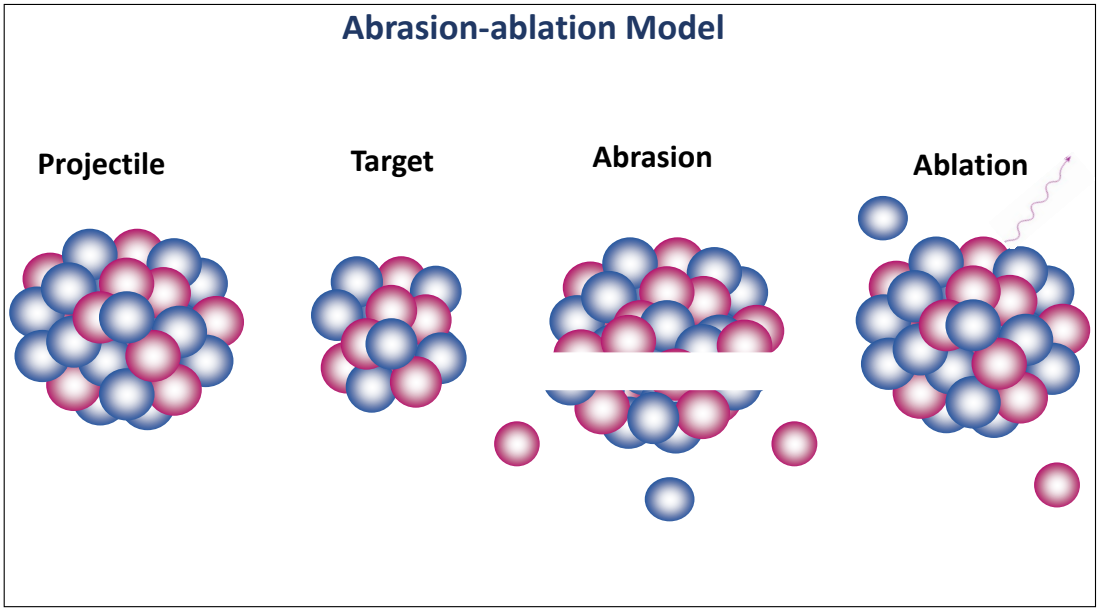

Figure 2.8: Abrasion-ablation fragmentation model. Adapted from [52].

2.3.2 Nucleon Knockout

Direct reactions are classified as a type of nuclear reactions. The processes happen in a single step at the nuclear surface and involve only a few nucleons. The direct reaction involves the projectile that may exchange some energy and angular momentum or have nucleons transferred to or removed from it.

Knockout reactions are direct reactions that involve the removal of a nucleon from the projectile as a result of interacting with the target. In a direct reaction, the probability of the reaction occurring depends on the specific structure of the initial and final states. Nucleon knockout reactions are performed using high-energy beams of $\sim$ 100 MeV/u and light targets, usually ^{9}Be. A knockout reaction is a very powerful method to probe the nuclear structure and the wave function of exotic nuclei, as well as to obtain spectroscopic information (detailed discussion in [25, 53, 54]).

The nucleon removal mechanisms can be classified into two groups: inelastic breakup (stripping) and elastic breakup (diffraction). In the inelastic breakup process, the removed nucleon is absorbed by the target, and the target nucleus

is left in an excited state. On the other hand, in the elastic breakup process, the removed nucleon is emitted in the beam direction, and the target nucleus is left in its ground state. Both reactions are calculated from the target-core and target-nucleon scattering matrices described in [54, 55]. The reaction mechanism is presented in the diagram. 2.9.

The probability of removing a nucleon from a particular state in the parent nu-

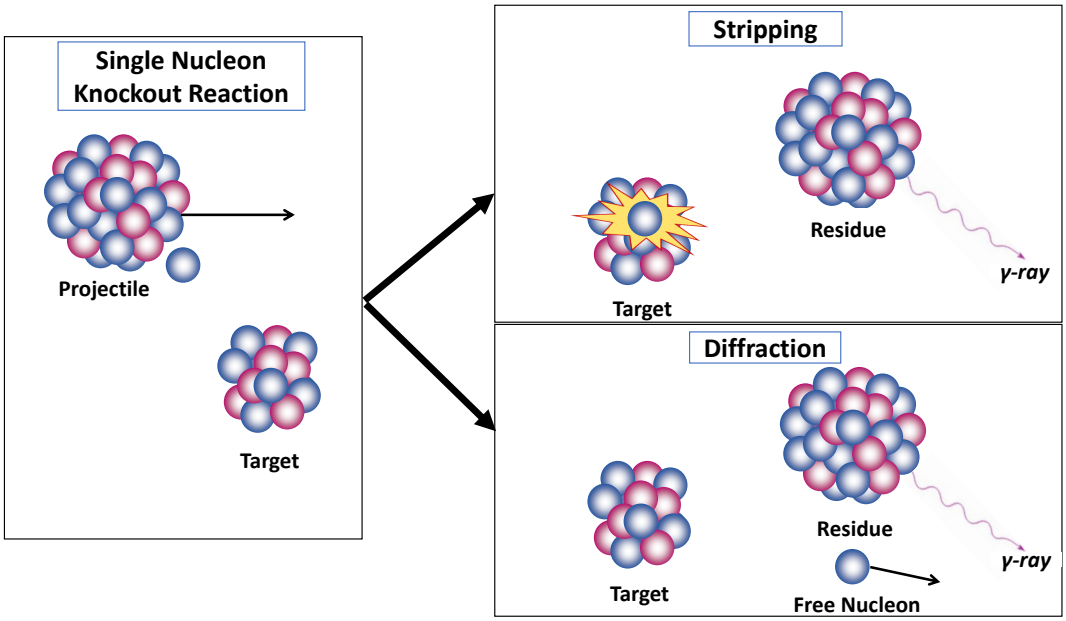

Figure 2.9: The single-nucleon knockout reaction types: stripping reaction process (on the top right) and diffraction reaction process (on the bottom right).

cleus to populate a specific state in the final nucleus is proportional to the overlap of the wave function of the two states, and this overlap is defined as the Spectroscopic factor C^2S. The ability to investigate the single-particle spectroscopic information could be a significant test of the nuclear wave function. A quality of a good spectroscopic probe is the capacity to cleanly distinguish the effects of the reaction mechanism. Nucleon knockout reactions are assumed to be a direct reaction with negligible residual interaction between the $(A-1)$ spectator core and the nucleon removal. To compare the calculated partial cross section for removal of a nucleon, from a single-particle cross sections σ_{sp}, with experimental ones, they should be normalised by C^2S between the initial and final (α) states [53, 54, 56]. The theoretical cross section for a specific knockout path from a particular state in

the parent nucleus to individual states in the daughter nucleus can be calculated, where one particle is removed from a single particle orbit (j) from a nucleus with A nucleons to the residual core with $(A-1)$ nucleons and total angular momentum and parity J^π.

$$\sigma_{th}(E_x, J^\pi, j) = \left(\frac{A}{A-1}\right)^N C^2 S_{SM}(\alpha, j)\sigma_{sp}(j, S_n + E_x) \tag{2.19}$$

where C^2S_{SM} is the spectroscopic factor calculated from the shell model, S_n is the projectile ground-state to residue ground-state nucleon (either proton or neutron) separation energy, and E_x is the excitation energy of the residual. The mass dependent term, $(\frac{A}{A-1})$, is the centre of mass correction for the shell model spectroscopic factors, as illustrated in [57], with the main harmonic oscillator number $N = 3$ for the fp-shell, as shown in Fig. 2.4.

A spectroscopic factor implies values within the 0 to 1 range and represents the overlap between the wave functions of the initial and final state configurations. C^2S determines the nature and occupancy of the single-particle orbits of a nucleus. Hence, it contains information that extends beyond the knockout reaction mechanism.

For a specific final state, there can be more than one orbital involved in the knockout process. For all final states of the mass $(A-1)$ residue, the theoretical inclusive nucleon-removal cross section (the total probability of populating any bound state of the fragment residue from the projectile), σ_{inc}, is computed as the sum over all j values of the orbital of the removed nucleon and over all final states, i.e., the sum of the exclusive cross sections $\sigma_{th}^{exc}(E_x, J^\pi)$ that is calculated from the sum of the partial cross sections (Eq. 2.19).

2.3.2.1 Single Nucleon Knockout Reactions (Eikonal Approximation)

The single-particle cross sections (σ_{sp}) are extracted from the sum of two separate processes

$$\sigma_{sp} = \sigma_{sp}^{str} + \sigma_{sp}^{dif} \tag{2.20}$$

where σ_{sp}^{str} and σ_{sp}^{dif} are the single-particle stripping and diffraction cross sections, respectively. There is also a third reaction process known as Coulomb dissociation. In this process, the projectile is broken up as a result of Coulomb interactions with the target. However, as the contributions of Coulomb dissociation are normally very small with the choice of a low atomic number Z target, these effects are considered negligible [58].

The importance of each process is different based on the beam energy. At a high beam energy, the single-particle cross section for one nucleon knockout is dominated by stripping reactions, whereas at a lower energy, typically with 50–60 MeV/nucleon, the contributions of stripping and diffraction reactions are similar [58]. The single-nucleon removal cross sections presented here were calculated using the eikonal reaction theory [54, 59, 60].

The eikonal reaction theory implements the "spectator-core" approximation, assumes the nuclear core is not excited during the reaction. The three-body reaction model adopted in this study consists of the target, projectile core, and projectile valence nucleon, as presented in Fig. 2.10. Projectiles travelling at high energies allow for a significant simplification of the reaction model used to study the sudden removal of a nucleon. The internal motion of the projectile can be assumed to be adiabatic or in a frozen state. The adiabatic approximation, first discovered by Johnson and Soper (1970), assumes that the internal motion of the projectile is slow compared with the external motion at the centre of mass of the projectile. This suggests that at high beam energies, the core and valence system barely change within the time taken for the nucleus to traverse the target, basically reducing the system from three-body to two-body. The eikonal approximation is a semi-

classical solution of the scattering problem presented in Fig. 2.10. This method is employed to calculate the elastic-scattering functions or elastic S-matrices of the projectile, representing the amplitude of the forward-going scattered wave over a range of incident impact parameters. The S-matrix for the projectile can first be obtained by solving the time-independent Schrödinger equation (see [61, 62] for more details).

After the S–matrices are calculated, it is possible to calculate the two single-nucleon knockout cross sections separately by integrating over the projectile's centre of mass impact parameter, b [63]. The stripping σ_{str} and similarly diffractive breakup σ_{dif} cross sections may be found using the following equation

$$\sigma_{sp}^{str} = \frac{1}{2J+1} \int db \sum_{m} \left\langle \phi_{JM}^{c} \left| \left(1 - |S_n|^2\right) \right| S_c \right|^2 \mid \phi_{JM}^{c} \right\rangle, \tag{2.21}$$

$$\sigma_{sp}^{dif} = \frac{1}{2J+1} \int db \left[\sum_{m} \left\langle \phi_{JM}^{c} \| \left(1 - S_n S_c\right)|^2 \mid \phi_{JM}^{c} \right\rangle - \sum_{m,m'} \left| \left\langle \phi_{JM}^{c} \left| \left(1 - |S_n S_c|\right) \right| \phi_{JM}^{c} \right\rangle \right|^2 \right], \tag{2.22}$$

where the quantities S_c and S_n are the elastic-scattering S matrices [64, 65] for the interaction of the core-target and the valence nucleon-target systems, respectively, and are expressed as functions of their individual impact parameters [54]. The nucleon-core relative motion wave functions, with total angular momentum J and projection M, are ϕ_{JM}^{c}. They are calculated in a Woods-Saxon potential whose local potential has been adjusted to reproduce the separation energy of the nucleon from the initial state with a given nlj. Equation 2.21, ($|S_c|^2$), refers to the probability that the core survives the reaction, whilst $(1 - |S_n|^2)$ indicates the probability that the valence nucleon is absorbed [58]. Thus, the partial cross section for single–particle removal is the probability of both processes occurring together, Eq. 2.20.

In this work, full-pf shell-model calculations using the KB3G [45] interaction

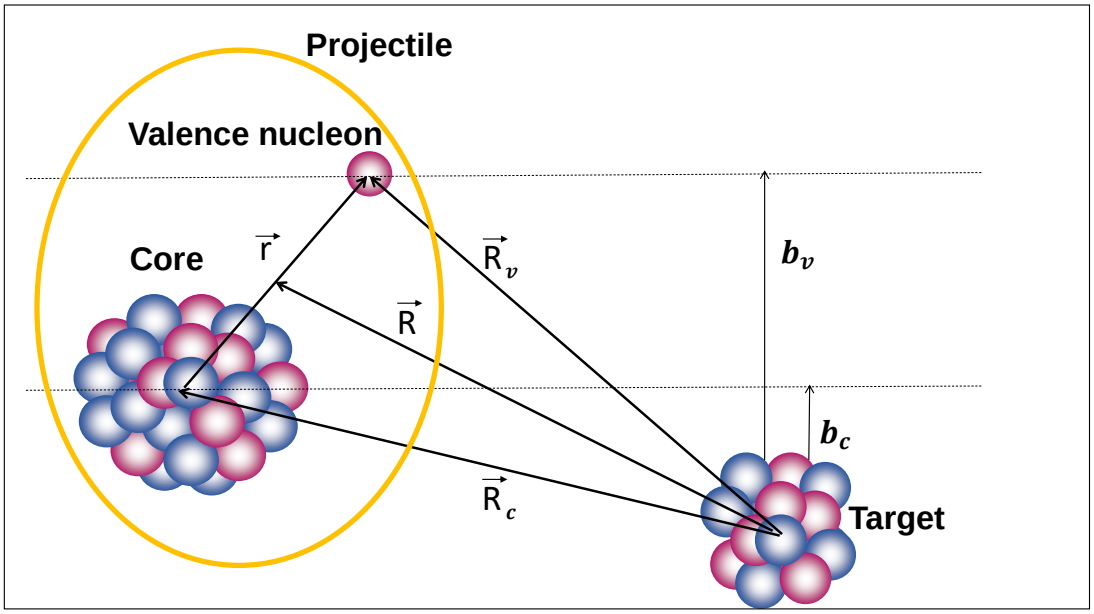

Figure 2.10: The coordinate system adopted for the core, valence nucleon, and target three–body systems. Adapted from [66].

in the ANTOINE code [43] were employed to compute the spectroscopic factors, enabling a calculation of a specific knockout path.

The single-particle cross sections, σ_{sp}, can be understood to include information related to the reaction mechanism, which can be explained by the condition where exactly one nucleon is removed from a specified state. Moreover, the spectroscopic factors provide all the nuclear structure information by measuring the overlap between the initial and final state configurations.

A description of the specific steps of these calculations (reaction models and C^2S calculations) used for obtaining theoretical cross sections for nuclei in this work will be described in Chapter 6.

Chapter 3

Experimental Details

This chapter will briefly review the experiment performed in the current work (Section 3.1). The following section (Section 3.2) will describe the detector systems and experimental setup as well as the γ-ray detectors utilized in the experimental work for this thesis. The experiment performed here will be referred to in this thesis by the label E14027.

3.1 Experimental Overview

The primary aim of using γ-ray spectroscopy in this work was to study the exotic proton-rich nuclei, and their neutron-rich mirror partners, $A = 48, T_z = \pm 2$ and $A = 45,\ T_z = \pm\frac{1}{2}$, see Fig. 3.1.

Radioactive beam facilities such as the National Superconducting Cyclotron Laboratory (NSCL) at Michigan State University (MSU) provide the opportunity to investigate exotic nuclei through in-beam γ-ray spectroscopy experiments. A study of exotic proton-rich ^{48}Fe was undertaken via a one-neutron knockout reaction from a radioactive ^{49}Fe beam, and subsequently, the analogue one-proton knockout reaction was performed from ^{49}V to populate states in ^{48}Ti. In addition, the exotic

proton-rich ^{45}V nucleus and its mirror ^{45}Ti were produced via one-neutron and one-proton knockout reactions, respectively, from the same incoming beam ^{46}V. The products were detected and identified by detection systems at the end of the S800 spectrograph (Section 3.2.4), and GRETINA was used for the identification of γ rays (Section 3.2.5). Thus, the study of energy-level schemes of these nuclei by the use of a one-nucleon knockout reaction mechanism provided an opportunity for determining the cross sections of the observed states in these nuclei and determining the MED.

3.2 Experimental Setup

3.2.1 Experimental Settings and Plans

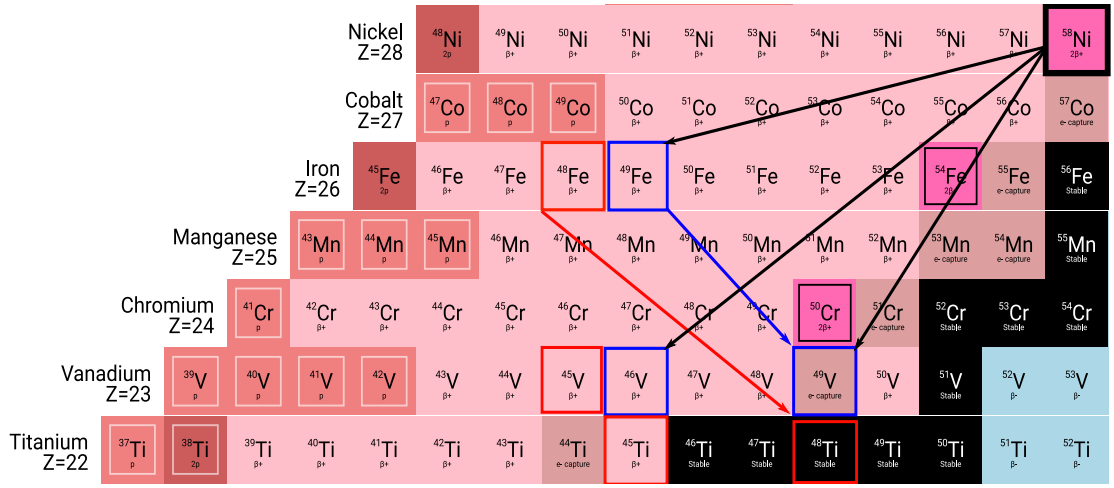

Figure 3.1: The ^{58}Ni primary beam is fragmented into the cocktail secondary beams of interest (squared in blue), such as ^{49}Fe/^{49}V and ^{46}V (see text for more details) at the entrance of the A1900 separator. The mirror pairs of interest (squared in red), ^{48}Fe/^{48}Ti and ^{45}V/^{45}Ti, are populated via one nucleon-knockout reaction from these secondary beams.

The experiment was conducted in 2016, (code E14027). A $\sim$ 160 MeV/u primary beam ^{58}Ni was fragmented on a 802 mg/cm^2 ^{9}Be production target into secondary beams that were dispersed via the A1900 separator [67]. The resulting fragments were separated by the A1900 separator [67] into a cocktail beam

that contained ^{49}Fe, ^{48}Mn, ^{47}Cr, ^{46}V, etc. in one setting of A1900 (see Fig. 3.3) and the mirror secondary beams, ^{49}V, ^{48}V, and ^{47}V, etc. in the other setting. For the secondary beam of interest, the fragment beam rates for ^{49}Fe (^{49}V) were $\sim$ 300 (2×10^5) particles per second, respectively, constituting $\sim$ 0.5%(64%) of the secondary beam cocktail. A set of adjustable slits and a degrader wedge were used to block and disperse the array of secondary beams before impinging on the 188 mg/cm^2 ^{9}Be secondary target. The secondary beams used for this study are ^{49}Fe (T_z = -$\frac{3}{2}$) and ^{49}V (T_z = $\frac{3}{2}$), which represent a mirror pair, and $N = Z$ ^{46}V ($T_z = 0$). One-nucleon knockout reactions occur at the secondary target where the nuclei of interest are produced and where the excited states in the mirror nuclei ^{48}Fe and ^{48}Ti ($T_z = \pm 2$) are populated via one-neutron and one-proton removal from ^{49}Fe and ^{49}V secondary beams, respectively. Moreover, the excited states in the mirror nuclei ^{45}V and ^{45}Ti ($T_z = \pm\frac{1}{2}$) are populated via one-neutron and one-proton knockout from the same secondary beam ^{46}V.

The deexcitation γ rays from the knockout reaction residues at the ^{9}Be secondary target position were recorded by the HPGe detector array GRETINA [68,69]. The beam-like residues resulting from the reactions within the target then traverse the S800 spectrograph [70], which is used to identify and resolve the reaction products using energy loss and time of flight measurements. Moreover, the S800 spectrograph provides crucial information on recoil angles and momentum distributions of the reaction products, which allows for accurate event-by-event γ-ray Doppler corrections.

A summary of the ten different combinations of A1900 and S800 settings and, description of the experiment undertaken in this work are presented in Table 3.1. Throughout the experiment, $\sim$109 hours of the main data taking, separated into 123 data runs, were obtained. Data runs were interrupted several times to carry out unreacted beam runs, mirror nuclei settings and the mask calibrations (Table 3.1). Periodically, through the experiment, A1900 settings were kept unchanged and then the settings of the S800 spectrograph were switched to the unreacted beam setting. The unreacted beam runs were performed to measure the number of

beam particles to determine the inclusive cross sections. To carry out the mirrored knockout reaction, the A1900 settings were changed to the mirrored settings with corresponding unreacted beam settings (Table 3.1).

Mask calibration runs were also performed, which were used in particle trajectory mapping (more details in Chapter 4). The beam purity varied for each secondary beam and was determined during the experiment (Table 3.1). For instance, ^{49}Fe has a beam purity of 0.5%, while ^{49}V has a very large beam purity, 64% (hence only one-run, 113, Table 3.1). The reactions of interest are highlighted in blue, while the other reactions were used for a different analysis, see Table 3.1. It should be noted that the ^{46}V-^{45}V knockout setting is the same setting as the ^{49}Fe- ^{48}Fe knockout setting.

The following sections will discuss the components of the experimental setup at the NSCL and demonstrate the step-by-step process of deriving the obtained measurements, from beam production to γ-ray detection and reaction product identification.

Table 3.1: Summary of the different settings and data for the sub-experiments performed at the NSCL. The beam purity, Downscaler (Ds) and duration of the runs are also shown. The nuclei used in this analysis are highlighted in blue.

Run Number	A1900 Settings	Purity	S800 Settings	Ds	Time(h, min)	Comments
19-109 133-189	^{49}Fe	0.5%	^{48}Fe	1	106:00	Data
Mirror Beam Setting						
113	^{49}V	64%	^{48}Ti	3	01:00	Data
123-124	^{48}V	42%	^{47}Ti	1	01:17	Data
128	^{47}V	28%	^{46}Ti	3	01:13	Data
183	^{46}V (^{49}Fe)	40%	^{45}Ti	2	00:50	Data
21-22						Mask Calibration
85-86						-
114-115						-
178-179						-
Total					**00:50**	
32	^{49}Fe	0.5%	^{49}Fe	1		Unreacted
56		-	-	-		-
154		-	-	-		-
180		-	-	-		-
Total					**00:37**	
111	^{49}V	64%	^{49}V	1	00:6	Unreacted
121	^{48}V	42%	^{48}V	1	00:9	Unreacted
126	^{47}V	28%	^{47}V	1	00:6	Unreacted
182	^{46}V(^{49}Fe)	40%	^{46}V	1	00:17	Unreacted

3.2.2 Primary Beam Production

The Coupled Cyclotron Facility (CCF) [71, 72] at the NSCL consists of a Superconducting Source for Ions (SuSI), which is an electron cyclotron resonance (ECR) source, and the two cyclotrons, K500 and the K1200 at the NSCL, as shown in Fig. 3.2. In this case, it was used to produce the ^{58}Ni primary beam. The first step starts at the ECR ion source, which produces a stable beam of positive ions, accelerated through the K500 cyclotron up to energies of around 8–12 MeV/u. Subsequently, the primary beams are extracted from K500 cyclotron and injected into the second cyclotron, K1200 [73], where they are accelerated to energies 160 MeV/u for a velocity of $\sim$ 0.4c. The K1200 cyclotron is equipped with a carbon foil for the removal of the remaining atomic electrons such that the ^{58}Ni primary beam used in this experiment is in a 28+ charge state. The beam is shaped using several quadrupole and sextupole magnets before impinging upon the 802 mg/cm^2 ^{9}Be production target at the beginning of the A1900 separator. After fragmentation of the primary beam at the production target, a variety cocktail of secondary beams was produced.

3.2.3 Secondary Beam: A1900 Separator

The A1900 separator is a high-resolution fragment separator that can provide a wide range of fast exotic beams across the nuclear chart for nuclear physics studies and is aimed at separating the secondary beams, which are a result of the fragmentation of the primary beam in the ^{9}Be production target. The momentum acceptance of this separator was adjusted to 0.5%.

The A1900 separator consists of a series of four 45° steering dipole superconducting magnets, 24 superconducting focusing quadrupole and other sextupole and octupole magnets for aberration correction, energy-degrading wedges, and

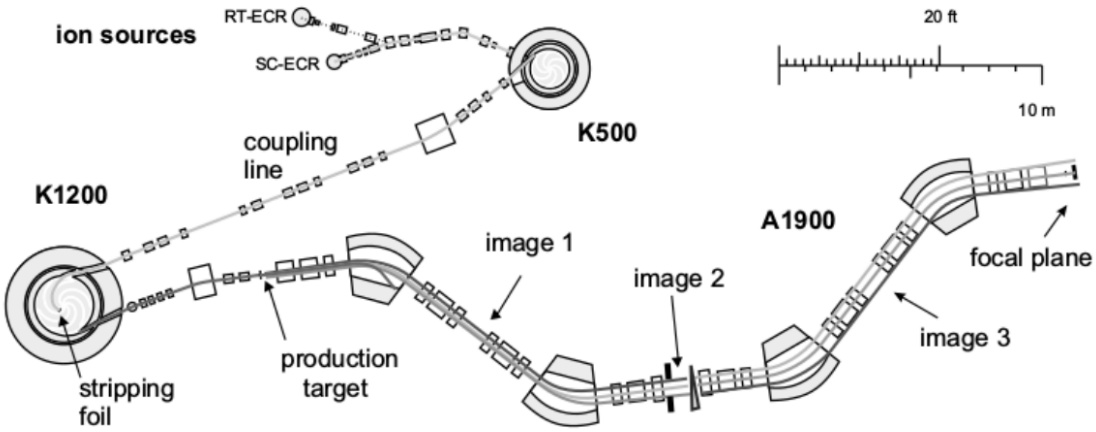

Figure 3.2: A schematic of the ion source (SuSI) coupled with K500/K1200 cyclotrons and the A1900 separator. Taken from [67].

slits situated at image 2 (see Fig. 3.2) [67]. These components of the separator are located immediately after the production target and can be utilised to disperse the cocktail of secondary beams, reduce the level of certain contaminants, block any undesired secondary beams from coming through slits located at the second image (Fig. 3.2) after dispersion, and adjust the momentum acceptance of the cocktail beam. Each beam with mass A and charge Z, moving at a velocity v, is deflected by four dipole magnets. This allows for the use of the magnetic rigidity, $B\rho$, of the dipole magnets to select the beam of interest,

$$B\rho = \frac{p}{q} = \frac{mv}{q} = \frac{m\beta c}{q} \propto \frac{A}{Z}\,\beta c \tag{3.1}$$

where B is the magnetic field strength, ρ is the radius of curvature of the particles orbit, $\beta = v/c$; m and q are the mass and charge of the particles, respectively.
The achromatic aluminium wedge (the triangle shape at image 2, as shown in Fig. 3.2) in A1900 is used for isotopic beam selection. This also enables the identification of the isotopes of interest before focusing the secondary beams to impinge on the secondary ^{9}Be target. High momentum particles hit the thick part of the wedge and low momentum particles hit the thin part of the wedge. Each beam experiences various levels of energy loss through the wedge and beam components

with the same $B\rho$, which will appear with different momenta depending on their atomic numbers, Z. A further separation occurs, wherein the emerging, filtered beam is passed through the remaining two dipole magnets along a dispersive beamline. Subsequently, the final secondary cocktail beam of interest arrives at the focal plane of the A1900 separator. The desired secondary cocktail beam is then transferred along an analysis line before impinging on a reaction target ^{9}Be, located at the secondary target position on the S800 spectrograph (Section 3.2.4). The cocktail secondary beam was produced after the separation process in the A1900 separator, consisting of primarily 0.5% ^{49}Fe, 4.9% ^{48}Mn, 29.8% ^{47}Cr, 40% ^{46}V, 23% ^{45}Ti, and 1.7% ^{44}Sc (Fig. 3.3).

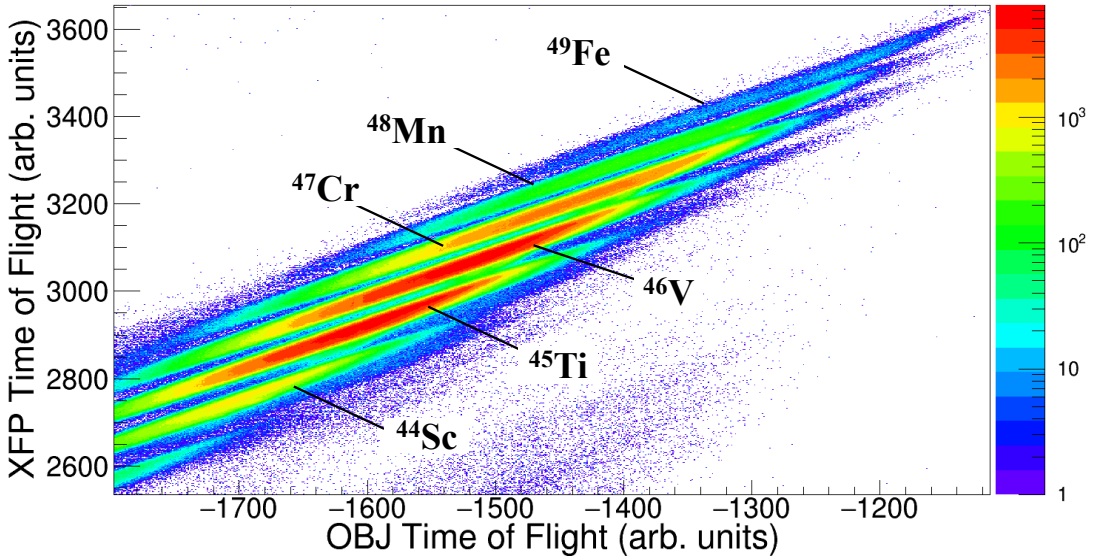

Figure 3.3: The incoming secondary beams are shown with the A1900 tuned to produce ^{49}Fe and the other beams produced with same setting, which can be observed from the XFP and OBJ scintillators times of flight relative to the E1 scintillator in the S800 spectrograph focal plane.

These secondary beams were then sent through a transfer hall between the A1900 fragment separator and the S800 spectrometer. The beam species were identified, on an event-by-event basis, by time of flight (ToF) measurements between two plastic scintillator detectors located after the A1900 fragment separator and an E1 scintillator at the focal plane in the S800 spectrometer, located behind

the final (reaction) target. The two scintillator detectors are the extended focal plane (XFP) positioned at the end of the A1900 separator and the object (OBJ), which is located further down the beamline at the object position of the S800. They are separated by a distance of $\sim$ 30 m and can be used to identify different incoming beams. Figure 3.3 shows the different incoming ions appear on diagonal lines (see labels), allowing one to gate on a selected incoming beam.

3.2.4 The S800 Spectrometer

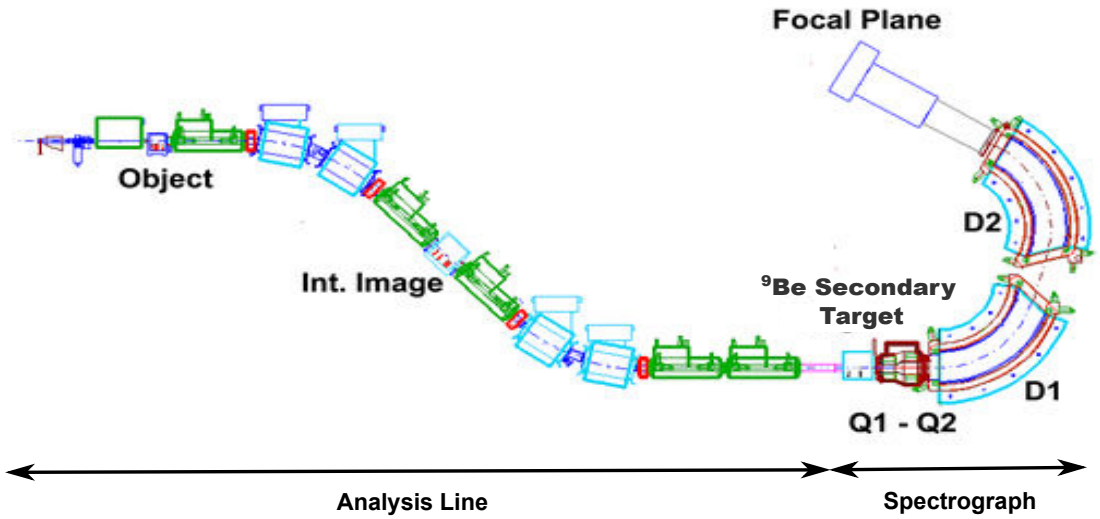

Figure 3.4: The S800 spectrometer consists of the analysis line and spectrograph. The beam of interest enters the S800 spectrometer at the object and then passes through the analysis line. The resulting particles are separated using the spectrograph after the reaction at the secondary target [74].

The S800 spectrometer is a high-resolution, large acceptance magnetic spectrometer [70]. The first part – the analysis line – is used to identify and focus secondary cocktail beam from the A1900, and the second part – the spectrograph – is used to separate and transport outgoing fragments after the secondary reaction target, see Fig. 3.4.

In the experiment performed for the current work, $\sim$81–84 MeV/u ^{49}Fe, ^{49}V, and ^{46}V secondary beams were transferred along the S800 analysis line and impinged

on a ^{9}Be secondary reaction target of thickness 188 mg/cm^2 where mirrored one-nucleon knockout reactions occurred. The γ rays from the excited states populated the nuclei of interest ^{48}Fe ($T_z = -2$), ^{48}Ti ($T_z = +2$) and ^{45}V ($T_z = -\frac{1}{2}$), ^{45}Ti ($T_z = +\frac{1}{2}$) and were detected using GRETINA (Section 3.2.5). The reaction products were transported to the S800 focal plane detectors system, where they were identified by measuring position, angle, energy loss, and ToF [75]. A description of S800 components and the detector systems will be provided in the following sections.

3.2.4.1 S800 Analysis Line

This part of the S800 spectrometer extends from the object (OBJ) scintillator position to the reaction target position. It is designed to receive the secondary beam from the A1900 fragment separator and direct it into the high-resolution spectrograph using a series of magnets. It comprises four superconducting magnetic dipoles, five superconducting magnetic quadrupole triplets, and a few correcting sextupoles. These dipole magnets have the maximum magnetic rigidity, $B\rho$, of 5 Tm [70]. The purpose of the analysis line is to direct and focus the incoming secondary beams onto the reaction target and measure the characteristics of the incoming particles produced in A1900.

The S800 analysis line can be operated in two different modes: the focused mode and the dispersion matching mode [70]. In the focused mode, the beam is concentrated on the target position and dispersed in the focal plane, and a larger momentum acceptance of roughly $\pm 2\%$ is achieved. In contrast, the dispersion matching mode is achromatic on the whole S800, where the beam is momentum dispersed on the target with a dispersion of about 10 cm/%. Thus, in this mode, the momentum acceptance of the analysis line is limited to $\pm 0.5\%$, and it can be used in the experiments requiring the highest momentum resolution. In the

experiment described in this work, the S800 analysis line was run in a focused mode in which the beam was focused on the reaction target.

3.2.4.2 S800 Spectrograph and Focal Plane Detectors

The S800 spectrograph consists of two large focusing quadrupole magnets, followed by two 75° superconducting dipole magnets and detector systems located just past these dipoles at the focal plane of the spectrometer. This is the large acceptance section of the S800 with a maximum magnetic rigidity $B\rho$ that is limited to 4 Tm. The quadrupole magnets are situated after the target chamber, which helps focus the outgoing particles after the reaction target in the non-dispersive plane (the y-position) and then in the dispersive plane (the x-position). Furthermore, the two 75° superconducting dipole magnets serve to direct and disperse the residue of interest at S800's focal plane and block any unwanted unreacted secondary beam using a beam blocker.

The position and angle of each product are recorded at the S800 spectrometer's focal plane, which includes two Cathode Readout Drift Chambers (CRDCs), ionisation chambers (IC) and three plastic scintillators E1, E2, and E3 (see Fig. 3.5). The detectors used in the experiment for this work will be described in detail in the following subsections.

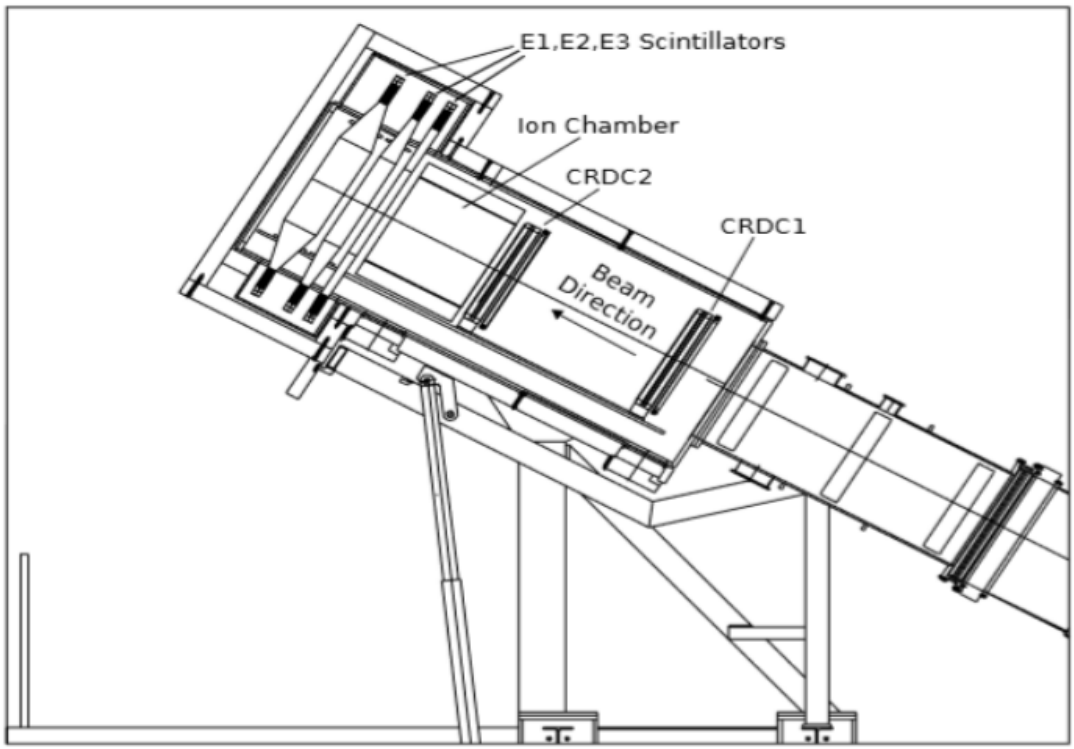

Figure 3.5: Schematic of the detectors located in the focal plane of the S800 spectrometer [75].

3.2.4.3 Cathode Readout Drift Chambers (CRDCs)

The first detector device in the S800 spectrometer's focal plane is a pair of CRDCs. The two CRDCs are gas-filled detectors, located approximately 1 m apart. They are filled with 80% CF_4 and 20% C_4H_{10} at a typical pressure of around 140 Torr. The detectors have an active area of 26 cm $\times$ 56 cm in the non-dispersive (y) and dispersive (x) planes, respectively, and a depth of 1.5 cm. Both CRDCs have 224 pads in x direction with a pitch of 2.54 mm and are used to detect particle position and trajectories of nuclei after the interaction with the secondary production target.

The traversing particles ionise the gas in the CRDCs, creating of a number of electron-ion pairs. This results in a drift of free electrons towards an anode wire under the influence of an electric field. The charge collected at the anode wire induces a positive charge on the cathode pads (Fig. 3.6). The x-position in the

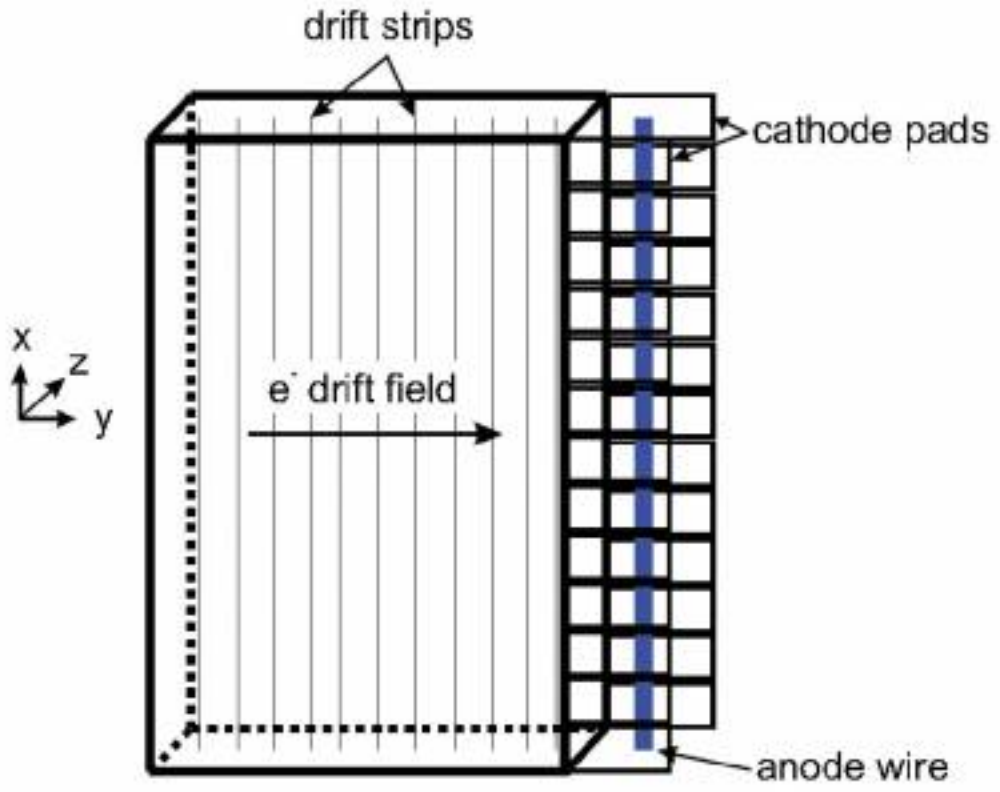

Figure 3.6: A diagram illustrating the CRDC detector, where the particles are ionised as they pass through each CRDC, creating free electrons that drift towards the anode wire. As a result, a positive ion is produced on one of the cathode pads. A Gaussian function is fitted to determine the x-position of the particle, and the y-position is calculated based on the electron drift time to the anode wire in relation to the trigger at the E1 scintillator. Taken from [74].

dispersive plane is determined by measuring the induced signal on the neighbouring cathodes by fitting a Gaussian function to the charge distribution across the cathode pads. The y-position in the non-dispersive position is determined by recording the drift time of the electrons in the gas, whereby the time is measured while collecting charge on the anode wire by a comparison to the S800 timing signals trigger provided by the E1 scintillator. Each CRDC detector has a spatial resolution of less than 0.5 mm FWHM and a maximum rate of 5,000 counts per second [76]. A higher count rate would lead to efficiency losses.

The recoil trajectories can be reconstructed using the x- and y-position information

provided by the two CRDC detectors. This also allows for the determination of the incident angle at the focal plane in the dispersive (a_{fp}) and non-dispersive planes (b_{fp}). The focal plane angles are then used in conjunction with the inverse map (subsection 3.2.4.6) to reconstruct the recoil angles at the target position. The dispersive angle at the focal plane (a_{fp}) can be calculated using the following equation

$$a_{fp} = tan^{-1}\left(\frac{x_2 - x_1}{d}\right), \tag{3.2}$$

where x_1 and x_2 are the dispersive (x) positions measured in CRDC1 and CRDC2, respectively.

The pathway of the particular nuclei of A/Q can be extrapolated from the E1 scintillator back to the reaction target using the inverse map, which also uses the dispersive and non-dispersive positions and angles data pertaining to each CRDC, thus yielding event-by-event vector tracking of all particles at the target position.

3.2.4.4 Ionisation Chamber (IC)

The S800 IC is located immediately after the two CRDC detectors. It is used for the energy loss measurement of the nuclei of interest that pass through the chamber with the energy loss depending on their mass and charge. The chamber consists of 16 segments, each with a narrow anode-cathode gap perpendicular to the beam direction. It is filled with P10 gas, which consists of 90% Ar and 10% CH_4 at a pressure of 300 Torr [77].

Electron-ion pairs are generated as a particle passes through the ion chamber and ionises the gas; the electrons drift towards the anode and the ions are collected on the cathodes. The resulting signals in the 16 anode segments are then summed to produce the total energy loss for that particular particle. The charge collected on the IC anodes is determined by the number of pairs produced, giving a direct

measurement of the particle's energy loss, which is approximately proportional to the square of the charge of the particle Z^2. The energy losses of a charged particle are indicative of an atomic number as per the Bethe-Bloch formula

$$-\left\langle \frac{dE}{dx} \right\rangle = \frac{4\pi n Z^2}{m_e c^2 \beta^2} \left(\frac{e^2}{4\pi\epsilon_o} \right)^2 \left[\ln\left(\frac{2m_e c^2 \beta^2}{I\left(1-\beta^2\right)} \right) - \beta^2 \right], \tag{3.3}$$

where n is the electron density of the material; m_e is the mass of an electron; c is the speed of light; $\beta = \frac{v}{c}$ is the velocity of the particle; e is the electron charge; ε_0 is the permittivity of a vacuum, and I is the average excitation potential of the material. This energy loss measurement can be used in combination with ToF measurements to identify the reaction products.

The efficiency of IC detection is approximately 100% for the beam rate utilised in the present experiment. Based on this, the IC was used as the standard for measuring the relative efficiency of the other particle detectors.

3.2.4.5 Scintillation Detectors

Three plastic scintillators are closely coupled with the IC at the end of the S800's focal plane: E1, E2, and E3 scintillators of thicknesses 5 cm, 10 cm, and 20 cm, respectively (Fig. 3.5). They are used in conjunction with the S800 trigger to identify the final time of flight measurement [75].

The beam particles traverse through these scintillator detectors, which results in the generation of photons. These photons are collected by photomultiplier tubes (PMTs) [77], which are attached to both the top and bottom of each plastic scintillator and turned into an electrical signal. The average time signal from each PMT is used to determine the timing signal of each plastic scintillator. Besides the timing information, energy loss and total energy measurements of the incident particles can also be gathered [75].

The plastic scintillator detectors can handle rates of up to 1 MHz. However, the timing resolution of these detectors reduces at higher count rates and when the

trajectories of different nuclei cross at the focal plane, although this effect can be corrected through the use of the position and angle information provided by the CRDC detectors. The E1 scintillator situated at the focal plane of the S800 spectrograph is also utilised as the primary trigger for the data acquisition (DAQ) system [70].

3.2.4.6 Recoil Trajectory Reconstruction

The S800 focal plane detector system helps determine the position and angles of the reaction products, which can be used to extract their path through the spectrometer and reconstructs their trajectory back to the reaction target.
The trajectory reconstruction on an event-by-event basis is achieved through the use of an inverse map for each recoil by employing the code COSY Infinity [78]. Inverse maps are generated automatically for experiments conducted at the NSCL and can be requested remotely through a server that provides remote users with maps by entering some experimental parameters, such as the magnet strengths of the spectrometer, $B\rho$ and the residue's mass, velocity, and charge.
The inverse map S^{-1} relates the positions (x_{fp}, y_{fp}) and the angles (a_{fp}, b_{fp}) in both the dispersive and non-dispersive directions at the focal plane to the dispersive and non-dispersive angles at the target position (a_{ta}, b_{ta}) as well as the non-dispersive target position y_{ta} and the energy of the beam at the target position $d_{ta} = \delta E/E$ by the relation

$$\begin{pmatrix} a_{ta} \\ y_{ta} \\ b_{ta} \\ d_{ta} \end{pmatrix} = S^{-1} \begin{pmatrix} x_{fp} \\ a_{fp} \\ y_{fp} \\ b_{fp} \end{pmatrix} \tag{3.4}$$

For this transformation, the average dispersive (x) position at the target is assumed to be negligible, $x_{ta} = 0$, in order to minimise the number of parameters needed to calculate the particle's trajectory so that the uncertainty of this parameter can be included in the energy resolution of the S800 spectrograph [70]. As the recoil vector at the target position needs to be reconstructed from the position and angle measurements taken at the focal plane of the S800, it is necessary to precisely calibrate and correct these measurements (Section 4.2).

3.2.5 Gamma Ray Spectroscopy: GRETINA Array

The Gamma-Ray Energy Tracking In-beam Nuclear Array (GRETINA) is a high-resolution gamma-ray spectrometer that consists of electrically segmented high-purity germanium (HPGe) modules designed for nuclear structure studies, see Fig. 3.7.

In this experiment, GRETINA had nine detector modules, each with four high-purity germanium crystals with 36 segmented electrodes. Four of these modules (quads) were centred at 58° and five were centred at 90° in relation to the beam direction.

When placed surrounding the reaction target, the array covers a solid angle of $\sim 1\pi$ in the laboratory frame, providing good solid angle coverage downstream of the target, which is useful for fast isotope beams, as shown in Fig. 3.7. This improves the detection efficiency of forward-focused γ rays as a consequence of the Lorentz boost [68]. GRETINA is the first implementation of the γ-ray energy-tracking array (GRETA) [79].

Each GRETINA crystal is divided along the longitudinal direction into six slices of width 8 mm, 14 mm, 16 mm, 18 mm, 20 mm, and 14 mm from the face

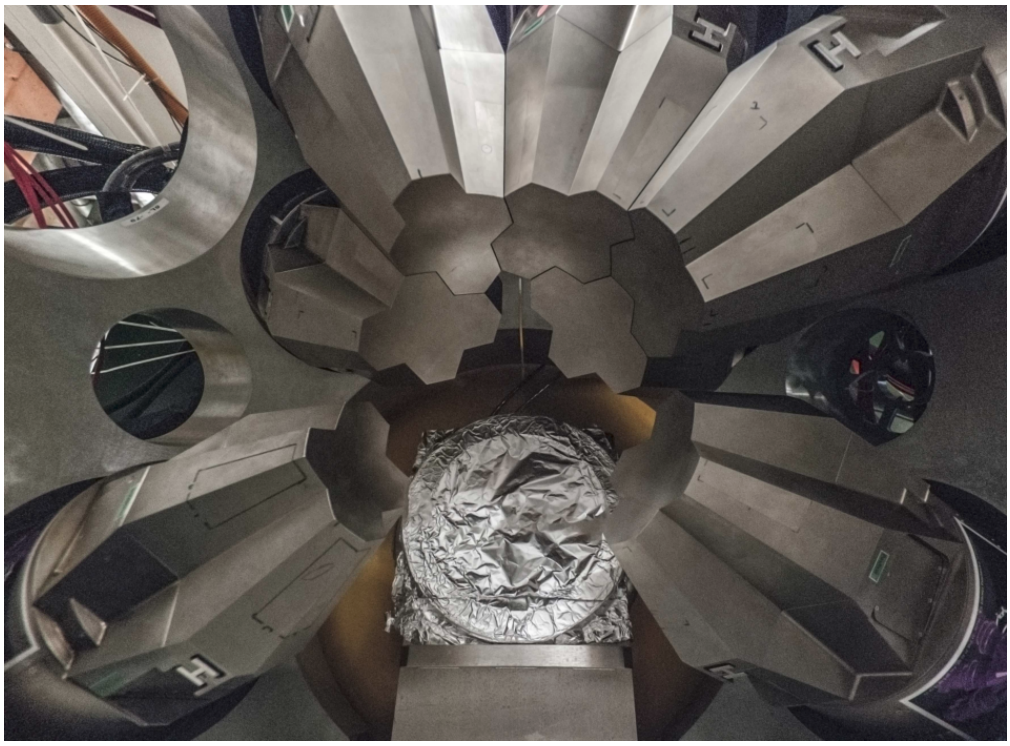

Figure 3.7: The standard configuration of GRETINA at the NSCL located in front of the S800 spectrograph's entrance and surrounding the secondary target. This figure shows seven GRETINA modules (taken from different work [68]), four of which are mounted in the 58° ring and the remaining three modules are mounted at 90°. The data presented in this work were obtained with nine GRETINA modules. Four modules are mounted in the 58° ring and five are located at 90° ring. Taken from [68].

of the crystal to the back. The slices are also split into six segments, accounting for a total of 36 segments per crystal, as shown in the illustrations on the left side of Fig. 3.8. Electronics are placed behind the crystal to read the charge of each electrode. The HPGe detector must operate at liquid nitrogen temperature to suppress electrical noise in the crystal. In the GRETINA system, the input Field-Effect Transistor (FET) of the central contact's preamplifier, used to measure the total energy, is inside the cryostat's vacuum and kept cold. However, the input FETs of the preamplifiers of the 36 segments crystal are located outside the cryostat's vacuum (warm FETs) [69]. The GRETINA detector modules and the segmentation of the crystals are illustrated in Fig. 3.8.

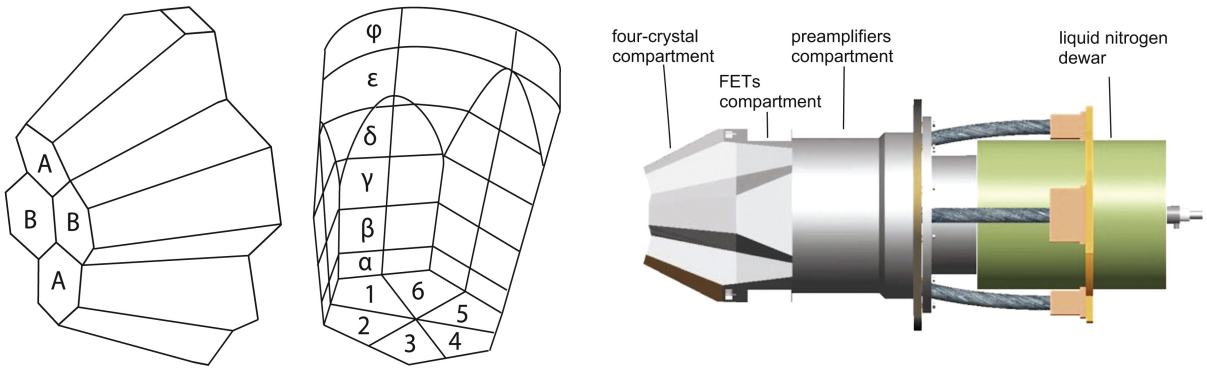

Figure 3.8: An illustration of four crystals packed in one module, each crystal is segmented into six separate electrical contacts along the length of the crystal α to ϕ, and a further six segments in the radial direction (numbered one to six), resulting in a total of 36 segments. On the right, the preamplifier compartment for each module is shown to amplify and extract signals from the detector and a liquid nitrogen dewar of the GRETINA detector module. Taken from [69].

There are two steps of the analysis of the GRETINA gamma-ray tracking data:

(i) measuring the position and energy of every interaction of the γ ray in the crystal(s) through pulse-shape analysis (PSA).

(ii) using a tracking algorithm to arrange the interactions in a proper order, reconstruct the full-energy and separate multiple γ-ray paths from each other.

Step (i) is completed in this analysis; however, although GRETINA has excellent γ-ray tracking capabilities, for the experiment performed in this work, step (ii) is replaced by an add-back procedure, which is standard for GRETINA analysis at the NSCL [68]. Hence, the performance of GRETINA results from a combination of determining the position well to obtain a good Doppler correction and add-back of γ rays to improve the efficiency of GRETINA.

A precise reconstruction of the individual interaction positions of the γ rays in GRETINA is possible with the use of a PSA algorithm [80] capable of improving the sub-segment position resolution with GRETINA.

PSA methods are used to compare the digitised pulse shapes for the segment,

and its neighbouring segments, to the simulated basis data of signals. These basis datasets of net and transient charge signals pertain to different interaction points in the segment. The closest match provides the reconstructed position of the interaction points (x, y, z, E).

One of the main uses of GRETINA is γ-ray tracking, which is used to determine the most probable order of the interactions, where the paths of Compton-scattered γ rays are tracked inside the detector modules and neighbouring crystals using a tracking algorithm. This allows the paths of Compton-scattered γ rays to be reconstructed. However, a comparison of the use of the first interaction point as the highest energy deposition point, compared with the γ-ray tracking figure of merit (FoM) decomposition process with GRETINA, was conducted in [68]. It was found that, for intermediate energies such as NSCL, for γ-ray energies ranging from 275 keV (^{19}Ne) to 6.1 MeV (^{16}O) [68], using the highest energy deposition point for Doppler reconstruction, improved peak to background. As a result, in this analysis, the highest detected energy in each crystal was assumed as the first interaction point for any γ-ray Doppler correction performed.

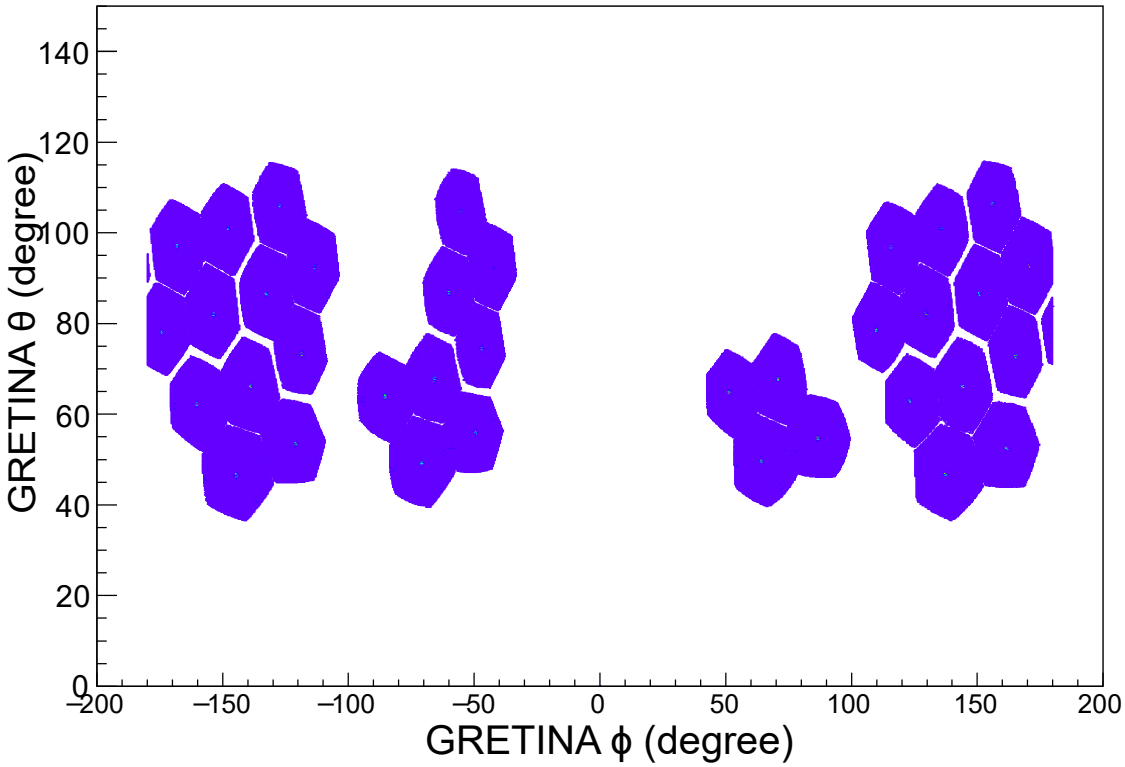

Figure 3.9: A demonstration of the angular coverage of GRETINA extracted from the current data, which consists of 36-fold segmented HPGe detectors (four detectors at 58° and five detectors at 90°) directed at the secondary target position.

Fig. 3.9 shows a unique feature of this array; it illustrates accessibility for the measured event-by-event angle of every γ ray emitted from the reactions. This shows the potential to examine an event in which the array experienced multiple photon scattering events in the crystals. The spatial coordinates of each γ-ray interaction are recorded in the 36 segments of each detector. Instead of using γ-ray tracking, an addback method was used to account for events that scatter between crystals (i.e reconstruct the total energy). If the γ ray interacts with only a single crystal depositing its full energy, the generated charge will be proportional to its energy. However, there is the possibility that a γ ray may scatter from one crystal to another, leading in the total energy being distributed by many crystals. To correct this effect, the energy deposited in the neighbouring crystals in the quad module was added by means of a process known as add-back. Add-back is a procedure through which algorithms are used to identify Compton-scattered events across different detector crystals, which are then summed (summation of all the γ-ray interactions across neighbouring crystals) to give the initial energy of the γ ray before Compton scattering, thereby dramatically reducing the Compton background. Different add-back methods may be used with GRETINA, such as neighbouring add-back, calorimeter add-back, and cluster add-back. The neighbouring add-back means that addback occurs only for nearest neighbours and for particular geometric conditions while the calorimeter method indicates adding all the energies recorded by the entire array.

The cluster add-back method involves the summation of neighbouring crystals if the first interaction points in the crystals are within a specified relative angle. The effects of each method of add-back are presented in Fig. 3.10 for a stationary ^{133}Ba calibration source.

Since Compton-scattered events dominate at low energy in the spectrum, neighbouring add-back was applied to this dataset. Hence, neighbouring add-back was utilised only for the Doppler corrected spectra observed in this work.

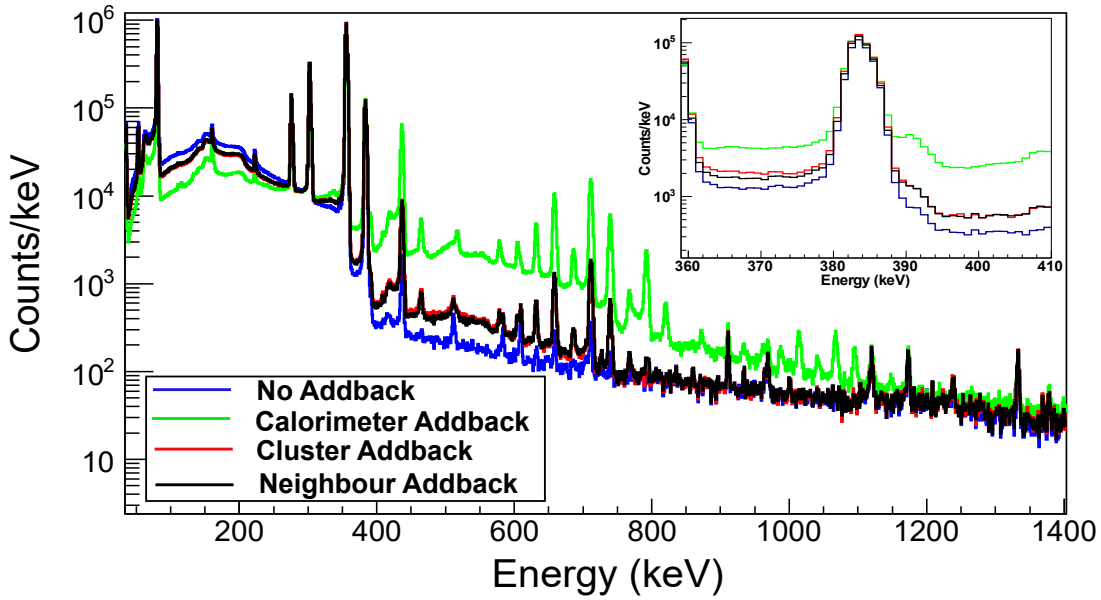

Figure 3.10: Comparison of the add-back methods of GRETINA, the calorimeter (green), cluster (red) and neighbour (black) and without add-back (blue) implemented for the same ^{133}Ba calibration source γ-ray run taken at the beginning of the experiment. The inset spectrum displays the same plot at the 383 keV peak of ^{133}Ba, where it clearly shows the difference of the improved peak-to-background ratio for add-back.

In summary, for the Doppler correction analysis performed in this work, the PSA-determined positions are reconstructed, and then, the first interaction point used for the Doppler correction is taken to be the point of the largest energy interaction. Instead of using a full tracking algorithm, the peak-to-total is optimised using the nearest-neighbour add-back method, where γ-ray energies observed in neighbouring crystals (that have been fired in the same event) are added together given that they meet certain geometric criteria. It has been shown in [68] that this simpler procedure gives comparable results for the full tracking of the NSCL-type experiments, where gamma-ray multiplicity is relatively low. It is important to note that the huge benefit of using GRETINA for these experiments is the high-position resolution that gives excellent energy resolution. In this experiment, the best energy resolution achieved for a fast transition was about 1.4% (FWHM) for 1-MeV γ ray and is limited not by the intrinsic energy resolution but by the target thickness, which introduces a spread in velocity values.

3.3 Data Acquisition Triggers

The DAQ system used in this experiment was a combination of the individual DAQs of GRETINA and S800 systems. There are two types of events that are needed in this experiment; (i) S800 (single particle) events where the E1 scintillator has fired, but GRETINA has not, and (ii) COINC events where the E1 scintillator and GRETINA both have fired. Each type of event generates its own trigger - i.e., S800 triggers and COINC triggers. The coincidence events are needed to measure the γ rays, while the S800 singles events are required to calculate cross sections. Due to rate limits, it is not possible to record all the S800 events, therefore a downscaler (Ds) is sometimes applied to the S800 events. Ds is used to take a reduced number of events from the trigger sources. It rejects a certain fraction of the events. For a Ds value of N, only one event for every N is written to the disk. For example with a Ds of three, only one of three events is written to a disk.

Identifying the type of event is crucial for determining cross sections. Fig. 3.11 shows the recorded event data, where there are three channels; 1, 2, and 3 corresponding to the S800 trigger, COINC trigger, and both S800 and COINC trigger events, respectively. If the downscaler is not applied to the data, then only two types of events would seen (S800 or both S800 and COINC trigger (Fig. 3.11 (a)). However, if Ds is more than 1, then there will be three different combinations of triggers that exist in the data; (a) S800 only events (downscaled), (b) COINC events with no S800 trigger present, and (c) events where both S800 and COINC triggers are present, as shown in Fig. 3.11 (b).

Both types of events, the S800 and the GRETINA are important in this experiment, and it is required to analyse both of them.

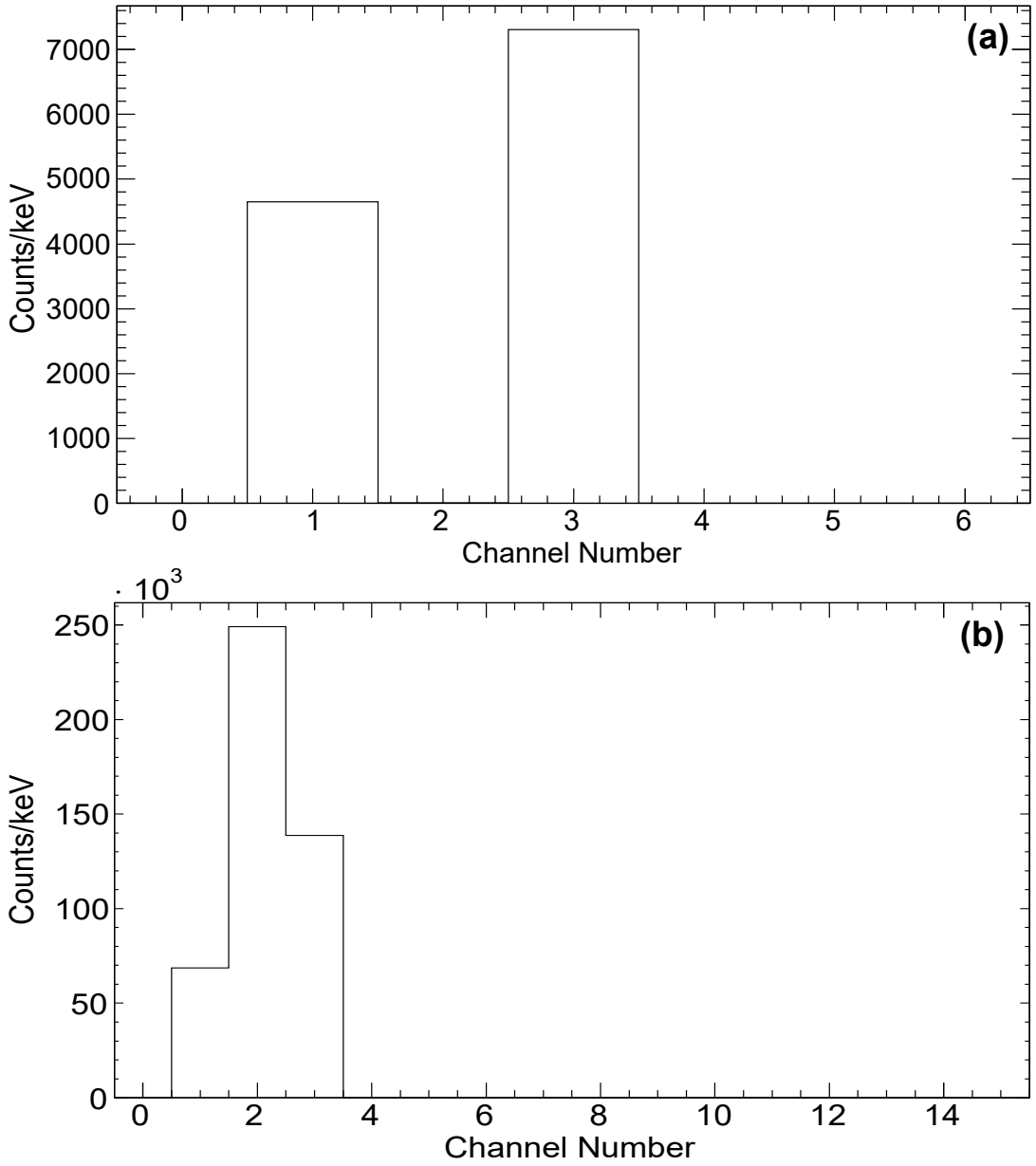

Figure 3.11: The histograms of recorded events of the triggers-register pattern is plotted against their channel number (a) with and without applying Downscaler (which rejects a fraction of the incoming events) (a) and (b), respectively. Channel 1 represents S800 events only; channel 2 represents COINC events only; channel 3 represents both S800 and COINC events.

Chapter 4

Calibrations and Corrections Data and Analysis Technique

The initial step of the data analysis is ensuring that all the components of the experimental setup are well calibrated. The GrROOT analysis code [81] is used to calibrate the present data. It is a specific ROOT [82] data analysis package for A1900, S800 components, and GRETINA. GrROOT was used to convert the raw data recorded at the NSCL into ROOT-format objects, which split the data into ROOT 'trees', allowing the examination of the correlated recorded values on an event-by-event basis.

The chapter will describe all the calibration procedures employed to ensure that any measurement taken by the experiment components was reliable, as well as the analysis techniques in order to identify the γ-ray transitions observed in this work.

4.1 XFP-OBJ Time Shift Correction

The ToF of incoming secondary beams is measured between the XFP and OBJ scintillators and the E1 scintillator at the focal plane of the S800 spectrograph.

However, throughout the experiment, a time shift has been found for some of the runs of $\sim$ 40ns, which results in a shift in the incoming secondary beams plot. To correct this effect, a reference point with high statistics and long run time was chosen and all the data was aligned to match this reference point. The corrected final data are shown in Fig. 3.3.

4.2 S800 Calibrations and Corrections

After selecting an incoming secondary beam, as described in Section 3.2.3, the outgoing recoil of interest must be selected. The particle identification (PID) plot of nuclei shows poor separation before the corrections (Fig. 4.1 (a)). Therefore, it is difficult to distinguish fully the nuclei of interest, which is why it is impossible to select a clean gate around them. Therefore, the various focal plane detectors in the S800 spectrometer must be properly calibrated and corrected in order to allow for the identification of nuclei while removing contamination as a result of unreacted beams. For the first stages of the calibration, the nucleus ^{46}Cr [4], one neutron knockout from ^{47}Cr, was used to benefit the calibration with higher statistics. Different calibrations and corrections of S800 detectors were undertaken and have been detailed in the following sections.

4.2.1 Ionisation Chamber Gain Matching

The first step involves calibrating the IC used to produce the energy loss signals (y-axis) for the PID plots. The signals from the 16 segments of the IC are gain matched such that each segment records the same energy loss signal for the same event, which is then collected to calculate the total energy loss in the detector. This can be performed by first creating gates for both an incoming secondary beam and more than three outgoing recoils with high statistics from the PID plot. Next, the energy loss distribution measured in each anode segment is fitted

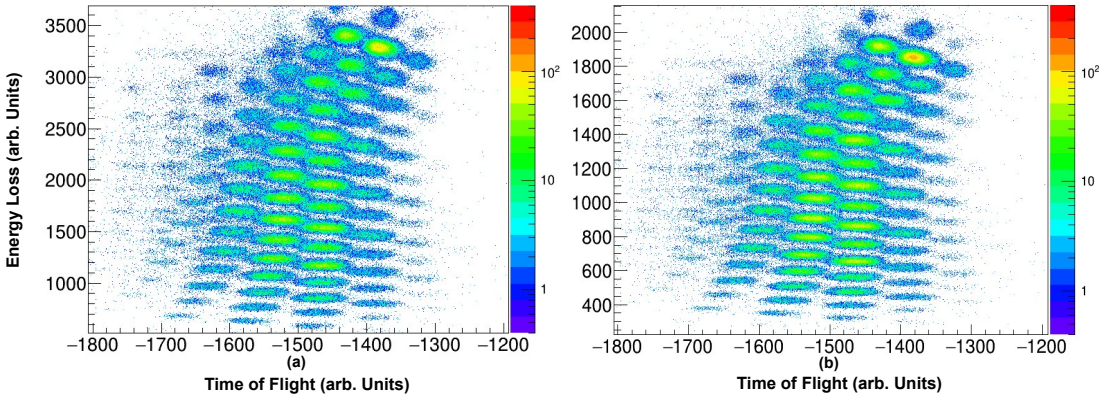

Figure 4.1: The outgoing PID plot of the energy loss in the IC against the ToF measured in between the OBJ scintillator and the E1 scintillator, gated by the ^{47}Cr secondary beam, where (a) before and (b) after the IC calibrations were applied. There is an apparent decrease in background counts post calibration and an increase in statistics for some of the outgoing recoils.

with a Gaussian function in each of the outgoing recoils that have been gated to identify the centroid. The calibration parameters (gains and offsets) are then determined by comparing the amplitudes and the centroids obtained from the Gaussian functions from each of the channels in the IC and nuclei, which are then matched to a preferred reference channel. The total energy loss (dE) of a particle traversing the IC is then established by the sum of the 16 segments in the chamber. A comparison of the 16 segments before and after calibration is shown in Fig. 4.2. The three gates on the PID used for this calibration employed an incoming beam of ^{47}Cr as this secondary beam has the most number of counts. The effects of this calibration on the PID are illustrated in Fig. 4.1, which compares the PID plot before and after the IC calibrations. Although the changes are minimal, mainly due to the fact that a majority of channels were relatively close before calibration (Fig. 4.2 (a)), it can be observed that a significant number of counts previously not associated with a particular nucleus might now contribute to a nucleus on the PID as a result of the reduction in the number of background counts.

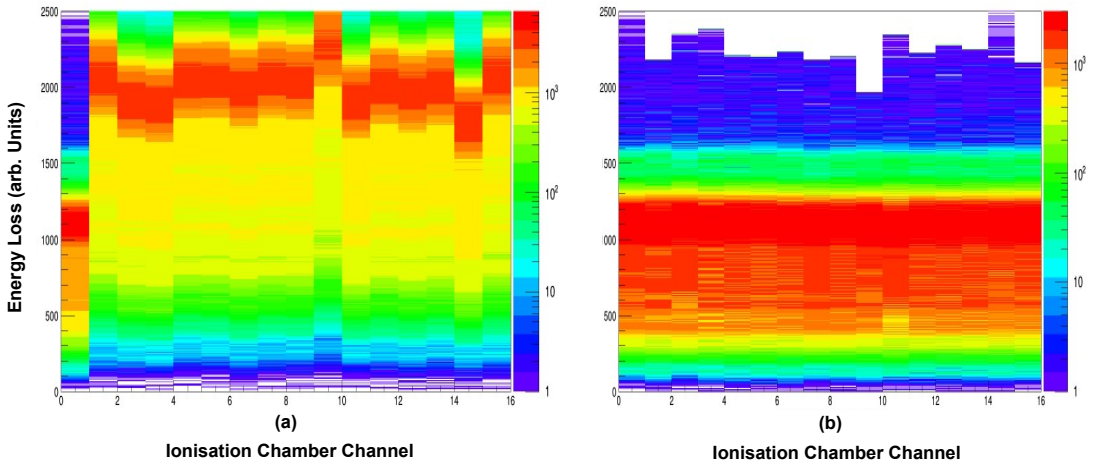

Figure 4.2: Plot of the 16 channels in the IC before (a) and after (b) correcting the IC. All the channels were matched to channel 0 such that the gains and offsets produced are not overestimated.

4.2.2 CRDC Calibration

The CRDC calibrations comprised two main steps. First, the CRDC pad amplitudes were corrected through a gain-matching procedure to obtain the corrected dispersive (x) position information. The next step was the mask calibration runs performed to gather calibrated non-dispersive (y) position information. In both CRDC detectors, the calibrated (xy)-position information can then be utilised to track the paths taken by different nuclei crossing the S800 focal plane on an event-by-event basis.

4.2.2.1 CRDC Pad Corrections

As the beam particles pass the CRDCs, their dispersive (x) positions at the CRDC detectors are identified from the induced charge distributions on the 224 cathode pads of the CRDCs detectors, which run either side of an anode wire on both sides of the x plane of each CRDC. The cathode pad positions are fixed and have a pitch of 2.54 mm. Therefore, the positions of these pads can be directly translated into their dispersive (x) positions. The 448 pads in both of the CRDCs need to

be calibrated relative to each other since the signal responses from the individual pads can vary greatly. Hence this calibration was essential in order to assure that the signals are consistent across one another. This can be accomplished through an iterative gain-matching procedure.

This procedure matches the gain and offset of each CRDC pad to a specific pad chosen as a reference in a similar method to the IC calibration process using four outgoing gates from the PID plot. All the CRDC pads were matched to pad 70, as this pad contained high statistics. The gains and offsets were determined by applying Gaussian fits to each of the CRDC pads. This correction purpose is achieved using an iterative process, which typically takes around two iterations in order to successfully gain match all the pads. It is important to note that this method could be compromised by low statistics in the selected outgoing recoils, which may produce gaps for some pads due to failed fitting procedures. The binned-likelihood fitting is applied to each pad with low statistics, allowing these pads to be fitted without overestimation. Hence, the gains and offsets were obtained by utilising the binned-likelihood fit for the pads that had low statistics and the Gaussian fit for the pads with high statistics. Finally, the gains and offsets produced from both methods for each pad were combined together to be applied to the settings file and were recompiled for the data. The CRDC pads gated on outgoing ^{46}Cr recoil before and after calibrations were applied and are shown in Fig. 4.3.

4.2.2.2 Mask Run Calibrations

Once the pads of the CRDC are gain matched, the next step was calibrating the actual dispersive (x) and non-dispersive (y) positions of the CRDCs and to ensure that the (x, y) position of the holes present on the mask are consistent throughout the experiment, as the beam passes through these detectors. These positions need to be calibrated so that any arising drift is eliminated.

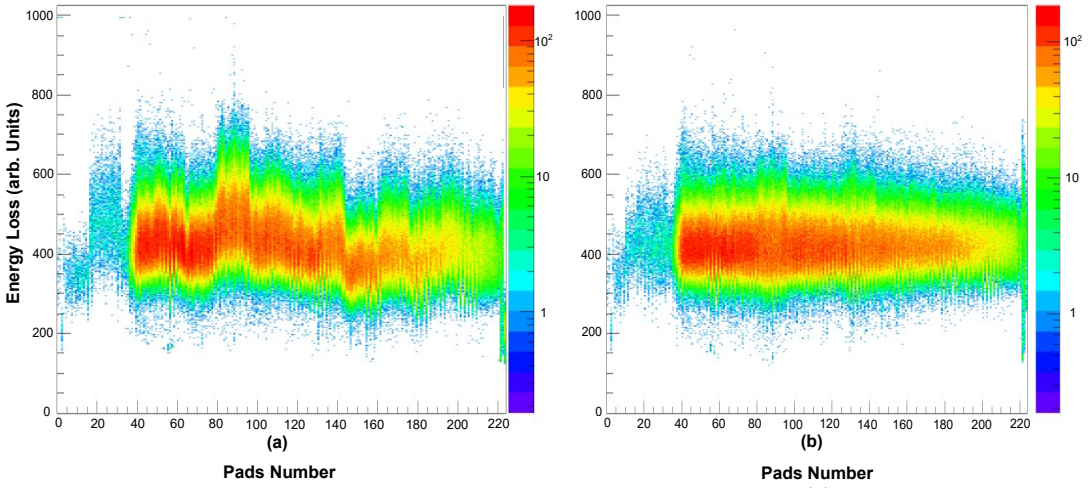

Figure 4.3: The CRDC pads vs energy loss before (a) and after (b) pad calibrations have been applied to an outgoing beam.

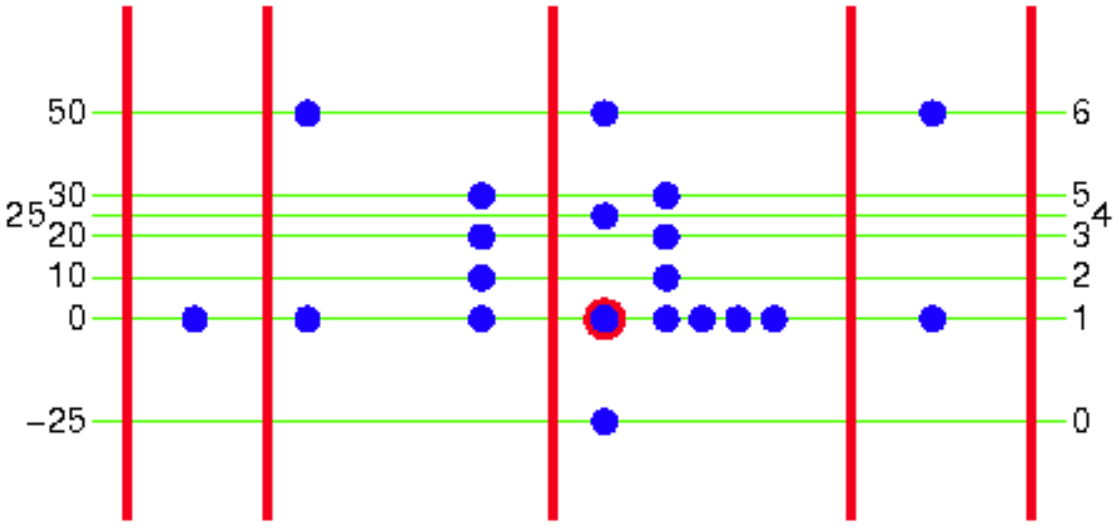

Figure 4.4: The CRDC mask pattern used for the mask calibrations. The blue circles correspond to holes in the mask, while the red lines correspond to slits through which particles can pass. The four points forming the L shape in blue are used as reference points at 0, 10, 20, and 30 mm. Left-hand values correspond to the y-position of the points on the mask in mm, while right-hand values are used to denote the rows of blue points.

It is necessary to calibrate the measured CRDC in x- and y-positions with known values to ensure that the arbitrarily measured particle positions in CRDCs correspond to their actual positions. It is carried out by applying separate gains and offsets to the recorded x and y values of each CRDC to match the measured positions of distinct patterns (Fig. 4.4) with the known values.
Ten of these mask runs are taken throughout the experiment, with the mask placed on top of each CRDC, where five of the runs are for CRDC1 and the remaining five for CRDC2. The mask used had holes and slits drilled in at known positions. The calculated positions were found to drift with time due to the changes in pressure and temperature of the gas within each CRDC, which results in inconsistencies in the x- and y- positions of the recoiling nuclei. These fluctuations caused drift in the y-position of each CRDC, while the dispersive (x) position calibration is fixed by the pad pitch (2.54 mm). A built-in GrROOT script was used where the actual positions of the holes on the mask were matched to the dots observed on the CRDC x against y plot to identify the gradient, which gives the gain for each CRDC. The positions of the holes on the mask were determined by observing a pattern from the 10 mask runs, where each of the dots from the **L** shape shown in Fig. 4.5 (a) were used to record the value of y. Subsequently, the actual y-position of the holes in the mask seen in Fig. 4.4 was plotted against the measured values of the y-positions of the mask runs to define a line of best fit in which the gradient is suitable for the gain obtained.

In order to obtain offsets, the y-position of the CRDCs were plotted by using a run taken immediately after the CRDC mask runs, where a Gaussian was fitted to the plot in order to determine the mean value of the y-position. The y offset was determined by centring the peak at $y = 0$ for the first run after the mask calibration. The results of calibrating the mask run with these gains and offsets can be seen in Fig. 4.5. To apply mask calibration, the experimental runs were split according to the mask runs, in that half of the runs after the mask run was sorted using the gains and offsets, while the other half were assigned gains and offsets from the next mask run (Table 4.1). Mask corrections are necessary to attain

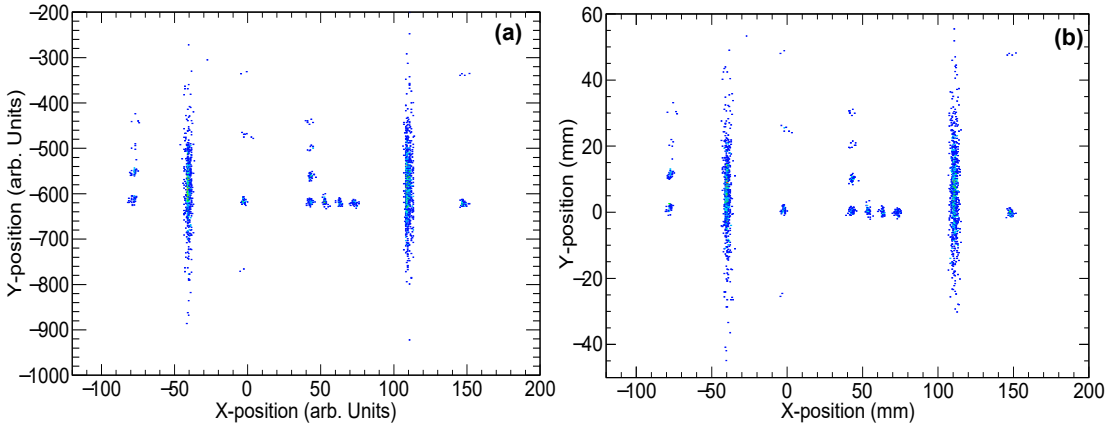

Figure 4.5: (a) The CRDC1 mask run before calibration, with dots from the distinctive L shape, was used to measure the y-positions of the dots, which were plotted versus the actual positions of the masks, to obtain the gain. (b) Demonstrates the same mask run after a gain and offset calibration was applied to match the positions of each dot on the pattern to the values shown in Fig. 4.4.

Table 4.1: An overview of the CRDC mask run used for CRDC position calibrations for each experimental run. The experimental runs began with run 19, and all runs before it were test runs and calibration of the γ-ray efficiency using sources.

Mask Run	Mask Run Numbers for CRDC1 / CRDC2	First Run	Last Run
1	21/22	19	50
2	85/86	53	102
3	114/115	103	143
4	152/153	144	166
5	178/179	167	189

accurate positional information from CRDCs when generating an inverse map (see Section 3.2.4.6), which can be used later for the Doppler-correction process (see Section 4.3.3).

4.2.2.3 CRDC Drift Corrections

Since the temperature of the environment changes throughout the experiment, the pressure of the gas in the CRDCs can vary. This, consequently, impacts the electron drift time through which the particle's non-dispersive (y) position is iden-

tified. The CRDC gain is corrected in each run in order to ascertain that the y-position drift of the CRDC is made accurate on a time-dependent basis. The gains are corrected by appropriately configuring the mask gain factor such that the y-position remains centred at 0 mm between mask runs and, consequently, throughout the experiment. Such corrections were performed to carry out the position calibrations, and the steps in this process are summarised in the following sections.

- Create settings files for each run to ensure that only gains from the mask runs (attained from the linear fit) are applied. At this stage of calibration, the calculated dispersive and non-dispersive angles (a_{ta}, b_{ta}) and non-dispersive position (y_{ta}) of the particle at the target position were all configured to zero for the offsets.

- The gain factor was determined from the drift factors to align the y-positions of the data files to the mask runs. CRDC drift-correction factors were determined in each run and separately optimised for each concerning recoiling nucleus due to the fact that the drift resulting from temperature variations was not constant across particles of different mass and charge.

This method reduced the effects of CRDC drifts in between mask runs, thereby improving PID separation. The position calibrations performed using the mask run calibrations can be checked by plotting the drift of the y-position against the run number to observe any changes before and after the calibrations have been applied. Notably, as expected, the x-position will remain the same since the drift only occurs in the y-position of each run. The changes in the y-position drifts is shown in Fig. 4.6.

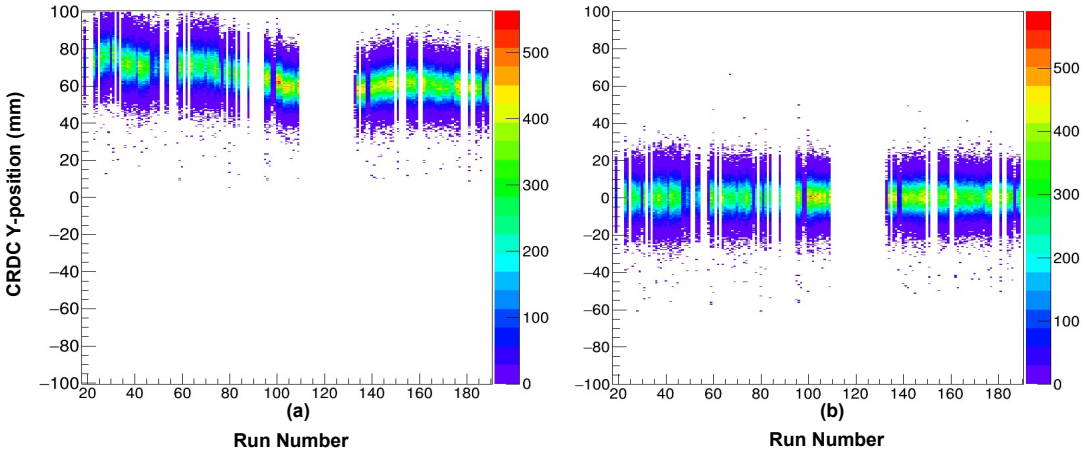

Figure 4.6: The change in the CRDC y-position in each of the runs while gated on ^{46}Cr populated through the ^{47}Cr secondary beam. (a) before the CRDC drift correction and (b) after the offsets and gains × gain factors have been applied. It can be seen that after applying the drift correction, the y-position of the runs was shifted to 0 mm.

4.2.3 Timing Corrections

The ToF of ions are measured between the OBJ and E1 scintillators. It is also used to identify the reaction products as Eq. 3.1. The nuclei having the same atomic number and mass number, but with small differences in momentum, will also be transmitted through A1900 and S800 but follow slightly different trajectories and, hence, reach at different positions and angles at the focal plane. According to the different trajectories of the beam particles in the S800 spectrograph, there is a correlation between the ToF measured by the scintillators and the measured position and angle of the particle trajectories, as they pass through the CRDCs. Therefore, removing this correlation is particularly important for better identification of recoils in the S800 focal plane.

Corrections have been made to the experimental ToF data considering the dispersive x-position focal plane (x_{fp}) and dispersive angle focal plane (a_{fp}) coefficients of the OBJ and XFP scintillators. The S800 x_{fp} and a_{fp} of a specific recoil in the focal plane were plotted against a common scintillator time in the OBJ scintillator, and then adjusted in order to straighten them as much as possible. This is achieved by iteratively adjusting the tilting parameters until the streaks appeared to be as

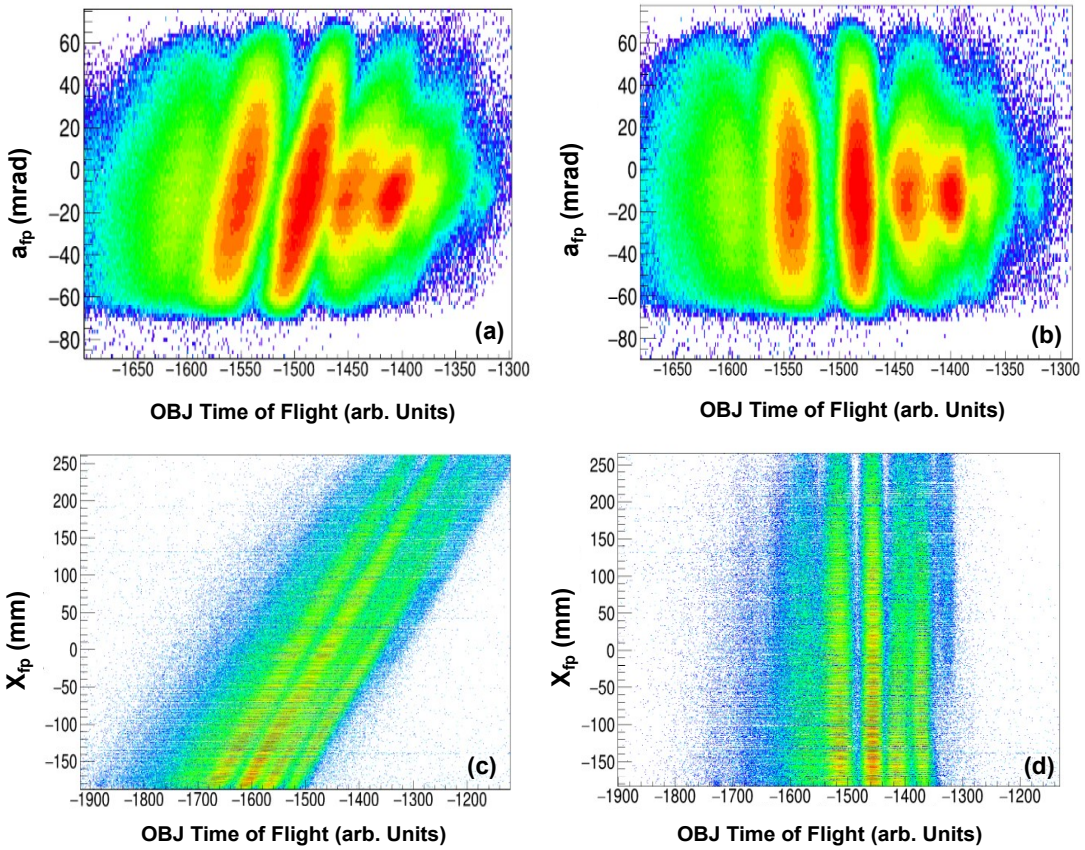

Figure 4.7: CRDC spectra of dispersive x position (x_{fp}) and dispersive angle (a_{fp}) at the S800 focal plane relative to the time-difference between E1 and OBJ scintillators (i.e. ToF). These spectra are shown before (a,c) and after (b,d) applying the ToF corrections (see text for more information). The effects of applying ToF corrections display that the blobs in (b) and the streaks in (d) have become vertical and separated.

vertical as possible in the x_{fp} plots, and the blobs also presented vertically and not merged in the a_{fp} plots. The results for this calibration are shown in Fig. 4.7; as a result, the PID spectrum appeared to be sharper and well separated.

4.2.4 Ionisation Chamber Corrections

The final stage of the calibrations and corrections was correcting the energy loss in each of the 16 segments of the IC for the particle trajectory. Different positions on the IC mean different angles, which indicates that different amounts of gas will

be encountered.

This correction for the ionisation chamber energy-loss measurements is required to account for the longer/shorter path lengths through the chamber depending on the trajectory of the particle, which can have a significant effect on the PID plot. The different positions of the beam on the IC mean different angles, which cause different amounts of energy loss that need to be corrected. The energy loss detected in each of the 16 channels of the ion chamber can be corrected, where the correction parameters are related to the energy-loss gain with respect to the y and x planes of the IC, respectively and to the x-position of the particle at the focal plane (x_{fp}).

The correction is performed by identifying particular gates for both an incoming secondary beam, ^{47}Cr, and the outgoing recoil, ^{46}Cr, to determine the IC x- and y-positions and the initial position measured at the focal plane, x_{fp}. These parameters were optimised separately based on the energy loss of a given reaction product, versus the x- and y- position of a particle at the S800 focal plane, x_{fp} and y_{fp}, respectively, until any dependence is eliminated. As a result of this correction procedure, it is shown in Fig. 4.8 that the distribution of ion chamber energy loss measurements are all aligned so they appear at a constant arbitrary value for all

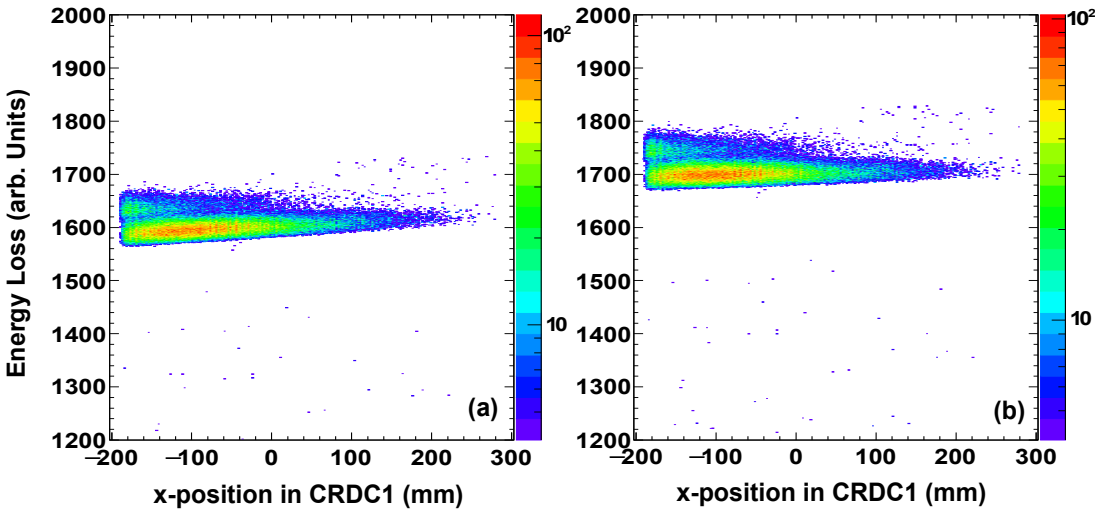

Figure 4.8: Spectra of ion chamber energy loss (dE) against x-position measured of the first CRDC, before (a) and after (b) the positional corrections when gating on ^{46}Cr outgoing recoil (populated through the ^{47}Cr secondary beam).

x values, where (a) is before and (b) is after the ion chamber energy loss position correction has been applied.

4.2.5 Particle Identification

The outgoing recoils are identified at the focal plane using a dE-ToF method, where the IC provides the total energy loss information, and the OBJ and E1 scintillators provide the ToF information. The combination of these corrections outlined in the previous sections must be as accurate as possible to allow unique identification of all isotopes; each blob in the PID plot corresponds to a different isotope that can be clearly distinguished from its neighbours. The final PID spectrum plot that includes the outgoing recoils with all the calibrations and corrections and in coincidence with incoming ^{47}Cr secondary beam is shown in Fig. 4.9.

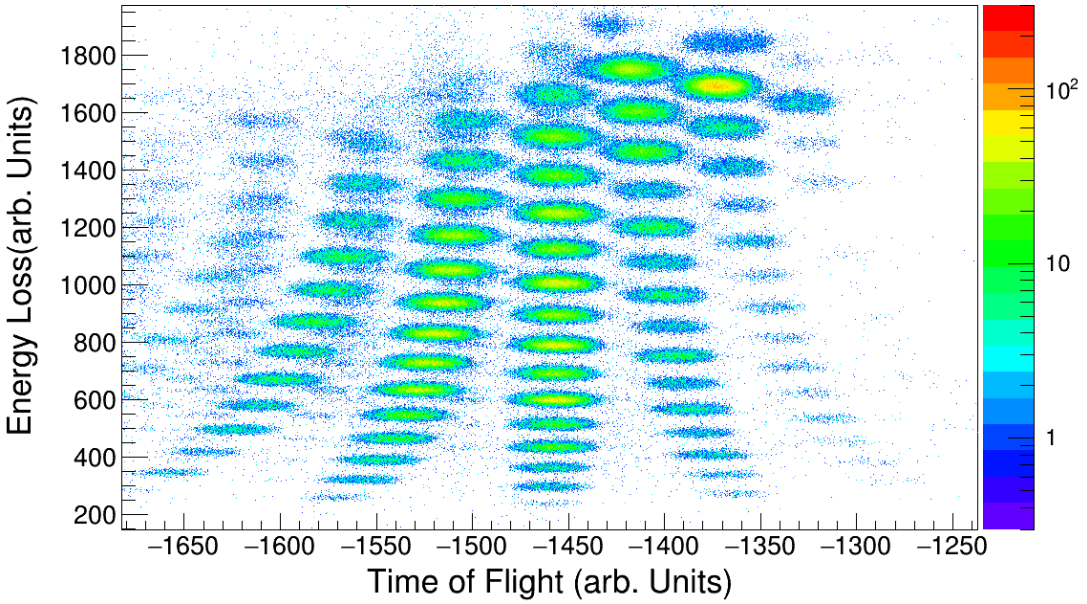

Figure 4.9: The outgoing PID in coincidence with incoming ^{47}Cr secondary beam shows the effect of S800 focal plane detector corrections. The outgoing recoils in the PID plot appear to be sharper and well separated.

The same calibrations and corrections were applied to all nuclei presented

in the current work. All of the PID plots were additionally produced by using gates in the secondary beams of interest, as discussed in Section 3.2.3 to avoid any contamination from other reaction channels. Gates can also be applied to the outgoing recoils with reduced contamination and may be uniquely selected. The PIDs for all the nuclei of interest in this thesis, ^{48}Fe, ^{48}Ti, ^{45}V, and ^{45}Ti, are clearly identified and are shown in Figs. 4.10, 4.11, 4.12, and 4.13; all of these recoils are in coincidence with the secondary beams of ^{49}Fe, ^{49}V, and ^{46}V, respectively. The identified outgoing recoils are indicated by vertical lines of total isospin, T_z, as seen in Fig. 4.10.

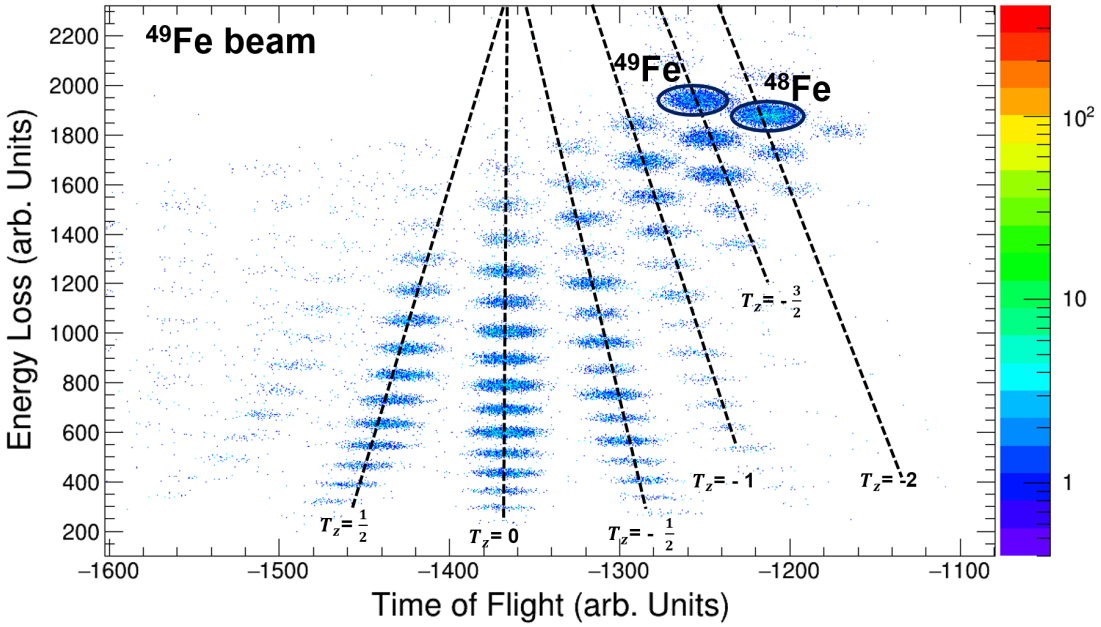

Figure 4.10: The PID spectrum produced from the reaction at secondary target gated on incoming ^{49}Fe secondary beam. The vertical lines represent the total isospin, T_z. The labels refer to the ^{49}Fe beam and the main nucleus of interest, ^{48}Fe.

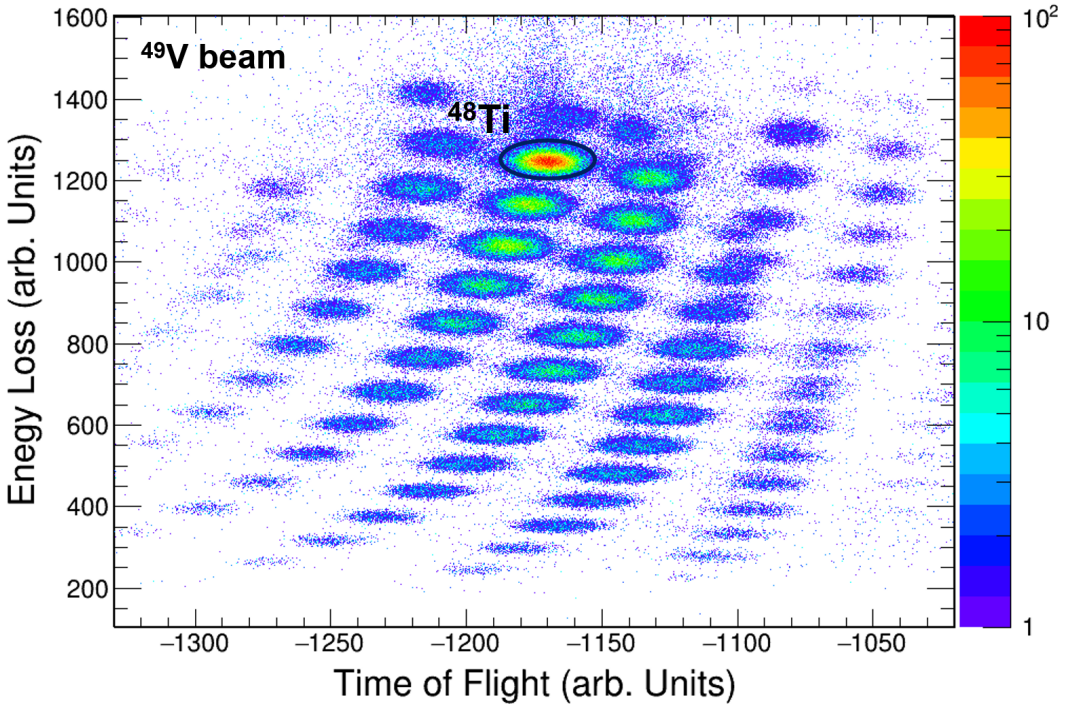

Figure 4.11: The PID spectrum produced from the reaction at the secondary target gated on incoming ^{49}V secondary beam. The labels indicate the ^{49}V beam and the main nucleus of interest, ^{48}Ti.

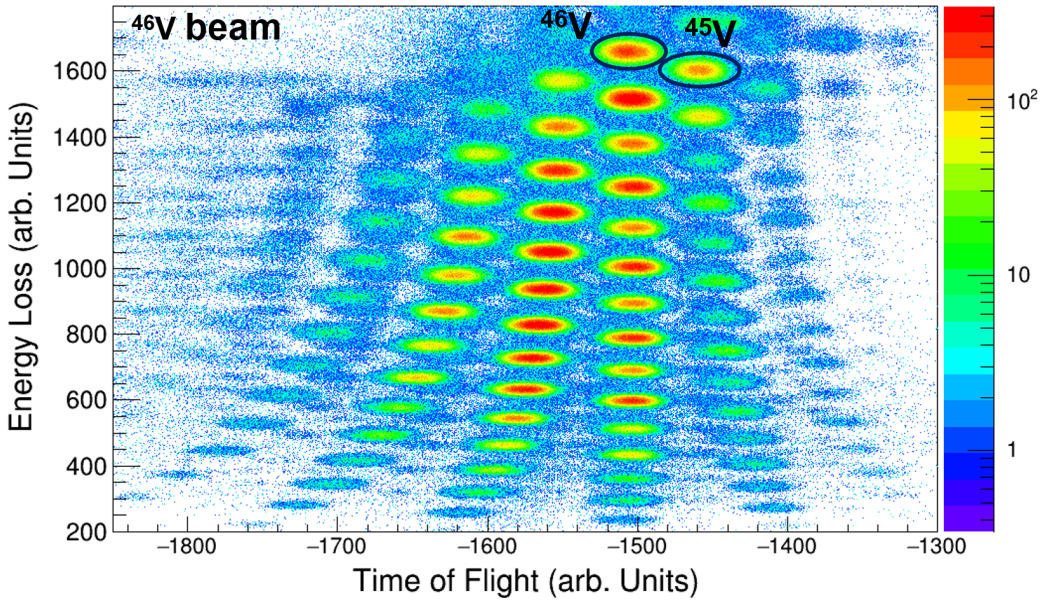

Figure 4.12: The PID spectrum produced from the reaction at the secondary target gated on incoming ^{46}V secondary beam. The labels indicate the ^{46}V beam and the main nucleus of interest, ^{45}V.

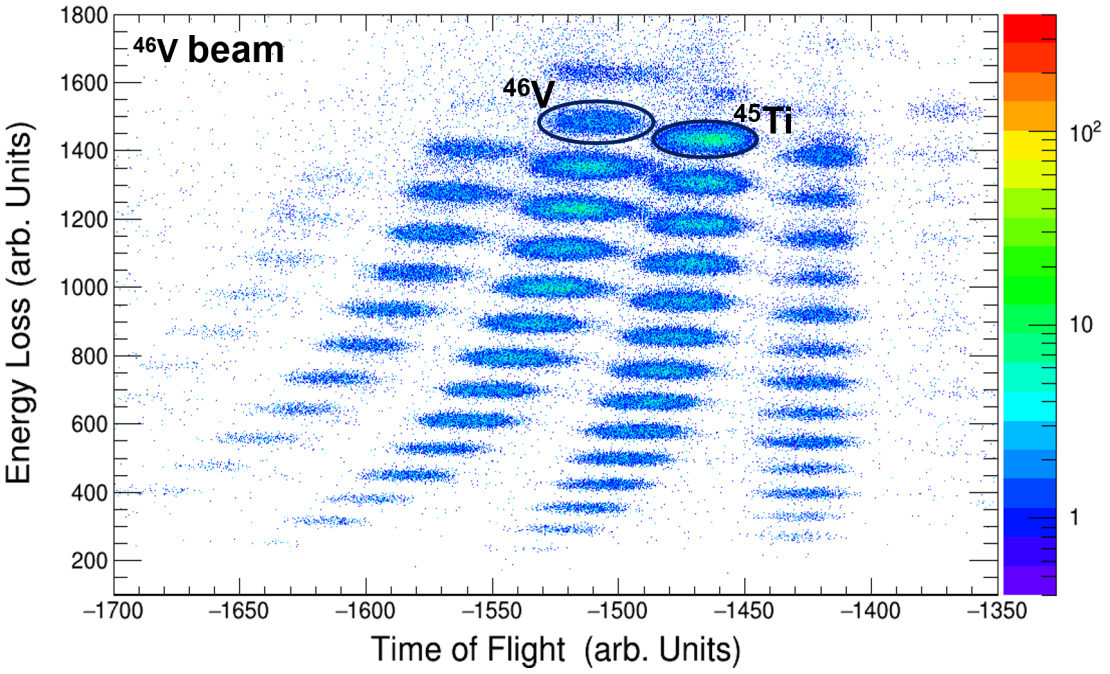

Figure 4.13: The PID spectrum produced from the reaction at secondary target gated on incoming ^{46}V secondary beam. The labels indicate to the ^{46}V beam and the main nucleus of interest, ^{45}Ti.

4.2.6 Particle Detection Efficiency

One of the aims of this experiment is to calculate the inclusive cross sections of the single-nucleon knockout reactions. This calculation requires an accurate understanding of the total number of beam particles incident on the target and the absolute number of reaction residues of interest that are produced. For the limited counting rate of the focal-plane detectors, the efficiency of the focal-plane ion chamber-counting rate is considered to be approximately 100% for the incident particle energies and charge states in the current experiment. Using the ion chamber as the standard, the detection efficiency of all other particle detectors utilised in the experimental setup can be determined by creating a coincidence logic gate around the region of interest in the ion chamber energy loss spectrum. The efficiency can be calculated as the ratio of the number of counts seen in coincidence with the ion chamber logic gate in that detector and the total number of events detected in the ion chamber's gated region. The efficiencies of the XFP, OBJ scin-

tillators, and CRDCs detectors in the current experiment were determined to be $\sim 98\%$.

4.3 GRETINA Corrections and Calibrations

After all the calibrations and corrections, different reaction channels were selected by creating gates to each incoming and outgoing particle (PID) spectra, as described in the previous sections. This results in the ability to produce γ-ray spectra, exhibiting only the γ-ray detected in coincidence with the reaction channel of interest. To produce a clean γ-ray spectrum in coincidence with the reaction channel of interest, with a sharp peak at the correct energy, and a reduced level of contamination, a number of additional calibrations and corrections needed to be carried out. This will be discussed in this section.

4.3.1 Efficiency of GRETINA

To perform energy and efficiency calibrations before and after the experiment for GRETINA, radioactive sources were used. At the beginning of the experiment, an energy calibration was performed for each segment and crystal, and then the decomposition algorithm output calibrated energies. No further energy calibration was performed as any uncertainty associated with these energies is very small compared to the uncertainties due to the Doppler reconstruction.

The efficiency of GRETINA was calculated to measure the γ-ray efficiency of the detectors for each ring. The calibrations were performed using source runs ^{56}Co [83], ^{133}Ba [84], and ^{152}Eu [85] of known strength/activity placed at the centre of the array. Corrections were made to account for the decay at the time of the source production. The efficiency of GRETINA was calculated using both an add-back mode to reduce the Compton background and no add-back mode. The no add-back mode, also known as the single-crystal mode, refers to the way a γ-ray detector operates by treating one crystal as a single detector and then detecting the total energy deposited inside a single crystal. If two γ rays hit two separate detectors, the detectors are treated as separate detectors, and their energies within each crystal are measured. In contrast, in the add-back mode, each detector has a

signal, but the event is treated as if only one γ ray hits one detector and scatters into the other. These are then added together depending on the type of add-back used (as discussed in Section 3.2.5).

The activity $A(t)$ (in Bq) of the sources after time t were corrected for time passed since the manufacture of the source. To measure the efficiency of GRETINA, a number of strongly observed transitions in the source runs ^{56}Co, ^{133}Ba, and ^{152}Eu were fitted with a Gaussian function plus background. The absolute efficiency, ϵ(E), could then be calculated using the following equation.

$$\epsilon(E) = \frac{N_\gamma}{I \times A(t) \times t \times t_{live}} \tag{4.1}$$

where N is the measured integral of the γ-ray transition; I is the intensity of a particular γ-ray transition; $A(t)$ is the activity of the source calculated using the activity of a radioactive material formula; t is the duration of the source run (in seconds), and t_{live} is the live time of the GRETINA detectors during the source run. Based on the scaler data collected throughout the experiment, the dead time, and hence live time, was accurately identified. After fitting a large number of strongly observed transitions in the sources, the absolute efficiency of GRETINA was plotted against γ-ray energy and is shown in Fig. 4.14. The efficiency curve is fitted using the following equation [68]

$$\epsilon(E) = A \ . \ (E_\gamma \ (keV) \ - \ C)^{-B}, \tag{4.2}$$

where E is the measured energy of the γ-ray transition in keV, and A, B, and C are coefficients produced by the fit. The uncertainty is dominated by the source activity. Due to the high precision of the scaler data, the uncertainty of t_{live} is assumed to be negligible. The uncertainty of ϵ(E) for each decay was obtained by combining the uncertainties of N, A, and I in quadrature. The uncertainty on the activity (ΔA) was assumed to be 1%.

In the current analysis, the highest-energy γ-ray transition (with efficiency correction) noticed was a $\sim$ 3000 keV transition; therefore, data points were collected

for the GRETINA efficiency up to 3 MeV to obtain an accurate measurement of efficiency for such high-energy γ-ray transitions, as illustrated in Fig. 4.14.
The add-back efficiency curve shown in Fig. 4.14 does not provide a reliable method for determining the true in-beam efficiency under real experimental conditions. It is shown here in order to illustrate how such a process can improve the peak to the background. Since the add-back efficiency depends on the number of γ rays emitted from the reaction, it is not possible to produce a real efficiency curve for add-back. The addback curve shown in Fig. 4.14 is unsuitable for use with experimental data since the source measurements have been made with one γ ray (^{137}Cs), two γ rays (^{56}Co), and several γ rays (^{152}Eu). This add-back procedure was not applied to determine efficiency-corrected γ-ray intensities. The measured photo-peak efficiency, without add-back or tracking using GRETINA configuration, was determined to be 6.4(1)% for a 1-MeV γ ray emitted at rest, which rises to 6.7(1)% when moving at $v/c \sim 0.4$, as in the current work.

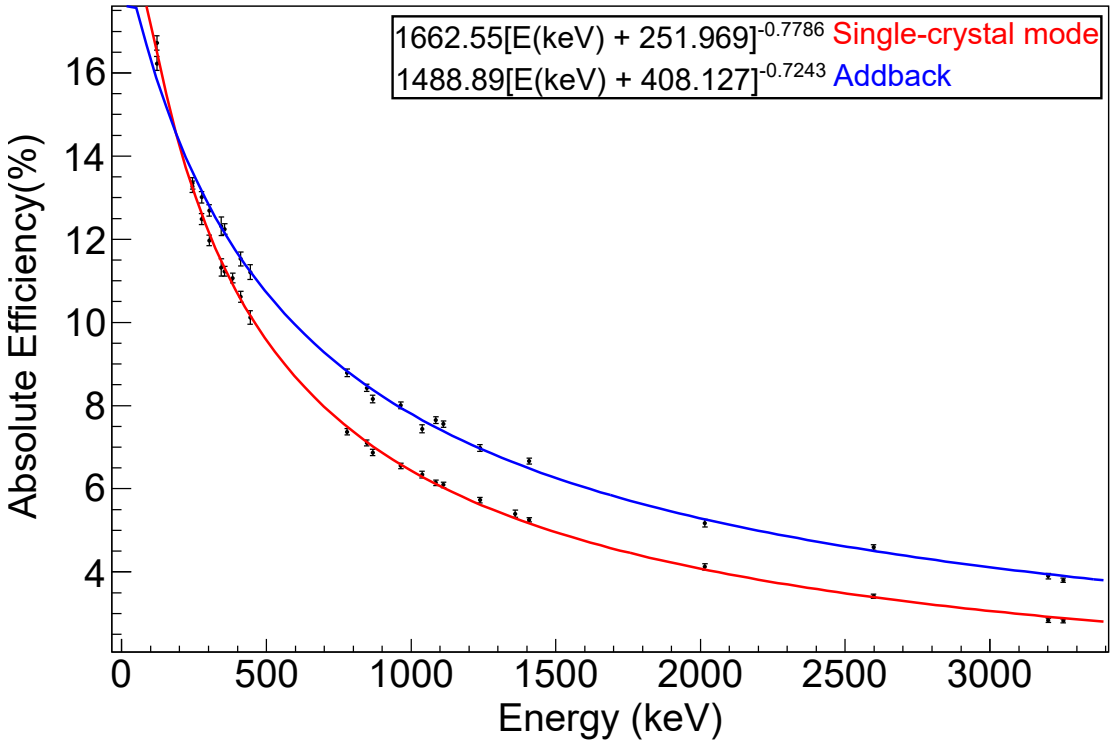

Figure 4.14: The singles efficiency of GRETINA in the nine-module configuration without add-back (single-crystal) (red) and with add-back (blue) using ^{56}Co, ^{133}Ba, and ^{152}Eu sources placed at the centre of GRETINA.

4.3.2 Boosted Efficiency and Doppler Reconstruction of Gamma Rays

The experiment performed for this work utilised fast beams of rare isotopes and is typically carried out at beam energies of $\sim$ 80–85 MeV/u, corresponding to velocities of 40% the speed of light. This produces two effects on the analysis, Lorentz-boost and Doppler-shift effects of the γ rays measured in the laboratory frame. A correction of these effects is necessary to achieve optimal energy resolution in the measured γ-ray spectra and valid γ-ray efficiencies [68].

4.3.2.1 Boosted Efficiency

The configuration of GRETINA results in higher detection efficiency for Lorentz-boosted gamma rays, which are emitted mostly forwards. The emission of γ rays during the experimental beam runs at high velocities is more forward focused due to a relativistic velocity of the recoil in this experiment of $\beta \approx 0.4$. The result, therefore, is a higher efficiency for detectors at smaller angles and a lower efficiency for detectors at larger angles. This has a further effect on the analysis, known as the Lorentz boost, which is measured by the application of a Lorentz boost factor $\epsilon(E)_{boost}$. The boosted efficiency is based on the velocity of the beam (β) and it is given by

$$\epsilon(E)_{boost} = \epsilon(E) \; . \; \frac{1-\beta^2}{(1-\beta \; cos\theta)^2} \tag{4.3}$$

where θ is the angle between the beam and γ-ray trajectories. As the angle (θ) between the beam vector and the first interaction position of the γ ray in GRETINA is a continuous variable, Eq. 4.3 cannot be applied analytically. Therefore, the GRETINA simulation code is used with the experimental conditions, and the absolute efficiency is compared at $\beta = 0$ and $\beta = 0.4$ (approximately) to determine the gains caused by the Lorentz boost.

To obtain the boosted efficiency curve, the data for the simulated efficiency ratios

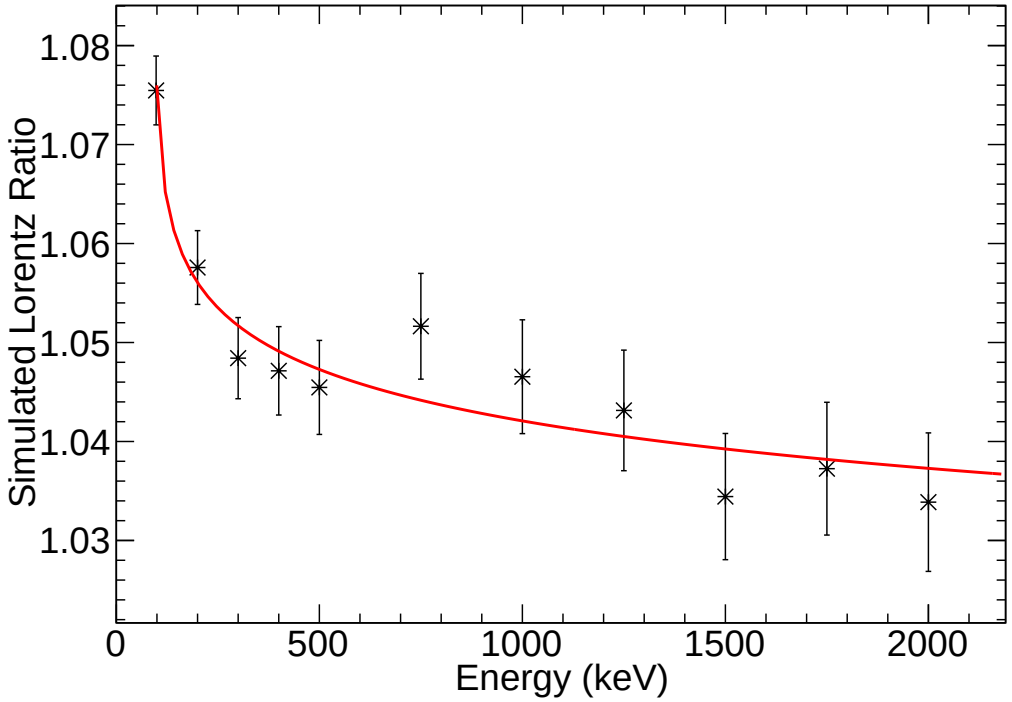

Figure 4.15: The boosted efficiency curve based on the configuration of the nine detectors used in the current experiment.

was plotted against the energy and then fitted using a function similar to that used to obtain efficiency curve of GRETINA (Eq. 4.2). This data was provided by MSU based on the configuration of the detectors (nine detectors) used in the current experiment. As a result of the ratios of the efficiencies, while stationary and in motion in the beam at $\beta = 0.4$, the efficiencies were corrected to their Lorentz boost-corrected values (Fig. 4.15).

4.3.3 Doppler Reconstruction of Gamma Rays

Since this experiment used a fast beam with energy of up to $\sim$ 160 MeV/u and a velocity of 40% the speed of light, a considerable Doppler shift will affect the γ ray detected by GRETINA. This effect should be considered and corrected to achieve the optimal energy resolution in the measured γ-ray spectra and best γ-ray efficiencies.

The position of the first interaction of each γ ray in GRETINA and the path of recoils through S800 are required for determining the angle θ and velocity β for the Doppler correction on an event-by-event basis. These can be calculated using positional information from the GRETINA detector segments and vector information of the beam from S800. Therefore, this position resolution allows for the determination of Doppler corrections event-by-event through the following equation

$$E_{rest} = E_{lab}\frac{1-\beta\cos\theta}{\sqrt{1-\beta^2}}, \tag{4.4}$$

where $\beta = \frac{v}{c}$ is the velocity of the recoil at the point from where it emits the γ ray; E_{rest} is the γ-ray energy in the frame of the moving nucleus, and E_{lab} is the γ-ray energy in the lab frame; θ is the angle between γ-ray emission vector to the direction vector of the nucleus $\vec{v}$. The vector of the recoiling nucleus $\vec{v}$ can be accurately determined by using the S800 spectrometer while the point of the γ-ray interaction in GRETINA can be defined as the highest detected energy interaction. Detected γ rays will be corrected through a sophisticated event-by-event Doppler process using a specific value of β. The S800 spectrometer also provides a value for dT/T, where T represents the particle's kinetic energy. This allows for a mid-target β value to be adjusted event-by-event using the d_{ta} value calculated by the inverse map that corresponds to dT/T through Eq. 4.5 [68] to further improve the Doppler reconstruction.

$$\frac{d\beta}{\beta} = \frac{1}{\gamma(\gamma+1)}\frac{dT}{T}, \tag{4.5}$$

where $\gamma = \frac{1}{\left(\sqrt{1-\beta^2}\right)}$.

Since the x- and y-positions of particles traversing the S800 spectrograph are determined event-by-event using the CRDC data, these are used to determine a_{ta}, b_{ta}, and y_{ta} through the application of the inverse map. These are then adjusted

run by run to be zero on average.

For the Doppler correction, initial assumption is that the recoiling nucleus decayed at the target position at the midpoint, which is supposed to be the precise central position of GRETINA. Next, from the inverse map again, an event-by-event shift in the y-direction is performed to the centre of the target, corresponding to the y_{ta} value. The inverse map is used to calculate the recoil angles a_{ta} and b_{ta}. These are then combined with the Doppler reconstruction procedure to ensure that the vector of the recoiling nucleus $\vec{v}$ is slightly modified from the central beam axis to that determined using the inverse map. This leads to a necessary event-by-event correction to the computed angle of emission, θ, utilised for the Doppler-correction process.

The a_{ta}, b_{ta}, and y_{ta} factors were determined run by run to shift both distributions of the recoil angles a_{ta} and b_{ta} and the non-dispersive beam position on the secondary target y_{ta}. This step had to be performed, as with the CRDC corrections, due to the drifting secondary beams throughout the experiment, primarily as a result of the beam focusing changes in A1900.

These corrections are essential in the Doppler-correction process and the effect of these is reflected in the resolution in any Doppler-corrected γ-ray spectra (Fig. 4.16). However, systematic errors are present in the tracking from S800 with regard to reconstructing the recoil vector $\vec{v}$. Therefore, additional corrections are required to optimise the Doppler correction in order to account for these systematic effects. This is achieved by adjusting the calculated angle of emission, θ, used for the correction process, ϕ of the beam, and X and Y of the beam event by event. This is carried out by adjusting the effective x- and y-positions of the centre of the target. The z position of the centre of the reaction target utilised for the γ-ray Doppler correction process could also be adjusted manually in the settings file for each run. This will be explored in Section 4.4.1.2.

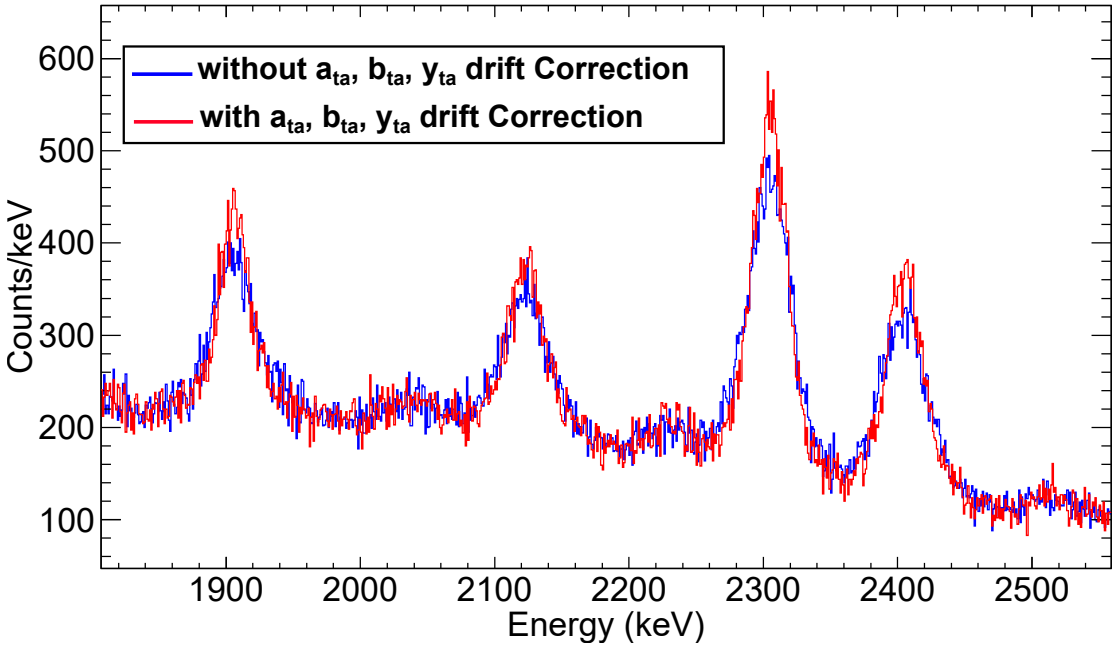

Figure 4.16: A comparison of the Doppler-corrected γ-ray spectra for ^{46}Cr (1n knockout from ^{47}Cr secondary beam) with (red) and without (blue) including the drift correction through using the inverse map (a_{ta}, b_{ta}, and y_{ta}) in the Doppler correction process.

4.4 Analysis Techniques

4.4.1 Doppler Correction Analysis

Since γ rays may interact with several segments of GRETINA through Compton scattering events, the partial energy is recorded in each segment to help identify which segments were hit during the interaction and how much energy was recorded in each segment (as discussed in Section 4.3.3). Event-by-event Doppler reconstruction of γ rays is achieved by identifying the first point of interaction in the Ge crystal and hence the angle of emission of the γ rays by determining recoil velocity vector.

4.4.1.1 Optimising the β Value

In the Doppler-correction process, the β value was optimising by selecting the two recorded energies of a particular transition in the 58° and 90° GRETINA detector rings separately. The transition in both detector rings spectra can be aligned to obtain the narrowest peak. The optimum recoil velocity, β, used for the Doppler correction was set by varying β until any angular dependence of the observed gamma-ray energy was eliminated. Eq. 4.4 indicates that if β is correct, then this will result in the Doppler-corrected γ-ray energy being constant for all θ angles of the GRETINA array under the assumption that the θ and $\vec{v}$ values have been calculated correctly. The two measured energies of E_1 and E_2 for a particular transition from the Doppler-corrected spectra of the forward and back angle detectors, respectively, are corrected using a given β value, which is used to correct these two spectra to the same energy. Denoted by β_{new}, this value is given by Eq. 4.6 [86]

$$\beta_{new} = \beta + \frac{E_1 - E_2}{-\beta^2\gamma^3(cos\theta_1 + cos\theta_2) + \gamma(cos\theta_1 - cos\theta_2)}, \tag{4.6}$$

where $\gamma = 1\ /\sqrt{1-\beta^2}$ and θ_1 and θ_2 are the average detector angles from the angle detector rings of 58° and 90°, respectively. As a result of different reaction mechanisms from the secondary beams with varying masses and charges, the optimal β value will vary from nucleus to nucleus. Thus, in this case, the β value ranges from 0.38 to 0.4. This was measured using the precisely known energies of very intense and clean transitions and a lifetime of roughly less than a few ps in other reaction products. The effective lifetime of the states emitting the γ ray and that of the states feeding them determine the optimum recoil velocity. The fast decays on sub-ps timescales will occur at the centre of the target, while the decay of longer-lived states of the order of $>$ 10 ps will happen outside the target and have a lower recoil velocity.

The known nucleus ^{46}Cr (1n knockout from ^{47}Cr) was used first due to its high statistics and short-lived state ($T_{1/2} \sim 1.6$ ps) $4^+ \rightarrow 2^+$ at high energy of 1094.9 keV (γ rays emitted within the target) [4] in order to find the β value that would shift the spectra from the GRETINA detector rings to the correct energy.

Fig. 4.17 shows a spectrum of 1094.9 keV energy transition in ^{46}Cr in the x-axis against the y-axis with the angle θ in radians (Figs. 4.17 (a) and (b)) and corresponding the γ-ray spectra (Figs. 4.17 (c) and (d)), to examine any possible dependence of the Doppler reconstruction on θ. The effects of removing the θ dependence through varying β can be seen in Fig. 4.17, where β is optimised at $\beta = 0.383$.

Decays having a short lifetime will take place within the target and yield a higher β value, since the particle has not slowed down as much as a fully-attenuated particle that has passed through the whole length of the target and decayed downstream, resulting in a smaller β value. Therefore, each nucleus has a different optimum for mid- and after-target decays. Optimising the β value is subject to systematic error arising from the uncertainty in the alignment of the transition energies in the two detector rings.

4.4.1.2 Determining Effective Target z-Position

The target was positioned approximately at the centre of the chamber manually, creating an additional potential shift in z and hence θ. Moreover, the target was taken out of the chamber and put back in again between the main runs. Therefore, the target position, z, along the beam axis, was assumed to be shifted and, hence, needs to be determined carefully for the first and second halves of the main runs. This part of Doppler corrections was performed to determine an offset in the target z-position and then to ensure that γ-ray events were reconstructed precisely.

The z and β values were modified simultaneously for each half of the data in order to align a specific transition at the correct γ-ray energy. This was achieved by adjusting z until peaks in both rings lined up and changing β until the peak was at

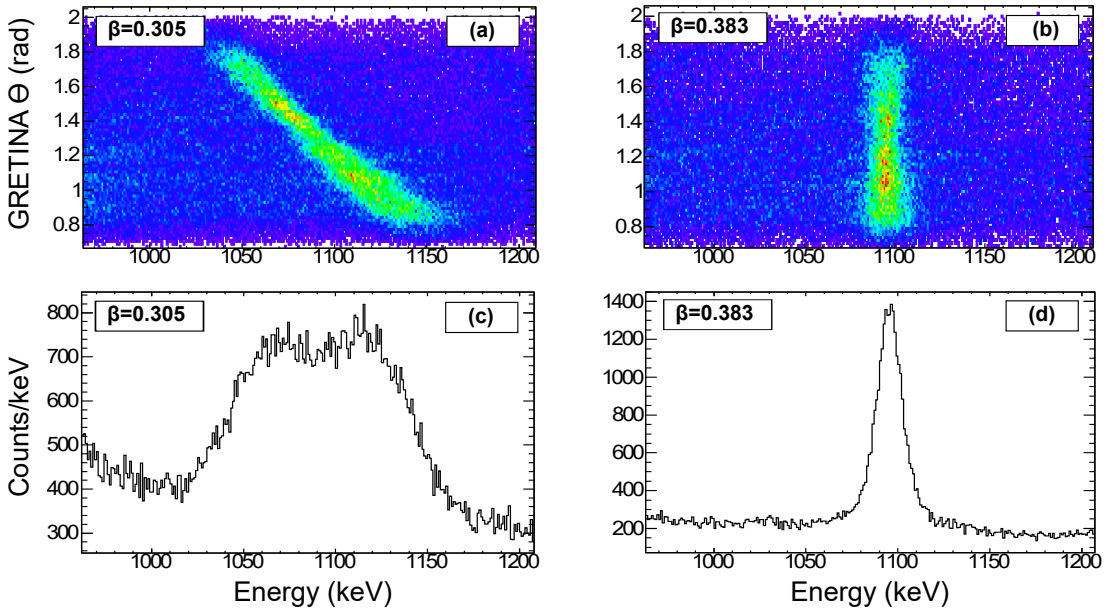

Figure 4.17: Optimising β value for decays with a short lifetime, 1094.9 keV corresponding to $4^+ \rightarrow 2^+$ transition in ^{46}Cr to examine any possible dependence of the Doppler reconstruction. (a) and (c) demonstrate the dependence of the Doppler-corrected energy on the GRETINA θ angle, as well as the corresponding γ-ray spectrum, respectively, corrected to $\beta = 0.305$. The same plots are shown in (b) and (d) with Doppler correction having an optimum value of $\beta = 0.383$, eliminating any dependency on the GRETINA θ angle.

the correct energy. This was done through an iterative procedure. The z-position of the mid-point of the target (z_{mid}) was deduced through measuring the energy of decay from a short lifetime ($T_{1/2} \sim 1.6$ ps) 4^+ state at high energy of 1094.9 keV of ^{46}Cr [4] while varying the z value after optimising the mid-target β so that the peak could be centered at the known energy. Since the data was split into two halves, as the target was taken out and returned to the target chamber between the main runs, z_{mid} values were determined for each half. Therefore, this analysis yielded z_{mid} value of -1.2 mm for the first half and -0.2 mm for the second half relative to the centre of GRETINA with the mid-target β value of 0.383 (as discussed in Section 4.4.1.1) for both halves. The effects of applying this z_{mid} position in the Doppler correction process for 1094.9 keV γ-ray decay are displayed in Fig. 4.18. The systematic error in z results from the estimate of the uncertainty associated with aligning the transition energies in the two detector rings for energy correction.

The mid-target z-position is the same for every nucleus; the values calculated above are only correct for short lifetime ($\sim$ ps) states. However, long lifetime states of the order $>$ 10 ps will decay outside the target, with a lower recoil velocity. These states must be treated separately since the standard Doppler reconstruction of these states will not produce the correct γ-ray energy. The effective z-position for these was set to the end of the target (z_{mid} + 0.5 mm), as β will not change beyond this point. Accordingly, the after-target z-position for the first half and second half of the data relative to the centre of GRETINA was set to be -0.7 mm and 0.2 mm, respectively.

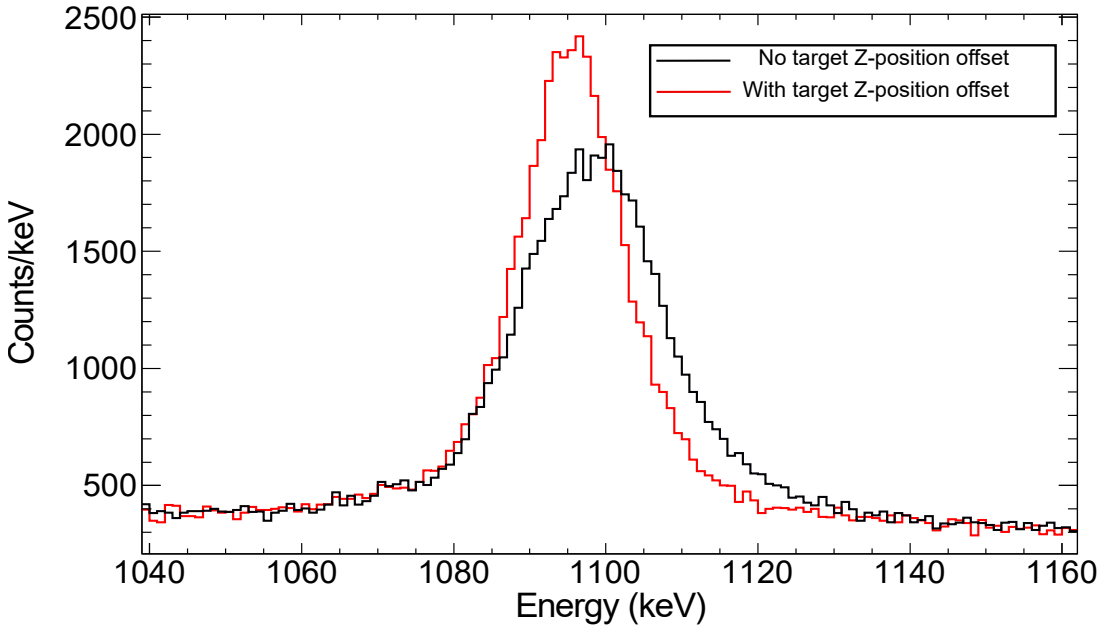

Figure 4.18: A comparison of the Doppler-corrected γ-ray energy of 1094.9kev with no target z-position offset (black) and with using an optimum target z-position (red) (the combined effect of z_{mid} value of -1.2 mm for the first half and -0.2 mm for the second half of the data) where the measured energy aligned with that in the literature. The two spectra are Doppler corrected with a β value of 0.383.

4.4.1.3 Determining Effective Target x- and y-Positions

A good estimate for these parameters defined earlier, was probed through a histogram of the dependence of the Doppler-corrected γ-ray energy relative to the angle ϕ of the deduced first-interaction point of GRETINA.

As shown in Figs. 4.19 and 4.20, this dependence was determined separately for 58° and 90° detector rings. This was done by measuring the Gaussian from each band for front and back detector rings in the histogram until the best combination of x- and y-offset values, was determined. While adjusting the effective target x and y positions, the spectrum from the 58° detector ring was initially slightly bowed, which was reduced by adjusting the x position. In contrast, the dependence of the 90° detector ring was far less dependent on the x- and y-positions of the target since they were at 90° to the target. It was observed that there was a slight bowing with the 90° detector ring and the 58° detector ring, which was reduced slightly by obtaining the optimum values of effective x and y target positions. This analysis yielded x and y values of -9.25 and -0.25 mm, respectively, for ^{47}Cr beam experiment and the other beams produced with the same settings of the A1900 separator. The result of these corrections is shown in Figs. 4.19 and 4.20 for front and back angle of GRETINA detectors, respectively, where (a) before and (b) after the x- and y-offset values are applied.

It should be noted that every secondary beam (different settings) is shifted in the target; thus, the target x, y, z, and β must be applied separately for each recoil with different runs such as the mirror nuclei runs.

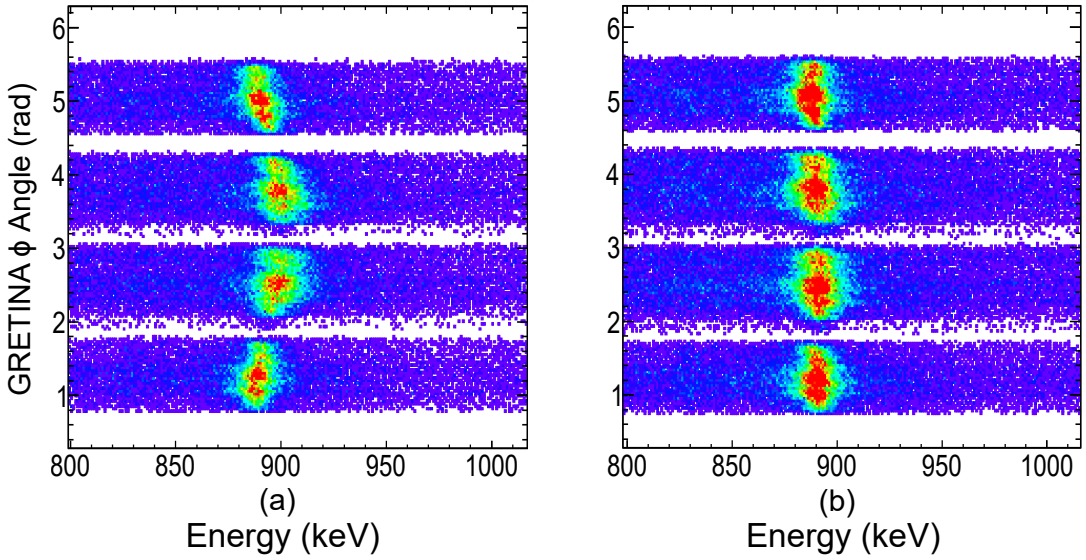

Figure 4.19: A comparison of the Doppler-corrected γ-ray energy indicates the literature energy of 892.16 keV, $2^+ \rightarrow 0^+$ decay of ^{46}Cr while adjusting the effective target x- and y-positions used in the Doppler correction process. (a) and (b) show the same plots of the 58° detector ring of GRETINA before and after adjusting the effective target positions, respectively.

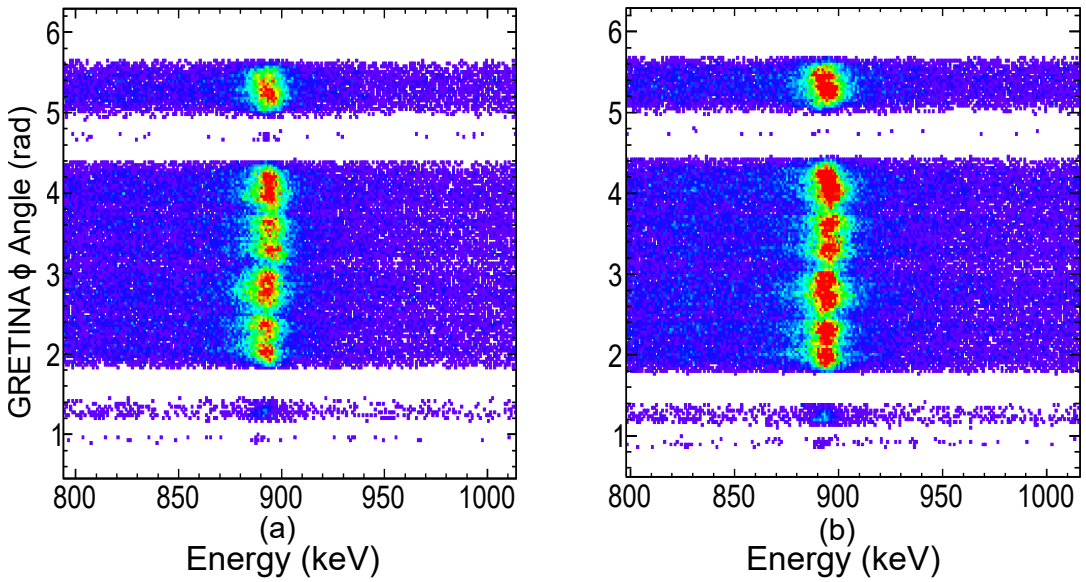

Figure 4.20: A comparison of the Doppler-corrected γ-ray energy indicates the literature energy of 892.16 keV, $2^+ \rightarrow 0^+$ decay of ^{46}Cr while adjusting the effective target x- and y-positions used in the Doppler correction process. (a) and (b) show the same plots of the 90° detector ring of GRETINA before and after adjusting the effective target positions, respectively.

4.4.1.4 Examining the ϕ-Dependence of the Doppler-Corrected γ-Ray Energies

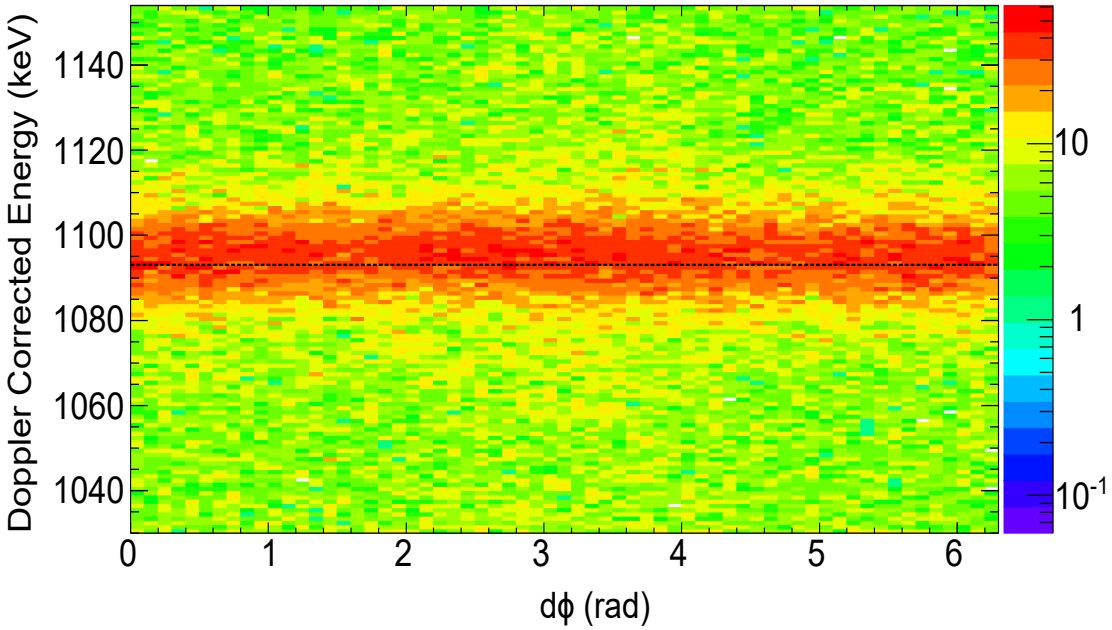

Figure 4.21: Examining the dependence of Doppler-corrected energy of 1094.9 keV, $4^+ \rightarrow 2^+$ decay of ^{46}Cr with respect to the difference in the angle of the beam and the front and back angles of the position of detection in GRETINA, dϕ. The spectrum appears flat at 1094.9 keV, which means that there is no dependence on the angle of the beam θ with respect to dϕ.

After optimisation of the effective target x-, y-, and z-positions and β, the effects of the offset ϕ of the beam were examined by investigating the dependence of Doppler-corrected γ-ray energies with respect to dϕ. The dϕ is the difference between the beam polar angle ϕ and the azimuthal angle ϕ of the position of detection in GRETINA.

These additional corrections for the beam axis must be made to produce Doppler-corrected γ-ray energies that remain constant regardless of GRETINA's angles, θ and ϕ [68]. It is done by applying offsets to the θ and ϕ of the beam, normally of the order of a few mrad. This could be adjusted by modifying the θ angle of the beam until the spectrum becomes flat, which means that there is no dependence of θ with respect to dϕ. Fig. 4.21 shows the dϕ dependence of the 1094.9 keV, $4^+ \rightarrow 2^+$ decay of ^{46}Cr. No additional corrections to the θ of the beam were made

since no dϕ dependence is apparent.

4.5 Production of clean γ-ray spectra

The Doppler-corrected γ-ray spectra for the reaction channels of interest can now be produced by gating on the incoming beam particles and outgoing recoils from which further γ-ray analysis can take place. Therefore, the well-known energy spectrum of ^{46}Cr(^{47}Cr $- 1n$) after calibration and correction had been applied with a suitable approximate β value of 0.383, as shown in Fig. 4.22. It is assumed that all the interaction points in a single crystal originate from the same γ ray. To improve the peak-to-total ratio, an add-back procedure is utilised where all adjacent crystals with an interaction are grouped using neighbour add-back and presumed to arise from the same γ ray. Fig. 4.22 illustrates the difference between the results obtained using the two methods.

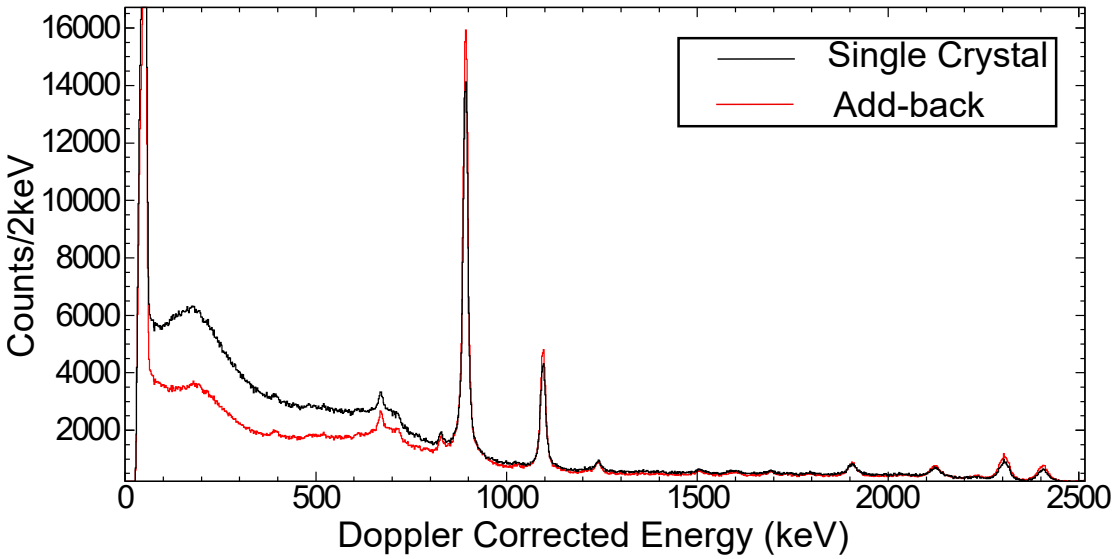

Figure 4.22: Doppler-corrected γ-ray energy spectra of ^{46}Cr obtained by summing all interactions within one crystal (black histogram) and using the add-back method (red histogram).

4.6 $\gamma - \gamma$ Coincidence Analysis

Gamma-gamma coincidence is a type of analysis that is mainly concerned with identifying the transitions that a form part of the same cascade. The γ-ray events detected are identified within the same coincidence window of the detector system, which, as a result, determines the multiplicity of a γ-ray event. However, this method also introduces the possibility of uncorrelated background events, for instance Bremsstrahlung radiation detected in coincidence, which need to be taken into account. An analysis was conducted by creating a symmetrical $\gamma - \gamma$ matrix of all coincident γ-ray events using the add-back method. Fig. 4.23 shows an example of a 2D histogram of γ-ray energy versus γ-ray energy that is completely symmetric across the diagonal, where each entry indicates a coincidence between two γ-ray energies. To obtain $\gamma - \gamma$ coincidence spectra for individual transitions, the 2D histogram along either the x- or y-axis can be projected around the transition of interest. To remove random coincidence events in the spectrum, a local background subtraction was applied. This includes subtracting a spectrum that represents of the background arround the energy of the transition. This is usually done by subtracting the mean of the two background spectra, which is generated by projecting on the right-hand side and left-hand side of the transition, with the same width of the transition. Then the two background spectra subtracted from the desired energy gate spectrum to exclude any background events, leaving only a real coincidence event.

This technique was utilized to confirm the known γ-ray transitions for nuclei present in this thesis and the new γ-ray transitions in ^{48}Fe, allowing a new decay scheme of ^{48}Fe to establish.

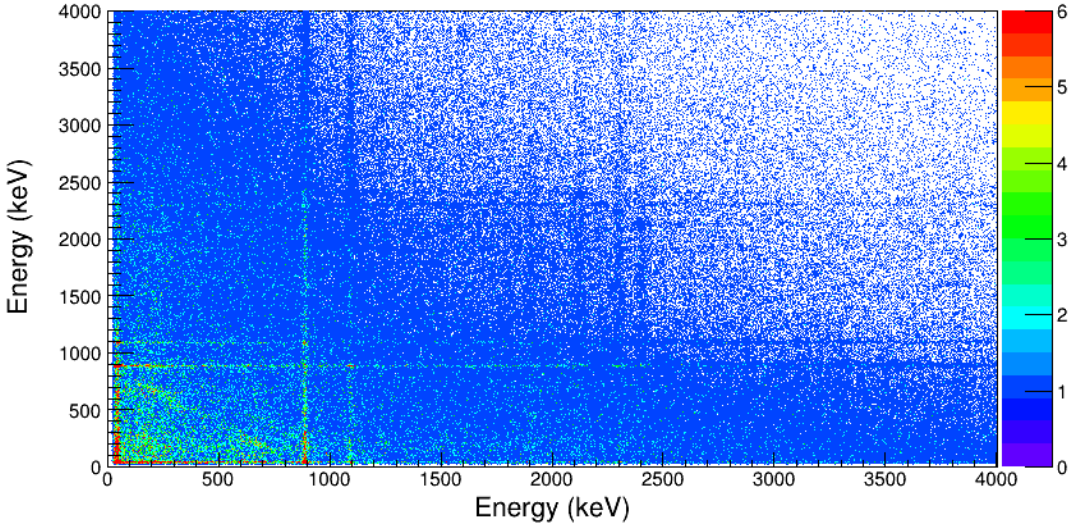

Figure 4.23: A 2D histogram of $\gamma - \gamma$ matrix, gated on incoming ^{47}Cr beam and outgoing ^{46}Cr nucleus. The x and y axes both show γ-ray energies for coincident events.

Chapter 5

Results of Mirrored One-Nucleon Removal Reactions

This chapter will detail the results obtained from the mirrored knockout reactions. The first successful identification of the excited states in the proton-rich nucleus $T_z = -2$ system ^{48}Fe was achieved, and the nucleus was compared to its mirror nucleus ^{48}Ti (Section 5.1). These allowed for the study of MED and mirrored knockout cross sections in this $T_z = \pm 2$, pair in the $f_{\frac{7}{2}}$ shell (Sections 5.2 and 5.3).

A large range of isotopes were produced in this experiment, whose runs were performed with two separate A1900 settings and two S800 magnetic rigidity settings centred on the products of the $T_z = -\frac{3}{2}$ and $T_z = +\frac{3}{2}$ reactions. The two settings were run for approximately $\sim$ 106 hours and $\sim$ 1 hour (Table 3.1) for the proton-rich and neutron-rich isotopes, respectively, due to the large differences in production of cross sections for the secondary beams.

The γ-ray spectra observed in this chapter for the nuclei of interest were all produced in coincidence with both incoming and outgoing nuclei to ensure that the γ rays detected were both related with the correct nuclei and reaction channel. The angle for the Doppler correction was determined from the recorded position

in GRETINA of the first interaction point for that gamma-ray event [68]. In this experiment, for decays from states with short lifetimes, the best energy resolution obtained was 1.4% (FWHM) for 1-MeV γ ray.

To maximise photo-peak efficiency and improve the $\gamma - \gamma$ coincidence analysis for all the spectra shown in this chapter, a nearest-neighbour add-back method was applied where energies were deposited in neighbouring GRETINA crystals (fired in the same event) and then summed. This add-back procedure, which was used instead of a full gamma-ray tracking algorithm (e.g. [68]), was not used to compute efficiency-corrected γ-ray intensities, because of the challenges in determining the correct in-beam efficiency.

This chapter will also detail the process of measuring the experimental inclusive and exclusive cross sections for ^{48}Fe/^{48}Ti. It will then go on to describe the stages involved in the process of measuring the MED of $A = 48$. Additionally, the measured inclusive cross sections of $A = 45$, $T_z = \pm\frac{1}{2}$ mirror nuclei resulting from one-neutron and one-proton knockout reactions, respectively, from the odd-odd $N = Z$, $T_z = 0$ beam, ^{46}V, are also studied (Section 5.4). The theoretical interpretation and discussion of these results will be presented in Chapter 6 (cross sections) and Chapter 7 (MED) respectively.

5.1 Population of States in the $T_z = \pm 2$ Mirror Pair

Since the underlying wave functions of mirror nuclei are considered as identical, one-nucleon knockout reactions should populate the same set of analogue states with similar intensities in both nuclei. Thus, under identical conditions, the resulting γ-ray spectra can help confirm the mirror transitions through spectral comparison. Studies of proton-rich nuclei in this region have indicated the potential of this new approach to MED studies, as noted in [6, 18, 87].

The reactions ^{9}Be (^{49}Fe,^{48}Fe) and ^{9}Be (^{49}V,^{48}Ti) were both employed to perform a spectroscopic study of the nuclei in this experiment.

The technique of "mirrored" knockout reactions was applied [3, 27, 28], which provides a comprehensive comparison of both of the analogue reaction process and the resulting level schemes of the mirror pair via mirror symmetry arguments. By exploiting the direct nature of the knockout process, the assignment of the unknown states in the proton-rich system, ^{48}Fe in this case, can be made confidently. This approach allows for the measurement of MED, which provide a stringent test of the state-of-the-art microscopic nuclear models. Measurements from such analogue reactions also have the potential to determine the mirrored cross sections as a further test of isospin symmetry. The experimental results will be explained in the following sections.

5.1.1 Spectroscopy of ^{48}Ti

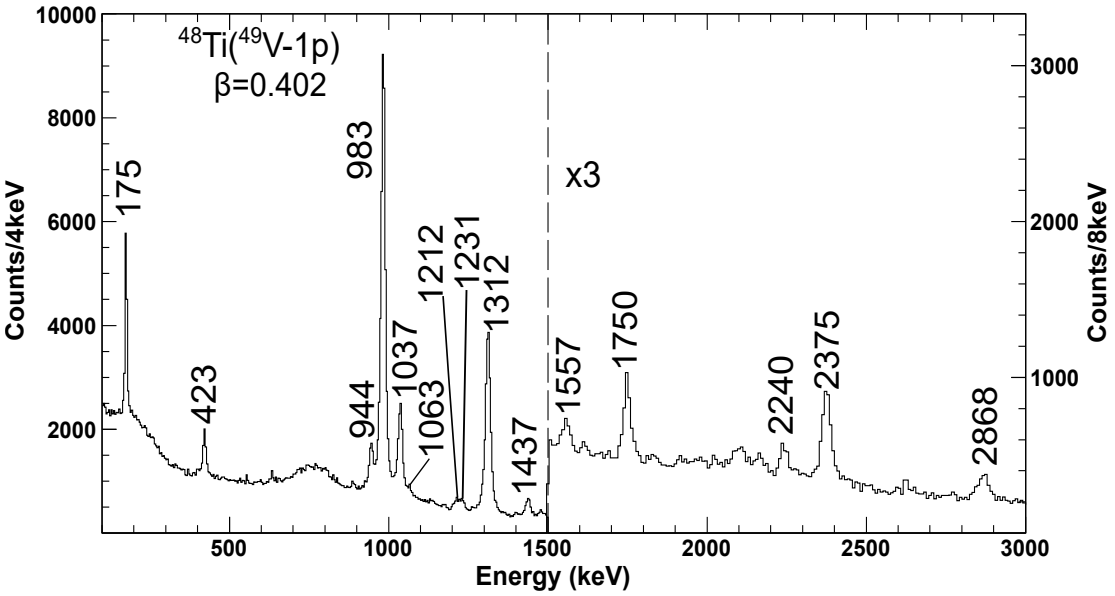

Figure 5.1: The Doppler-corrected energy spectrum for γ rays, using an add-back procedure, in coincidence with ^{48}Ti fragments, populated via one-proton knockout reactions from ^{49}V. The $\beta = v/c = 0.402$ value used for the Doppler reconstruction is optimised for fast transitions.

To identify the excited states in proton-rich nucleus ^{48}Fe from one-neutron knockout from ^{49}Fe, the analogue reaction (one-proton knockout channel from

^{49}V to the well-known nucleus, ^{48}Ti [29]) was examined first. This is because, structurally, the reaction processes are expected to be very similar (the analogue properties of the reactions). The Doppler-corrected γ-ray spectrum of ^{48}Ti from the current work is found in Fig. 5.1, with optimum recoil velocity $\beta = 0.402$. This value of β is found to optimise the Doppler correction for the majority of peaks seen in Fig. 5.1, most of which decay from short-lived states with lifetimes of < 1 ps.

The spectrum for ^{48}Ti, shown in Fig. 5.1, shows the γ-ray transitions from positive-parity states, with $J^\pi = 2^+$, 4^+, and 6^+, with two states of each J^π observed. All these observed states can be populated directly from one-proton knockout from the $\frac{7}{2}^-$ ground state of the ^{49}V secondary beam. The negative-parity states, observed in the spectrum, can be populated directly through knockout from any of the deeply-bound *sd* orbitals.

For the strongest transitions, the ordering of these excited states were confirmed by a γ-γ coincidence analysis afforded by the high resolving power and efficiency of GRETINA. Gamma-ray coincidence analysis was carried out by projecting the 2D gamma-gamma matrix, around the observed gamma-ray peak in the gamma-ray spectra. This matrix represents all the γ-ray events with multiplicity ≥ 2 detected within the same coincidence time window of the detector system to confirm the order of the excited states. Some examples are shown in Figs. 5.2 (a-f) of spectra from a γ-γ coincidence analysis. Gamma rays measured to be in coincidence with the strong transitions, 983, 175, 1037, 1312, 1212, and 1557 keV, are shown, demonstrating the expected γ-ray transitions in coincidence with these transitions.

The sequence of γ rays observed in ^{48}Ti in this work is shown in the partial level scheme on Fig. 5.3. All the labelled gamma rays observed in Fig. 5.1 have been previously assigned to ^{48}Ti [29], and all the energies measured here are consistent with those of [29]. The more precise energies from [29] are used in Figs. 5.1 and 5.3. Tentatively observed γ-ray transitions are indicated by dashed lines.

Though $J^\pi = 6^+$ is the maximum spin that can be populated directly from knockout of the $\frac{7}{2}^-$ ground state of the ^{49}V, there is weak evidence for decay from the

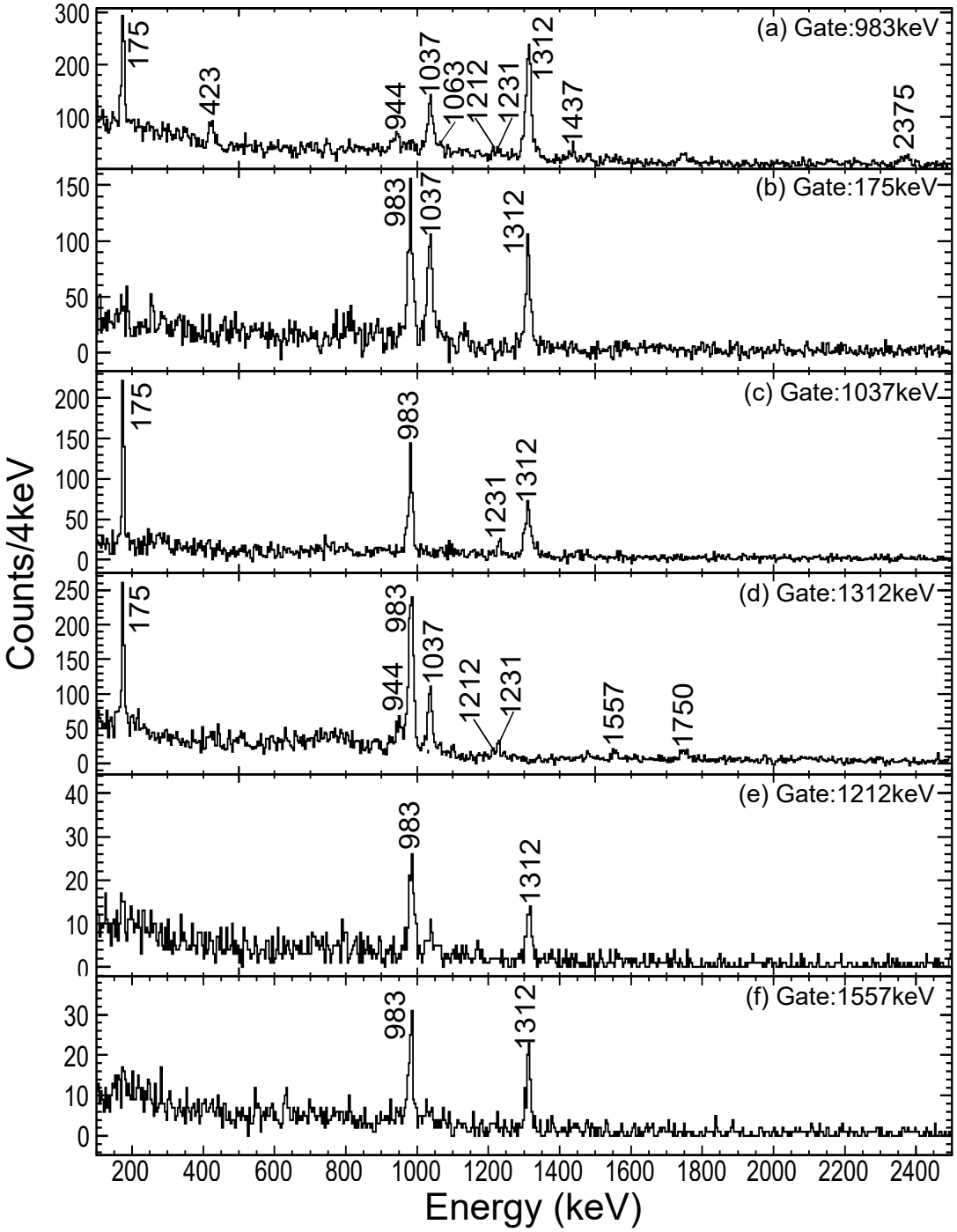

Figure 5.2: γ-γ coincidence spectra of ^{48}Ti when gating on (a) 983, (b) 175, (c) 1037, (d) 1312 (e) 1212, and (f) 1557 keV transitions. These spectra were produced by projecting 2D $\gamma - \gamma$ matrix spectrum around these peaks and performing a local background subtraction from the right and left the peak. (a–f) spectra have been produced using an average $\beta = v/c$ value of 0.402.

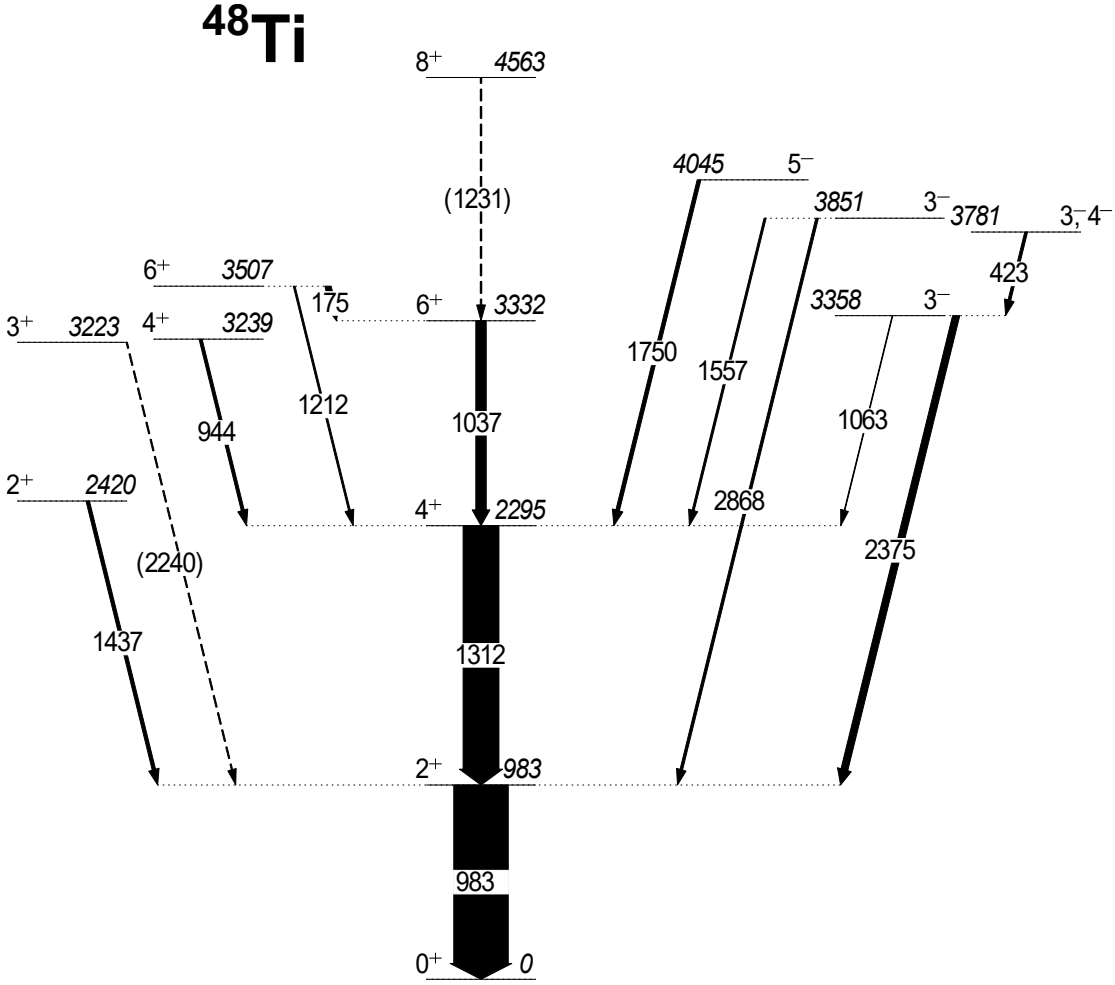

Figure 5.3: Level scheme of ^{48}Ti showing the γ rays observed in this work. Energies, ordering, and spins and parities are taken from [29], and the ordering was also confirmed in the present work through γ-γ coincidence analysis. The dashed lines indicate tentative transitions, and the tentative γ rays are presented in parentheses. Transition widths are proportional to γ-ray intensities measured in this work and are determined relative to the intensity of the $2_1^+ \rightarrow 0^+$ transition.

8^+, presumably populated indirectly through unobserved decays from higher-lying states (discussed later in Chapter 6). In addition, another weak transition observed at 2240 keV is tentatively assigned as the transition from a 3^+ state (Fig. 5.3).

The relative intensities of the γ rays were measured by fitting peaks and dividing the measured intensities by the corresponding detector efficiencies and Lorentz boost (calculated using Eq. 4.2). The efficiency and Lorentz boost-corrected intensities of transitions were normalised to the measured intensity of the 983 keV $2_1^+ \rightarrow 0^+$ transition. The efficiency-corrected intensities were determined with and

without add-back. Although the deduced efficiencies for the two methods are not fully consistent as listed in Table 5.1, some systematic differences dependent on the incident energy can be seen. The relative γ-ray intensity (with and without add-back) results along with the state energy, spin, and parity assignments have been classified and presented in Table 5.1. The branching ratios of the measured γ rays of ^{48}Ti observed in this work are also consistent (within the error) with the published data [29].

Table 5.1: The energy for excited states, γ-ray energies (in keV) and relative intensities (with and without the add-back procedure) for γ decays for the ^{48}Fe and ^{48}Ti mirror pair.

$J_i^\pi \rightarrow J_f^\pi$	^{48}Fe				^{48}Ti			
	E_x	E_γ	I_γ(NoAB)%	I_γ(AB)%	E_x	E_γ	I_γ(NoAB)%	I_γ(AB)%
0^+	0				0			
$2_1^+ \rightarrow 0^+$	971(1)	971(1)	100(14)	100(9)	983	983	100(2)	100(3)
$4_1^+ \rightarrow 2_1^+$	2255(1)	1284(1)	69(5)	65(5)	2296	1312	66(2)	63(2)
$2_2^+ \rightarrow 2_1^+$	2378(3)	1407(3)	7(3)	7(3)	2421	1437	6.2(6)	5.2(4)
$3_1^+ \rightarrow 2_1^+$					3224	2240	2.4(5)	2.5(5)
$4_2^+ \rightarrow 4_1^+$	3200(3)	944(2)	8(6)	9(3)	3240	944	5.5(6)	4.9(4)
$6_1^+ \rightarrow 4_1^+$	3244(3)	988(3)	21(11)	21(6)	3333	1037	19.1(7)	19.4(7)
$3_1^- \rightarrow 2_1^+$	3476(5)	2505(5)	7(3)	11(3)	3359	2375	12.8(7)	12.9(7)
$3_1^- \rightarrow 4_1^+$					3359	1063	1.3(3)	1.7(3)
$6_2^+ \rightarrow 4_1^+$	3500(2)	1244(2)	15(3)	13(3)	3509	1212	3.2(4)	2.8(5)
$6_2^+ \rightarrow 6_1^+$	3500(2)	256(1)	19(3)	14(2)	3509	175	11.1(3)	11.0(3)
$3_2^-, 4_1^- \rightarrow 3_1^-$					3782	423	5.0(4)	4.9(3)
$3_3^- \rightarrow 2_1^+$					3852	2868	4.7(6)	4.9(6)
$3_3^- \rightarrow 4_1^+$					3852	1557	3.7(8)	3.0(5)
$5_1^- \rightarrow 4_1^+$	4206(4)	1951(4)	6(3)	6(2)	4046	1750	6.6(5)	7.4(5)
$8_1^+ \rightarrow 6_2^+$					4564	1231	2.7(7)	1.5(2)

* The excitation energies of the states in ^{48}Ti and γ-ray transitions were taken from the evaluated nuclear structure data file (ENSDF) [88].

5.1.2 Spectroscopy of ^{48}Fe

The Doppler-corrected γ-ray spectra of ^{48}Ti and ^{48}Fe are presented in Figs. 5.4 (a) (this is the same spectrum as Fig. 5.1) and 5.4 (b), respectively. The γ rays from excited states of the highly proton-rich nucleus ^{48}Fe, which have been unambiguously observed for the first time in this work, are shown in Fig. 5.4 (b).

The only tentative transition previously assigned to ^{48}Fe is a 969.5(5) keV transition observed following beta-delayed proton emission of ^{49}Ni [4], where this transition was found to be weak, $\sim$ 4–5 counts, but tentatively identified as the $2^+ \rightarrow 0^+$ transition in ^{48}Fe. However, in the current work, this transition was confirmed as 971(1) keV.

The optimum recoil velocity, $\beta = v/c$, used for the Doppler correction was determined based on the effective lifetime of the states. The β values of 0.402 and 0.395 were found to optimise the Doppler correction for ^{48}Fe and ^{48}Ti, respectively, for the majority of peaks (which, for ^{48}Ti, are fast transitions with half-lives $\sim$1 ps), as seen in Figs. 5.4 (a) and 5.4 (b). Fast transitions with half-lives $\sim$1 ps decay at different points within the target. However, a lower recoil velocity was needed to optimise the two largest transitions of 983 keV and 971 keV in ^{48}Ti and ^{48}Fe, respectively. This is consistent with the finding in the literature [29] that the 983 keV, $J^\pi = 2_1^+$ state in ^{48}Ti has a longer half-life of $\sim$ 4 ps, decaying mostly downstream of the target. Therefore, based on the mirror symmetry argument, the analogue transition in ^{48}Fe is likely to have a similar half-life. This is illustrated in the inset to Fig. 5.4 (b), which shows the spectrum generated using $\beta = 0.390$, optimised for the 971(1) keV transition.

The high γ-ray resolution of GRETINA, along with the lower optimum velocity applied for Doppler correction, $\beta = 0.390$ (see inset to Fig. 5.4 (b)), allows three close-lying transitions in ^{48}Fe to be observed, corresponding to 944(2) keV, 971(1) keV, and 988(3) keV. The 988(3) keV transition appears as a tail on the right of the 971(1) keV peak. The comparison of the γ-ray energies and intensities with ^{48}Ti results in the conclusion that the isobaric analogue states with $J^\pi = 2^+$,

4^+ and 6^+ are populated in both reactions.

The uncertainties listed in Table 5.1 associated with the newly-identified γ-ray energies comprise statistical and systematic errors, with the latter being associated with uncertainties in β and the effective target position. The systematic error in determining the velocity used for the Doppler correction was estimated by varying β by eye until a noticeable change in the width of the peaks occurred. As a result, there was a systematic uncertainty of ± 0.005 in establishing values on the velocity. This variation was used to determine a systematic error in the γ-ray energies. Moreover, the effective target position (z) can have a significant effect on the γ-ray energy, and indeed, the apparent value of z was not constant throughout the run (the target was removed and replaced at one point). The uncertainty regarding determining z was estimated. This was then used to determine a second systematic error in the γ-ray energy. These two systematic errors (from β and z) were combined to give the final systematic error on the gamma-ray energy, and this combined with the statistical error from fits to provide the final error in the γ-ray energies, which is the error quoted in Table 5.1.

A comparison of the Doppler corrected γ-ray spectra in Figs. 5.4 (a) and (b) shows a one-to-one correspondence between the strongest γ-ray transitions observed, which allows for an initial identification of the proposed analogue transitions in the mirror nuclei. The assignment of most of the stronger transitions in ^{48}Fe to their analogues in ^{48}Ti was further confirmed by $\gamma - \gamma$ coincidence analysis.

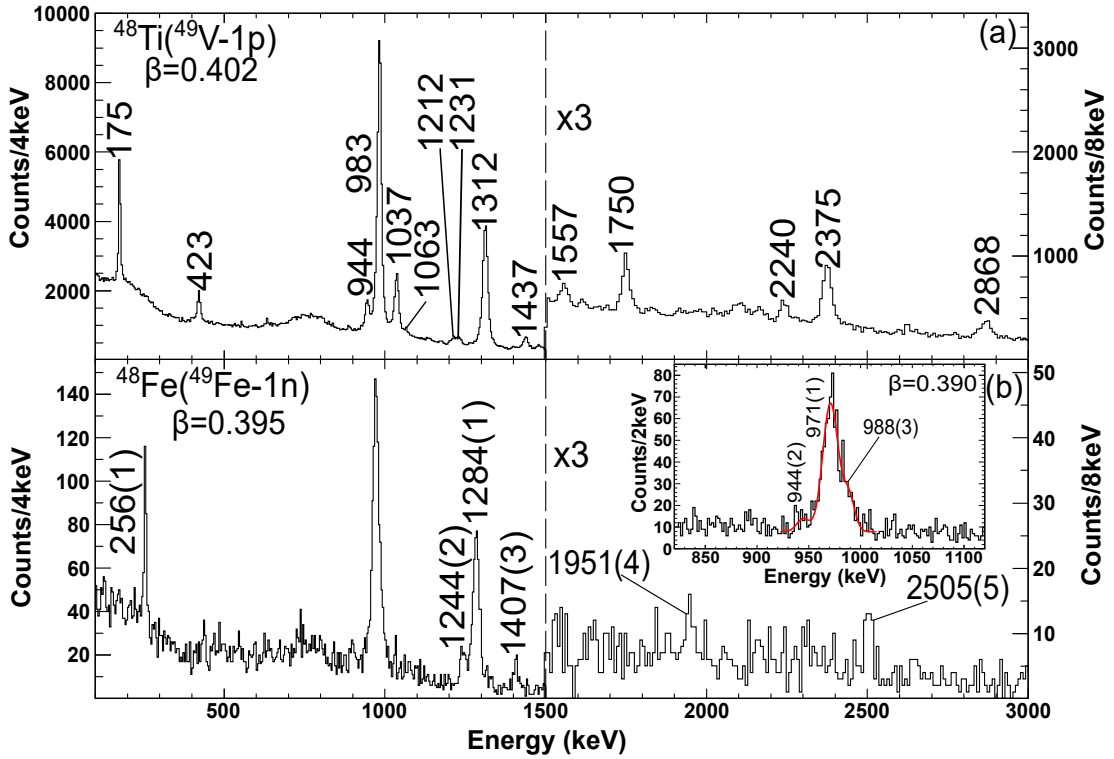

Figure 5.4: The Doppler-corrected γ-ray spectra using the add-back procedure (see text) for (a) ^{48}Ti and (b) ^{48}Fe populated through one-nucleon knockout from ^{49}V and ^{49}Fe. The $\beta = v/c$ value is optimised for fast transitions in (a) and (b), while a lower β value is utilised for the spectrum insert of (b) for the 971-keV transition (see text). The spectrum used in the insert in (b) was created without add-back, as the fits in the analysis were applied to spectra without add-back.

Based on the knockout mechanism (direct reaction), the same states are expected to be populated. However, more states were observed in ^{48}Ti than ^{48}Fe, especially high-energy negative-parity states. This is due to the much higher intensity and beam current of ^{49}V than for ^{49}Fe beam, where only the strongest transitions were observed in ^{48}Fe.

The $\gamma - \gamma$ coincidence analysis was performed for the strongest transitions observed in Fig. 5.4 (b) in order to help establish a new-level scheme for ^{48}Fe. A 2D $\gamma - \gamma$ coincidence matrix spectra (as described in Section 4.6) for ^{48}Fe produced by one-neutron knockout from ^{49}Fe, with and without add-back, are shown in Figs. 5.5 (a) and (b), respectively. The improvement utilising the add-back procedure is evident in the $\gamma - \gamma$ spectra as well as in the projections from the $\gamma - \gamma$ matrices (as shown in the insets of Fig. 5.5). This demonstrates how add-back,

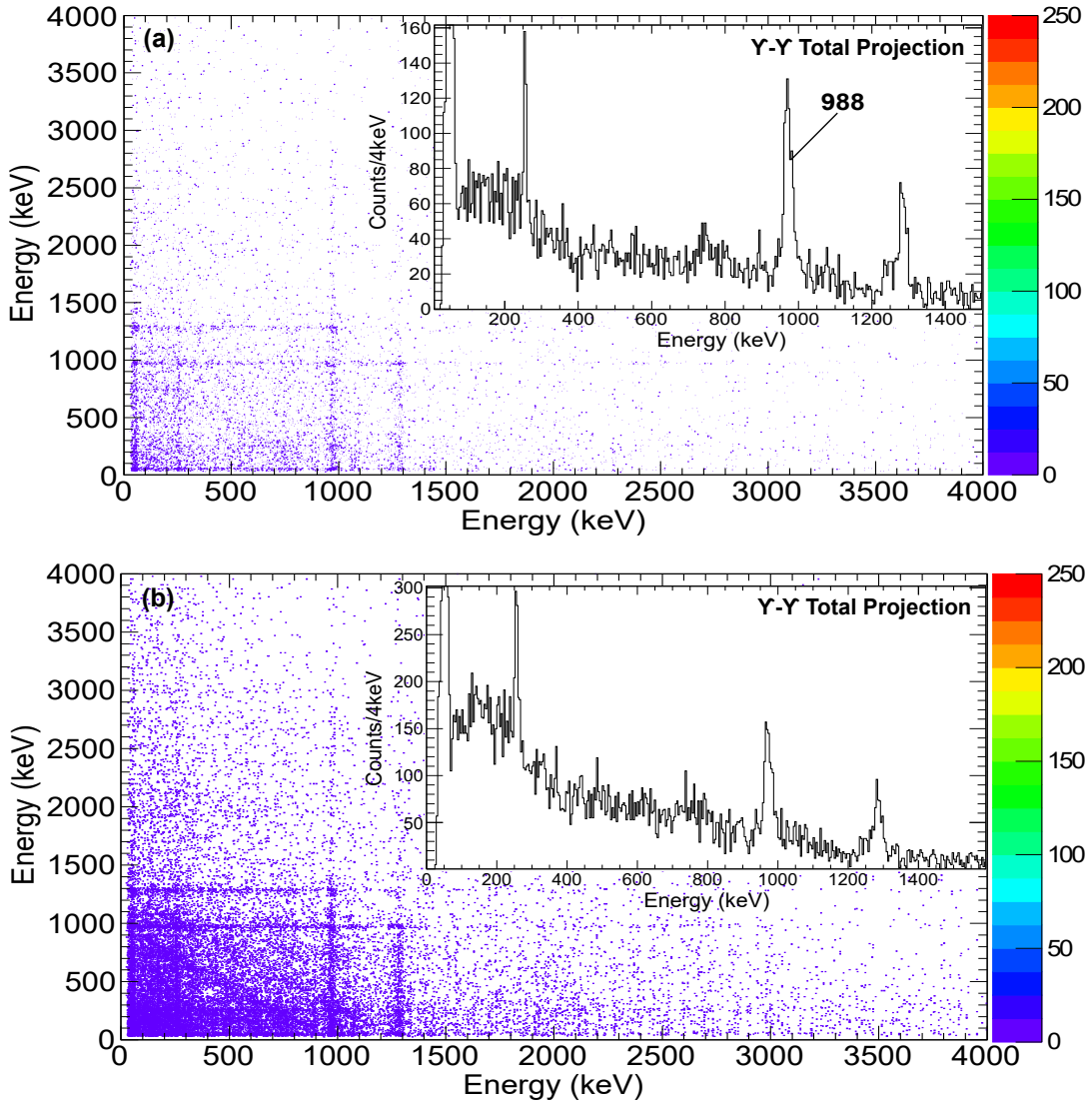

Figure 5.5: Gamma-gamma coincidence matrices using (a) add-back and (b) no add-back for ^{48}Fe were produced in one-neutron knockout from ^{49}Fe. The insets show the projections of the $\gamma - \gamma$ coincidence matrices. This illustrates the effect of add-back, especially in $\gamma - \gamma$ coincidence analysis, which moves the counts from the background into peaks.

especially in $\gamma - \gamma$ coincidence analysis, moves the counts from the background into peaks. For example, the transition at 988 keV at the right-hand tail of 971 keV peak is difficult to spot in the $\gamma - \gamma$ projection when treating GRETINA as single crystals (Fig. 5.5 (b)). However, it can be clearly identified in the $\gamma - \gamma$ projection when using the add-back approach (Fig. 5.5 (a)). The transitions shown in the projection spectra have a substantially improved peak-to-background ratio for

add-back, while in the single-crystal approach, low-energy hits due to Compton scattering are more evident.

An example of γ-γ coincidence analysis is presented in Fig. 5.6, which show the γ-ray spectra measured in coincidence with the 256(1) keV (Fig. 5.6 (a)), 971(1) keV (Fig. 5.6 (b)), and 1284(1) keV (Fig. 5.6 (c)) transitions, where the expected γ-ray transitions in coincidence with them can be seen. In Fig. 5.6 (a), the background-subtracted γ-γ spectrum in coincidence with the 256(1) keV transition is presented, where three strong transitions were detected at energies 971(1), 988(3), and 1284(1) keV. In Fig. 5.6 (b), the background-subtracted γ-γ coincidence spectrum gated on the 971(1) keV transition is shown, where the expected transitions were detected in coincidence with γ rays at energies of 256(1), 944(2), 988(3), 1241(1), 1284(1), 1407(3), and 2505(5) keV. However, the two transitions at 1407(3) and 2505(5) keV were only weakly observed in the 971(1) keV coincidence spectrum (Fig. 5.6 (b)) due to the low statistics. In Fig. 5.6 (c), the background-subtracted γ-γ spectrum for transitions in coincidence with the 1284(1) keV transition is shown, where four transitions were also identified in coincidence at energies of 256(1), 944(2), 971(1), and 988(3) keV. Moreover, the two $\gamma - \gamma$ coincidence spectra gated on the very weak 1407(3) and 2505(5) keV transitions can be seen gathering intensities around the peak 971(1) keV, which may indicate that these two transitions are in coincidence with 971(1) keV transition. The results of these are shown in Figs. 5.7 (a) and (b).

The level of statistics of the γ-γ coincidence spectra generally is low. This would probably lead to the conclusion that only the ordering of the strong transitions were confirmed and weak transitions were difficult to be placed in this analysis. The close proximity of the 944(2), 971(1), and 988(3) keV transitions makes confirmation of the 988(3) keV and the 944(2) keV transitions challenging. However, a gate on the 256(1) keV peak clearly shows a broad peak shape containing both the 971(1) keV and 988(3) keV (Fig. 5.6 (a)), as expected, with no hint of the 944(2) keV transition. Moreover, the 944(2) keV transition was also observed in coincidence with the 971(1) keV transition.

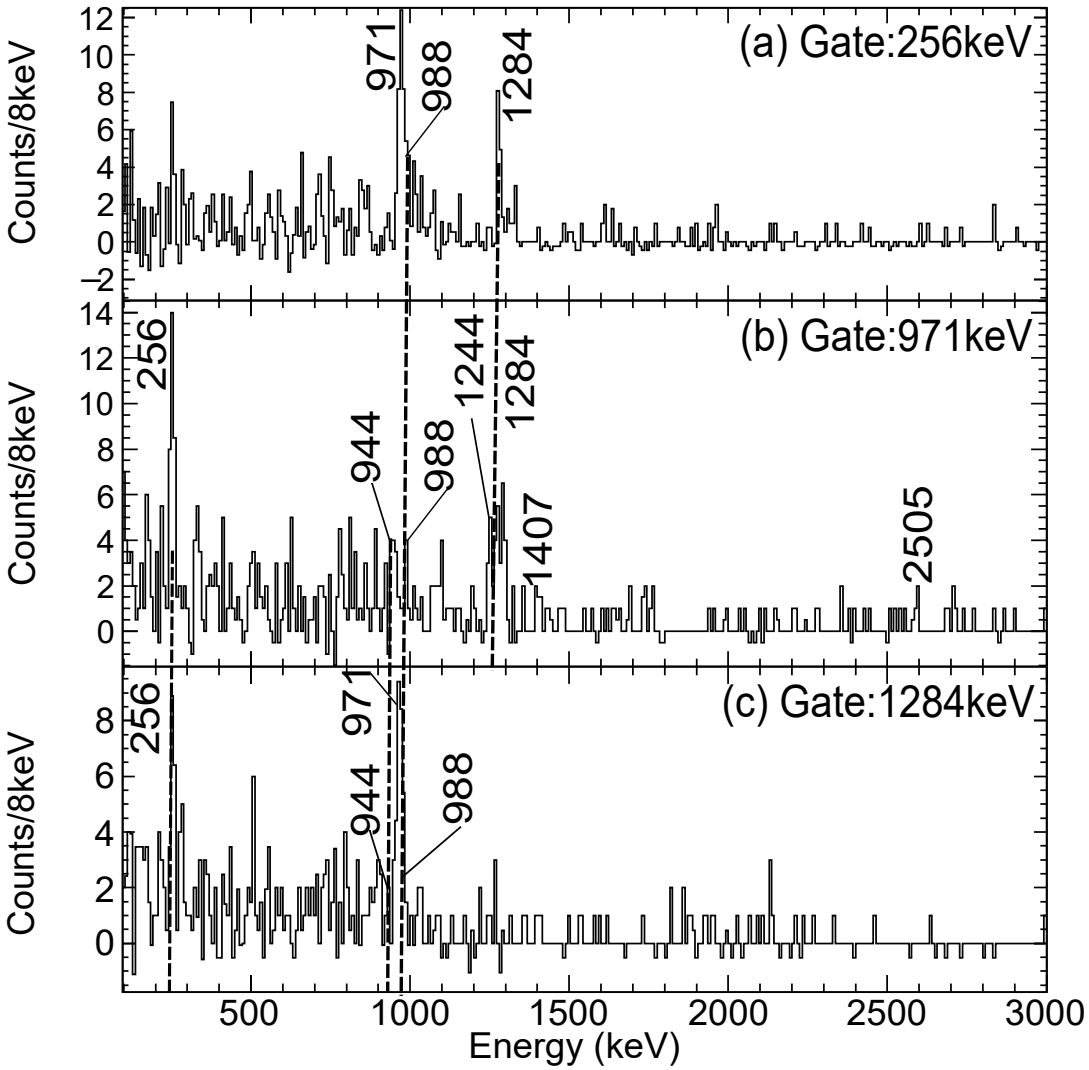

Figure 5.6: A spectra from γ-γ coincidence analysis, using add-back, was measured to be in coincidence with the (a) 256 keV(1), (b) 971 keV(1), and (c) 1284(1) keV transitions in ^{48}Fe. These spectra were produced by projecting Fig. 5.5 around the 971, 256, and 1284 keV peaks and performing a local background subtraction from the right and left of the peak. The dashed lines indicate the strongest peaks that have been observed from the gamma-ray coincidence analysis. (b) and (c) spectra have been produced using an average $\beta = v/c$ value of 0.395, while (a) spectrum has been produced with the lower β value of 0.390 (see text).

It is worthy of note that the bin of 4 keV per channel was used for the single spectra (Fig. 5.4) and the gamma-gamma coincidence spectra for the ^{48}Ti nucleus (Fig. 5.2). Due to the high statistics, 4 keV per channel is a good compromise because most gamma rays are at 1 MeV or higher. For the gamma ray at 1 MeV, a typical resolution is going to be $\sim$ 20 keV ($\sim$ 1.5-2%), hence, 4 keV is sufficient bins

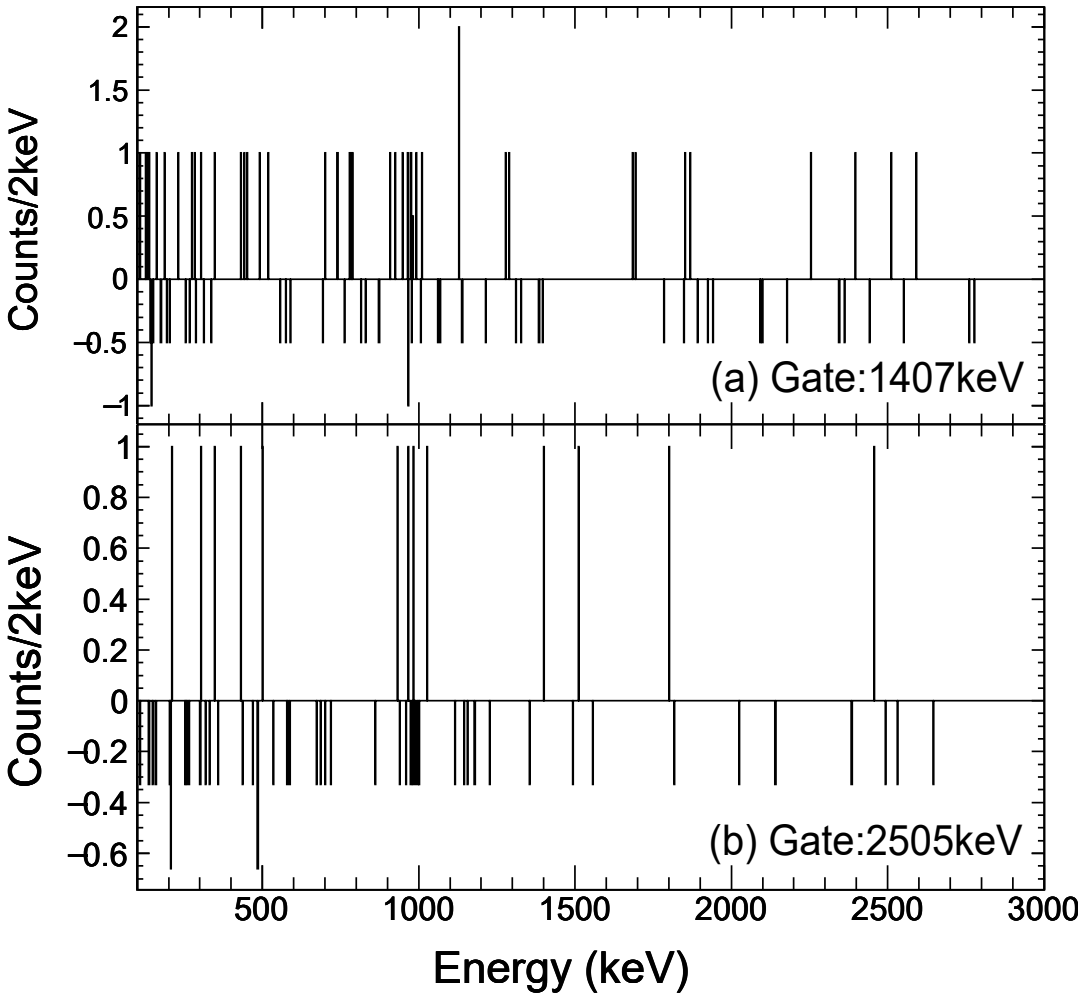

Figure 5.7: A spectra from γ-γ coincidence analysis, using add-back, was measured to be in coincidence with the (a) 1407 keV(3) and (b) 2505(5) keV transitions in ^{48}Fe. These spectra were produced by projecting Fig. 5.5 around the 1407 and 2505 keV peaks and performing a local background subtraction from the right and left of the peak. (a) and (b) spectra have been produced using an average $\beta = v/c$ value of 0.395.

to see the peak shape. However, due to the very-low statistics in some cases, such as in the ^{48}Fe nucleus, a larger binning (8 keV) was used for the gamma-gamma spectra (Fig. 5.6). This is necessary to improve the chance to observe the peaks above the background level, even though information is lost on the peak shape.

The observed transitions in the current work following this analysis have been placed in a new-level scheme for ^{48}Fe in the top part of Fig. 5.8, compared with known transitions in ^{48}Ti. The placement and ordering of the γ-ray transitions

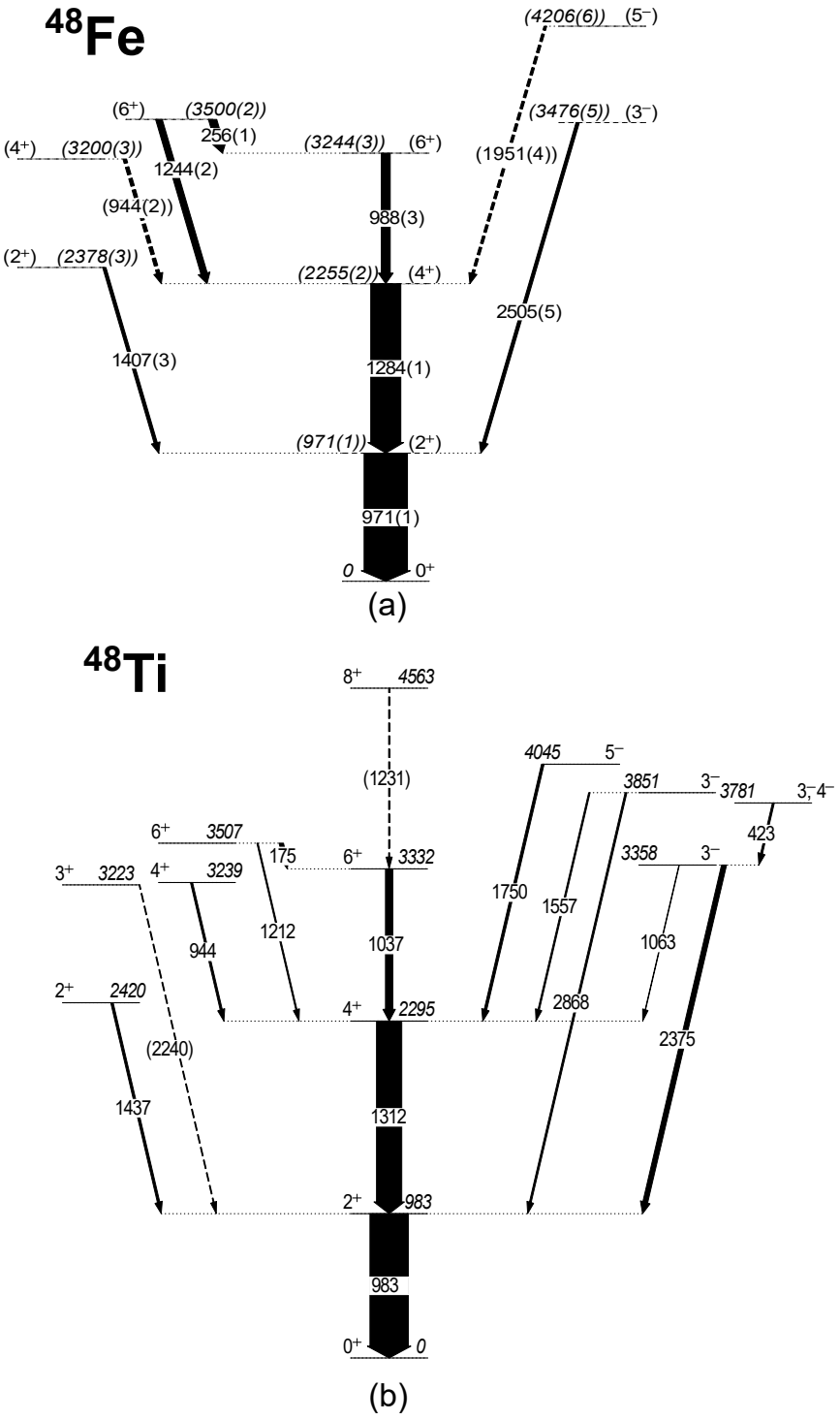

Figure 5.8: The new energy level scheme for ^{48}Fe (a) observed in this work compared with the level scheme of ^{48}Ti (b) as observed in this experiment. The intensities of the γ rays are indicated by the width of the arrows and are determined relative to the intensity of the $2_1^+ \rightarrow 0^+$ transition. Tentative transitions are represented by the dashed lines.

initially was made on the basis of mirror symmetry arguments, i.e. the analogue knockout reactions and the γ-ray energy similarities, as well as intensity arguments, and then confirmed by $\gamma - \gamma$ analysis where possible. The spins and parities of the state in ^{48}Fe were assigned only by mirror symmetry arguments, i.e. based on comparison with the well-known ^{48}Ti scheme [29]. There remain some tentative transitions in the level scheme of ^{48}Fe, where due to low statistics, it is not possible to perform $\gamma - \gamma$ coincidence measurements for these weak transitions, or there are large shifts in the analogue γ-ray energies; hence, these transitions are shown by dashed lines in Fig. 5.8 (a).

For instance, although the 944(2) keV transition was extremely weak; on the balance of probabilities, suggests that it exists (given also the mirror symmetry arguments). The evidence for this transition is shown in Figs. 5.4 (b) and 5.6 (b), both of which are a little tentative, which is why the transition was dashed in the level scheme Fig. 5.8 (a). In addition, another weak transition from the 5^- state is observed and tentatively assigned as 1951(4) keV (see Fig. 5.8 (a)).

One of the most interesting aspects in the current context is that for the excited states of positive parity, two states were observed for each J^π. In both level schemes, the knockout process populates both the lowest-energy states of each J ($J^\pi = 2_1^+$, 4_1^+ and 6_1^+, referred to as *yrast*), and the next lowest-energy states ($J^\pi = 2_2^+$, 4_2^+ and 6_2^+, referred to as *yrare*). Furthermore, it can be seen in the level scheme of ^{48}Fe that there is also evidence for the population of the analogue states of the odd-parity states observed in ^{48}Ti.

The widths of the arrows in Fig. 5.8 are based on the relative intensity of the γ-ray transitions, which are listed in Table 5.1 along with the measured γ-ray energies, the excitation energy and spin and parity assignments. Intensities were measured using Gaussian fits. The relative intensities of the γ rays have been corrected for efficiencies and the Lorentz boost and are quoted relative to the intensity of the $2_1^+ \rightarrow 0^+$ transition.

The experimental level scheme of ^{48}Fe deduced from the current work has been interpreted in the framework of the large-scale shell-model calculations using the

KB3G interaction [45] in the pf model space. The model space consists of the full pf shell and uses a ^{40}Ca core and valence space $f_{\frac{7}{2}}$, $p_{\frac{3}{2}}$, $f_{\frac{5}{2}}$, and $p_{\frac{1}{2}}$ (described in Section 2.2.2). The calculated levels are shown in Fig. 5.9 in comparison with the level scheme from the experiment. The calculations for ^{48}Fe in the large model space accurately reproduce the data. These calculations are later used to deduced the spectroscopic factors for the cross-section calculations (Chapter 6) and the MED (Chapter 7).

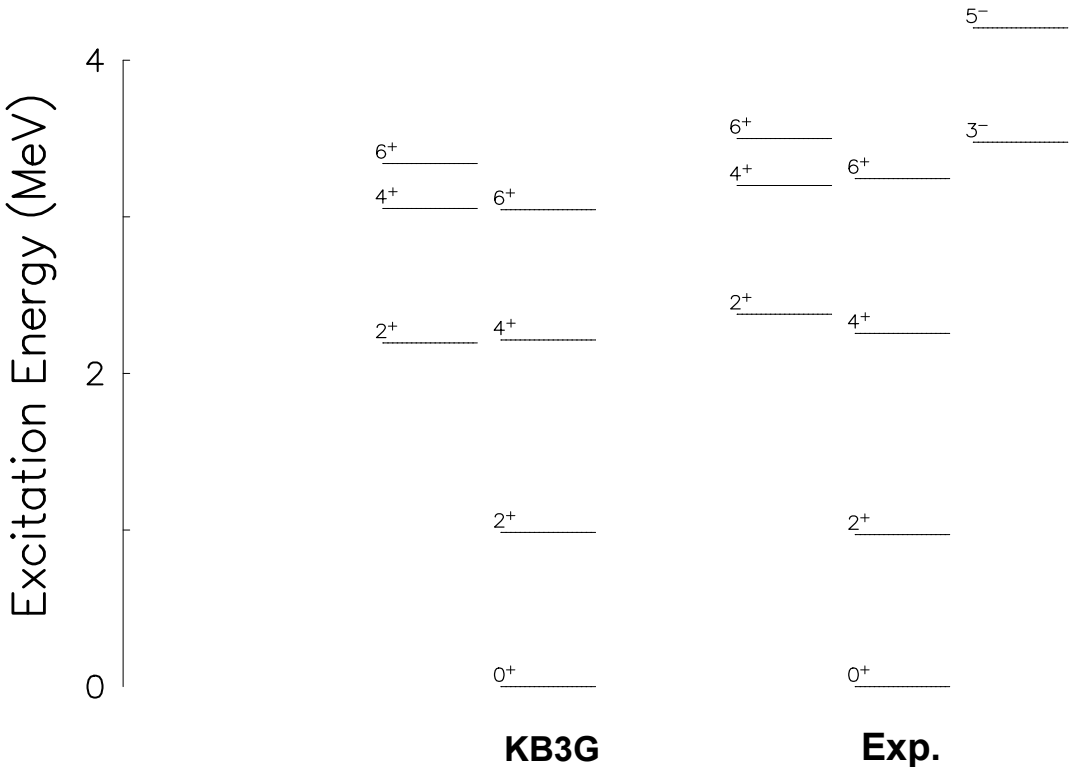

Figure 5.9: Experimental level scheme for ^{48}Fe alongside shell-model predictions. The shell-model calculations have been performed in ANTOINE with the KB3G interaction [45].

5.2 Knockout Cross Sections T_z=±2 Mirror Pair

The aim of experiment E14027 was to measure direct one-nucleon knockout cross sections to the pairs of analogue states in question, providing information on spectroscopic factors for both sets of analogue states. Using the GRETINA-S800 setup, one can determine the inclusive and exclusive cross sections, from the γ-ray energies and relative intensities of the states directly populated in the reaction. In the following sections, experimental inclusive and exclusive cross section results will be presented for the $A = 48$, $T_z = \pm 2$ mirror pairs.

5.2.1 Inclusive Cross-Section Measurements

As described in Chapter 2, measurements of the cross sections associated with nucleon knockout reactions can be used to deduce spectroscopic information pertaining to single-particle occupational strengths, which represent a measurement of the overlap between the initial and final state configurations. A cross section is a measurement of the probability of a projectile yielding a specific reaction, which for a direct reaction means a reaction populating a specific state of the residual nucleus from a specific initial state of the projectile.

The experiment seeks to measure a set of observables, one of which is the inclusive cross section for single nucleon removal (σ_{inc}). The σ_{inc} is the total probability for removing a single nucleon from the ground state of the projectile, leading to any final excited state of the fragment residue.

The inclusive cross section is determined experimentally as the ratio of the number of collected residual core nuclei, N_f (^{A-1}Z), to the number of incoming beam nuclei, N_i (^{A}Z), with a multiplicative constant of the number of target particles per unit area, N_T. A 188mg/cm^2 ^{9}Be target was used in this experiment, which determines N_T. The inclusive cross section is expressed as follows

$$\sigma_{inc} = \frac{1}{N_T} \cdot \frac{N_f}{N_i}. \tag{5.1}$$

The N_f and N_i were determined experimentally from separate data runs, knock-out/reaction runs and unreacted beam normalisation runs, respectively.
In order to count the total number of incoming particles, N_i, normalisation runs, were performed by periodically sampling the incident beam using runs known as unreacted beam runs. To determine the N_f and N_i, the total number of recorded single events, N_{obs} (i.e. the detection of an ion only) for both residue and incoming beam need to be determined. However, these require the application of some additional corrections; see the equations below.

$$N_f = \frac{N^R_{obs}\ Ds}{\epsilon_{det}\ C_{live}\ A}, \tag{5.2}$$

$$N_i = \frac{N^u_{obs}\ Ds}{\epsilon_{det}\ C_{live}\ A}\ \ K_{norm}, \tag{5.3}$$

$$K_{norm} = \frac{N^R_{norm}}{N^u_{norm}} \tag{5.4}$$

where N^R_{obs} is the observed number of final residue in reacted beam runs, N^u_{obs} is the observed number of beam particles in unreacted beam runs, Ds is downscaler (see Section 3.3), A is the acceptance and C_{live} is a correction factor to account for dead time. K_{norm} is a normalisation factor used to normalise the total secondary beam intensity between the reaction runs (N^R_{norm}) and the unreacted beam runs (N^u_{norm}). N^R_{norm} and N^u_{norm} are taken as the total scaler outputs for the XFP and OBJ scintillators.
The "A" accounts for losses in parallel-momentum distribution for reasons such as the blocking of unreacted beams for the residue of interest or incoming beam, which can be measured from the parallel momentum distribution spectrum d_{ta}.
The total particle detection efficiency of the S800 beam line and focal-plane detectors relative to the ionization chamber was measured using the following equation:

$$\epsilon^i_{det} = \epsilon_{OBJ} \times \epsilon_{XFP} \times \epsilon_{CRDC1} \times \epsilon_{CRDC2} \tag{5.5}$$

where ϵ_{OBJ}, ϵ_{XFP}, ϵ_{CRDC1}, and ϵ_{CRDC2}, are the detection efficiencies of the OBJ scintillator and XFP scintillator CRDC1 and CRDC2.

Systematic errors in the inclusive cross-section measurements are to be considered in addition to statistical errors. The systematic errors result from the uncertainty of the particle identification gates ($\sim 0.4\%$), the fluctuations in the beam purity ($\sim 8-17\%$), the corrections for the S800's limited momentum/angle acceptance ($\sim 4\%$), and the systematic error for the target thickness $\sim 1\%$. These systematic errors will be discussed in more detail below. These systematic uncertainties are added in quadrature to the statistical errors to obtain the error in the inclusive cross sections of the nuclei of interest.

5.2.1.1 N_f

The number of residues of interest, N_f, from Eq. 5.1 can be determined by first measuring the number of observed fragment residues (see Eq. 5.2), for the data collection runs combined, by creating a logic gate on the particle of interest in the 2D PID spectrum in the S800 described in Section 4.2.5 and another logic gate on the incident beam particle. Therefore, the total number of observed particle of interest, N_{obs}^R value, can be determined.

Since the N_{obs}^R value was measured from the S800 only events, the dead time comes from the S800 trigger only (see Section 3.3). The dead time was corrected using the correction factor C_{live} for reacted runs, defined as

$$C_{live} = \frac{S800\ trigger\ events(from\ data)}{S800\ trigger\ events(from\ scaler)}. \tag{5.6}$$

Due to the limited acceptance angle of the S800 spectrograph, there was some loss of counts that appear as clipping the edges of the parallel momentum distribution spectrum (d_{ta}) (Fig. 5.10). The acceptance for the reacted runs A is calculated as the ratio number of particles passing through and reaching the focal plane (events in the histogram) and the number of true events (determined by a Gaussian fit)

(Fig. 5.10). The systematic uncertainty in A derives from the uncertainty in the fit used to extract the missing intensity and the parameters used in that fit.

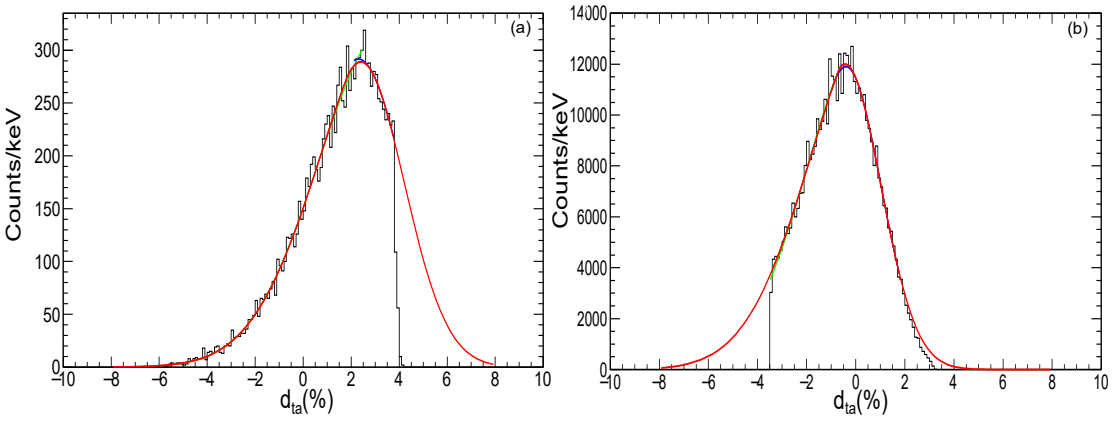

Figure 5.10: Spectra of the parallel momentum distribution, d_{ta} against the number of counts, gated on the (a) incoming ^{49}Fe beam and outgoing ^{48}Fe recoil and (b) incoming ^{49}V beam and outgoing ^{48}Ti recoil. These spectra show quite a substantial loss of counts due to the limited acceptance angle of the S800 spectrograph. Since the spectra are asymmetric, a Gaussian fit was applied separately to the right-hand side (blue line) and the left-hand side (green line) of the histogram, while the red fit considered the total number of events, including the missing part, to correct the acceptance of the residue, A.

5.2.1.2 N_i

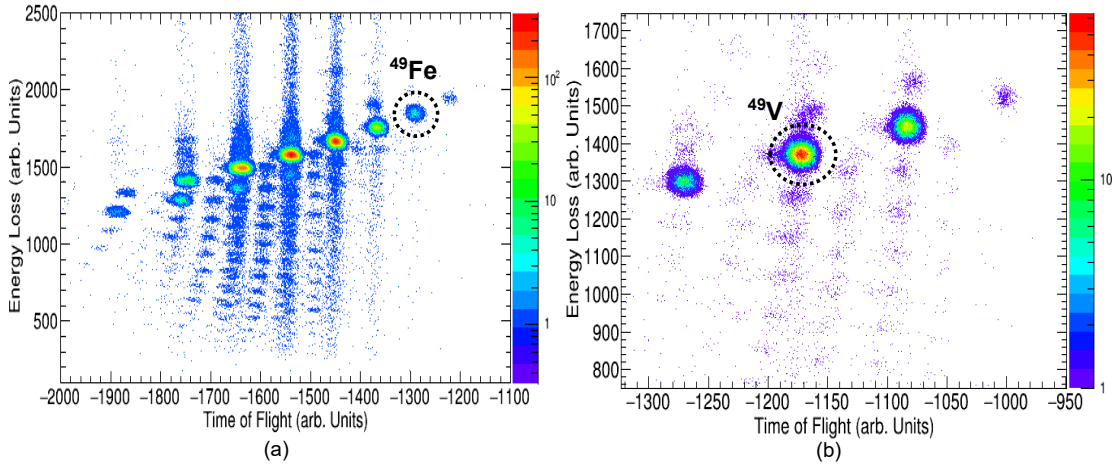

Figure 5.11: The particle identification spectra of the ^{49}Fe and ^{49}V secondary beams from the unreacted beam runs. The particle identification gates used in the ^{49}Fe and ^{49}V unreacted beam runs are shown.

Four normalisation runs were performed for ^{49}Fe and one run for ^{49}V, see Table 3.1, and these unreacted beam runs were averaged to account for any small modifications in beam consistency and detector degradation throughout the reaction data runs.

The total number of observed particles of the unreacted beam, N^u_{obs}, was determined, as described in Section 5.2.1.1, and Fig. 5.11. The C_{live} for unreacted beam runs was determined using a different method since only the S800 triggers were used for this part of the experiment. Hence, the C_{live} for the unreacted runs is simply the ratio of the live trigger to the raw trigger as measured by the scalers. The acceptance for the unreacted beam runs A was essentially 100% since the slits do not interfere in the unreacted beam, and hence, the d_{ta} spectrum has no cut-off.

5.2.1.3 Systematic Errors

During the experiment, beam purity was naturally subject to fluctuations. To consider the systematic effects of purity, the total experimental run time for the reaction data was divided into ten-run blocks on either side of the four unreacted beam runs, yielding a total of 40 runs. The determination of N^R_{obs} was performed on these 40 runs combined (all of the reaction runs). To find the systematic error on the purity as a function of the time, the ratio of the number of events from the PID gate of the residue N^R_{obs} to the total beam scalers for 20 pairs of runs was determined. This provides a good indication of the systematic error in the purity. The fractional systematic errors in the purity were determined from this and estimated to be approximately 17% (Fig. 5.12). Since ^{48}Ti was only one run and was followed by the unreacted beam run (Table 3.1), the systematic error in the purity was estimated from Fig. 5.12 by looking at the change from one run to the next run, estimated to be 8%.

The systematic error is also associated with how the logical PID gate is drawn around the nucleus of interest. The change in the size of the gate slightly affects the number of observed particles created from the S800 events. This yields an

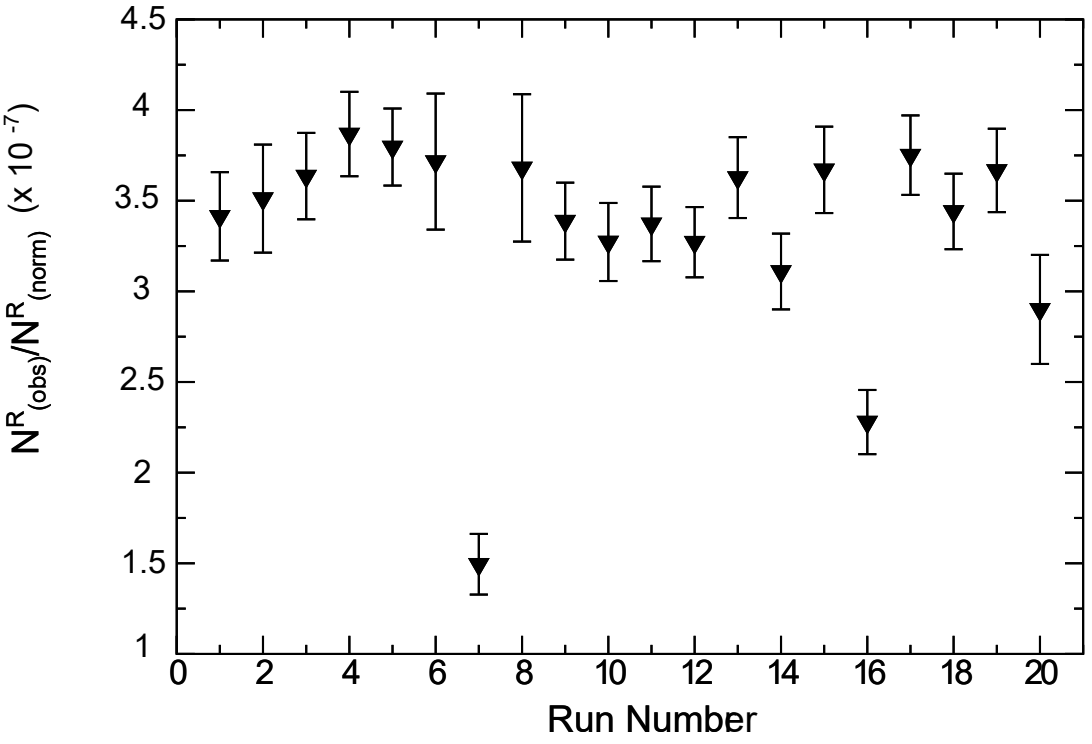

Figure 5.12: Change in the purity from one run to the next as a function of the run number.

estimated $\sim 0.4\%$ error.

5.2.1.4 Inclusive Reaction Analysis

The values that were used to determine the cross sections are shown in Tables 5.2 and 5.3.

Table 5.2: The data for the ^{48}Fe and ^{48}Ti residues in reacted beam runs. The correction factor C_{live}, the total particle detection efficiency ϵ, downscaler factor Ds, the number of observed residue N^R_{obs}, and the acceptance for the reacted runs A calculations are described in Section 5.2.1.1.

Reacted Beam	C_{live}	ϵ	Ds	N^R_{obs}	A
^{48}Fe	0.89	0.98	1	4265	0.85
^{48}Ti	0.82	0.95	3	207492	0.89

Table 5.3: The data for the ^{49}V and ^{49}Fe secondary unreacted beam runs. The live-time correction factor C_{live}, the total particle detection efficiency ϵ, downscaler factor and the unreacted beam normalisation rate K_{norm}, downscaler factor Ds, the number of observed bean particle N^u_{obs} and the acceptance for the unreacted runs A calculations are described in Section 5.2.1.2.

Unreacted Beam	C_{live}	ϵ	K_{norm}	Ds	N^u_{obs}	A
^{49}Fe	0.76	0.99	4708	1	8669	1
^{49}V	0.77	0.99	4496	1	161531	1

Following the methods described above, N_f and N_i values are calculated using the information provided in the Tables 5.2 and 5.3, and applying Eq. 5.1, the experimental inclusive cross sections for the mirror reaction ^{49}Fe to ^{48}Fe and ^{49}V to ^{48}Ti are measured (Table 5.4). A large difference (a factor ~ 9) between the cross sections for the two mirrored reactions were observed and interpreted in terms of different degrees of binding energies in the mirror nuclei (see Sections 6.1.2 and 6.3.1 for a full discussion).

Table 5.4: The experimental inclusive cross section for the two reactions ^{49}Fe $\rightarrow$ ^{48}Fe and ^{49}V $\rightarrow$ ^{48}Ti determined from the number of measured particles in the A1900 separator and S800 spectrometer.

Residue	σ_{inc}(mb)	Error(mb)
^{48}Fe	8.4	± 0.2(stat.) ± 1.5(sys.)
^{48}Ti	74.4	± 0.4(stat.) ± 6.2(sys.)

5.2.2 Exclusive Cross-Sections Analysis

The partial cross section is a measure of the probability of removing a single nucleon (proton/neutron) from the ground state of the projectile to a specific state in the residue. The experimental exclusive cross sections, σ_{exc} (each individual state), have been determined for both members of the mirror pair ^{48}Fe/^{48}Ti for both of the ground and excited states. The net population of an excited state, i, (N_i^{pop}), i.e., how many events were measured in which that state was directly populated, is determined directly from the associated γ-ray intensities by taking the sum of all observed decay intensities of the γ rays from the state, then subtracting the sum over all intensities of the γ rays feeding directly into the state. All gamma-ray intensities are corrected individually for the GRETINA efficiency Lorentz boost. Each detected γ-ray event corresponds to a COINC trigger event (see Section 3.3). Since the COINC trigger was not downscaled, the factor Ds was not included in any calculations related to the γ-ray events.

Once N_i^{pop} has been determined, the ratio of this value to the observed number of recoils of interest, N_{obs}^R (see Section 5.2.1.1) will provide a fraction of the inclusive cross section that goes to that specific state. There are additional corrections that are necessary to be included in this analysis. These corrections involved the live time of the DAQ system due to the different dead times for the two different types of events (S800 trigger only and COINC trigger) and for the S800 downscaler, Ds. All these can be represented by the following expression

$$\sigma_{exc}(i) = \left(\frac{N_i^{pop}}{N_{obs}^R \; Ds} \cdot \frac{C_{live}^{S800}}{C_{live}^{COINC}} \right) \sigma_{inc}, \tag{5.7}$$

where C_{live}^{S800} and C_{live}^{COINC} are the S800 trigger and COINC trigger live time corrections that were determined separately for S800 single events and COINC events, respectively. The C_{live}^{S800} is the same as that obtained from Eq. 5.6, and C_{live}^{COINC} was measured as the ratio of the COINC trigger events from data to those from the scaler data.

Unlike the excited states, the ground state does not have any associated γ-ray

emission tag, so after calculating the population of the excited states, the cross section to populate the ground state of the residue directly in the reaction was found as

$$\sigma_{GS} = \sigma_{inc} - \sum_i \sigma_{exc(i)}, \tag{5.8}$$

where $\sigma_{exc(i)}$ is summed over all observed excited state cross sections and is subtracted from the total inclusive cross section σ_{inc} (Table 5.4).

The resulting experimental exclusive cross sections for the excited and ground states of ^{48}Fe and ^{48}Ti resulting from one-neutron/one-proton knockout from the ^{49}Fe and ^{49}V ground state, respectively, are shown in Table 5.5. In both mirror nuclei, for all the positive-parity states observed, 2^+, 4^+, and 6^+, both the yrast and yrare states relative cross sections are measured, as well as the population of the analogue states of the negative-parity states. Figs. 5.13 (a) and (b) show the relative cross section for each state ($\sigma_{exc}/\sigma_{inc}$) in both mirror nuclei. The sum of the statistical and systematic uncertainties was determined, where the statistical uncertainties from the efficiency-corrected γ-ray intensities and observed γ-ray feeding dominate. The strong direct population of the yrare states is evident. Further details will be provided in Sections 6.1.2 and 6.3.1.

However, there are a number of differences, particularly regarding the observed strengths of the ground state and the yrast states such as 2^+_1, 4^+_1, and 6^+_1 (Figs. 5.13 (a) and (b)), and this will be discussed in detail in Section 6.3.1.

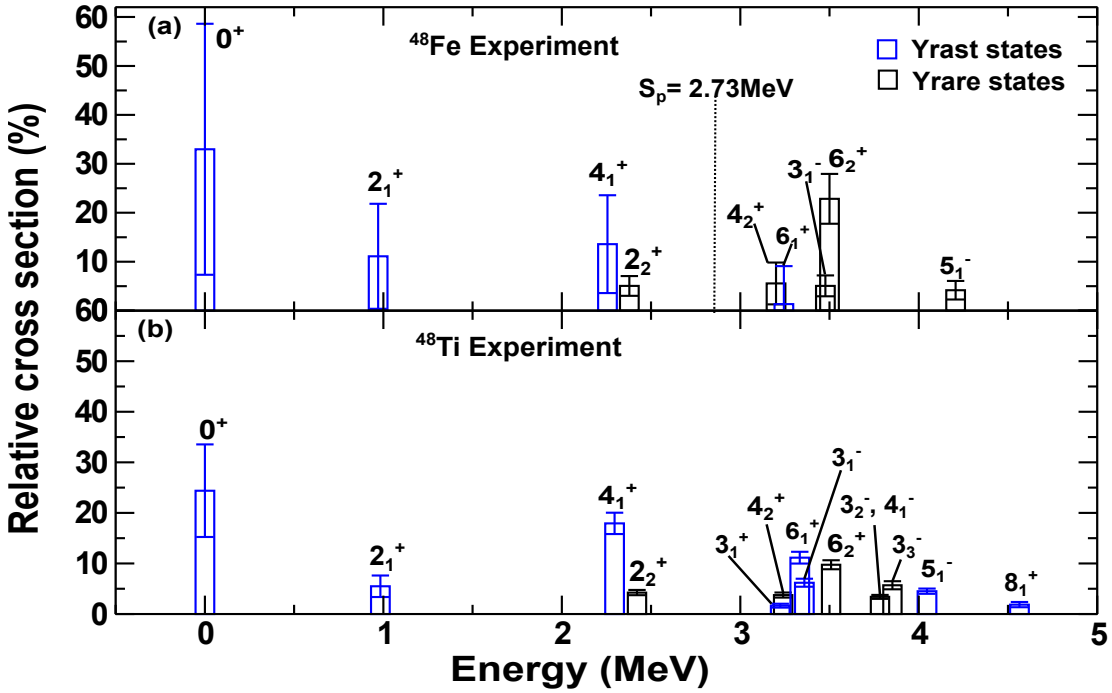

Figure 5.13: The measured relative cross sections to states in (a) ^{48}Fe and (b) ^{48}Ti via one-neutron and one-proton knockout, respectively. The sum of the statistical and systematic uncertainties are given.

Table 5.5: The experimental exclusive cross sections for states directly populated in this work through one-nucleon knockout, see text for details.

J_i^π	^{48}Fe σ_{exc}(mb)	^{48}Ti σ_{exc}(mb)
0^+	3(2)	18(7)
2_1^+	0.9(9)	4(2)
4_1^+	1.1(8)	13(2)
2_2^+	0.4(2)	3.2(4)
3_1^+		1.2(3)
4_2^+	0.5(4)	2.8(4)
6_1^+	0.1(6)	8.3(9)
3_1^-	0.4(2)	4.6(6)
6_2^+	1.9(4)	7.2(7)
$3_2^-, 4_1^-$		2.5(3)
3_3^-		4.2(6)
5_1^-	0.3(2)	3.4(4)
8_1^+		1.4(4)
inclusive	8(2)	74(6)

5.3 Mirror Energy Differences of ^{48}Fe/^{48}Ti

After the level schemes were established for ^{48}Fe and ^{48}Ti, the experimental MED were extracted by comparing the excitation energies for the analogue states in the mirror nuclei ^{48}Fe and ^{48}Ti using Eq. 2.7. All positive-parity states were observed

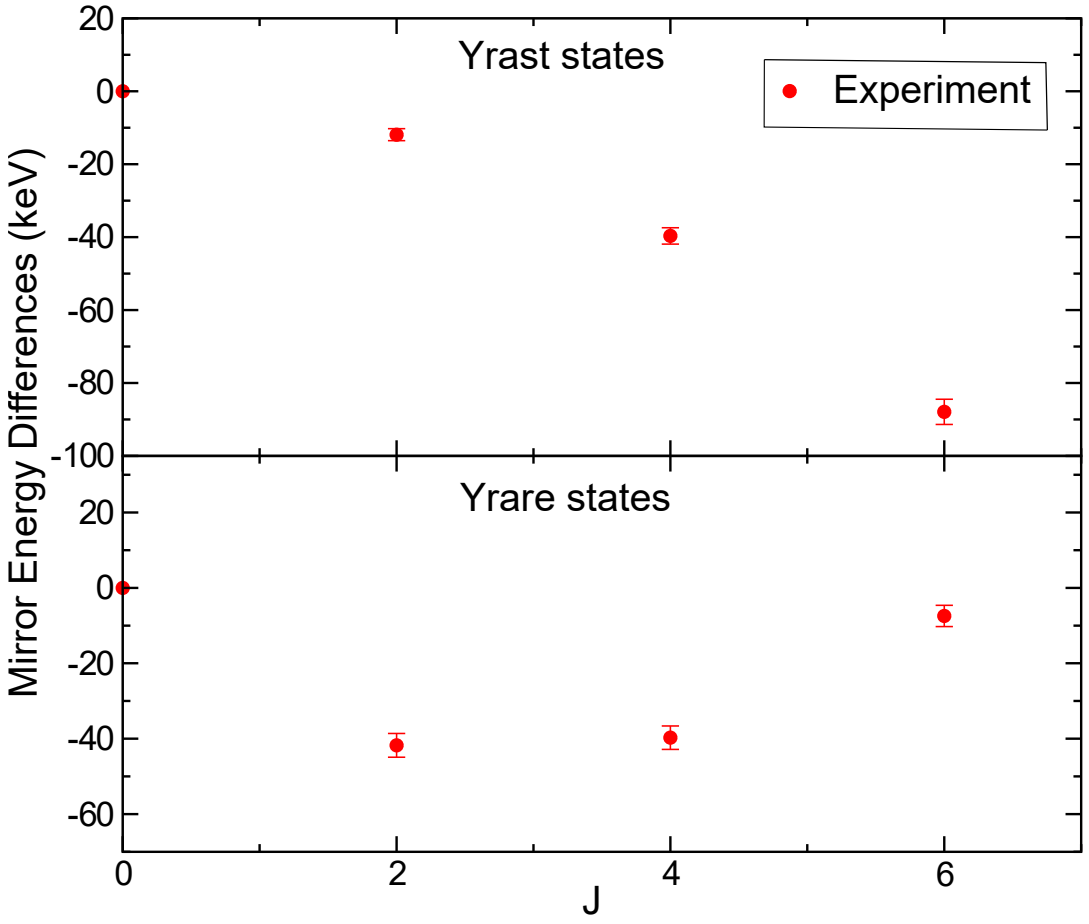

Figure 5.14: Experimental MED for the $A = 48$, $T_z = \pm 2$ mirror pair that were measured using Eq. 2.7. The MED for the $J \neq 0$ yrare states in (b) are plotted relative to the $J = 0$ ground state.

(the yrast and yrare states) in both mirror nuclei, allowing the performance of an MED analysis of both types of state (Fig. 5.14). To interpret these data, large-scale shell-model calculations using the ANTOINE code [43] were performed for the ^{48}Fe and ^{48}Ti mirror pair. Using the full fp valence space and the KB3G interaction [45], details of the results of these calculations will be provided in Chapter 7, as well as comparing this calculation with the experimental MED result.

5.4 The $A = 45, T_z = \pm\frac{1}{2}$ mirror pair

The well-studied mirror nuclei ^{45}V ($T_z = -\frac{1}{2}$) and ^{45}Ti ($T_z = +\frac{1}{2}$) [89] were also populated in this work via mirrored one-nucleon knockout reactions from both the ground state, $J^\pi = 0^+$, and from the high-spin isomeric state, $J^\pi = 3^+$, $T_{\frac{1}{2}} = 1.02$ ms, of the $N = Z$ ^{46}V secondary beam ($T_z = +1$). It is possible to produce radioactive nuclei in high-spin isomeric states in fragmentation reactions at relativistic velocities (e.g. [90]). A method of knockout reaction on an isomeric beam was first performed by S. Milne *et al.* [91] who performed an initial study of a beam of radioactive ^{53}Co in a high-spin isomeric state.

The ^{46}V secondary beam was produced from which mirrored one-nucleon knockout reactions occurred to populate states in the mirror nuclei $A = 45$. The resulting reaction products were identified in S800 where the particle identification plots of ^{45}V and ^{45}Ti gating on the secondary beam ^{46}V are demonstrated in Figs. 4.12 and 4.13. All the γ-ray transitions observed have been previously assigned to ^{45}V and ^{45}Ti via a fusion-evaporation reaction [89].

It is important to note that the analysis performed for the mirror nuclei $A = 45$ is still ongoing due to the complexity of the analysis, and the analysis in this thesis is restricted to comparison of inclusive cross sections in the $A = 45$ mirror pair.

5.4.1 Spectroscopy of ^{45}V/^{45}Ti Mirror Nuclei

The Doppler-corrected γ-ray spectra for ^{45}V and ^{45}Ti produced in this work, populated via direct one-neutron and one-proton knockout from ^{46}V, are presented in Fig. 5.15. All the labelled transitions could be identified with known γ-ray decays [89]. The β values of 0.386 and 0.380 were used to optimise the γ-ray spectra (Figs. 5.15 (a) and (b), respectively) to attain the best resolution for the observed transitions.

The one-nucleon knockout from fp orbitals from the 0^+ ground state of ^{46}V can populate negative-parity states up to $J^\pi = 7/2^-$. On the other hand, the one-

neutron knockout reaction, from the 3^+ isomer state in ^{46}V, can populate negative-parity states up to J^π=$13/2^-$ in both mirror nuclei ^{45}V and ^{45}Ti. Similarly, positive-parity states up to J^π=$5/2^+$ or up to J^π=$11/2^+$ can be populated directly through knockout from the 0^+ ground state or from the 3^+ isomer, respectively, through removal of *sd* orbitals. In this work, the maximum negative-parity states were observed up J^π=$13/2^-$ in both mirror nuclei and the positive-parity states were observed up to J^π=$11/2^+$ in ^{45}Ti and J^π=$13/2^+$ in ^{45}V. The strongest γ-ray peaks were observed in the spectra, with the one-to-one correspondence between the mirrored transitions highlighted using the dashed lines.

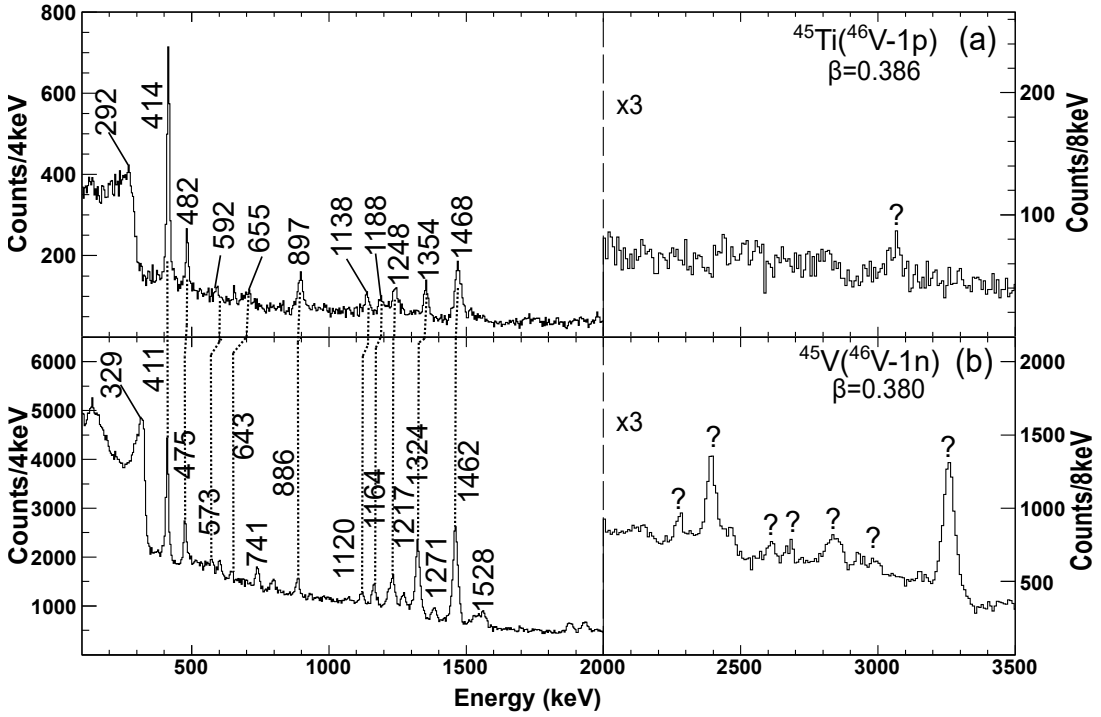

Figure 5.15: The Doppler-corrected spectra for (a) ^{45}Ti and (b) ^{45}V identified following one-nucleon knockout from ^{46}V. The $\beta = v/c$ values utilised in (a) 0.386 and (b) 0.380 were chosen to optimise the γ-ray spectra to acquire the best resolution for the observed transitions. A number of the new γ rays were observed at high energy and require further analysis to assign these transitions.

A number of the new γ rays were observed at high energies (Figs. 5.15 (a) and (b)). However, further analysis is required to assign these transitions. A detailed understanding of how these unknown transitions in ^{45}V and ^{45}Ti are being populated and the mechanism of this process, is essential for understanding the

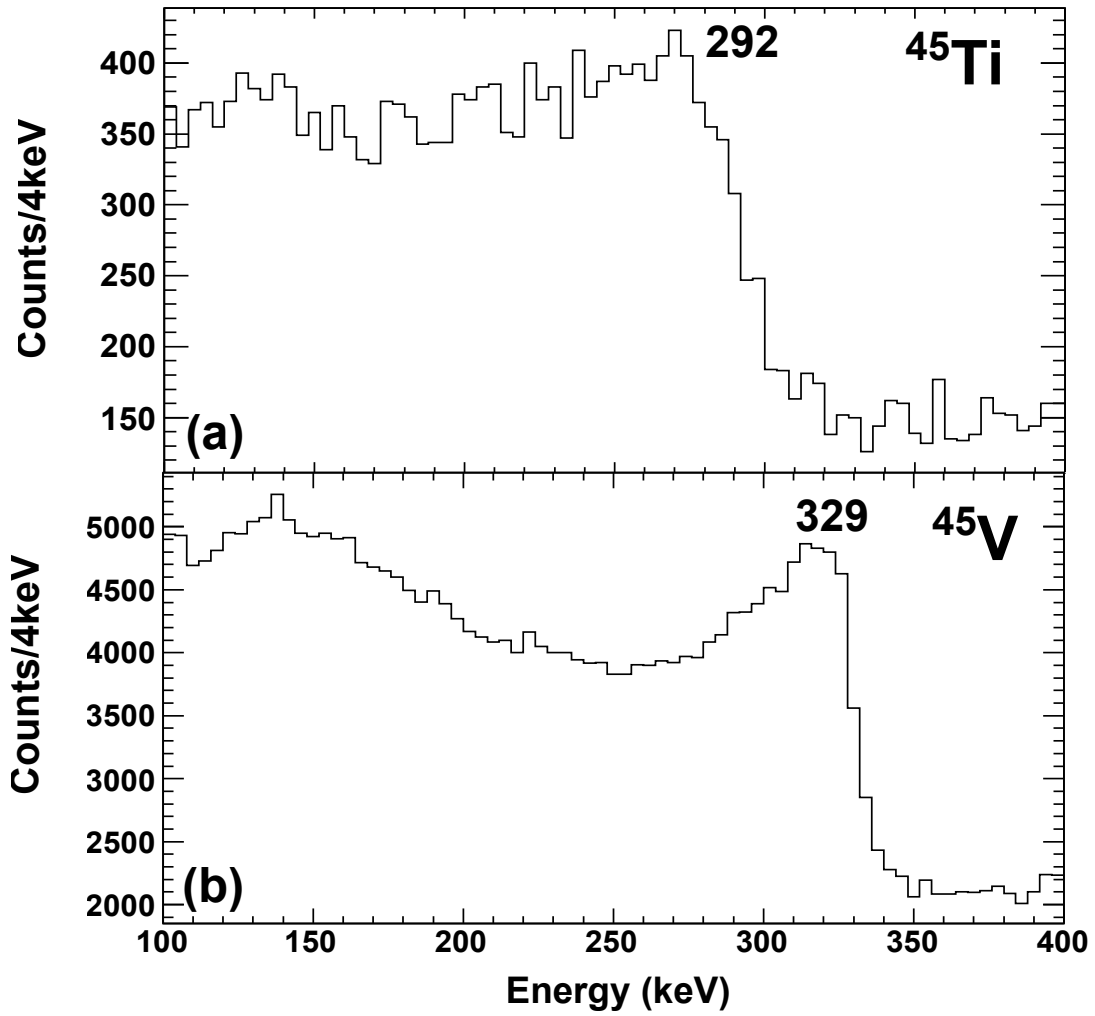

Figure 5.16: A large γ-ray peak at (a) 292 keV and (b) 329 keV in ^{45}Ti and ^{45}V Doppler-corrected spectra, respectively, associated with the decay of states with a long lifetime.

analogue knockout process.

It is worth noting that there are large γ-ray peaks at 329 keV and 292 keV in ^{45}V and ^{45}Ti spectra, respectively, which are associated with the decay of states with a long lifetime Fig. 5.16. The $\frac{3}{2}^+$ state decays to $\frac{3}{2}^-$ state by 292 keV in ^{45}Ti and 329 keV in ^{45}V. This is consistent with the fact that the 292 keV, J^π=3/2$^+$ state in ^{45}Ti is known to have a long half-life of $\sim$ 1.1 ns (taken from ENSDF [92]), which will decay downstream of the target (1 ns corresponds to approximately $\sim$ 10 cm

flight path). Consequently, the Doppler correction was incorrectly applied due to the decay at a different angle. The angle used for calculation is smaller than the real angle when the nucleus decays, causing the left tail to appear. The decay from the $3/2^+$ state to the $3/2^-$ state is a mixed $E1$ and $M2$ transition in ^{45}Ti, although the $M2$ in ^{45}Ti is known as very weak. If the equivalent transition in ^{45}V, 329 keV, is assumed to decay with the same $E1$ transition strength (based on the mirror symmetry arguments), the half-life of the $3/2^+$ in the ^{45}V would be $\sim$ 700 ps. However, the $E1$ in ^{45}V appears, at first sight from Fig. 5.16 (b), to be faster than in its mirror ^{45}Ti. Further work, using simulation, is needed to extract the lifetime and intensity.

The energy-level schemes for ^{45}V and ^{45}Ti extracted from this work are shown in Fig. 5.17. Since these mirror nuclei are well known, the ordering of the transitions, spins, and parities have been assigned based on the literature [89]. Although $J^\pi = 11/2^+$ is the maximum spin that can be populated directly from *sd* orbitals, there is some evidence of decay from the $13/2^+$ observed in ^{45}V, as shown in the bottom portion of Fig. 5.17.

All the labelled γ rays observed in Figs. 5.15 (a) and (b), as well as all the energies measured in Fig. 5.17, are consistent with the findings in [89], and the latter are used in Figs. 5.15 (a) and (b) and Fig. 5.17. The widths of the arrows in Fig. 5.17 are proportional to the relative intensity of the γ-ray transitions populated from the knockout reaction in this work. The measured γ-ray energies, intensities of the γ-ray, the state energy, spin, and parity assignments are listed in Table 5.6.

Table 5.6: The excitation energy for excited states, γ-ray energies (in keV) and relative intensities measured in this work for γ decays for the ^{45}V and ^{45}Ti mirror pair.

$J_i \rightarrow J_f$	^{45}V			^{45}Ti		
	E_x	E_γ	I_γ	E_x	E_γ	I_γ
$3/2^-$	57	-	-	36	-	-
$5/2^-$	56	-	-	-	-	-
$7/2^-$	0	-	-	0	-	-
$9/2^- \rightarrow 7/2^-$	1324	1324	60(1)	1353	1354	48(5)
$11/2^- \rightarrow 7/2^-$	1462	1462	100(2)	1468	1468	100(21)
$13/2^- \rightarrow 11/2^-$	2626	1164	14(1)	2656	1188	14(6)
$3/2^+ \rightarrow 3/2^-$	386	329	-	328	292	-
$5/2^+ \rightarrow 3/2^+$	797	411	31.8(9)	743	414	115(4)
$5/2^+ \rightarrow 3/2^-$	797	741	5.5(6)	-	-	-
$5/2^+ \rightarrow 5/2^-$	797	741	5.5(6)	-	-	-
$7/2^+ \rightarrow 7/2^-$	1272	1272	10(2)	-	-	-
$7/2^+ \rightarrow 3/2^+$	1272	886	9(1)	1225	897	25(4)
$7/2^+ \rightarrow 5/2^+$	1272	475	14.1(9)	1225	482	26(3)
$9/2^+ \rightarrow 7/2^+$	1916	644	3(1)	1881	655	6(1)
$9/2^+ \rightarrow 5/2^+$	1916	1120	7(1)	1881	1138	16(8)
$11/2^+ \rightarrow 9/2^+$	2489	573	3(1)	2473	592	5(2)
$11/2^+ \rightarrow 7/2^+$	2489	1217	5(1)	2473	1248	27(14)
$13/2^+ \rightarrow 9/2^+$	3444	1528	6(1)	-	-	-

* The excitation energies of the states and γ-ray transitions in ^{45}V and ^{45}Ti were taken from [89], and the γ-ray transition at 1272 keV in ^{45}V is taken from the ENSDF [92].

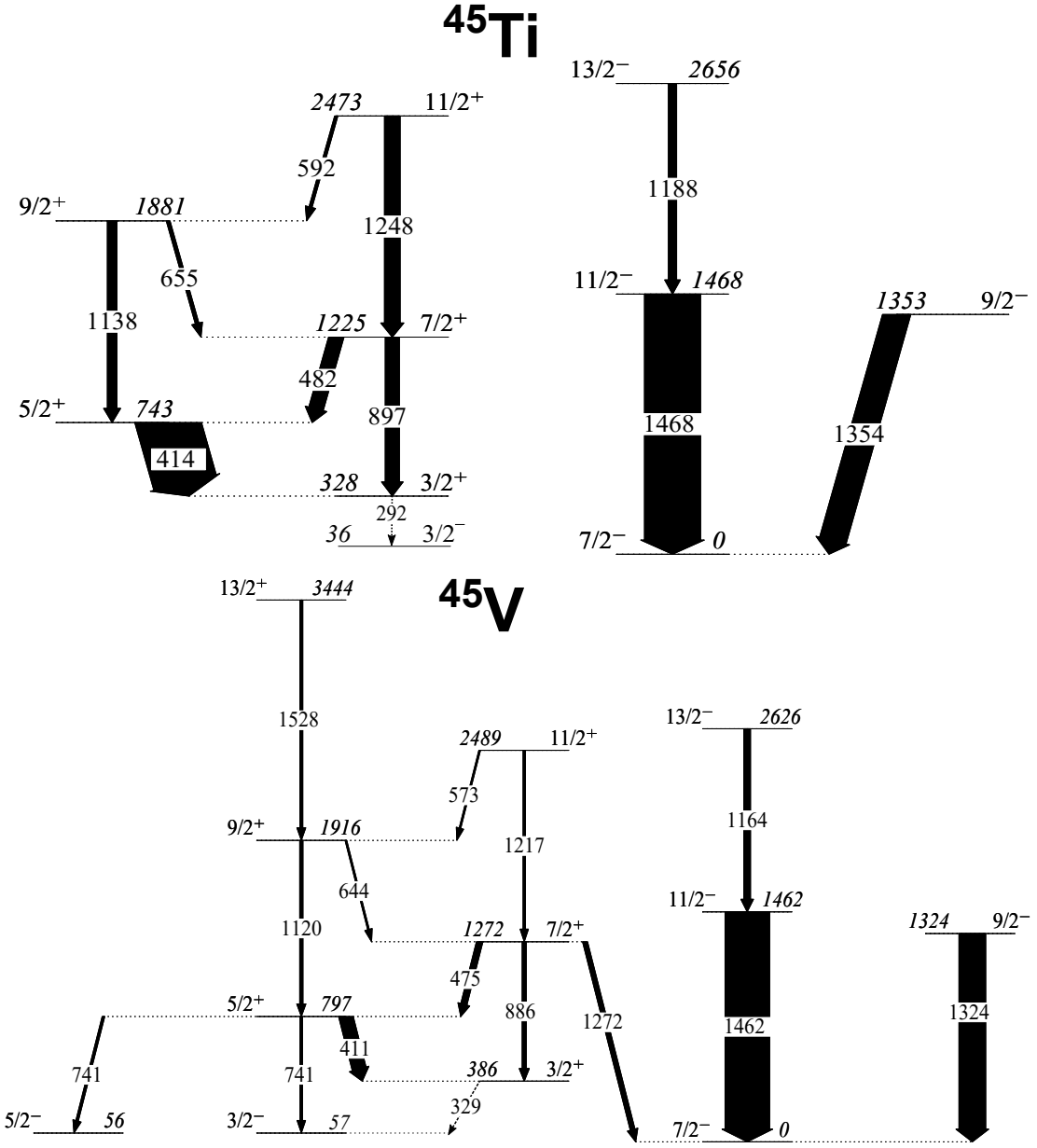

Figure 5.17: Energy level schemes for ^{45}Ti (top) and ^{45}V (bottom). Energy of states, γ-ray energies, spins and parities were assigned based on the previous study [89] and confirmed in the present work. The widths of the arrows are proportional to the relative intensity of the γ-ray transitions populated through knockout reactions and are determined relative to the intensity of the $11/2^- \rightarrow 7/2^-$ transition. For the decays of the $3/2^+$ states, the intensity is not known hence they are indicated by dashed lines.

5.4.2 Inclusive Cross-Sections of ^{46}V(−1p,−1n)^{45}Ti,^{45}V Reactions

The inclusive cross sections for the two reactions have been determined using the same technique described in Section 5.2.1. The inclusive cross sections for one-neutron removal (σ_{inc}^{1n}) and one-proton removal (σ_{inc}^{1p}) from ^{46}V to ^{45}V and ^{45}Ti, respectively, are shown in Table 5.7. A factor of ~ 9 times difference was observed between the two reactions even though the resulting residues were produced, this time, by the same parent nucleus ^{46}V. This large asymmetry of the reaction cross sections is similar to that observed in the mirror nuclei $A = 48$ (see Section 5.2.1). Theoretical cross sections for the two reactions are not determined here, as determining the isomeric ratio of the ^{46}V beam is a challenging task that is still being undertaken. Since the cross sections depend on whether the beam is in the ground state or in the isomeric state, this makes the theoretical calculation more complicated. In addition, for the strongly bound system ^{45}Ti, it is not possible to determine the theoretical inclusive cross section (see Section 6.3.2 for more details). Further work on cross-section measurements will be done in the future for these nuclei ^{45}V/^{45}Ti.

Table 5.7: The experimental inclusive cross section for the two reactions populated from the same secondary beam, ^{46}V → ^{45}V and ^{46}V → ^{45}Ti.

Residue	σ_{inc}(mb)	Error(mb)
^{45}V	13.8	± 0.03(stat.) ± 1.9(sys.)
^{45}Ti	120	± 1(stat.) ± 10(sys.)

Chapter 6

Knockout Cross Sections

The use of one-nucleon knockout reactions to populate the nuclei of interest, the $A = 48$ mirror pair, allows for a detailed cross-section analysis of the observed states populated in these nuclei. Theoretical values for the cross sections in each state of the core fragment are the product of the spectroscopic factors and the cross section of the single–neutron/proton removal reaction. Shell–model code ANTOINE [43] in the full fp space, using the KB3G interaction [45], can be implemented to identify the spectroscopic factors that depend on the orbital occupancy of each state. The cross sections for one-nucleon knockout were then computed using the spectator-core approximation, assuming eikonal reaction dynamics [54, 59, 60], as discussed in Section 2.3.2.1, as well as shell-model structure input to interpret the experimental cross sections, as presented in Chapter 5.
The methods of performing these cross-section calculations are described in Section 6.1, and the experimental data will be compared with the theoretical results for the $A = 48$, $T_z = \pm 2$ mirror pair in Section 6.2. A discussion of the results of the mirrored one-nucleon knockout analysis will also be presented in Section 6.3.

6.1 Shell-Model and Cross-Section Calculations $T_z = \pm 2$ Mirror Pair

6.1.1 Spectroscopic Factors C^2S

In order to calculate the theoretical cross sections for the mirror nuclei of interest ^{48}Fe and ^{48}Ti, the spectroscopic factors (C^2S) were calculated, as they contain all of the nuclear wave function information. The spectroscopic factor gives the probability of a particular state being populated, which informs the extent to which the final state will resemble the initial state, with a hole in a specific orbital.

The shell-model calculations could only be performed in the fp valence space, so the spectroscopic factors for one-nucleon removal from the sd shell could not be calculated from the shell model since there was no available shell-model interaction encompassing both the sd and fp regions. The calculated spectroscopic factors for both mirrored reactions, neutron removal from ^{49}Fe to ^{48}Fe and one proton from ^{49}V to ^{48}Ti, should be identical in the shell-model approach using an isoscalar interaction.

The spectroscopic factor identifies the valence orbital from which the nucleon has been removed. For instance, one-neutron (proton) knockout reactions from ^{49}Fe (^{49}V), with a ground state of $7/2^-$, whose wave function is presented in Table 6.1, are predicted to populate a range of positive-parity states in ^{48}Fe (^{48}Ti) with $J^\pi = 0^+$ to 7^+ through the removal of $f_{\frac{7}{2}}$, $p_{\frac{3}{2}}$, $f_{\frac{5}{2}}$ and $p_{\frac{1}{2}}$ neutrons (protons) near the Fermi level. However, only 0^+, 2^+, 3^+, 4^+, and 6^+ were observed in this work (Fig. 5.8). Furthermore, the negative-parity states, $J^\pi = 1^-$ to 6^-, can be populated directly through knockout from any of the more-bound sd orbitals ($d_{\frac{5}{2}}$, $s_{\frac{1}{2}}$, and $d_{\frac{3}{2}}$). However, only $J^\pi = 3^-$, 4^-, and 5^-, observed in this work.

The spectroscopic factors in the case of a one-neutron (proton) knockout reaction from parent nuclei ^{49}Fe (^{49}V), with a ground state of $7/2^-$, to the daughter nuclei ^{48}Fe (^{48}Ti) were calculated using the KB3G interaction [45]. Therefore, the KB3G

Table 6.1: The ground state of ^{49}Fe/^{49}V calculated using the ANTOINE code [43] in the full fp valence space using the KB3G interaction [45]. This table displays all the ground state admixtures greater than 1%.

^{49}Fe/^{49}V	Proton Occupation				Neutron Occupation			
Probability	$1f_{\frac{7}{2}}$	$2p_{\frac{3}{2}}$	$1f_{\frac{5}{2}}$	$2p_{\frac{1}{2}}$	$1f_{\frac{7}{2}}$	$2p_{\frac{3}{2}}$	$1f_{\frac{5}{2}}$	$2p_{\frac{1}{2}}$
0.496650	6	0	0	0	3	0	0	0
0.049650	6	0	0	0	2	1	0	0
0.015489	6	0	0	0	2	0	0	1
0.010541	6	0	0	0	1	2	0	0
0.016552	6	0	0	0	1	0	0	2
0.075591	5	1	0	0	3	0	0	0
0.026517	5	1	0	0	2	1	0	0
0.047144	5	0	0	1	3	0	0	0
0.020534	5	0	0	1	2	0	0	1
0.032311	4	2	0	0	3	0	0	0
0.014229	4	1	0	1	3	0	0	0
0.044080	4	0	0	2	3	0	0	0

interaction represents the full charge symmetric and full charge independent nature of the nuclear force.

Although the shell-model calculations predict that a lot of states are populated, the spectroscopic factors C^2S from ^{49}Fe to ^{48}Fe and ^{49}V to ^{48}Ti were calculated only for a subset of states observed, 0^+, 2^+, 3^+, 4^+ and 6^+, since only these states were observed in the mirror pair. Both yrast and yrare states were calculated. The C^2S values of the states observed (0^+, 2^+, 3^+, 4^+, and 6^+), by removing a nucleon from the $f_{\frac{7}{2}}$ orbital, were calculated. However, in the case of removing a nucleon from the $p_{\frac{3}{2}}$ orbital, only the 2^+, 3^+ and 4^+ can be populated. Similarly, on removal of a neutron from $f_{\frac{5}{2}}$ or $p_{\frac{1}{2}}$, these yield only 2^+, 3^+, 4^+ and 6^+ states or 3^+ and 4^+ states, respectively. It is worth noting that, in the case of ^{48}Ti, a 3^+ state was observed as a result of removing a proton from fp valence

Table 6.2: C^2S of $A = 48$ mirror nuclei in the full fp valence space was calculated using the ANTOINE code [43] using the KB3G interaction [45].

	C^2S			
J^π	$1f_{\frac{7}{2}}$	$2p_{\frac{3}{2}}$	$1f_{\frac{5}{2}}$	$2p_{\frac{1}{2}}$
0^+	0.513			
2_1^+	0.001	0.015	0.014	
2_2^+	0.358	0.004	0.006	
4_1^+	0.355	0.016	0.002	0.002
4_2^+	0.181	0.009	0.004	0.002
6_1^+	0.127		0.000	
6_2^+	0.724		0.000	
3_1^+	0.000	0.032	0.002	0.000
Summed: C^2S	**2.260**	**0.076**	**0.004**	**0.028**
Summed: C^2S $for\ all fp$				2.367

space in the ^{49}V (Fig. 5.8). Thus, the C^2S for this state was also calculated. The results of these calculations are shown in the Table 6.2. As the table illustrates, C^2S values are very small ($<< 1$), except for the $f_{\frac{7}{2}}$ orbital. This is expected since if removing one nucleon from the $p_{\frac{3}{2}}$ orbital, for example, this orbital is above the Fermi level. Therefore, the probability of removing a particle from that orbital is quite low, see Table 6.1.

6.1.2 Theoretical Reaction Cross Sections

For each of the deduced excited states in the residual core nuclei, ^{48}Fe and ^{48}Ti, the single-particle cross sections (σ_{sp}) must be calculated using eikonal approximation reaction dynamics [54, 59, 60] (described in Chapter 2). The reaction-model calculations enable the single-particle cross sections for one-nucleon (proton or neutron) removal (σ_{sp}) from each of the single-particle levels in the fp shell to be determined. The single-particle cross section represents the probability of re-

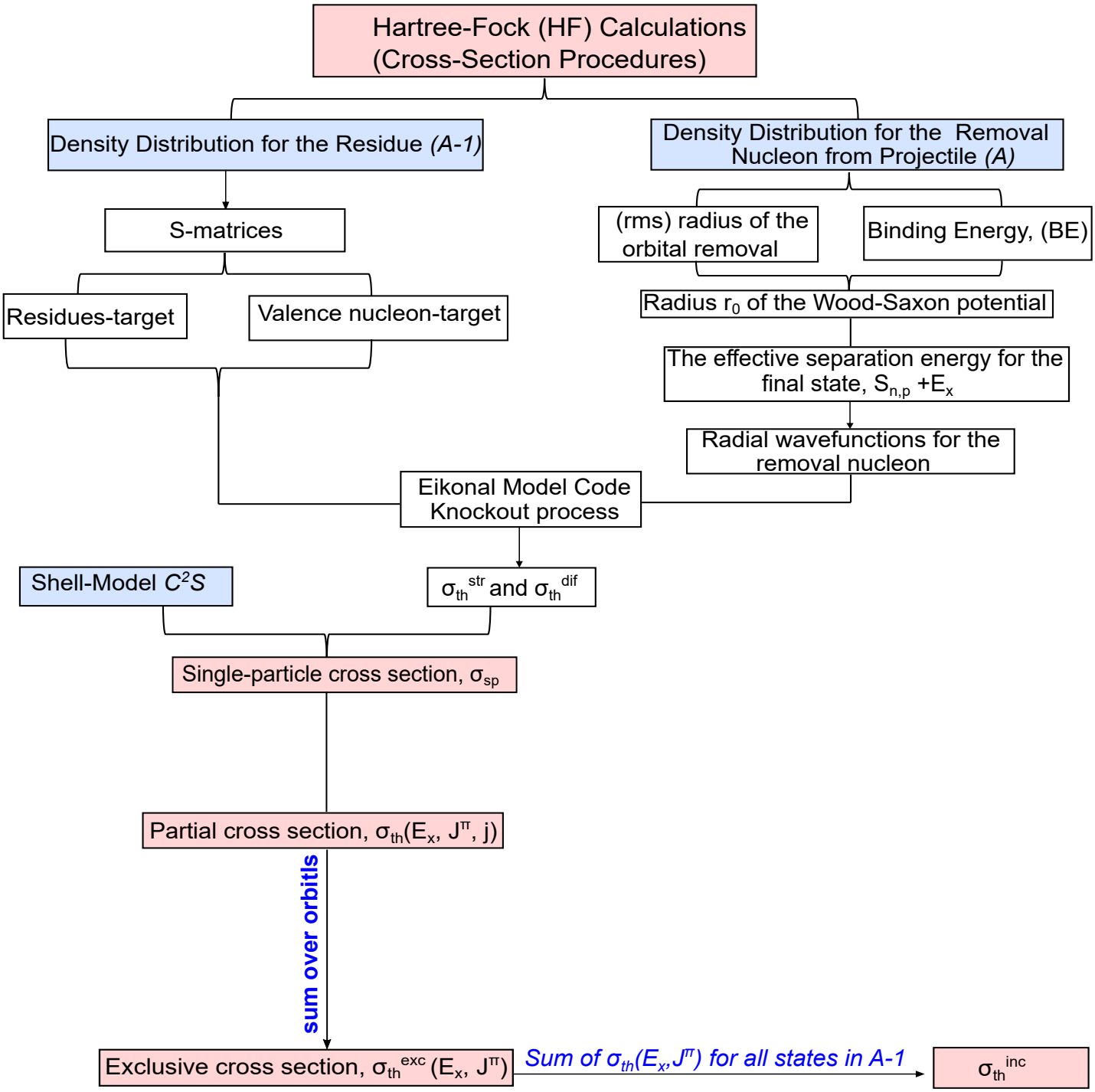

Figure 6.1: A flowchart of the procedure for calculating the nucleon removal cross sections from the projectile.

moving a nucleon from a single-particle orbit, assuming that precisely one single nucleon occupies that state.

The single-particle cross section σ_{sp} is the sum of contributions from both the stripping mechanism and the diffractive breakup mechanism, $\sigma_{sp}^{str} + \sigma_{sp}^{dif}$ (explained in Chapter 2). These stripping and diffractive contributions are computed separately from the residue-target and nucleon-target elastic eikonal scattering matrices [55]. A reaction dynamics code (J. Tostevin [55, 93]) was used to calculate the partial production cross section (single particle) for that orbital for the energy of the final state. The theoretical partial cross sections for the removal of a nucleon from a specific orbital (j) from the projectile A, $\sigma_{th}(E_x, J^\pi, j)$, populating the final state of the mass $A-1$ is calculated using Eq. 2.19, reproduced again below

$$\sigma_{th}(E_x, J^\pi, j) = \left(\frac{A}{A-1}\right)^N C^2 S_{SM}(j) \sigma_{sp}(j, S_n + E_x), \tag{6.1}$$

where j is the angular momentum of the orbital from which the particle is removed. For each final state, the total theoretical exclusive cross section, $\sigma_{th}^{exc}(E_x, J^\pi)$, was calculated as the sum of all the possible removal paths (all possible orbitals for that reaction i.e., the sum of Eq. 6.1), see Eq. 6.2. Then, the theoretical inclusive nucleon-removal cross section, σ_{th}^{inc}, is calculated as the sum of all theoretical exclusive cross sections for all populated states in the residue (i.e., the sum of $\sigma_{th}^{exc}(E_x, J^\pi)$ for all the possible orbitals for the removed nucleon).

$$\sigma_{th}^{exc}(E_x, J^\pi) = \sum_j \sigma_{th}(E_x, J^\pi, j) \tag{6.2}$$

A flowchart in Fig. 6.1 illustrates the process for calculating one nucleon removal exclusive cross section (discussed above). A number of inputs must be taken into account for calculating the theoretical cross section [25] for each state. These are summarised as

1. C^2S values obtained from shell-model calculations (as discussed in Section 6.1.1).

2. Complex optical potentials of residue-target and valence nucleon-target and their elastic scattering S matrices, which enter the eikonal model, affect the parameter integrals of σ_{sp}^{str} and σ_{sp}^{dif} and localise the reactions spatially.

3. The geometries of the radial wave functions for the removed nucleons in the projectile ground state is determined. The Hartree-Fock (HF) calculations of neutron and proton densities for the residues and the root-mean-squared (rms) radii of orbitals in the HF mean field were used in order to constrain the shapes and radial size parameters for inputs (2) and (3) [26].

As listed above, the calculation was achieved by computing the density distribution of the residue and projectile using the SkX interaction Skyrme Hartree-HF calculations of [94]. The target ^{9}Be matter was assumed to have a Gaussian nucleon density with an rms radius of 2.36 fm, and that can be used as input to calculate the radial wave function later.

Based on the assumption that the residue (core) and the valence nucleon are separate, they approach and interact with the target separately. Therefore, the elastic scattering S-matrices [64, 65] for the interaction of the residue-target (^{48}Fe(^{48}Ti)-^{9}Be) and the valence nucleon-target (neutron(proton)-^{9}Be) system were calculated separately. The secondary beam energies (MeV/u), from the centre of the reaction target, were required for calculating the S-matrices; the mid-target beam energies were found to be 80.1 MeV/u for ^{49}Fe and 83.8 MeV/u for ^{49}V, which were calculated through the use of LISE^{++} [95].

The purpose of this calculation was to determine elastic and reaction cross sections for both the target core and the neutron/proton-target separately. The outputs of these calculations were subsequently used for the knockout process. The probability of knockout depends on the probability of the core surviving the reaction (elastically scattered), and the valence nucleon is absorbed by the target (i.e. reacting), see Section 2.3.2.1. In the next part of the calculation, the binding potential of the removal nucleon can be constrained using HF calculations by computing the density distribution for the projectile as a whole. As a result, an HF radius and the

binding energy for each orbital were produced (Tables 6.3 and 6.4). These tables show different radii and binding energies (highlighted in blue) for the neutron and proton removal from ^{49}Fe and ^{49}V, respectively, from the fp orbitals used in the single-single nucleon cross-section calculations of each state in the ^{48}Fe and ^{48}Ti. It should be noted that all the above calculations are independent of the final state in the residue.

Table 6.3: Hartree-Fock neutron single-particle radii (rms) and energies for each orbital of ^{49}Fe projectile, where the fp orbitals (highlighted in blue) were used in the single-nucleon cross-section calculations.

k	n	l	J	r(2)(fm)	Energy/MeV
1	1	s	1 / 2	2.623	-42.520
2	1	p	3 / 2	3.199	-34.205
3	1	p	1 / 2	3.107	-32.015
4	1	d	5 / 2	3.644	-24.954
5	1	d	3 / 2	3.586	-20.237
6	2	s	1 / 2	3.558	-20.525
7	1	f	7 / 2	3.997	-14.965
8	1	f	5 / 2	4.095	-7.821
9	2	p	3 / 2	3.998	-10.173
10	2	p	1 / 2	4.152	-8.552
11	1	g	9 / 2	4.343	-4.177
12	1	g	7 / 2	4.514	-0.200
13	2	d	5 / 2	5.852	-0.200
14	2	d	3 / 2	5.885	-0.200
15	3	s	1 / 2	9.110	-0.200

Table 6.4: Hartree-Fock proton single-particle radii (rms) and energies for each orbital of ^{49}V projectile, where the fp orbitals (highlighted in blue) were used in the single-nucleon cross-section calculations.

k	n	l	J	r(2)(fm)	Energy/MeV
1	1	s	1 / 2	2.651	-34.000
2	1	p	3 / 2	3.229	-25.795
3	1	p	1 / 2	3.138	-23.540
4	1	d	5 / 2	3.680	-16.670
5	1	d	3 / 2	3.636	-11.869
6	2	s	1 / 2	3.622	-12.120
7	1	f	7 / 2	4.048	-6.844
8	1	f	5 / 2	4.193	-0.200
9	2	p	3 / 2	4.194	-2.098
10	2	p	1 / 2	4.426	-0.598
11	1	g	9 / 2	4.282	-0.200
12	1	g	7 / 2	4.205	-0.200
13	2	d	5 / 2	4.378	-0.200
14	2	d	3 / 2	4.424	-0.200
15	3	s	1 / 2	4.708	-0.200

The next step is using a Wood-Saxon plus spin-orbit potential, rather than a HF potential, to calculate the bound-state wave functions for the removed particle with constrained geometries, diffuseness $a = 0.7$ fm, and spin-orbit strength $V_{so} = 6$ MeV. Then, the radius parameter r_0 of the binding potentials was constrained by the rms radius of this orbital and binding energy, as given by the HF calculations using a Skyrme SkX interaction [94], these are shown in Table 6.5. The final step in the model is then to parameterize the reaction by adjusting the depth of the central potential to give the final states' appropriate effective binding energies ($E_x + S_{n,p}$). The excitation energy, E_x, of a given state in the residue was therefore required to calculate the corresponding single-particle cross section. The S_n and S_p separation energies of ^{49}Fe and ^{49}V are 14.813(9) MeV and 6.758(8) MeV,

respectively, (taken from the most recent mass evaluations by [96]).

Each radial wave function between the removal nucleon and the final state in the residue was then obtained to calculate the cross section for each state expected to populate in the mirror nuclei, using the eikonal S-matrices.

Table 6.5: The potential radius r_0 parameters of the nucleon removal from fp and sd (in case of ^{49}V (-1p) only) orbitals with diffuseness $a = 0.7$ fm and spin-orbit strength $V_{so} = 6$ MeV.

	^{49}Fe (-1n)	^{49}V (-1p)
orbital	r_0 (fm)	r_0(fm)
$f_{\frac{7}{2}}$	1.287	1.260
$p_{\frac{3}{2}}$	1.152	1.097
$f_{\frac{5}{2}}$	1.299	1.264
$p_{\frac{1}{2}}$	1.201	1.128
$s_{\frac{1}{2}}$	-	1.269
$d_{\frac{3}{2}}$	-	1.279
$d_{\frac{5}{2}}$	-	1.293

Table 6.6: A summary of the relevant results from the present study, where the predicted cross sections for states observed in ^{48}Fe (^{49}Fe - 1n) reaction, 0^+, 2^+, 4^+, and 6^+ states resulted from a direct neutron removal from the fp orbital in the projectile. The S_n of ^{49}Fe is 14.813(9) MeV [96], and the mass dependent, $(A/A-1)^3$, is 1.0638. The individual stripping and diffraction break-up components, as well as their summed single-particle reaction cross section, were calculated using the reaction model. The C^2S are taken from the ANTOINE [43] shell-model calculations from Table 6.2. j value is the orbital of the neutron removal from the initial state of the projectile.

Predicted Cross Sections for One-Neutron fp Removal								
E_x	$S_n + E_x$(MeV)	J^π	j	σ_{sp}^{str}(mb)	σ_{sp}^{dif}(mb)	σ_{sp}(mb)	C^2S	$\sigma_{th}(E_x, J^\pi, j)$(mb)
0.000	14.813	0^+	$1f_{\frac{7}{2}}$	2.1	7.9	10.1	0.513	5.5
0.971	15.783	2_1^+	$1f_{\frac{7}{2}}$	2.0	7.7	9.7	0.001	0.0
			$2p_{\frac{3}{2}}$	2.2	7.7	10.0	0.015	0.2
			$1f_{\frac{5}{2}}$	1.7	6.6	8.3	0.014	0.1
2.378	17.191	2_2^+	$1f_{\frac{7}{2}}$	1.9	7.3	9.2	0.358	3.5
			$2p_{\frac{3}{2}}$	2.0	7.2	9.3	0.004	0.0
			$1f_{\frac{5}{2}}$	1.6	6.4	7.9	0.006	0.0
2.255	17.068	4_1^+	$1f_{\frac{7}{2}}$	1.9	7.3	9.2	0.355	3.5
			$2p_{\frac{3}{2}}$	2.1	7.3	9.3	0.016	0.2
			$2p_{\frac{1}{2}}$	2.2	7.7	9.9	0.002	0.0
			$1f_{\frac{5}{2}}$	1.6	6.4	8.0	0.002	0.0
3.200	18.013	4_2^+	$1f_{\frac{7}{2}}$	1.8	7.1	8.9	0.181	1.7
			$2p_{\frac{3}{2}}$	1.9	7.0	8.9	0.009	0.1
			$2p_{\frac{1}{2}}$	2.1	7.4	9.5	0.002	0.0
			$1f_{\frac{5}{2}}$	1.5	6.2	7.7	0.004	0.0
3.244	18.057	6_1^+	$1f_{\frac{7}{2}}$	1.8	7.1	8.9	0.127	1.2
			$1f_{\frac{5}{2}}$	1.5	6.2	7.7	0.000	0.0
3.498	18.313	6_2^+	$1f_{\frac{7}{2}}$	1.8	7.1	8.9	0.724	6.8
			$1f_{\frac{5}{2}}$	1.5	6.1	7.7	0.000	0.0
						Total	**2.333**	**22.9**

Table 6.7: A summary of the relevant results from the present study, where the predicted cross sections for states are observed in ^{48}Ti(^{49}V - 1p) reaction, 0^+, 2^+, 3^+, 4^+ and 6^+ states as a result of a direct proton removal from the fp orbital in the projectile. The S_p of ^{49}V is 6.758(8) MeV [96] and the mass dependent, $(A/A-1)^3$, is 1.0638. The individual stripping and diffraction break-up components, as well as their summed single-particle reaction cross section, were calculated using the reaction model. The C^2S are taken from the ANTOINE [43] shell-model calculations from Table 6.2. j value is the orbital of the proton removal from the initial state of the projectile.

Predicted Cross Sections for One-Proton fp Removal								
E_x	$S_p + E_x$(MeV)	J^π	j	σ_{sp}^{str}(mb)	σ_{sp}^{dif}(mb)	σ_{sp}(mb)	C^2S	$\sigma_{th}(E_x, J^\pi, j)$(mb)
0.000	6.758	0^+	$1f_{\frac{7}{2}}$	2.6	9.6	12.2	0.513	6.7
0.983	7.741	2_1^+	$1f_{\frac{7}{2}}$	2.5	9.2	11.7	0.001	0.0
			$2p_{\frac{3}{2}}$	2.7	9.2	11.9	0.015	0.2
			$1f_{\frac{5}{2}}$	2.0	7.8	9.8	0.014	0.1
3.223	9.982	3_1^+	$1f_{\frac{7}{2}}$	2.2	8.5	10.6	0.000	0.0
			$2p_{\frac{3}{2}}$	2.3	8.1	10.4	0.032	0.4
			$2p_{\frac{1}{2}}$	2.3	8.3	10.6	0.000	0.0
			$1f_{\frac{5}{2}}$	1.8	7.2	9.0	0.002	0.0
2.421	9.179	2_2^+	$1f_{\frac{7}{2}}$	2.3	8.7	11.0	0.358	4.1
			$2p_{\frac{3}{2}}$	2.4	8.5	10.9	0.004	0.0
			$1f_{\frac{5}{2}}$	1.9	7.4	9.2	0.006	0.1
2.295	9.054	4_1^+	$1f_{\frac{7}{2}}$	2.3	8.8	11.0	0.355	4.2
			$2p_{\frac{3}{2}}$	2.4	8.5	11.0	0.016	0.2
			$2p_{\frac{1}{2}}$	2.5	8.7	11.2	0.002	0.0
			$1f_{\frac{5}{2}}$	1.9	7.5	9.3	0.002	0.0
3.239	9.998	4_2^+	$1f_{\frac{7}{2}}$	2.2	8.5	10.6	0.181	2.0
			$2p_{\frac{3}{2}}$	2.3	8.1	10.4	0.009	0.1
			$2p_{\frac{1}{2}}$	2.3	8.3	10.6	0.002	0.0
			$1f_{\frac{5}{2}}$	1.8	7.2	9.0	0.004	0.0
3.333	10.091	6_1^+	$1f_{\frac{7}{2}}$	2.1	8.4	10.6	0.127	1.4
			$1f_{\frac{5}{2}}$	1.8	7.2	9.0	0.000	0.0
3.508	10.267	6_2^+	$1f_{\frac{7}{2}}$	2.1	8.4	10.5	0.724	8.1
			$1f_{\frac{5}{2}}$	1.8	7.2	8.9	0.000	0.0
						Total	**2.367**	**27.8**

This gave the single-particle cross section that consists of stripping σ_{sp}^{str} and diffraction σ_{sp}^{dif} (as explained in Chapter 2) and the total, which is the knockout cross section. By summing up the normalised single-particle cross sections (σ_{sp}^{str} and σ_{sp}^{dif}) for each sub-shell considered, see Eq. 2.20, with C^2S calculated from the shell model as discussed in Section 6.1.1, the partial theoretical cross section (j), $\sigma_{th}(E_x, J^\pi, j)$, for populating a specific residue state was calculated using Eq. 6.1. Different single-nucleon knockout reaction calculations were carried out for different fp orbitals, with different r_0 parameters to a number of excited states in the residue, $(S_{n,p}) + E_x$. The theoretical exclusive cross section was calculated as the sum of Eq. 6.1 over all the possible j values.

The theoretical single-particle cross sections for each state populated in this study as a result of removing a neutron and a proton from fp orbital for both the ^{48}Fe(^{49}Fe - 1n) and ^{48}Ti (^{49}V - 1p) reactions using the method described above are given respectively in Tables 6.6 and 6.7 for both yrast and yrare states. The theoretical inclusive cross section for the population in all the final states of the fragment residue ^{48}Fe from the ^{49}Fe that includes all the fp orbital removal, see Table 6.6, is 22.9 mb. In this work, the inclusive cross section was calculated as the sum of all the exclusive cross sections for all the observed states, regardless of the proton separation energy. All bound states predicted by the shell model were observed in this work. The predicted exclusive cross sections for both mirror nuclei and the theoretical inclusive cross section ^{48}Fe are listed in Table 6.8. In the more bound system ^{48}Ti, however, a theoretical inclusive cross section cannot be precisely determined by utilising the usual method described above [24, 25] due to the high separation energies of the ^{48}Ti residual nucleus, which makes shell-model calculations of all bound final states impossible.

Due to the use of the shell-model space, this model can only access positive-parity states. The calculated spectroscopic factors for each member of the mirror pair are also identical within the shell-model approach (Table 6.2), resulting in similar theoretical cross sections, $\sigma_{th}^{exc}(E_x, J^\pi)$, as shown in Table 6.8. As mentioned before, due to the lack of available shell-model interaction containing the *sd* shell regions,

Table 6.8: The experimental and theoretical exclusive cross sections for states directly populated in this work through one-nucleon knockout. The inclusive cross sections are listed in the final row (the theoretical inclusive cross section could not be determined for ^{48}Ti, see text for details). The theoretical cross sections are calculated using the experimental separation- and residue-excitation energies.

J_i^π	^{48}Fe		^{48}Ti	
	σ_{exp}^{exc}(mb)	$\sigma_{th}^{exc}(E_x, J^\pi)$(mb)	σ_{exp}^{exc}(mb)	$\sigma_{th}^{exc}(E_x, J^\pi)$(mb)
0^+	3(2)	5.5	18(7)	6.7
2_1^+	0.9(9)	0.3	4(2)	0.3
4_1^+	1.1(8)	3.6	13(2)	4.4
2_2^+	0.4(2)	3.7	3.2(4)	4.3
3_1^+			1.2(3)	0.4
4_2^+	0.5(4)	1.9	2.8(4)	2.2
6_1^+	0.1(6)	1.2	8.3(9)	1.4
3_1^-	0.4(2)		4.6(6)	
6_2^+	1.9(4)	6.8	7.2(7)	8.1
$3_2^-, 4_1^-$			2.5(3)	
3_3^-			4.2(6)	
5_1^-	0.3(2)		3.4(4)	
8_1^+			1.4(4)	
inclusive	8(2)	22.9	74(6)	-

the reaction model does not predict the theoretical cross sections for negative-parity states.

6.2 Comparison of Experimental and Theoretical Data

The experimental cross sections, both inclusive σ_{inc} (summed over all states) and exclusive σ_{exc} (each individual state), are displayed in the Table 6.8. The theoretical and measured relative cross sections ($\sigma_{exc}/\sigma_{inc}$) for knockout to the ground state, and all the observed excited states in the ^{48}Fe residue are shown in Fig. 6.2. Although the theoretical exclusive cross sections are generally much larger than the absolute values of the measured exclusive cross sections (Table 6.8), there is good agreement between the distributions of relative cross sections. Some of the key observations of the experimental data, such as the strong direct population of the yrare states, are well reproduced. These observations provided additional confidence in the level scheme in Fig. 5.8. For instance, the reaction model predicted that the 6_2^+ state accumulate more intensity than the 6_1^+ state, and this was seen in the experimental data as well. It is important to note that in the proton-rich nucleus ^{48}Fe, there are a number of positive-parity states, 4_2^+, 6_1^+ and 6_2^+, that are observed to lie above the proton separation energy ($S_p = 2.731$ MeV [96]).

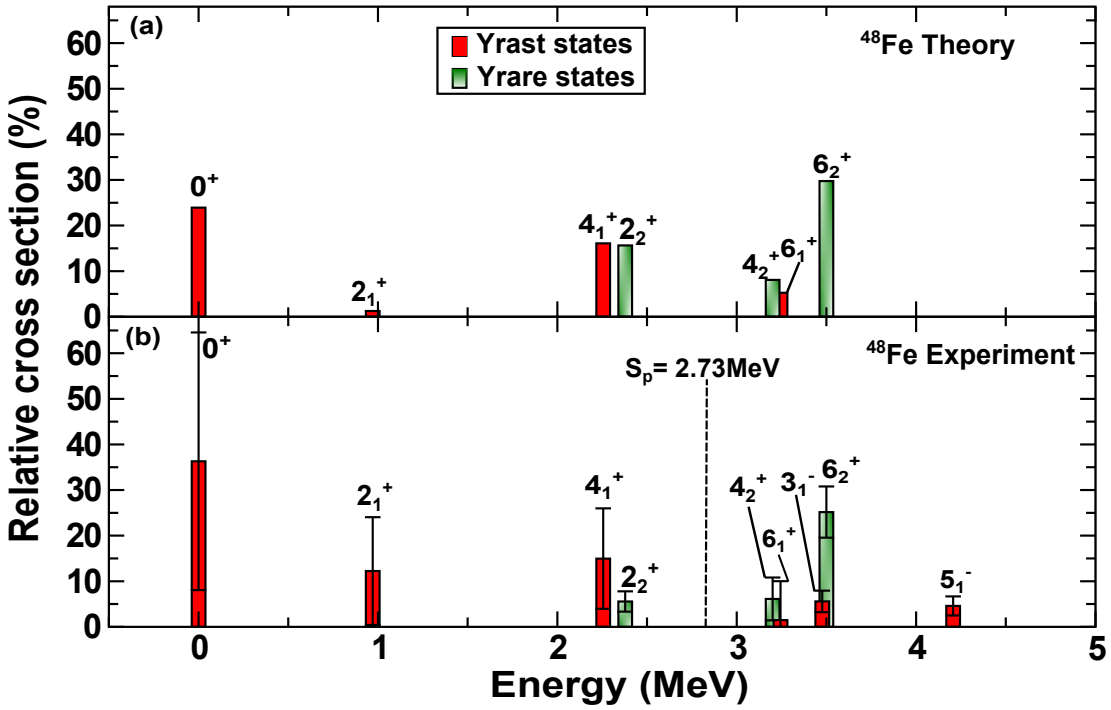

Figure 6.2: (a) Calculated and (b) experimental relative cross sections for excited states in ^{48}Fe populated via one-neutron knockout from ^{49}Fe ground state ($J^\pi = 7/2^-$). The sum of the statistical and systematic uncertainties are presented. The model-space used for (a) is limited to positive-parity states; therefore, for (b), the total experimental cross section is determined based on the positive-parity states only.

A comparison of the calculated and experimental cross sections for ^{48}Ti are shown in Fig. 6.3. As can be seen, the agreement is quite poor between the experimental data Fig. 6.3 (b) and the theoretical values (a). As will be discussed later, unseen indirect feeding for these states is the likely explanation.

Due to the much higher separation energies in ^{48}Ti, more states at higher energy can be directly populated, feeding into the low-lying states. This is discussed in more detail in 6.3.1. It is also important to note that it is possible to overestimate the cross section to the ground state if there are high-lying states populated that directly feed the ground state. This is especially likely in ^{48}Ti.

In summary, assuming symmetry between the spectroscopic factors of the mirror pair, the relative population of states in both nuclei can be understood by a direct knockout process. This indicates further confidence in the assignments of newly

identified states in ^{48}Fe.

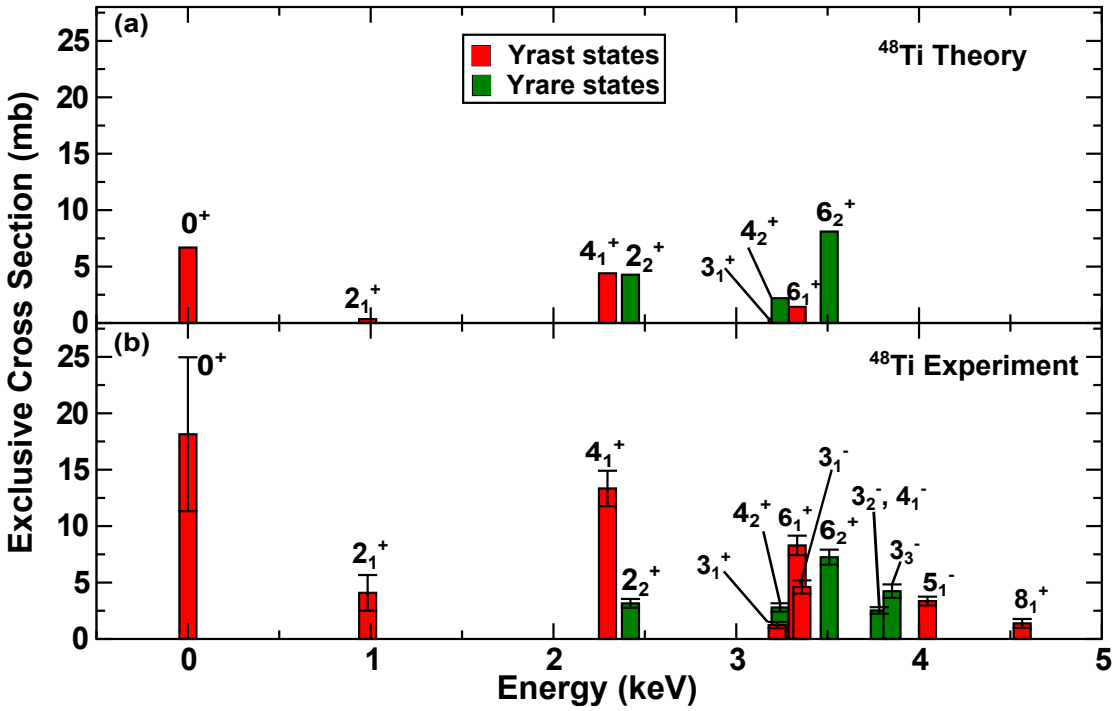

Figure 6.3: (a) Calculated and (b) measured final state exclusive cross sections for the population of individual states in ^{48}Ti populated through one-proton knockout from ^{49}V ground state $7/2^-$.

6.3 Discussion

In the following sections, some of the key findings and results related to the mirrored one-nucleon knockout analyses in both $A = 48$ and $A = 45$ will be discussed.

6.3.1 Interpretation of $A = 48$ Data

Based on a number of previous studies [6, 18, 20, 28, 87, 91], one of the most effective tools for studying IAS in mirror nuclei is the use of mirrored reactions. It is due to mirrored reactions leading to similar γ-ray spectra that easy identification and assignment of mirror transitions occur, assuming that they are well known in the neutron-rich mirror partner. This is particularly useful when studying exotic proton-rich nuclei that are far from stability, as the intensity of the γ rays may not be enough to perform γ-γ analysis or to measure state spins and parities.
The results obtained for both ^{48}Fe and ^{48}Ti represent the first attempt to inform discussions on the suppression of spectroscopic strength in analogue knockout reactions [25].

6.3.1.1 Inclusive Cross Section

Based on the isospin symmetry, e.g. the spectroscopic factors for specific knockout paths are expected to be close to identical. Hence, the mirrored reactions, might be expected to yield similar results. In fact, an inspection of the level schemes, and the relative intensities in Fig. 5.8 illustrate a similar population pattern. The experimental inclusive cross section for ^{49}V to ^{48}Ti, however, was 74(6) mb, a factor of ~ 9 times greater than the analogue reaction to ^{48}Fe, 8(2) mb.
There are two other examples of analogue cross-section measurements in mirrored-knockout reactions in the literature [27, 28], and in both cases, the inclusive cross sections were also asymmetric, although not as much as observed here. There was about a factor of ~ 4 and a factor of ~ 3 difference in the inclusive cross

sections for mirrored one-nucleon knockout to the $T = 1$, $A = 70$ mirror pair in Wimmer *et al.* [27] and to the $T = \frac{1}{2}$, $A = 55$ mirror pair in Spieker *et al.* [28], respectively. The authors suggest that the asymmetry could potentially be a result of the different binding of the mirror nuclei in both cases. For the mirror nuclei studied here, the nucleon separation energies in ^{48}Fe are indeed highly asymmetric – the most recent mass evaluations [96] (including a recent mass measurement of ^{48}Fe [97]) yield separation energies of $S_p = 2.73$ MeV, $S_n = 18.95$ MeV compared to $S_p = 11.4$ MeV, $S_n = 11.6$ MeV for the more bound nucleus ^{48}Ti. Therefore, the large inclusive cross-section asymmetry might be explained by the large population of highly excited ^{48}Ti bound states, whereas its analogue states, in ^{48}Fe, are unbound and decay by proton emission and, hence, are excluded from the measurement.

Using the measured cross sections from Chapter 5 (Section 5.2) and the theoretical single-particle cross sections obtained from Section 6.1, both of which are presented in Table 6.8, it is possible to calculate the inclusive cross sections for both nuclei, which allow for the determination of the ratio, $R_s = \sigma_{exp}^{inc}/\sigma_{th}^{inc}$. The recent studies from [24–26] have examined the strong suppression of experimental cross sections for the one-nucleon knockout at intermediate energies, compared to model predictions. As shown in that study, the ratio R_s appears to be strongly dependent on the asymmetry of the proton and neutron separation energies (Fig. 1.1). This difference is defined as the difference in separation energy ΔS between the proton separation energy S_p and the neutron separation energy S_n, where $\Delta S{=}S_p - S_n$ for proton removal and $\Delta S{=}S_n - S_p$ for neutron removal. The excitation energies are considered for determining ΔS [25] as follows

$$\Delta S = \begin{cases} (S_n + E_x) - S_p & : for\ neutron\ removal, \\ (S_p + E_x) - S_n & : for\ proton\ removal, \end{cases} \tag{6.3}$$

Hence, the values of ΔS are different for each state observed for both nuclei

^{48}Fe and ^{48}Ti, varying by $\sim$ 4 MeV (Table 6.9).

As specified in [25], where multiple states are populated, the effective separation energy is determined from an average of the populated states, weighted by the theoretical cross section. Hence, for n-removal, for example, the S_n value was replaced with an "effective" S_n, which is given as follows:

$$S_n^{eff} = \frac{\sum_i (S_n + E_x^i)\sigma_{th}^i}{\sum_i \sigma_{th}^i} \tag{6.4}$$

It was shown that for the removal of strongly-bound nucleons from weakly-bound systems (such as neutron removal from nuclei near the proton-drip line, as in the current study), the suppression was strong with R_s reducing from $\sim$ 0.6(1) to $\sim$ 0.3(1) for positive values of ΔS from 0 to 20 MeV [26]. For the one-neutron removal reactions of ^{49}Fe to ^{48}Fe, $\Delta S = 14.3$ MeV, and the inclusive cross section indicates a value of R_s of 0.36(6), consistent with the observations in Ref [25].

In the current work, there is also evidence of the removal of *sd*-shell nucleons (approximately 10% of the total cross sections), which are excluded from the shell-model calculation. The result seems to indicate a modest underestimation of the theoretical inclusive cross section, thereby reducing R_s even further. Hence, the R_s value of ^{48}Fe is set as upper limit, as seen in Fig. 6.4, which shows the R_s value of ^{48}Fe deduced from this work with ΔS, where the trend line was plotted using the equation $R_s = 0.61 - 0.016\ \Delta S$ (as reported in [26]).

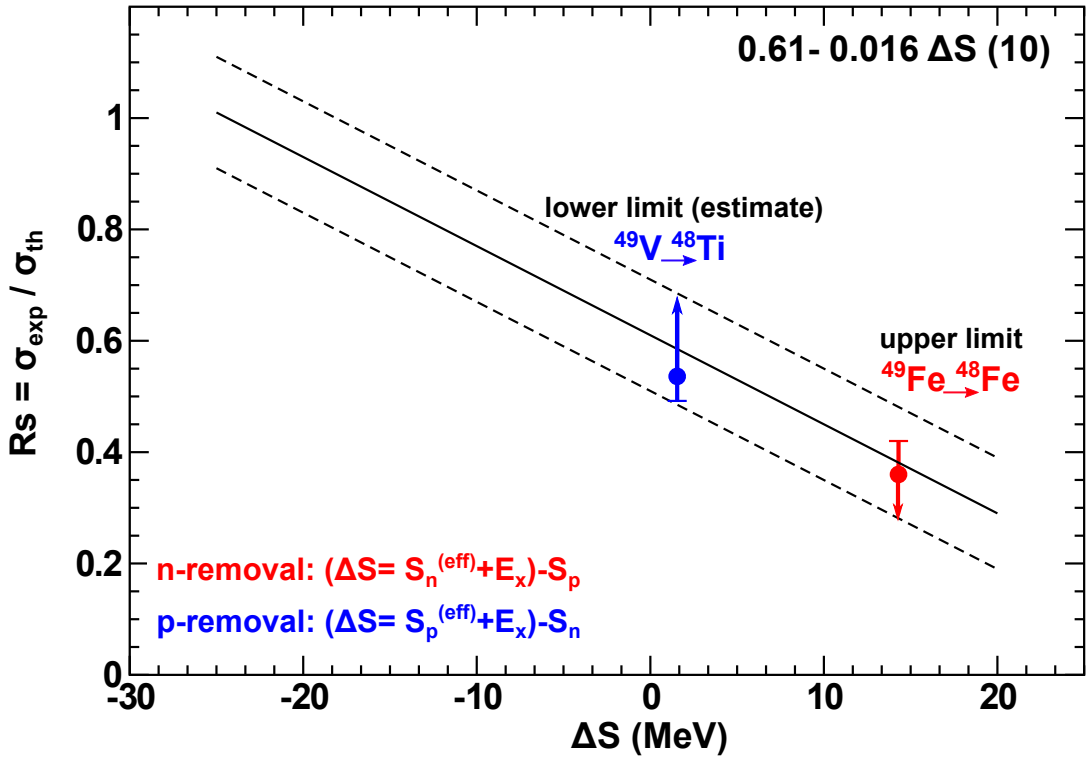

Figure 6.4: The ratios, R_s, of the experimental and theoretical inclusive one-nucleon removal cross sections for each of the projectile nuclei indicated to ^{48}Fe (red) as an upper limit (due to missing *sd* strength) and ^{48}Ti (blue). R_s is shown as a function of the parameter ΔS. The trend line (solid line) given in Eq. (2), as reported in [26], and a band of half-width 0.1 (dashed lines) have been applied, which represent the totality of the collected data points. The R_s value of ^{48}Ti was plotted as the lower limit (estimate) since a theoretical (maximum) inclusive cross section to ^{48}Ti was estimated by evaluating the sum-rule strength for removal of $f_{7/2}$- and *sd*-shell protons, see text for details.

However, in the case of the strongly bound nucleus ^{48}Ti, it is not possible to precisely calculate a theoretical inclusive cross section due to the high proton and neutron separation energies, both are $\sim$ 11.6 MeV, making a shell-model calculation of all bound final states impracticable. There will be many states populated in that range that are accessible to one proton removal, and there is no possible way to do that calculation in the shell model.

This analysis indicates that the removal of *sd*-shell particles is likely to play a significant role in the inclusive cross section for ^{48}Ti. J. Tostevin [98] provided the solution of evaluating the combined sum-rule strength for the removal of all $f_{7/2}$- and *sd*-shell nucleons. To account for the *sd* removal, the excitation-

Table 6.9: This table shows the relevant results from the present study. The experimental and theoretical exclusive cross sections for both ^{48}Fe and ^{48}Ti and the angular momentum and parity J^{π} values. The separation energy differences ΔS, $(S_n + E_x) - S_p$ for neutron knockout (^{48}Fe) and $(S_p + E_x) - S_n$ for proton knockout (^{48}Ti) for the positive-parity yrast and yrare states are shown, as well as the ratio between the experimental to the theoretical inclusive cross sections (R_s) with the separation energy differences ΔS only for ^{48}Fe is listed. The theoretical inclusive cross section could not be determined for ^{48}Ti; hence, the R_s also could not be determined, see text for details.

Residue	ΔS (MeV)	J^{π}	σ_{exp}^{exc}(mb)	σ_{th}^{exc}(mb)	σ_{exp}/σ_{th}
^{48}Fe	12.1	0^+	3(2)	5.5	0.5(4)
	13.0	2_1^+	0.9(9)	0.3	3(3)
	14.3	4_1^+	1.1(8)	3.6	0.3(2)
	14.4	2_2^+	0.4(2)	3.7	0.1(4)
	15.2	4_2^+	0.5(4)	1.9	0.2(1)
	15.3	6_1^+	0.1(6)	1.2	0.1(5)
	15.5	3_1^-	0.4(2)	-	-
	15.6	6_2^+	1.9(4)	6.8	0.3(1)
	16.2	5_1^-	0.3(2)	-	-
Total	14.3	inclusive	8(2)	22.9	0.36(6)
^{48}Ti	-4.8	0^+	18(7)	6.7	2.7(1)
	-3.8	2_1^+	4(2)	0.3	12(4)
	-2.5	4_1^+	13(2)	4.4	3.0(3)
	-2.3	2_2^+	3.2(4)	4.3	0.7(1)
	-1.6	3_1^+	1.2(3)	0.3	3.2(7)
	-1.5	4_2^+	2.8(4)	2.2	1.3(2)
	-1.46	6_1^+	8.3(9)	1.4	5.8(5)
	-1.43	3_1^-	4.6(6)	-	-
	-1.3	6_2^+	7.2(7)	8.1	0.9(1)
	-1.0	$3_2^-, 4_1^-$	2.5(3)	-	-
	-0.9	3_3^-	4.2(6)	-	-
	-0.7	5_1^-	3.4(4)	-	-
	-0.2	8_1^+	1.4(4)	-	-
	-	inclusive	74(6)	-	-

energy centroids of the *sd* orbitals were estimated using the HF-binding energy for each orbital as listed in Tables 6.3 and 6.4 for both projectiles ^{49}Fe and ^{49}V, respectively (as described in Section 6.1.2). The HF density calculations provided neutron-bound state results (^{49}Fe) and proton-bound state results (^{49}V) for the different orbitals ($f_{7/2}$ orbital along with *sd* orbitals) to give a good description of the binding energies of all these different particles, and these can be used to extract estimates of the centroids of the spectroscopic strength. As the strength (e.g. all the states populated by knockout from a particular orbital) is distributed over a range of excitation energies, the weighted average value of these states is estimated to be the single-particle centroid. The $f_{7/2}$ centroid can be assumed to be at the ground state (Fermi level); hence, when the particle is removed from the deep orbital, the centroid will be higher.

Since the Fermi level is the $f_{7/2}$ orbital, this means that the binding energy of the $f_{7/2}$ neutron should be the neutron separation energy S_n in ^{49}Fe, whereas the binding energy of the $f_{7/2}$ proton should be the proton separation energy S_p in ^{49}V. The neutron and proton separation energies of the ground state of ^{49}Fe and ^{49}V nuclei were calculated (Tables 6.3 and 6.4) to be 14.9 MeV (the energy required to remove $f_{7/2}$ neutron to the ground state in ^{48}Fe) and 6.84 MeV (the energy required to remove $f_{7/2}$ proton to the ground state in ^{48}Ti), respectively. The excitation-energy centroids for *sd*-shell proton/neutron removal were estimated by subtracting the binding energies of the *sd* orbital from the binding energy of the $f_{7/2}$ ground state of the ^{49}Fe/^{49}V nuclei, and these binding energies are shown in Tables 6.3 and 6.4.

For ^{49}V (the beam used for proton removal to ^{48}Ti), this analysis suggests that the excitation energy centroids for the *sd*-shell proton orbitals are about 5.1 MeV ($d_{3/2}$), 5.3 MeV ($s_{1/2}$), and 9.9 MeV ($d_{5/2}$). Similarly, for ^{49}Fe (the beam used for neutron removal to ^{48}Fe), the *sd*-shell neutron orbitals were about 5.3 MeV ($d_{3/2}$), 5.6 MeV ($s_{1/2}$), and 10.0 MeV ($d_{5/2}$). Hence, these provide reasonable estimates for the excitation energy centroids, in ^{48}Ti and ^{48}Fe, for the *sd*-shell proton/neutron removal. These excitation-energy centroids are illustrated in Fig. 6.5.

The majority of this *sd*-shell knockout strength would, thus, populate **bound** states in ^{48}Ti ($E^* < 12$ MeV) and **unbound** states ($E^* > 3$ MeV) for the analogue neutron-removal reactions to ^{48}Fe. According to this interpretation, the significant asymmetry evident in inclusive cross sections, therefore, is most likely due to this ~ 9 MeV difference, between ^{48}Ti and ^{48}Fe, in the excitation energy range within which bound states occur. This also explains the weak population of low-energy negative-parity states in ^{48}Fe, which are assumed to be in the tail of the centroids. It is instructive to estimate a theoretical (maximum) inclusive cross section to ^{48}Ti by evaluating the sum-rule strength for the removal of all $f_{7/2}$- and *sd*-shell protons (i.e. those at and below the Fermi level). Their centroids are all expected to be bound for ^{48}Ti. In this estimate, the average excitation energies of the states populated by *sd*-shell knockout are taken to be above the centroid estimates. The C^2S values of the *sd* orbital were assumed to be 4, 2, and 6 (the maximum number of particles in each orbital) for $d_{3/2}$, $s_{1/2}$ and $d_{5/2}$, respectively. Subsequently, the theoretical cross sections for the *sd* removal were estimated using the mirrored knockout reaction that is described in Section 6.1.2 to be $\sim$103.8 mb. The included pf shell-model states, to $E^* = 3$ MeV, account for a summed spectroscopic strength of 2.4 (Table 6.2). The remaining 0.6 units, to states at higher energy, can account for a maximum additional cross section of 7 mb, given the calculated pf-shell orbital cross sections. By adding removals from the assumed-filled *sd*-shell orbitals, as well as the missing $f_{7/2}$ strength, to the total theoretical cross sections of the fp removal (27.8 mb, see Table 6.7), a maximum (sum-rule) inclusive cross section of $\sim$ 139 mb is yielded (Table 6.10).

Fig. 6.5 provides a visual explanation for the large asymmetry in the mirrored cross sections, where the estimated centroids of the $f_{7/2}$, $ds_{1/2}$, $d_{3/2}$, and $d_{5/2}$ orbitals are shown. Since $f_{7/2}$ and *sd* shell orbitals are partly and fully occupied at the Fermi surface, and in the case of knockout of a particle from these four orbitals from the projectiles (^{49}V and ^{49}Fe), this will end up with bound states in ^{48}Ti and mostly unbound states in ^{48}Fe (Fig. 6.5). Hence, this diagram can interpret the large difference in the mirrored inclusive cross sections, where the negative-parity states

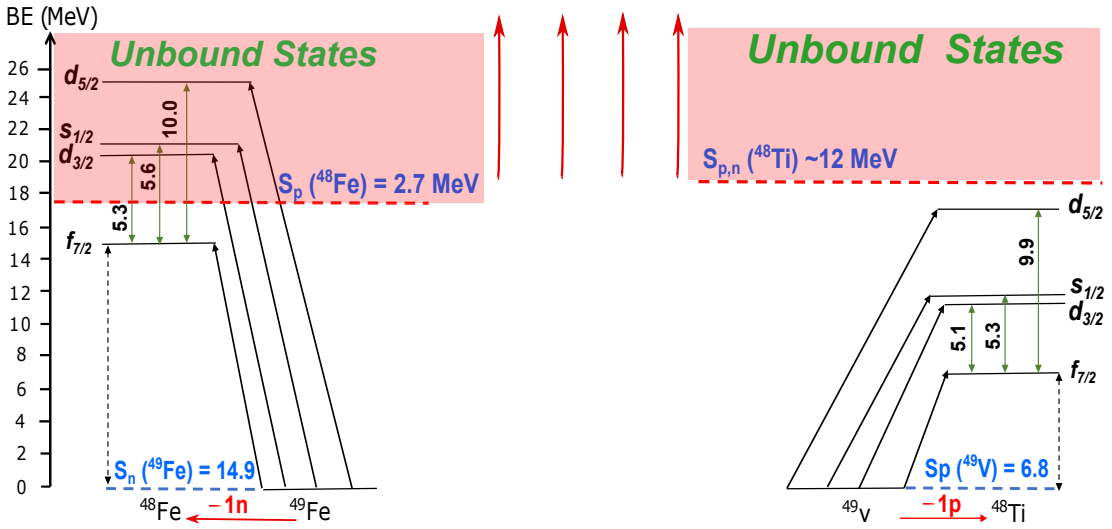

Figure 6.5: A diagram demonstrating the estimated excitation-energy centroids of the single-particle strength distribution (the sum-rule strength) for the removal of the $f_{7/2}$-shell and full *sd*-shells protons. All these final states are expected to be bound for ^{48}Ti, whilst, for the analogue states in ^{48}Fe, only the states resulting from $f_{7/2}$ removal are expected to be bound.

populated from *sd* removal are above the proton separation energy (unbound) in ^{48}Fe, while in ^{48}Ti, they are below the separation energy (bound).

Using the experimental inclusive cross section of 74(6) mb and the maximum predicted cross section of ^{48}Ti (139 mb), a minimum value of R_s was estimated to be 0.53(4) at $\Delta S = 1.5$ MeV. This value is plotted as the lower limit (Fig. 6.4). Since the R_s of ^{48}Ti is a lower limit (and actually, the ^{48}Fe is more likely to be an upper limit due to missing *sd* strength), the degree of suppression (R_s) in this mirrored knockout analysis (Fig. 6.4) has a similar trend to the published R_s systematics for inclusive cross sections, as shown in [25, 26].

Table 6.10: An estimate of the maximum possible cross sections of ^{48}Ti(^{49}V - 1p) reaction due to removals from the assumed-filled *sd*-shell orbitals.

The cross section of *sd*-shell knockout strength to bound states					
orbital	E^*(centroid)	E^*(centroid) + S_p	C^2S	σ_{sp}(mb)	$\sigma_{th}(E_x, J^\pi, j)$(mb)
$s_{\frac{1}{2}}$	5.3	11.7	4.0	7.7	32.2
$d_{\frac{3}{2}}$	5.1	12.1	2.0	10.7	22.3
$d_{\frac{5}{2}}$	9.9	16.5	6.0	7.8	49.2
Total	-	-	-	-	**103.8**
The cross section of **missing** knockout strength of *fp*-shell					
$f_{\frac{7}{2}}$	3.0	9.7	0.6	10.7	**7.2**
The cross section of knockout strength of *fp*-shell					
Total	-	-	-	-	**27.8**
Theoretical inclusive cross section of *fp* and *sd* orbitals					**∼139**

6.3.1.2 Exclusive Cross Section

By comparing the experimental exclusive cross sections between the mirror nuclei ^{48}Fe/^{48}Ti, there are two observations that can be seen instantly (Table. 6.9). The first one is that all the exclusive cross sections in ^{48}Ti are much larger than in ^{48}Fe by a factor of up to ~ 20. This is especially true of the yrast states. Secondly, the experimental cross sections for yrast states are larger than theoretical values of ^{48}Ti, which is unlikely to be correct (they are normally suppressed). For instance, the experimental exclusive cross sections of 2_1^+, 3_1^+, 4_1^+ and 6_1^+ states (yrast states) are much larger than the theoretical values by factors $\sim$ 13, 3, 4, and 6, respectively. Therefore, these values are not considered a reliable measure for the true exclusive cross section. However, this is not true in ^{48}Fe where the experimental cross sections are lower than theoretical cross sections in all cases, see Table. 6.9. These observations are consistent with the above discussion about the inclusive cross sections. That is, population of high-lying states in ^{48}Ti yields significant *unseen* feeding into the low-lying yrast states and ground state of ^{48}Ti, and this can

be seen in the level scheme of ^{48}Ti (Fig. 5.8) since states along the yrast line would be expected to gather intensity from statistical feeding from higher-energy states. Hence, these exclusive cross sections in ^{48}Ti may be significantly over estimated. As a matter of fact, the larger observed cross section to the ^{48}Ti ground state, in comparison with the smaller theoretical prediction (a factor of ~ 3), implies additional unseen feeding.

The above observations indicate that it is not possible to do a comparison (the ratio between the experimental and theoretical cross sections) between analogue exclusive cross sections for yrast states between these mirror nuclei.

On the other hand, the yrare states, predicted to contain strong direct populations in this specific case, may be less susceptible to this indirect feeding. Indeed, in fusion-evaporation reactions populating ^{48}Ti ([99]), where the low-spins states are fed indirectly through statistical feeding, the 2_2^+ and 4_2^+ states (that lie ~ 1 MeV above the yrast line) do not receive any population. The ratio between the experimental exclusive cross sections to the theoretical values ($\sigma_{exp}^{exc}/\sigma_{th}^{exc}$) were obtained for individual states observed (yrast and yrare states) for both mirror nuclei and both are given in Table 6.9. Upon comparing the exclusive cross section of the analogue yrare states (Table 6.9), a significant asymmetry of the cross section remains, which is consistent in magnitude for all three pairs of yrare states. The experimental exclusive cross sections to these states are ~ 5 times higher, on average, in ^{48}Ti than in ^{48}Fe. It should be noted that more indirect feeding cannot be excluded for these states, particularly for ^{48}Ti, and hence these exclusive cross sections should be regarded as upper limits.

The systematics of R_s=σ_{exp}(inc)/σ_{th}(inc) as a function of ΔS [25] have some interesting potential consequences for mirrored exclusive cross sections like the one presented here. The R_s data collected in that systematic analysis pertain only to inclusive cross sections. However, if the trend of the R_s plot is also followed, in reality, for analogue (i.e. mirrored) exclusive cross sections, it can only arise from the difference in the experimental cross sections, despite the supposed analogue nature of the knockout process – in qualitative agreement with the tentative ob-

servations here. The reasons for this argument are as follows: (i) the mirrored reactions with high-T are well separated in ΔS, with a difference of $\sim$ 16 MeV in this case, (ii) the theoretical spectroscopic factors for the knockout pathways in the shell model are essentially identical, and (iii) the theoretical single-particle cross sections do not have a strong ΔS-dependence in the reaction model used here ($\sim$ 20% in this case). The ratio of the experimental and theoretical exclusive cross sections for these three pairs of yrare analogue states $\sigma_{exp}(\text{exc})/\sigma_{th}(\text{exc})$ as a function of ΔS is shown in Fig. 6.6.

It can be seen that the degree of suppression (experiment compared to theory) again has a similar trend to the published R_s data (refer to Tostevin and Gade [98]) for inclusive cross sections. It is worth noting that although, the absolute values of the ratios shown in Fig. 6.6 for exclusive cross sections will be affected by the accuracy of the shell-model calculations for individual states, the trend with ΔS should be unaffected, as the mirror reactions probe the same spectroscopic factors. Whilst this analysis is possible for the yrare states, it was not possible to conduct such a detailed comparison of experimental and theoretical exclusive cross sections for the analogue yrast states due to the reasons mentioned before, the most important of which is the *unseen* feeding into these states and the incomplete model space (*sd* shell removal). This comparison of the analogue exclusive cross sections by mirrored knockout (for pairs of analogue final states) was performed here for the first time to understand the (a) symmetry of the analogue nature of the reactions, (b) the variation of cross sections with ΔS.

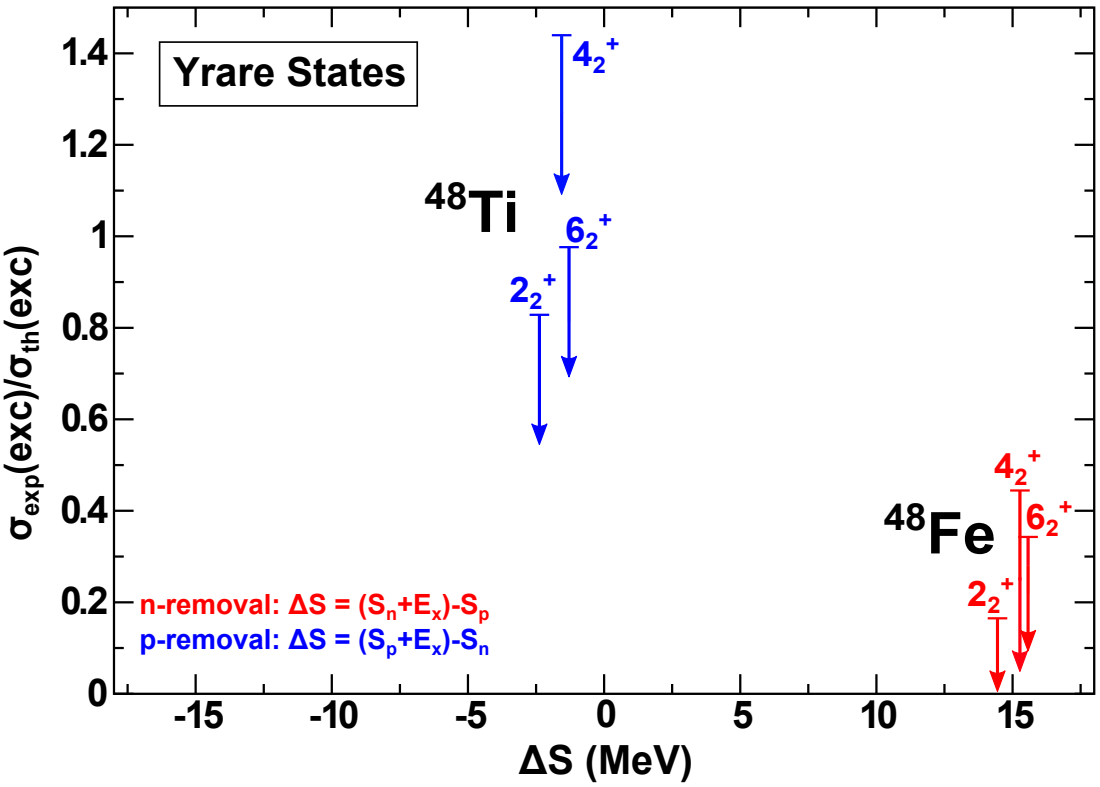

Figure 6.6: The ratio of the experimental to the theoretical cross sections for yrare states 2_2^+, 4_2^+ and 6_2^+ plotted against the separation energies ΔS for both mirrored one-nucleon-knockout reactions. The red data represent one neutron knockout from ^{49}Fe to ^{48}Fe and the blue data represent one-proton knockout from ^{49}V to ^{48}Ti.

6.3.2 Mirrored Knockout Reaction Result of $A = 45$

The secondary beam, ^{46}V, with equal numbers of neutrons and protons ($N = Z$) used in this analysis are of particular interest in order to simplify the (a)symmetry on the mirrored reaction with only one $N = Z$ secondary beam, instead of two secondary beams.

For the ^{46}V projectile, Table 5.7 collects the measured inclusive cross sections for each mirror nucleus ^{45}V and ^{45}Ti. The experimental inclusive cross section for $^{46}\text{V} \rightarrow {}^{45}\text{Ti}$, is again a factor of ~ 9 times larger than the analogue reaction $^{46}\text{V} \rightarrow {}^{45}\text{V}$. Despite using only one secondary beam ^{46}V in both reactions, the discrepancy was observed in the knockout cross section (Table 5.7), which is similar to that observed in $A = 48$ mirror nuclei.

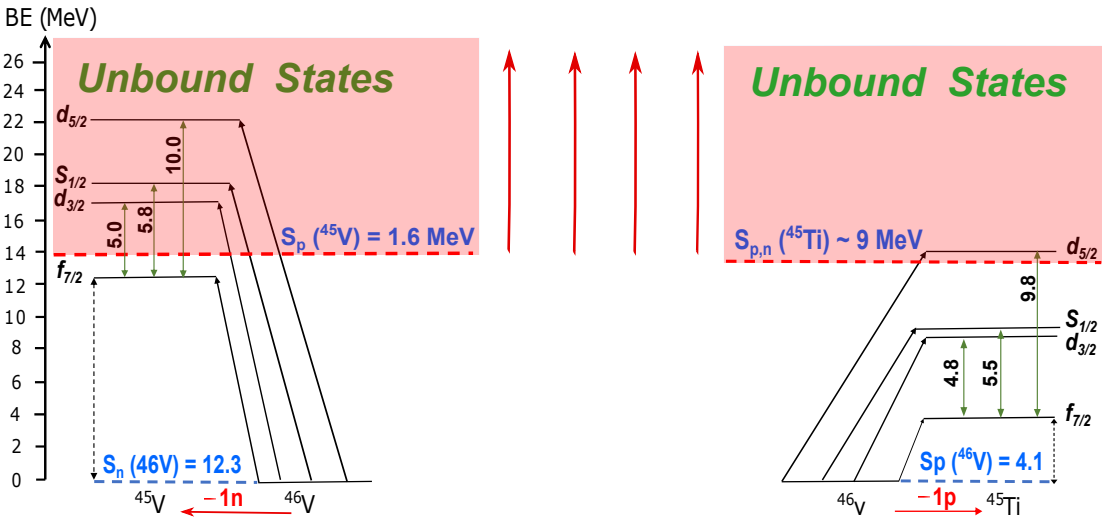

Figure 6.7: A diagram demonstrating the estimated excitation-energy centroids of the single-particle strength distribution (the sum-rule strength) for the removal of the $f_{7/2}$-shell and full *sd*-shells protons. All these final states are expected to be bound for ^{45}Ti (except the $d_{5/2}$ removal), whilst, for the analogue states in ^{45}V, only the states resulting from $f_{7/2}$ removal are expected to be bound.

Thus, one likely contribution to the large inclusive cross-section asymmetry, as discussed in $A = 48$ mirror nuclei (Section 6.3.1), is the population of highly-excited ^{45}Ti bound states, whose analogue states, in ^{45}V, are unbound and may decay by proton emission and, hence, are excluded from the measurement. The nucleon separation energies for ^{45}V are $S_p = 1.62$ MeV, $S_n = 16.14$ compared to $S_p = 8.48$ MeV, $S_n = 9.53$ MeV for ^{45}Ti [96]. Again, for ^{45}V, the nucleon separation energies are highly asymmetric, compared to ^{45}Ti, where a high level of population of bound states up to 9 MeV is possible. Hence, the total cross sections will be different again as a result of unseen feeding, which accounts for ^{45}Ti and is absent in ^{45}V, and again the removal of the *sd*-shell particles is likely to play a significant role (Fig. 5.17).

The same procedure as in Section 6.3.1 was followed to estimate the *sd* centroids and the excitation energies resulting in numbers shown in Fig. 6.7. One difference observed here is that, in the ^{45}Ti case, the excitation-energy centroid of the $d_{5/2}$ level is above the separation energies of ~ 9 MeV (Fig. 6.7).

These results provide further support for the conclusions the large inclusive cross-

section asymmetry observed in the $A = 48$ mirror pair, i.e., that the asymmetry may be due to the different binding of the mirror nuclei used in this work.
This $A = 45$ analysis is still underway and hence only interim results are included. However, it is complicated by the fact that the isomeric ratio is still unknown, which is required for the calculation of theoretical cross sections since the cross section depends on whether the particle was removed from ground state or isomer state, both of which have different separation energies. Due to the inability to calculate the theoretical inclusive cross section, the R_s is not calculated here. It is an interesting type of analysis for testing the symmetry of the analogue reaction, starting with the $N = Z$ secondary beam and knocking out a particle from the same nucleus. Further work, which take these variables into account, will be needed to be undertaken in the future.

Chapter 7

Mirror Energy Differences

The new excited states presented in Section 5.1 has allowed for the determination of mirror energy for $A = 48$, $T = 2$ states in the $f_{\frac{7}{2}}$ shell for the first time. In the following sections, these MED are compared to shell-model calculations, taking into account Coulomb and nuclear isospin-breaking forces, performed as part of this thesis work for the $A = 48$, $T_z = \pm 2$ mirror pair.

7.1 An Overview of Shell-Model Calculations

The large-scale shell-model approach using the ANTOINE code [43] was used to analyse MED for the ^{48}Fe - ^{48}Ti mirror pair. The results of the shell-model approach to MED studies are based on using the full fp valence space and the KB3G interaction [45], where no restrictions were placed on the movement of particles between the fp orbitals. The first step of performing realistic shell-model calculations is selecting an appropriate valence space (with an appropriate inert core). Then, a series of basis states with pure configurations, such as $\pi(\nu)f_{\frac{7}{2}}^{4}\nu(\pi)f_{\frac{7}{2}}^{4}$, were constructed, which will eventually mix to produce the real states. The wave functions of these states are then expressed as linear combinations of Slater de-

terminants [100] for protons and neutrons independently. With the intention of determining these linear combinations, the Hamiltonian matrix was diagonalised with the same dimensions as the number of basis states. This diagonalisation represents the primary function of the shell-model codes.
The shell-model calculations of an appropriate model space and corresponding interaction, which forms the Hamiltonian described in Section. 2.2. In Chapter 2, this Hamiltonian comprises kinetic energy operators and two-body interactions, i.e. single-particle energies and two-body matrix elements.

7.2 Calculations of Isospin-Breaking Terms

The shell-model calculations involve several inputs calculated by the user: (i) the fp valence space, (ii) truncation (restricting number of particles allowed to be excited), and (iii) the effective interactions (residual interactions), as described in Section 2.2.2. Several of the isospin-breaking phenomena discussed in Section 2.2.3 can be easily included into standard shell-model calculations to interpret experimental data. The shell-model method used is based on the description in Section 2.2.3, which accounts for multipole and monopole contributions to the MED of Coulomb and magnetic origins [7]. Fig. 7.1 shows a summary of the MED calculations within the shell-model calculations.

The MED calculation process comprise four steps, with each step entailing the addition of an extra term, V_{CM}, $V_{CM} + (V_{ll} + V_{ls})$, $V_{CM} + (V_{ll} + V_{ls}) + V_B$, and $V_{CM} + (V_{ll} + V_{ls}) + V_B + V_{Cr}$. This was done to evaluate and plot the contribution of each term separately. The calculations start with isoscalar interactions (KB3G interaction [45]); no Coulomb effects were involved, where the protons and neutrons are treated in an identical manner ($V_{pp} = V_{nn} = V_{np}$). Hence, the MED would be zero. Four contributions to the MED were calculated within the shell model. The Coulomb multipole term, (V_{CM}), accounts for the Coulomb effect of

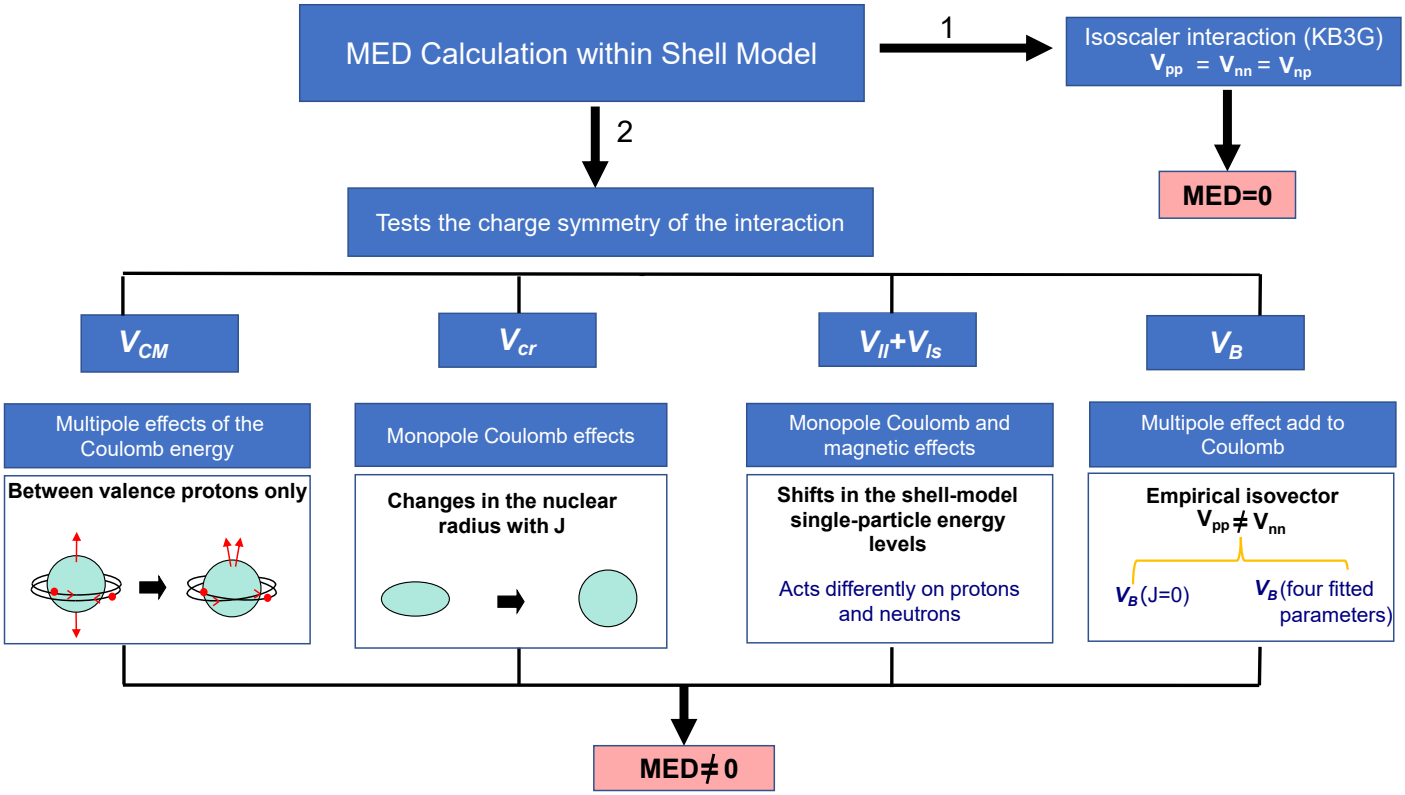

Figure 7.1: A schematic diagram of the MED calculations of the $A = 48$, $T_z = \pm 2$ mirror pair using the full fp space shell-model calculations, implemented using the ANTOINE code.

recoupling angular momenta of pairs of protons, which is achieved by adding the Coulomb two-body interaction (Coulomb matrix elements calculated using a harmonic oscillator potential) to the nuclear residual interaction for protons (existing two-body matrix elements) in order to produce a Coulomb-dependent interaction. By taking two such calculations with reversed numbers of protons and neutrons ($^{48}_{26}\mathrm{Fe}_{22}$ and $^{48}_{22}\mathrm{Ti}_{26}$) and subtracting one from the other, the Coulomb multipole contribution to MED can be determined for $T_z = \pm 2$ as

$$\Delta V_{CM}(J) = E^*_{CM}(J)_{T_{z=-2}} - E^*_{CM}(J)_{T_{z=2}}. \tag{7.1}$$

The next contribution to the shell-model calculation process is the monopole single-particle effects, $V_{ll} + V_{ls}$ (as described in Section 2.2.3.3). This is simply achieved by adding the shifts in single-particle energies calculated using Eqs. 2.17 and 2.18 to the single-particle energies in an existing interaction.

The next term V_B added to the shell-model calculations is an empirical isovector, $V_{pp} \neq V_{nn}$, contribution, which was found to be necessary in addition to V_{CM} [7]. This isospin non-conserving contribution V_B was shown in [9] to be strongly dependent on the angular-momentum coupling of nucleon pairs (as discussed in Section 2.2.3.4. The origin of the V_B term is presently unclear and a discussion on this is provided in [8, 9]. This is added to the matrix elements for protons.

This work used two different ways to define the INC term V_B, and both have been described in [9]. First, the single -100 keV INC matrix element for $J = 0$ for all fp-orbitals was used. Second, four parameters extracted from the fit across the $f_{\frac{7}{2}}$ shell [9] were used. In the first method, a single-matrix element for V_B of -100 keV INC matrix element for $J = 0$ couplings for all fp orbitals (i.e. added directly to the shell-model matrix element for protons). In the second method to determine the V_B term, effective isovector ($V_{pp} \neq V_{nn}$) matrix elements were extracted in the $f_{\frac{7}{2}}$ shell by fitting the shell model to a full set of all experimental MED data obtained across the whole shell. Matrix elements of $V_B = -72(7)$, $+32(6)$, $+8(6)$, $-12(4)$ keV [9] were obtained for $J = 0$, 2, 4, 6 couplings, respectively.

The last isospin-breaking contribution added to the normal shell-model calculation

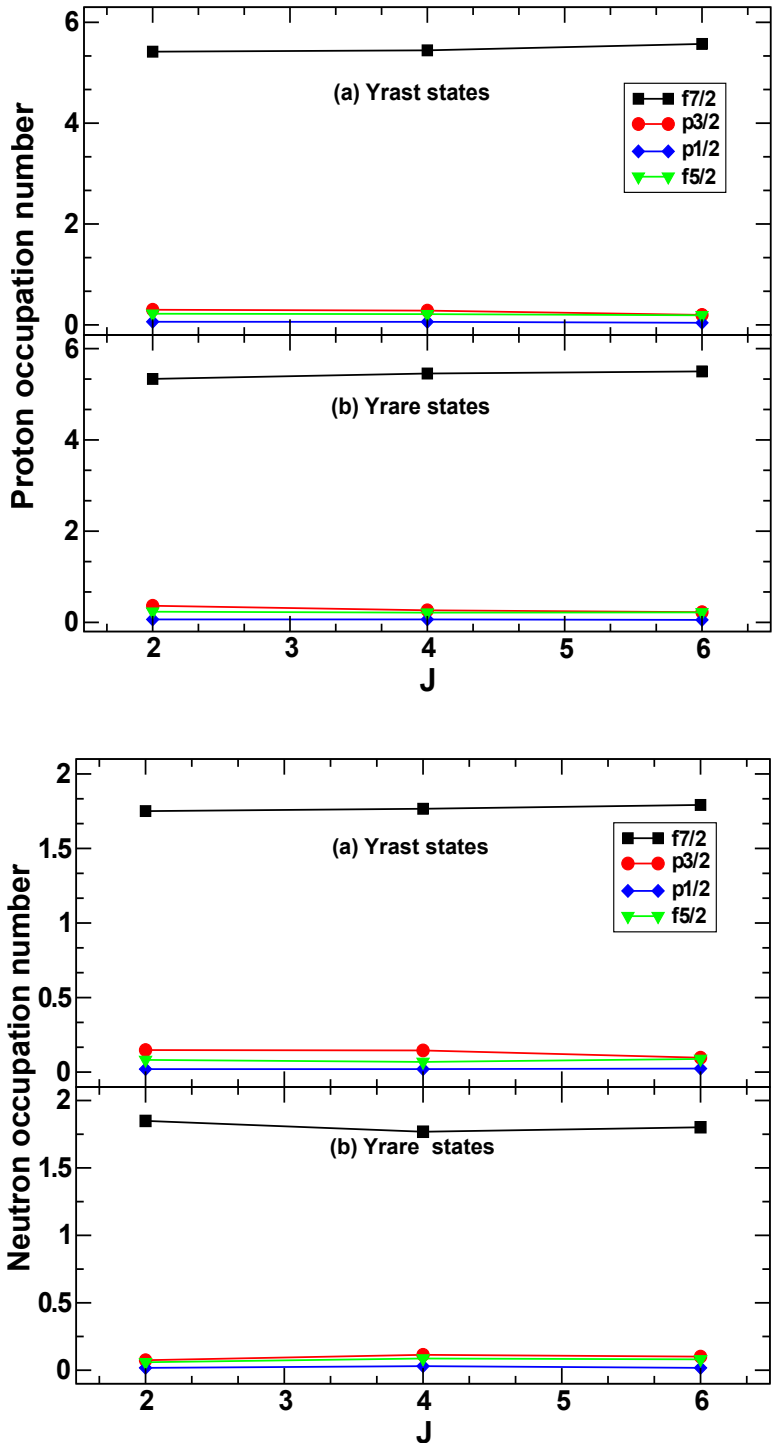

Figure 7.2: Proton and neutron fp-shell occupancies for states ((a) yrast states and (b) yrare states) in ^{48}Fe. Calculations performed with ANTOINE and the KB3G [45] interaction in the full fp-shell space. The $p_{\frac{1}{2}}$ occupation is negligible and the $f_{\frac{7}{2}}$ occupation increases with a corresponding decrease in $p_{\frac{3}{2}}$.

process is the radial contribution (V_{Cr}). It is the monopole Coulomb contribution associated with changes in the nuclear radius with J, it is calculated by tracking the occupation of the $p_{\frac{3}{2}}$ as a function of J. The occupation of the $p_{\frac{3}{2}}$ shell in the $f_{\frac{7}{2}}$ nuclei varies with spin, whereas the $p_{\frac{1}{2}}$ occupation is relatively small and fairly constant (Fig. 7.2), hence the $p_{\frac{1}{2}}$ is not tracked. Since the radius depends only on l, small l orbitals have larger radii [7] (see Section 2.2.3.2). Accordingly, it would be reasonable to consider only the total occupation (protons and neutrons) of the $p_{\frac{3}{2}}$ shell. Calculations were carried out in the fp valence space without the consideration of the core, so monopole effects of the radial change must be explicitly considered to account for the shape changes of the core. This can be achieved by computing the total occupation of the $p_{\frac{3}{2}}$ orbital, obtained directly from the shell-model calculation, for the states of interest (both yrast and yrare states). Assuming the radii of the mirror nuclei to be equal indicates that a calculation of the average of proton and neutron occupation numbers of the $p_{\frac{3}{2}}$, m_p and m_n, respectively, is required $\frac{m_p+m_n}{2}$. The change in this number is calculated relative to the ground state and the contribution to the MED of mirror nuclei $A = 48$ from the radial Coulomb monopole term (ΔV_{Cr}) can be determined by multiplying the strength of the interaction ($\alpha_r = 200$ keV) [8] and $|T_z| = \pm 2$ by the appropriate coefficients (Eq. 2.16). A value of 200 keV was used in this calculation, and it was found to reproduce experimental energy differences across the $f_{\frac{7}{2}}$ shell [8]. The result of the (ΔV_{Cr}) calculation was then added to the other terms' contribution to MED.

7.3 Results of MED Shell-Model Calculations

The contributions to the MED described above are added together for each state of interest in a $A = 48$, $T_z = \pm 2$ mirror pair to compare them with experimental data. This is equivalent to isovector energy differences. These calculations can be

compared with experimentally determined MED in order to obtain insights into the evolution of the structure of excited states. Additionally, they can test the shell model and the isospin-breaking calculations performed using the model.

The MED results for the yrast and yrare states of $A = 48$ mirror pair are presented in Table 7.1 and Fig. 7.3. Fig. 7.3 shows the results of isospin-breaking components

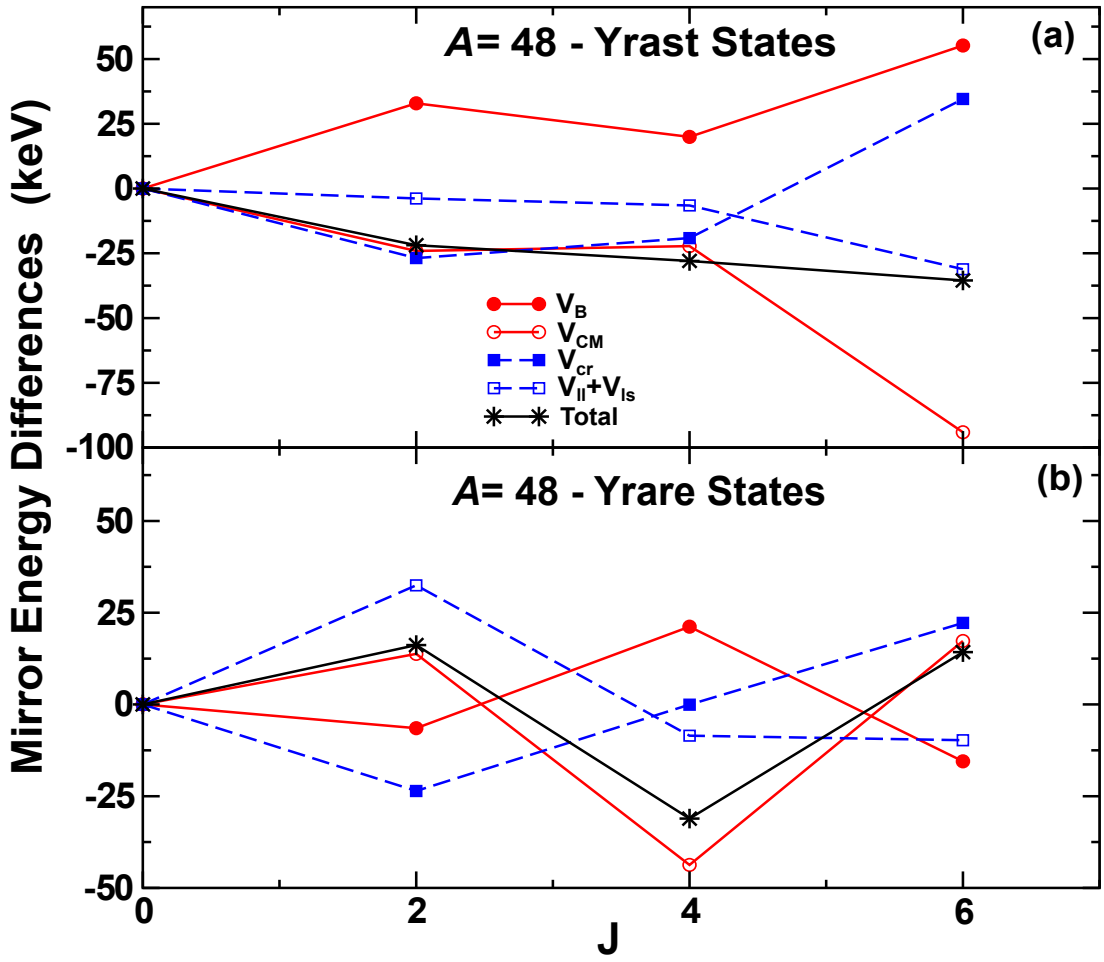

Figure 7.3: Contributions to the $A = 48$, $T_z = \pm 2$ MED (for both (a) yrast states and (b) yrare states) from individual isospin-breaking terms, along with the resultant predicted MED (the sum of the four components) in solid lines in (a) and (b). The solid line uses a single -100 keV INC matrix element for J=0 for all fp orbitals. In (b), the MED for the $J \neq 0$ yrare states are plotted relative to the $J = 0$ ground state.

calculated for both the yrast and yrare states of the $A = 48$, $T_z = \pm 2$ mirror pair, as described in Section 7.2. These calculations were performed in the full fp space using a single -100 keV INC matrix element for J=0 for all fp-orbitals.

Table 7.1: Experimental and theoretical $A = 48$ MED. The theoretical MED is presented with both $J = 0$ and fitted parameters for V_B term. This data has been graphed in Fig. 7.4.

MED Results			
J^π	Shell-Model $+V_{B\ (J=0)}$ (keV)	Shell-Model $+V_{B\ (fitted)}$ (keV)	Experiment (keV)
Yrast states			
0^+	0	0	0
2_1^+	-22	-25	-11(2)
4_1^+	-28	-32	-39(2)
6_1^+	-35	-68	-87(3)
Yrare states			
4_2^+	16	15	-41(3)
2_2^+	-31	-36	-39(3)
6_2^+	14	31	-7(3)

The monopole effect V_{Cr} is seen to increase smoothly with spin, similar to that of the $T_z = \pm 1$ odd—odd mirror pair with $A = 48$ [8]. This term depends on the $|T_z|$, which is shown in Eq. 2.16. This occurs as a result of a gradual reduction in the occupation of the $p_{3/2}$ orbital in both members of the mirror pair, resulting in a smaller radius and an increase in Coulomb energy. However, since the $T_z = -2$ member of the pair has more protons than the other member, the Coulomb energy increases more rapidly, which results in a positive energy difference. For the J^π=2_1^+ and 2_2^+ states, an increase in $p_{3/2}$ occupation yields a negative energy difference. The inclusion of the Coulomb multipole term, V_{CM}, is dominant in this calculation, and the INC term V_B, along with the other terms, yields as dramatic an improvement in agreement with experimental data, this will be discussed later.

7.4 Discussion

The following section will describe some of the key findings and results from the MED analyses between isobaric analogue states for $A = 48$ nuclei.

7.4.1 Interpretation of MED $A = 48$ Data

The results of the shell-model calculations performed for the ^{48}Fe/^{48}Ti mirror pair (as described in Section 7.2), in addition to the experimental MED obtained in this work, are presented for the yrast and yrare states in Figs. 7.4 (a) and (b), respectively. The four isospin-breaking components of the shell-model calculation are incorporated, whose total give the predicted MED (the solid line and dashed line). These two lines of theory correspond to two different ways of defining the INC term, V_B. The solid line uses single -100 keV INC matrix element for J=0 for all fp-orbitals, and the dashed line uses four parameters extracted from the fit across the $f_{\frac{7}{2}}$ shell [9]. Experimental MED and shell-model calculations have been compared for the yrast and the yrare states. The solid black lines in Figs. 7.4 (a) and (b) are the shell-model calculations, and the four individual components for this calculation were illustrated in Fig. 7.3. As part of the shell-model calculation, a single matrix element of -100 keV is included for $J = 0$ couplings for all fp orbitals. Based on [9], it was demonstrated that $J = 0$ coupling is by far the most significant contribution to V_B, and the best fit value of -79 keV was extracted. The $J = 0$ dominance suggests a monopole pairing effect underlies this empirical phenomenon. Additionally, for energy differences between states of isobaric triplets [101], a single isotensor matrix element of $+100$ keV for $J = 0$ was found to provide a good description of TED across the fp shell. Therefore, for simplicity an isovector component of -100 keV for $J = 0$ is used for V_B in the solid lines in Fig. 7.4.

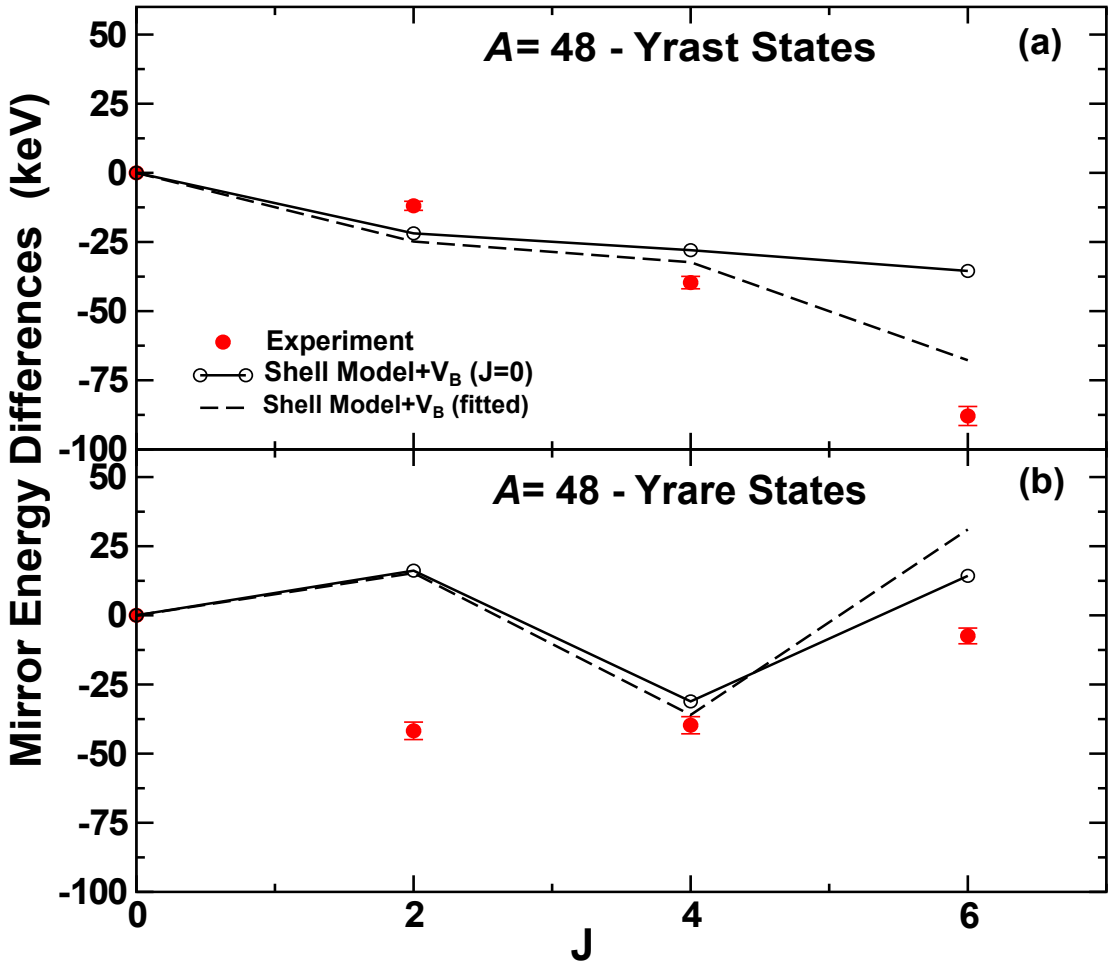

Figure 7.4: The experimental and theoretical MED for the A=48, $T_z = \pm 2$ mirror yrast (a) and yrare states (b). The solid line and the dashed line in (a) and (b) both are the shell-model calculations, which include all the four components and correspond to two different ways of defining the INC term V_B. The solid line uses single -100 keV INC matrix element for J=0 for all fp-orbitals and the dashed line uses four parameters extracted from the fit across the $f_{\frac{7}{2}}$ shell [9]. The sum of the four components of the shell-model calculations (defined in the text) is presented in solid lines in (a) and (b) and also were graphed in Fig. 7.3. In (b), the MED for the $J \neq 0$ yrare states are plotted relative to the $J = 0$ ground state.

As can be seen, the agreement between the MED experiment and theory is good for the observed states (yrast states), the $A = 48$ mirror pair. In terms of yrast states, the calculations reproduce the negative trend of MED, with good agreement for the 2_1^+ and 4_1^+ states, while the calculations vary from the experiments for the yrast 6_1^+ state. However, the inclusion of the V_B term, in this case, does not have the same dramatic effect as in other cases in the region [9]. As a

result of turning off the V_B term, the 6_1^+ state agreement improves and the 2_1^+ state significantly deteriorates. In the case of yrare states, the 2_2^+ state is not well reproduced by the calculations, either with or without V_B, having better agreement for the 4_2^+ and 6_2^+ states. The inconsistent agreement between experiment and model may be related to the inadequacy of the fp space, especially for protons (neutrons) in ^{48}Ti (^{48}Fe). There are only two such particles in the fp shell-model space. Similarly, poor agreement was observed for the $A = 46, T = 1$ mirrors [8], presumably for similar reasons (missing two-particle two-hole excitations across the ^{40}Ca shell closure).

Although a single, negative $J = 0$ matrix element for V_B is largely enough to account for the experimental MED data in the $f_{\frac{7}{2}}$ shell, a better overall fit to $f_{\frac{7}{2}}$ nuclei was obtained by a full set of effective isovector ($V_{pp} - V_{nn}$) matrix elements in the $f_{\frac{7}{2}}$ shell. The values for these matrix elements were $V_B = -72(7)$, $+32(6)$, $+8(6)$, $-12(4)$ keV for $J = 0$, 2, 4, 6 couplings, respectively, of the $f_{\frac{7}{2}}$ orbital. The result of a shell-model calculation, using these coefficients for V_B, added to the two-body interaction for protons in the $f_{\frac{7}{2}}$ shell, as shown by the dashed line in Figs. 7.4 (a) and (b). This results in a noticeable further improvement in the agreement with the experimental MED data for the yrast states.

From Fig. 7.3, it can be seen that all isospin-breaking contributions are significant for the observed states, particularly the $J^\pi = 2_1^+$, 4_1^+, 4_2^+ and 6_2^+ states. As a result, without all these terms, predictions for these states would be impossible.

In addition to a large difference in Z between the nuclei, this mirror pair also has two additional unique features. First, all the positive parity states observed, both the yrast and yrare states, were populated in both mirror nuclei. This allows MED analysis to be performed for both types of states. Second, being at the exact centre of an isolated $f_{\frac{7}{2}}$ shell, mirror nuclei with A=48 with 48 particles have a cross-conjugate symmetry [21] as well as mirror symmetry.

The cross-conjugate symmetry is a feature of a shell-model calculation performed in a single j-shell, where in such a single j, the particles behave like holes. The cross conjugate partners are usually obtained by swapping protons for neutron holes and

neutrons for proton holes. For example, ^{42}Ti (N=22, Z=20) is the cross-conjugate partner of ^{54}Ni (N=28, Z=26), and ^{42}Ca (N=20, Z=22) is the cross-conjugate partner of ^{54}Fe (N=26, Z=28) [21]. In the shell model, all these four nuclei have identical structures (assuming no Coulomb or INC terms are added) where there are two pairs of cross-conjugate partners and two pairs of mirror partners.
However, nuclei that are mid-shell, i.e., $A = 48$ (^{48}Fe/^{48}Ti) have a special property which is that they are their own cross conjugate partners. For example, in the case of ^{48}Fe, if swapping protons for neutron holes and neutrons for proton holes, it ends up back at ^{48}Fe. This means that the two fluids (protons and neutrons) have similar properties and behave the same way – the protons act like the neutrons, and the neutrons act like the protons. This happens in both mirror nuclei,^{48}Fe/^{48}Ti, and if this is the case, the MED will be zero. However, this is not quite true since the $f_{\frac{7}{2}}$ shell is not isolated and there are excitations.
Assuming an isolated $f_{\frac{7}{2}}$ shell, ^{48}Fe has two neutrons and two proton holes in the shell, while ^{48}Ti has two protons and two neutron holes. In this case, all multipole Coulomb effects contributing to the MED, which usually dominate, would be zero. Since the largest components of the wave functions are of the form $\pi(\nu)f_{\frac{7}{2}}^{6}\nu(\pi)f_{\frac{7}{2}}^{2}$, the Coulomb multipole contributions to the MED may therefore be predicted to be small. Despite the cross-conjugate nature of the mirror pair A=48, the magnitude of the experimental MED is large as compared to other cases in this region [8], and the multipole components of the MED in the shell model are the dominant components.

To demonstrate the effect of cross-conjugate symmetry, a calculation was truncated for A=48 to prevent any particles from being excited into the upper fp orbitals, i.e. $p_{\frac{3}{2}}$, $p_{\frac{1}{2}}$ and $f_{\frac{5}{2}}$. The results of this calculation shown in Fig. 7.5 indicate that all the four isospin-breaking terms, as described above, switch off to zero when there is no excitations allowed out of the $f_{\frac{7}{2}}$ shell. The cross-conjugate symmetry nuclei in the $f_{\frac{7}{2}}$ shell (as in this work, $A = 48$) results in the cancellation of isovector multipole effects ($V_{pp} - V_{nn}$) in a single j shell. The (V_{Cr}) term that was used to track changes in radius, has a contribution to the MED due to the

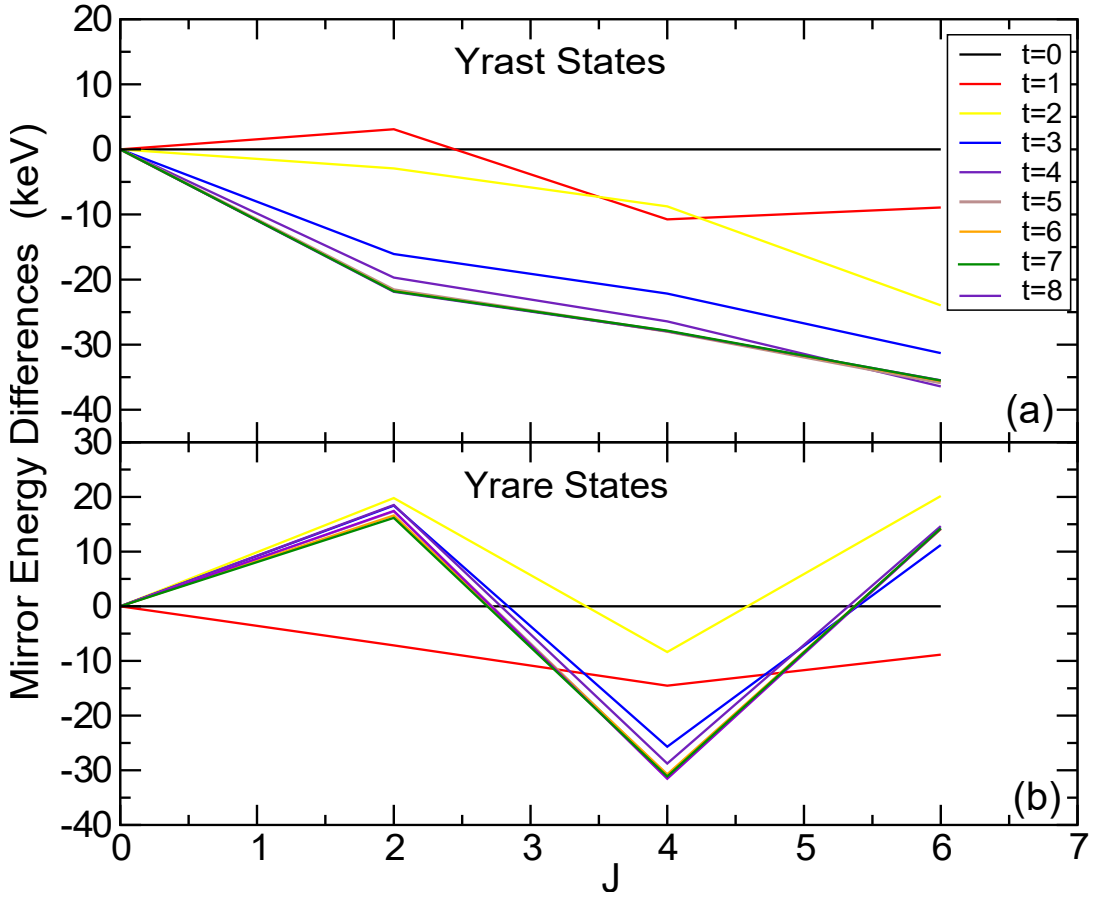

Figure 7.5: A theoretical MED results for the A=48, $T_z = \pm 2$ mirror yrast (a) and yrare states (b) with the particle restricted in $f_{7/2}$ shell ($t = 0$) where MED = 0. The MED changes dramatically once the particles are excited out of the $f_{7/2}$ shell (t = 1, 2, 3, 4, 5, 6, 7, and 8). In (b), the MED for the $J \neq 0$ yrare states are plotted relative to the $J = 0$ ground state.

difference in proton number. This term is dependent on the occupation of the $p_{\frac{3}{2}}$ shell, and since there is no excitation out the $f_{\frac{7}{2}}$ shell, that will stop all the occupations of the $p_{\frac{3}{2}}$ shell, hence the V_{Cr} is also turned to zero by default. The V_{ll}+V_{ls} term is zero since it results from the difference in the energy levels (shell-model levels) as a result of Coulomb and magnetic effects. Therefore, if there is no excitation out of the $f_{\frac{7}{2}}$ level, then this term also does not contribute to the MED. Shell-model calculations have been performed with the number of excitations (t) allowed in the upper fp shell. The results of these calculations show that the MED change dramatically once the particles are excited out of the $f_{7/2}$ shell (t = 1, 2, 3, 4, 5, 6, 7, and 8) (Fig. 7.5). Fig. 7.5 shows that all four INC components require

excitations out of the $f_{\frac{7}{2}}$ shell, to generate a non-zero MED.

The number t required in order for the calculations to converge can be determined by plotting the excitation energies versus t and observing where convergence occurs. An example of this is seen in Fig. 7.6, which demonstrates that in the $A = 48$ case, a good agreement with experimental data is achieved by $t >4$. Therefore, the MED results presented here due to their location within the shell and the resulting cross-conjugate symmetry, are especially sensitive to excitations out of the $f_{\frac{7}{2}}$ shell and present a stringent test of the shell-model prescription.

From Fig. 7.6, it is worth noting that there is a discrepancy in the energy levels between the shell model and experimental data for both the yrast 6_1^+ and yrare 2_2^+ states compared to the other states. Moreover, if there is no excitation particle out of the $f_{7/2}$ shell (t=0), the 6_1^+ and 6_2^+ states are far from each other, which disagree with the experimental data. Therefore, all these different excitations out of the $f_{\frac{7}{2}}$ shell are required to get the 6_1^+ and 6_2^+ states close to each other, and these two states stopped approaching together at $t = 7$ (Fig. 7.6). A similar observation was seen for the 2_2^+ state (Fig. 7.6). A similar discrepancy for the 2_2^+ and 6_1^+ states can also be seen in the MED results (Fig. 7.4).

The exclusion of the *sd* excitations across the ^{40}Ca shell closure in these models is likely to affect the capability of the model to reproduce data accurately. Mirror pairs such as this one are good test case for any shell-model approach that is capable of working in a space with both lower-fp and upper-*sd*-shell orbitals.

In summary, for the MED, the cross-conjugate nature is important and unique to mirror nuclei at the precise centre of an isolated single-j shell, i.e. $A = 48$ mirror pair at the centre of the $f_{\frac{7}{2}}$ shell. Since all non-zero contributions to the MED must originate from excitations out of the $f_{\frac{7}{2}}$ shell, this presents an ideal test of the shell model valence space.

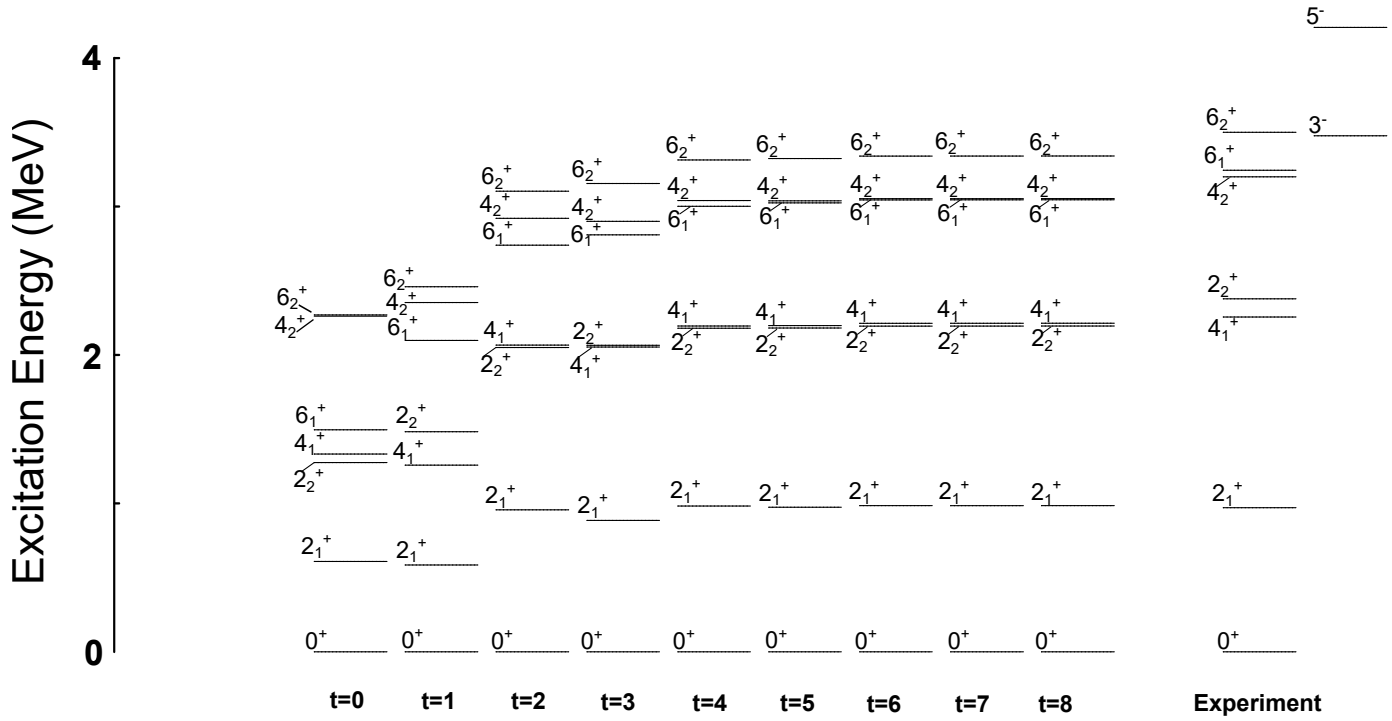

Figure 7.6: Theoretical energy-level schemes predicted by large-scale shell-model calculations using KB3G interaction in comparison with experimental energy-levels schemes of populated states in one-neutron knockout from ^{49}Fe to ^{48}Fe. The figure shows the evolution of theoretical levels with the number of excitations allowed to the upper fp shell, t. The negative parity states ($J^\pi = 3^-$ and 5^-) cannot be made from KB3G shell-model calculations and, hence, are not present in the t schemes. Theoretical energies converge towards experimental values, reaching good agreement from $t = 4$ up to 8.

Chapter 8

Conclusion and Future Work

In summary, an examination of isospin-symmetry breaking was performed for nuclei in the $f_{\frac{7}{2}}$ region, from which new results were obtained. An experimental run was performed at the NSCL with the primary aim of performing γ-ray spectroscopy on the $T_z = -2$ nucleus ^{48}Fe through the application of the mirrored-knockout approach. Many new γ rays were identified in the proton-rich nucleus ^{48}Fe ($T_z = -2$), from which a new-level scheme was established for the first time, using a wide range of analytical tools. These states were compared to those in its mirror nucleus ^{48}Ti, with both yrast and yrare states up to 6^+ state populated in both mirror nuclei as well as the negative parity states (resulting from *sd* removal). Both exclusive and inclusive cross sections were measured for the ^{48}Fe /^{48}Ti mirror pair, where significant differences were observed between the inclusive knockout reaction cross sections for the mirrored reactions. The difference between nucleon separation energies for the mirror pairs, which leads to very different degrees of *sd*-shell knockout strengths to bound states, is most likely to be the main cause for this observation. There are only two other recent studies of analogue knockout reactions for nuclei around the $N = Z$ line [27,28]; in both cases, the inclusive cross sections were also asymmetric (factor of $\sim$ 3–4 different). However, the asymmetry factor of $\sim$ 9 observed in the current work is significantly larger than anything

observed to date.

A detailed comparison of experimental and theoretical exclusive cross sections was performed for the mirrored one-nucleon knockout reactions populating the mirror pair. The theoretical cross sections also provided an additional confidence in the level scheme of ^{48}Fe that was produced, especially for the strong direct population of the yrare states. Generally, the absolute values of the measured exclusive cross sections were observed to be much smaller than the theoretical values for ^{48}Fe. However, a notable agreement between the distribution of relative cross sections, and some of the key observations of the experimental data, such as the strong direct population of the yrare states, were well reproduced.

Comparison of the experimental exclusive cross sections for some of the specific pairs of analogue states (yrare states) was also performed, where isospin symmetry suggests that the cross sections must be similar. The data tentatively suggested significant differences in these cross sections, although additional unseen feeding to the states cannot be ruled out.

Due to the significantly different degrees of binding energies between the two members of the mirror pair, the mirrored cross sections were investigated in the context of the well-documented systematic suppression of spectroscopic strength as a function of binding energy for knockout reactions at intermediate energies. The systematics of degrees of suppression (experiment compared with theory) of the yrare states have a similar trend as the published R_s systematics for inclusive cross sections [24–26]. This observation was not easy to explain since the spectroscopic factors were essentially identical, and there is only a small dependence on ΔS in the single-particle theoretical cross sections.

Moreover, the experimental inclusive cross section measured for the $A = 45$ (^{45}V/^{45}Ti) mirror pair provided a second example showing asymmetry in the mirrored knockout reaction, similar to what was observed in $A = 48$ mirror nuclei, even though this was an $N = Z$ beam. Hence, there must again be significant unseen feeding into the low-lying yrast states and ground states of ^{45}Ti, which may affect the inclusive cross section. This analysis has not been completed yet

and will be continued in future work.

The significant differences between the ratios of the experimental to theoretical cross sections for the mirror pairs observed in this work may indicate an issue with the reaction model that might be worthy of future investigation. Experimentally, the next logical step is to continue conducting mirrored knockout exclusive cross-section measurements along the $N \sim Z$ line in very weakly bound systems to observe whether a continuation of these asymmetries can be seen. Experiments have already been performed to measure the mirrored knockout cross section for the ^{47}Mn/^{47}Ti ($T_z = \pm\frac{3}{2}$) mirror pair. This $A = 47$ mirror pair has very different values of ΔS, where all the states above the ground state are unbound (S_p=0.383 MeV [96]). The statistics obtained for ^{48}Fe during this experiment were very low. Accordingly, the measurements presented in this thesis demonstrated the need for repeat measurements with high statistics experiments to obtain a high level of confidence in the exclusive cross-section measurements. In this work, for example, the exclusive cross sections of the yrare states were presented as upper limits due to the possibility that some unseen feeding may be taking place into these states of ^{48}Ti, despite their yrare nature. It is possible that with high statistics measurements, this unseen feeding can be taken into account for the cross-section measurements. Moreover, since no model to date has been able to evaluate the spectroscopic factors for the *sd* shell removal to reproduce these results, it would be challenging to obtain a shell-model calculation that accounts for all these missing spectroscopic strengths.

Finally, experimental MED between IAS in the $A = 48$, $T_z = \pm 2$ mirror pair have been computed and compared to large-scale shell-model calculations incorporating INC contributions. The results show strong evidence in support of the need to include all sets of these isospin-symmetry breaking terms in the analysis of mirror nuclei. Due to the additional cross-conjugate symmetry of these $A = 48$ mirror in the $f_{\frac{7}{2}}$ shell, the MED are shown to be especially sensitive to cross-shell excitations and, thus, allow for a probe into the validity of the shell-model space used. The success of the modelling of the $A = 48$ MED with the KB3G model is a

good achievement and a big step towards further development for explaining MED through a density-functional theory (DFT) model approach in the future. This approach will provide access to precise MED calculations in mass regions that may otherwise not have been available using the traditional shell-model calculation as it is computationally limited.

It is clear that the $A = 48$ mirror pair is a good test case for any shell-model approach capable of calculating in an orbital space containing the lower-pf and upper-sd shell orbitals. For MED, by excluding sd excitations across the ^{40}Ca shell closure in these calculations, the ability of the model to reproduce the data correctly might be undermined. Therefore, this indicates the need to provide a shell-model interaction that spans the sd and pf shells and accounts for sd-shell components in the wave functions of the $f_{\frac{7}{2}}$ nuclei.

Abbreviations

MSU - Michigan State University

NSCL - National Superconducting Cyclotron Laboratory

PID - Particle Identification

OBJ - Object Scintillator

GRETA - Gamma-Ray Energy Tracking Array

GRETINA - Gamma-Ray Energy Tracking In-beam Nuclear Array

HPGe - High-Purity Germanium

CRDC - Cathode Readout Drift Chamber

ToF - Time of Flight

XFP - Extended Focal Plane Scintillator

DAQ - Data Acquisition

DFT - Density Functional Theory

FoM - Figure of Merit

HF - Hartree-Fock

CSB - Charge Symmetry Breaking

MED - Mirror Energy Difference

IAS - Isobaric Analogue States

INC - Isospin-Non-Conserving

ECR - Electron Cyclotron Resonance

SuSI - Superconducting Source for Ions

ToF - Time-of-Flight

References

[1] Eugene Wigner. On the consequences of the symmetry of the nuclear hamiltonian on the spectroscopy of nuclei. *Physical Review*, 51(2):106, 1937.

[2] NS Pattabiraman, DG Jenkins, MA Bentley, R Wadsworth, CJ Lister, MP Carpenter, RVF Janssens, TL Khoo, T Lauritsen, D Seweryniak, et al. Analog E1 transitions and isospin mixing. *Physical Review C*, 78(2):024301, 2008.

[3] SA Milne, MA Bentley, EC Simpson, P Dodsworth, T Baugher, Dominique Bazin, JS Berryman, AM Bruce, PJ Davies, C Aa Diget, et al. Mirrored one-nucleon knockout reactions to the T_z=±3/2 A= 53 mirror nuclei. *Physical Review C*, 93(2):024318, 2016.

[4] C Dossat, N Adimi, F Aksouh, F Becker, A Bey, B Blank, C Borcea, R Borcea, A Boston, M Caamano, et al. The decay of proton-rich nuclei in the mass A= 36–56 region. *Nuclear Physics A*, 792(1-2):18–86, 2007.

[5] PD Cottle, Z Hu, BV Pritychenko, JA Church, M Fauerbach, T Glasmacher, RW Ibbotson, KW Kemper, LA Riley, H Scheit, et al. 0 $gs^+ \rightarrow 2_1^+$ excitations in the mirror nuclei ^{32}Ar and ^{32}Si. *Physical review letters*, 88(17):172502, 2002.

[6] PJ Davies, MA Bentley, TW Henry, EC Simpson, A Gade, SM Lenzi, T Baugher, D Bazin, JS Berryman, AM Bruce, et al. Mirror energy differences at large isospin studied through direct two-nucleon knockout. *Physical review letters*, 111(7):072501, 2013.

[7] AP Zuker, SM Lenzi, G Martinez-Pinedo, and A Poves. Isobaric multiplet yrast energies and isospin nonconserving forces. *Physical review letters*, 89(14):142502, 2002.

[8] MA Bentley and SM Lenzi. Coulomb energy differences between high-spin states in isobaric multiplets. *Progress in Particle and Nuclear Physics*, 59(2):497–561, 2007.

[9] MA Bentley, SM Lenzi, SA Simpson, and C Aa Diget. Isospin-breaking interactions studied through mirror energy differences. *Physical Review C*, 92(2):024310, 2015.

[10] K Kaneko, Y Sun, T Mizusaki, and S Tazaki. Variation in displacement energies due to isospin-nonconserving forces. *Physical Review Letters*, 110(17):172505, 2013.

[11] CD O'Leary, MA Bentley, DE Appelbe, DM Cullen, S Ertürk, RA Bark, A Maj, and T Saitoh. Mirror symmetry up to the band termination in ^{49}Mn and ^{49}Cr. *Physical review letters*, 79(22):4349, 1997.

[12] SM Lenzi, N Mărginean, DR Napoli, CA Ur, AP Zuker, G De Angelis, A Algora, M Axiotis, D Bazzacco, Nicola Belcari, et al. Coulomb energy differences in T= 1 mirror rotational bands in ^{50}Fe and ^{50}Cr. *Physical review letters*, 87(12):122501, 2001.

[13] Yi Hua Lam, Nadezda A Smirnova, Etienne Caurier, et al. Isospin nonconservation in *sd*-shell nuclei. *Physical Review C*, 87(5):054304, 2013.

[14] MA Bentley, CD O'Leary, A Poves, G Martınez-Pinedo, DE Appelbe, RA Bark, DM Cullen, S Ertürk, and A Maj. Mirror and valence symmetries at the centre of the $f7/2$ shell. *Physics Letters B*, 437(3-4):243–248, 1998.

[15] DMa Debenham, MAa Bentley, PJa Davies, Ta Haylett, DGa Jenkins, Pa Joshi, LFa Sinclair, Ra Wadsworth, Panu Ruotsalainen, J Henderson, et al. Spectroscopy of ^{70}Kr and isospin symmetry in the T= 1 fpg shell nuclei. *Physical Review C*, 94(5):054311, 2016.

[16] Jörgen Ekman, Claes Fahlander, and Dirk Rudolph. Mirror symmetry in the upper fp shell. *Modern Physics Letters A*, 20(39):2977–2992, 2005.

[17] K Kaneko, S Tazaki, T Mizusaki, Y Sun, M Hasegawa, and G De Angelis. Isospin symmetry breaking at high spins in the mirror pair ^{67}Se and ^{67}As. *Physical Review C*, 82(6):061301, 2010.

[18] JR Brown, MA Bentley, P Adrich, D Bazin, JM Cook, C Aa Diget, A Gade, T Glasmacher, SM Lenzi, S McDaniel, et al. First γ-ray spectroscopy of ^{49}Fe and ^{53}Ni: Isospin-breaking effects at large proton excess. *Physical Review C*, 80(1):011306, 2009.

[19] MJ Taylor, MA Bentley, JR Brown, PE Kent, R Wadsworth, CJ Lister, D Seweryniak, MP Carpenter, RVF Janssens, S Zhu, et al. Isospin symmetry in the odd-odd mirror nuclei ^{44}V/^{44}Sc. *Physical Review C*, 84(6):064319, 2011.

[20] Scott Alexander Milne. *Investigation of Isospin Symmetry Breaking in the $f7/2$ Region, Studied through One-nucleon Knockout and Lifetime Measurements*. PhD thesis, University of York, 2016.

[21] A Gadea, SM Lenzi, S Lunardi, N Mărginean, AP Zuker, G De Angelis, M Axiotis, T Martinez, DR Napoli, E Farnea, et al. Observation of ^{54}Ni: Cross-conjugate symmetry in $f7/2$ mirror energy differences. *Physical review letters*, 97(15):152501, 2006.

[22] SJ Williams, MA Bentley, DD Warner, AM Bruce, JA Cameron, MP Carpenter, P Fallon, L Frankland, W Gelletly, RVF Janssens, et al. Anomalous coulomb matrix elements in the $f7/2$ shell. *Physical Review C*, 68(1):011301, 2003.

[23] N Michel, Witold Nazarewicz, and M Płoszajczak. Isospin mixing and the continuum coupling in weakly bound nuclei. *Physical Review C*, 82(4):044315, 2010.

[24] A. Gade, P. Adrich, D. Bazin, M. D. Bowen, B. A. Brown, C. M. Campbell, J. M. Cook, T. Glasmacher, P. G. Hansen, K. Hosier, et al. Reduction of spectroscopic strength: Weakly-bound and strongly-bound single-particle states studied using one-nucleon knockout reactions. *Physical Review C*, 77(4):044306, 2008.

[25] JA Tostevin and A Gade. Systematics of intermediate-energy single-nucleon removal cross sections. *Physical Review C*, 90(5):057602, 2014.

[26] J. A. Tostevin and A. Gade. Updated systematics of intermediate-energy single-nucleon removal cross sections. *Physical Review C*, 103:054610, 2021.

[27] K. Wimmer, W. Korten, T. Arici, P. Doornenbal, P. Aguilera, A. Algora, T. Ando, H. Baba, B. Blank, A. Boso, et al. Shape coexistence and isospin symmetry in A= 70 nuclei: Spectroscopy of the $T_z = -1$ nucleus ^{70}Kr. *Physics Letters B*, 785:441–446, 2018.

[28] M Spieker, A Gade, D Weisshaar, BA Brown, JA Tostevin, B Longfellow, P Adrich, D Bazin, MA Bentley, JR Brown, et al. One-proton and one-neutron knockout reactions from N= Z= 28 ^{56}Ni to the A= 55 mirror pair ^{55}Co and ^{55}Ni. *Physical Review C*, 99(5):051304, 2019.

[29] TW Burrows. Nuclear data sheets for A= 48. *Nuclear Data Sheets*, 107(7):1747–1922, 2006.

[30] Werner Heisenberg. On the structure of atomic nuclei. *Z. Phys*, 77(1), 1932.

[31] DJ Dean, SE Koonin, K Langanke, and PB Radha. Rotational and pairing properties of ^{74}Rb. *Physics Letters B*, 399(1-2):1–7, 1997.

[32] J Garces Narro, C Longour, PH Regan, B Blank, CJ Pearson, M Lewitowicz, C Miehe, W Gelletly, D Appelbe, L Axelsson, et al. Fermi superallowed β^+ decays and T= 1 ground states of heavy odd-odd N= Z nuclei. *Physical Review C*, 63(4):044307, 2001.

[33] R Machleidt and I Slaus. The nucleon-nucleon interaction. *Journal of Physics G: Nuclear and Particle Physics*, 27(5):R69, 2001.

[34] EP Wigner. Proceedings of the robert a. welch foundation conference on chemical research. 1957.

[35] Walter Benenson and Edwin Kashy. Isobaric quartets in nuclei. *Reviews of Modern Physics*, 51(3):527, 1979.

[36] WE Ormand and BA Brown. Empirical isospin-nonconserving hamiltonians for shell-model calculations. *Nuclear Physics A*, 491(1):1–23, 1989.

[37] Maria Goeppert Mayer. On closed shells in nuclei. ii. *Physical Review*, 75(12):1969, 1949.

[38] Otto Haxel, J Hans D Jensen, and Hans E Suess. On the" magic numbers" in nuclear structure. *Physical Review*, 75(11):1766, 1949.

[39] Kenneth S Krane, David Halliday, et al. *Introductory nuclear physics*, volume 465. Wiley New York, 1988.

[40] J. Cubiss. Nuclear structure – spherical shell model, 2019.

[41] R Casten and Richard F Casten. *Nuclear structure from a simple perspective*, volume 23. Oxford University Press on Demand, 2000.

[42] Peter Navratil and Bruce R Barrett. Large-basis shell-model calculations for p-shell nuclei. *Physical Review C*, 57(6):3119, 1998.

[43] Etienne CAURIER. Antoine. man. *Acta Physica Polonica*, 30:705, 1999.

[44] Thomas Henry. *Mirror and Triplet spectroscopy in the fp shell with SeGA and GRETINA*. PhD thesis, University of York, 2015.

[45] A Poves, J Sánchez-Solano, E Caurier, and F Nowacki. Shell model study of the isobaric chains A= 50, A= 51 and A= 52. *Nuclear Physics A*, 694(1-2):157–198, 2001.

[46] M Honma, T Otsuka, BA Brown, and T Mizusaki. Shell-model description of neutron-rich pf-shell nuclei with a new effective interaction gxpf 1. *The European Physical Journal A-Hadrons and Nuclei*, 25(1):499–502, 2005.

[47] DD Warner, MA Bentley, and P Van Isacker. The role of isospin symmetry in collective nuclear structure. *Nature Physics*, 2(5):311–318, 2006.

[48] JA Nolen Jr and JP Schiffer. Coulomb energies. *Annual Review of Nuclear Science*, 19(1):471–526, 1969.

[49] J Duflo and AP Zuker. Mirror displacement energies and neutron skins. *Physical Review C*, 66(5):051304, 2002.

[50] J Hüfner, K Schäfer, and B Schürmann. Abrasion-ablation in reactions between relativistic heavy ions. *Physical Review C*, 12(6):1888, 1975.

[51] Jan Ryckebusch, Dimitri Debruyne, Pascal Lava, Stijn Janssen, Bart Van Overmeire, and Tim Van Cauteren. Relativistic formulation of glauber theory for a (e, eṕ) reactions. *Nuclear physics a*, 728(1-2):226–250, 2003.

[52] Dott Marco Selvi, Dott Matteo Franchini, and Riccardo Ridolfi. Study of the track reconstruction in the foot experiment for hadrontherapy.

[53] BA Brown, PG Hansen, BM Sherrill, and JA Tostevin. Absolute spectroscopic factors from nuclear knockout reactions. *Physical Review C*, 65(6):061601, 2002.

[54] PG Hansen and JA Tostevin. Direct reactions with exotic nuclei. *Annual Review of Nuclear and Particle Science*, 53(1):219–261, 2003.

[55] JA Tostevin. Single-nucleon knockout reactions at fragmentation beam energies. *Nuclear Physics A*, 682:320C–331C, 2001.

[56] Alexandra Gade and Thomas Glasmacher. In-beam nuclear spectroscopy of bound states with fast exotic ion beams. *Progress in Particle and Nuclear Physics*, 60(1):161–224, 2008.

[57] AEL Dieperink and T de Forest Jr. Center-of-mass effects in single-nucleon knock-out reactions. *Physical Review C*, 10(2):543, 1974.

[58] Dolores Cortina-Gil. Direct reactions at relativistic energies: A new insight into the single-particle structure of exotic nuclei. In *The Euroschool on Exotic Beams, Vol. IV*, pages 183–232. Springer, 2014.

[59] JA Tostevin and BA Brown. Diffraction dissociation contributions to two-nucleon knockout reactions and the suppression of shell-model strength. *Physical Review C*, 74(6):064604, 2006.

[60] EC Simpson, Jeffrey Allan Tostevin, D Bazin, BA Brown, and A Gade. Two-nucleon knockout spectroscopy at the limits of nuclear stability. *Physical review letters*, 102(13):132502, 2009.

[61] JA Tostevin. Core excitation in halo nucleus break-up. *Journal of Physics G: Nuclear and Particle Physics*, 25(4):735, 1999.

[62] Nicky Paul Patterson. *Study of $^{28,\ 27,\ 26,\ 25}$Ne and $^{29,\ 28,\ 27}$Na Isotopes via the Single Neutron Knockout Reaction Mechanism.* University of Surrey (United Kingdom), 2010.

[63] V Maddalena, T Aumann, D Bazin, BA Brown, JA Caggiano, B Davids, T Glasmacher, PG Hansen, RW Ibbotson, A Navin, et al. Single-neutron knockout reactions: Application to the spectroscopy of $^{16,\ 17,\ 19}$C. *Physical Review C*, 63(2):024613, 2001.

[64] JS Al-Khalili, JA Tostevin, and IJ Thompson. Radii of halo nuclei from cross section measurements. *Physical review C*, 54(4):1843, 1996.

[65] JA Tostevin and JS Al-Khalili. Sizes of the he isotopes deduced from proton elastic scattering measurements. In *AIP Conference Proceedings*, volume 455, pages 227–232. American Institute of Physics, 1998.

[66] Jim Al-Khalili and Filomena Nunes. Reaction models to probe the structure of light exotic nuclei. *Journal of Physics G: Nuclear and Particle Physics*, 29(11):R89, 2003.

[67] D _ J Morrissey, BM Sherrill, M Steiner, A Stolz, and I Wiedenhoever. Commissioning the a1900 projectile fragment separator. *Nuclear Instruments and Methods in Physics Research Section B: Beam Interactions with Materials and Atoms*, 204:90–96, 2003.

[68] D Weisshaar, D Bazin, PC Bender, CM Campbell, F Recchia, V Bader, T Baugher, J Belarge, MP Carpenter, HL Crawford, et al. The performance of the γ-ray tracking array gretina for γ-ray spectroscopy with fast beams of rare isotopes. *Nuclear Instruments and Methods in Physics Research Section A: Accelerators, Spectrometers, Detectors and Associated Equipment*, 847:187–198, 2017.

[69] S Paschalis, IY Lee, AO Macchiavelli, CM Campbell, M Cromaz, S Gros, J Pavan, J Qian, RM Clark, HL Crawford, et al. The performance of the gamma-ray energy tracking in-beam nuclear array gretina. *Nuclear Instruments and Methods in Physics Research Section A: Accelerators, Spectrometers, Detectors and Associated Equipment*, 709:44–55, 2013.

[70] D Bazin, JA Caggiano, BM Sherrill, J Yurkon, and A Zeller. The s800 spectrograph. *Nuclear Instruments and Methods in Physics Research Section B: Beam Interactions with Materials and Atoms*, 204:629–633, 2003.

[71] A Gade and BM Sherrill. Nscl and frib at michigan state university: Nuclear science at the limits of stability. *Physica Scripta*, 91(5):053003, 2016.

[72] PA Zavodszky, B Arend, D Cole, J DeKamp, G Machicoane, F Marti, P Miller, J Moskalik, J Ottarson, J Vincent, et al. Design of susi–superconducting source for ions at nscl/msu–ii. the conventional parts. *Nuclear Instruments and Methods in Physics Research Section B: Beam Interactions with Materials and Atoms*, 241(1-4):959–964, 2005.

[73] DJ Morrissey. The coupled cyclotron project at the nscl. *Nuclear Physics A*, 616(1-2):45–55, 1997.

[74] "S800 Documentation". https://wikihost.nscl.msu.edu/S800Doc/doku.php. [Online; Accessed: 2021-03-1].

[75] J Yurkon, D Bazin, W Benenson, DJ Morrissey, BM Sherrill, D Swan, and R Swanson. Focal plane detector for the s800 high-resolution spectrometer. *Nuclear Instruments and Methods in Physics Research Section A: Accelerators, Spectrometers, Detectors and Associated Equipment*, 422(1-3):291–295, 1999.

[76] D. Bazin. "S800 spectograph service level description,". https://www.nscl.msu.edu/users/s800_sld-Feb20171.pdf. [Online; Accessed: 25-Feb-2021].

[77] Joseph Grochowski, Brad Sherrill, and Daniel Bazin. Straggling effects in the S800 ion chamber. In *APS Division of Nuclear Physics Meeting Abstracts*, pages 3A–031, 2006.

[78] M Berz, K Joh, JA Nolen, BM Sherrill, and AF Zeller. Reconstructive correction of aberrations in nuclear particle spectrographs. *Physical Review C*, 47(2):537, 1993.

[79] IY Lee, MA Deleplanque, and K Vetter. Developments in large gamma-ray detector arrays. *Reports on progress in physics*, 66(7):1095, 2003.

[80] B Bruyneel, B Birkenbach, and P Reiter. Pulse shape analysis and position determination in segmented hpge detectors: The agata detector library. *The European Physical Journal A*, 52(3):1–11, 2016.

[81] K. Wimmer "ROOT based analysis software for GRETINA at NSCL". https://github.com/wimmer-k/GrROOT. [Online; Accessed: 2021-09-07].

[82] Rene Brun and Fons Rademakers. Root—an object oriented data analysis framework. *Nuclear Instruments and Methods in Physics Research Section A: Accelerators, Spectrometers, Detectors and Associated Equipment*, 389(1-2):81–86, 1997.

[83] M Hautala, A Anttila, and J Keinonen. Relative intensities of gamma-rays from/sup ^{56}Co standard source. *Nucl. Instrum. Methods;(Netherlands)*, 150(3), 1978.

[84] Shaheen Rab. Nuclear data sheets update for A= 133. *Nuclear Data Sheets*, 75(3):491–666, 1995.

[85] Yasukazu Yoshizawa, Yosei Iwata, and Yasuo Iinuma. Precision measurements of gamma-ray intensities. ii. ^{152}Eu, ^{154}Eu and ^{192}Ir. *Nuclear Instruments and Methods*, 174(1-2):133–139, 1980.

[86] Ryan David Owen Llewellyn. *Structure and Collectivity of Highly Deformed Nuclei Along the N= Z Line*. PhD thesis, University of York, 2020.

[87] MA Bentley, I Paterson, JR Brown, MJ Taylor, C Aa Diget, P Adrich, D Bazin, JM Cook, A Gade, T Glasmacher, et al. Isobaric analogue states studied in mirrored fragmentation and knockout reactions. *Modern Physics Letters A*, 25(21n23):1891–1894, 2010.

[88] T. W. Burrows. ENSDF full evaluation. https://www.nndc.bnl.gov/ensdf/EnsdfDispatcherServlet, Apr 2006.

[89] MA Bentley, C Chandler, P Bednarczyk, F Brandolini, AM Bruce, D Curien, O Dorvaux, Jörgen Ekman, E Farnea, W Gelletly, et al. High-spin spectroscopy of natural and unnatural parity states in the mirror-pair ^{45}V/^{45}Ti. *Physical Review C*, 73(2):024304, 2006.

[90] M Bowry, Zs Podolyak, S Pietri, J Kurcewicz, Michael Bunce, PH Regan, F Farinon, H Geissel, C Nociforo, A Prochazka, et al. Population of high-spin isomeric states following fragmentation of 238 u. *Physical Review C*, 88(2):024611, 2013.

[91] SA Milne, MA Bentley, EC Simpson, T Baugher, D Bazin, JS Berryman, AM Bruce, PJ Davies, C Aa Diget, A Gade, et al. Isospin symmetry at high spin studied via nucleon knockout from isomeric states. *Physical review letters*, 117(8):082502, 2016.

[92] T. W. Burrows. ENSDF full evaluation. https://www.nndc.bnl.gov/ensdf/EnsdfDispatcherServlet, Oct 2007.

[93] J. A. Tostevin. University of surrey.

[94] B Alex Brown. New skyrme interaction for normal and exotic nuclei. *Physical Review C*, 58(1):220, 1998.

[95] OB Tarasov and D Bazin. Lise++: Radioactive beam production with in-flight separators. *Nuclear Instruments and Methods in Physics Research Section B: Beam Interactions with Materials and Atoms*, 266(19-20):4657–4664, 2008.

[96] Meng W., W. J. Huang, F. G. Kondev, G. Audi, and S. Naimi. The ame 2020 atomic mass evaluation (ii). tables, graphs and references. *Chinese Physics C*, 45(3):030003, 2021.

[97] CY Fu, YH Zhang, M Wang, XH Zhou, Yu A Litvinov, K Blaum, HS Xu, X Xu, P Shuai, YH Lam, et al. Mass measurements for the T_z=- 2 *fp*-shell nuclei ^{40}Ti, ^{44}Cr, ^{46}Mn, ^{48}Fe, ^{50}Co, and ^{52}Ni. *Physical Review C*, 102(5):054311, 2020.

[98] J. A. Tostevin. University of Surrey, private communication, Jun. 2021.

[99] E. K. Warburton, C. W. Beausang, D. B. Fossan, L. Hildingsson, W. F. Piel, and J. A. Becker. High-spin $(f_{7/2})^{A-40}$ states in ^{47}Ti, ^{47}Sc, ^{44}Ca, ^{45}Ca, and ^{48}Ti via ^{36}C fusion-evaporation reactions. *Phys. Rev. C*, 34:136–151, 1986.

[100] Samuel SM Wong. *Introductory nuclear physics*. John Wiley & Sons, 2008.

[101] SM Lenzi, MA Bentley, R Lau, and C Aa Diget. Isospin-symmetry breaking corrections for the description of triplet energy differences. *Physical Review C*, 98(5):054322, 2018.